

ABSTRACT

Title of Dissertation: **INCREASING HELICITY
TOWARDS A DYNAMO ACTION
WITH ROUGH BOUNDARY
SPHERICAL COUETTE FLOWS**

Rubén E. Rojas
Doctor of Philosophy, 2022

Dissertation Directed by: **Professor Daniel Lathrop**
Department of Physics
Department of Geology

The dynamo action is the process through which a magnetic field is amplified and sustained by electrically conductive flows. Galaxies, stars and planets, all exhibit magnetic field amplification by their conductive constituents. For the Earth in particular, the magnetic field is generated due to flows of conductive material in its outer core. At the University of Maryland, our Three-meter diameter spherical Couette experiment uses liquid sodium between concentric spheres to mimic some of these dynamics, giving insight into these natural phenomena. Numerical studies of Finke and Tilgner (Phys. Rev. E, 86:016310, 2012) suggest a reduction in the threshold for dynamo action when a rough inner sphere was modeled by increasing the poloidal flows with respect to the zonal flows and hence increasing helicity. The baffles change the nature of the boundary layer from a shear dominated to a pressure dominated one, having effects on the angular momentum injection. We present results on a hydrodynamics model of 40-cm diameter spherical

Couette flow filled with water, where torque and velocimetry measurements were performed to test the effects of different baffle configurations. The selected design was then installed in the 3-m experiment. In order to do that, the biggest liquid sodium draining operation in the history of the lab was executed. Twelve tons of liquid sodium were safely drained in a 2 hours operation. With the experiment assembled back and fully operational, we performed magnetic field amplification measurements as a function of the different experimental parameters including Reynolds and Rossby numbers. Thanks to recent studies in the hydrodynamic scale model, we can bring a better insight into these results. Torque limitations in the inner motor allowed us to inject only 4 times the available power; however, amplifications of more than 2 times the internal and external magnetic fields with respect to the no-baffle case was registered. These results, together with time-dependent analysis, suggest that a dynamo action is closer than before; showing the effect of the new baffles design in generating more efficient flows for magnetic field amplification. We are optimistic about new short-term measurement in new locations of the parameter space, and about the rich variety of unexplored dynamics that this novel experiment has the potential to reach. These setups constitute the first experimental explorations, in both hydrodynamics and magnetohydrodynamics, of rough boundary spherical Couette flows as laboratory candidates for successful Earth-like dynamo action.

INCREASING HELICITY TOWARDS DYNAMO ACTION
WITH ROUGH BOUNDARY SPHERICAL COUETTE FLOWS

by

Rubén Eduardo Rojas Garcia

Dissertation submitted to the Faculty of the Graduate School of the
University of Maryland, College Park in partial fulfillment
of the requirements for the degree of
Doctor of Philosophy
2022

Advisory Committee:

Professor Daniel P. Lathrop, Chair/Advisor

Professor Rajarshi Roy

Professor Thomas M. Antonsen, Jr.

Professor James H. Duncan

Professor Yanne K. Chembo

© Copyright by
Rubén E. Rojas
2022

A mi padre.

Acknowledgments

I want to start thanking my advisor Daniel Lathrop, for his unconditional commitment to our personal and professional success. He is one of a kind. In a field that is known for the rough treatment towards grad students, that I have personally witnessed, he is one of the best advisors I could have been blessed to have. I am honored to call you my academic father, and of course, having Yoda as my academic grandfather as well. May the force be with you for ever.

I want another paragraph to express my gratitude and pleasure to have shared my PhD with my partner in crime, Artur Perevalov. I would not have been the same without you. You made these (sometimes) tormentous years go so easy (sometimes). Having someone to talk about your life, your experiences, your thoughts, on a daily basis, is definitely something I didn't value as I should have. I wish the future and our home countries would let us see each other on a more regular basis than we think. Nos vemos compadre. Sabes que tienes la casa en Margarita cuando quieras.

I want to thank all the staff in IREAP/Physics for all the unconditional help and assistance they provided. Judy, Dottie, Taylor, Roxanne Defendinni, Josiland, Jessica and of course the forever intimidating but incredibly efficient Nancy. Mis cariños. I also want a special mention to Nolan Ballew, for being there with me since the beginning, for all the infinite lessons and all the shared Youtube videos. I still need to be proficient in welding, which I will do with him after I submit this dissertation. I want a special mention as well to Daniel Serrano, who was

my publishing and writing mentor during all my PhD; por su paciencia, su consideración y su solidaridad incondicional. Finally, I want to thank Don Schmadel, Don Martin, Brian Quinn and Tom Weimar, not only for the impeccable work they do, but mostly for the casual talks in the hall and the office, when I showed up inadvertently, for those I will be forever grateful. Thanks for the lessons. Oh, a last mention: when Don Martin said that I should learn Imperial Units because I was not in Venezuela anymore, even then I learned. I continue learning.

I want to thank my gringo friends Landry, Harry, Jamie, Mary, Luc, for showing me that there are really precious people everywhere that you should treasure. Thanks for the complicity, the beers and the friendship. I want to thank my coworkers Peter, Itamar, Minh, Liam, Shiyi and Elaine. I want to also thank all my roommates: Paniz, Vicky, Valentina, Daybert, Walter, Pedro, Suraj, Juan, Alvaro y Alejandro. For sharing nada menos que su vida conmigo. No se dice fácil.

Ya vamos entrando en calor. Quiero agradecer especialmente a Juan, Walter y Daybert, por convertirse en más que mis roommates en mis panas. Que la vida nos siga uniendo en el futuro. Ojalá pudiera llevarlos a todos en el bolsillo. Capaz a Juan sí puedo jejej. Por supuesto quiero darle las gracias a todos mis panas que la distancia y la inmigración nos hizo más cercanos que cuando estábamos juntos (gracias Chiabes): a Pablo, Edgard, Diogenes, Luis, Sabrina, Julian, Irina, Kike y Gocho. Los últimos tres, mis compañeros podcasteros, que hicieron infinitamente más llevadero mis últimos años del infernal PhD. ¡Tenemos que grabar coño!

A los que siempre agradeceré sin importar lo que haga en la vida va ser a el trío de siempre, los que tal. No hay otros. Gracias David, Carlos y Alejandro. Mis hermanos de la vida. Ya uno empieza a quedarse sin palabras. Gracias por la hermandad, la humildad, los consejos, el cariño y sobre todo la incondicionalidad. Agarrense que ahora es que nos queda. No puedo irme sin hacer una especial mención al que tengo 20 años compartiendo la vida. Ni tu hermana mmg. Que

buen camino nos ha dado la vida. Pide el cambio a Zurich para seguir rompiendo el record. Te quiero que jode hermano.

De antepenultimo, quiero más que agradecer, dedicar; más que este trabajo, el tiempo, sudor, lágrimas, esfuerzos, emociones y logros alcanzados en este PhD. A mi compañera de vida. La única que hacía que valiera la pena mi semana. La que me pone los pies en la tierra. La que me enseña literatura y poesía. La que me complementa. Recuerda que el mundo no necesita ciencia. El mundo necesita humanidad, la humanidad que tú tienes. Eres el Teseo de mi Asterión, que me liberó de este laberinto. ¿Creerán ustedes?, apenas ofrecí resistencia.

Por último quiero agradecer a mis Padres. Las cosas que aprende uno en la vida. En mi tesis de pregrado les agradecí de primero: “A mis padres, porque me dieron lo más valioso e invaluable que uno puede pedir en la vida: educación, valores y principios. Un primer empujón que guía tus velas por el resto de tu vida. Los quiero mucho.” Hoy les digo que los amo con todo mi corazón. Que la vida es tan sublime como injusta. Pero dentro de ese balance nos hallamos a nosotros mismos. Gracias por siempre Madre. Que la vida me regale todos los años del mundo contigo. Gracias Padre porque desde donde estás sigues siendo el motor de este barco. Aquí seguiremos campeonando por el equipo.

Table of Contents

| | |
|---|------|
| Dedication | ii |
| Acknowledgements | iii |
| Table of Contents | vi |
| List of Tables | viii |
| List of Figures | ix |
| List of Abbreviations | xvii |
| Chapter 1: Introduction | 1 |
| 1.1 Motivation | 1 |
| 1.2 Background and Prior Work | 4 |
| 1.3 Outline of this dissertation | 11 |
| Chapter 2: Theory Fundamentals | 13 |
| 2.1 Hydrodynamics | 13 |
| 2.1.1 Navier-Stokes equation | 13 |
| 2.1.2 Vorticity | 14 |
| 2.1.3 Helicity | 16 |
| 2.1.4 Boundary Layers | 17 |
| 2.1.5 Kolmogorov Scaling Law | 18 |
| 2.1.6 Taylor’s Frozen Turbulence Hypothesis | 21 |
| 2.2 Magnetohydrodynamics (MHD) | 22 |
| 2.2.1 Maxwell’s Equations for MHD | 22 |
| 2.2.2 Induction Equation | 23 |
| 2.3 Dynamo Theory | 27 |
| 2.3.1 Kinematic Dynamo Problem | 28 |
| 2.3.2 Spherical Dynamos | 31 |
| 2.3.3 Mean field dynamo theory | 36 |
| 2.3.4 Dynamo Models: The α^2 and $\alpha\omega$ dynamo | 43 |
| 2.3.5 Kolmogorov Scaling Law for Magnetic Fields | 44 |
| 2.4 Dimensionless Parameters | 46 |
| Chapter 3: The 40-cm experiment: Hydrodynamics Studies | 48 |

| | | |
|--------------|---|-----|
| 3.1 | Experimental Set-up | 48 |
| 3.2 | Results | 56 |
| 3.2.1 | Torque Measurements | 56 |
| 3.2.2 | Velocimetry | 65 |
| Chapter 4: | The 3-m Upgrade | 78 |
| 4.1 | Before Transfer | 80 |
| 4.1.1 | SOP Overview | 80 |
| 4.1.2 | Storage Tank | 83 |
| 4.1.3 | Sodium Plumbing | 85 |
| 4.1.4 | Gas Injection System | 91 |
| 4.1.5 | Initial Disassembly | 92 |
| 4.2 | After Transfer | 95 |
| 4.2.1 | Final Disassembly | 95 |
| 4.2.2 | Fixing the Outer-Inner Sphere Coupler | 98 |
| 4.2.3 | Baffles design and construction | 100 |
| 4.2.4 | New Probe Installation | 102 |
| Chapter 5: | The 3-m Experiment: Magnetohydrodynamic Studies | 105 |
| 5.1 | Experimental Set-up | 105 |
| 5.2 | Results | 107 |
| 5.2.1 | Torque Scaling | 108 |
| 5.2.2 | Mean Field Amplification | 119 |
| 5.2.3 | Time-dependent dynamics | 136 |
| Chapter 6: | Conclusions and Recommendations | 148 |
| 6.1 | Conclusions | 148 |
| 6.2 | Recommendations | 152 |
| Appendix A: | Mechanical Drawings | 154 |
| Appendix B: | Standard Operation Procedure | 172 |
| Bibliography | | 184 |

List of Tables

| | | |
|-----|---|-----|
| 3.1 | Power law fit of the form $G_\infty = bRe^a + c$ of the plots in Figs. 3.6 and 3.7 and Taylor-Couette flows in [1]. | 58 |
| 3.2 | Location and amplitude of the maxima in Figure 3.8 and Taylor-Couette flows in [1]. | 65 |
| 5.1 | Power law fit of the form $G_\infty = bRe^a + c$ of the plots in Figure 3.7 and Taylor-Couette flows in [1]. | 110 |
| 5.2 | Location and amplitude of the maxima in Figure 5.3 | 112 |
| 5.3 | Power law fit of the form $G_\infty = bRe^a + c$ of the plots in Figures 3.7 and 5.5 . . . | 118 |

List of Figures

| | | |
|-----|---|----|
| 1.1 | The spherical 30 cm diameter apparatus and characteristic induced magnetic field instability patterns. The device (a) consists of a thin stainless spherical outer vessel, a rotating inner copper sphere, and liquid sodium in between. The resulting dynamics change character under the influence of an externally applied magnetic field coaxial with the rotation are shown in (b-c). From [2]. | 5 |
| 1.2 | The spherical 60 cm diameter apparatus and characteristic induced inertial modes spectrograms. From [3]. | 7 |
| 1.3 | The spherical 3-m diameter apparatus. Real (left) and schematic (center). On the right we see results from Zimmerman et al. [4] where amplification of the internal fields (B/b_{s0}) is shown for different runs. | 8 |
| 1.4 | Schematic representation of the alpha-omega dynamo. An applied external magnetic field (blue arrows) (a) gets stretched by a differential rotation (b) in the azimuthal direction of the experiment (c), then turbulent and helical flows (d) twist the magnetic field lines back in the direction of a dipole (e), which is the direction of the original applied magnetic field (a), closing the cycle for the amplification process. Adapted from a diagram in [5] | 9 |
| 2.1 | Schematic of the energy cascade to small scales in a viscous flow. Re , the Reynolds number, represents the ratio of the forcing and the viscous forces. | 19 |
| 2.2 | Schematic of the energy cascade to small scales in a viscous conductive flow. Re , the Reynolds number, represents the ratio of the forcing and the viscous forces and Rm , the magnetic Reynolds number, represents the ratio of the forcing and the magnetic diffusivity. The magnetic field lines in blue are dragged by the velocity field until the magnetic diffusivity, due to the non-infinite conductivity, dissipates them into currents. | 27 |
| 2.3 | Drawing of Faraday disk, the first electromagnetic generator, invented by British scientist Michael Faraday in 1831. The copper disk (D) rotated between the poles of a horseshoe shaped magnet (A), creating a potential difference between the axis and rim due to Faraday's law of induction. If an electrical circuit such as a galvanometer was connected between the binding posts (B) and (B') the motion induced a radial flow of current in the disk, from the axle toward the edge. The current flows into the spring contact (m) sliding along the edge of the disk, out of binding post (B') through the external circuit to binding post (B) , and back into the disk through the axle. From Alglave and Boulard [6] | 30 |
| 2.4 | Sketches of the Ponomarenko Dynamo model (a) and the Riga dynamo experiment (b). From Gilbert [7]. | 30 |

| | | |
|-----|---|----|
| 2.5 | Sketches of the flows proposed by Dudley and James to generate dynamos and shown respectively in equation 2.31. On the right, the meridional sections, on the left the azimuthal flow direction. From Dudley M. L. et al. [8] | 35 |
| 2.6 | The Love diamonds. The upper diamonds indicated the regions of the map (D, M) where dynamos occur and at which critical magnetic Reynolds number. Lower dynamo is the helicity of the flows. From Gubbins et al. [9] | 37 |
| 3.1 | Schematic of the 40-cm experiment. (a) 12 cm diameter inner sphere with straight baffles. The baffle height adds 5% or 10% to the inner sphere radius. (b) 40 cm diameter acrylic outer sphere filled with water. (c) 1 cm diameter inner shaft. (d) 3 kW inner motor. (e) 2.23 kW outer motor. (f) Gear belt. (g) Cylindrical lens for laser sheet. (h) 6 W NdYVO ₄ continuous laser. (i) High-speed camera positioned for measurements in the equatorial plane. (k) Polystyrene particles dispersed in the water. | 49 |
| 3.2 | Four types of inner spheres were tested in the 40-cm experiment. (a) Smooth, (b) Straight, (c) Chevron and (d) Alpha. The two rotation directions for (c) and (d) are called wedge mode and scoop mode. | 50 |
| 3.3 | Schematics of the 40-cm experiment control system. A Data Acquisition System (DAQ) communicates with a DC external power supply and with the outer motor driver. The power supply then control directly the inner motor by a series of logic inputs by the DAQ. The outer motor is controlled by its own driver who is controlled by the DAQ. A resistive load is located between the inner motor and the power supply to measure the current in the system. | 53 |
| 3.4 | Schematic of the doubling of the parameter space (Ω_o, Ω_i) by breaking the symmetry of the inner sphere with respect to the rotation direction. The Finke and Tilgner [10] parameter space corresponds to the vertical axis. In (a) an inversion with respect to the origin results in the same states, making this plane to be symmetric to inversion through the origin. In (b), an inversion results in different, yet unknown, states. State labels for (a) come from prior studies in the 3-m system [4]. State labels in (b) are for illustrative purposes only. | 54 |
| 3.5 | Inverse Ekman and Reynolds number parameter space for experiments (40-cm, 3-m), simulations (Wicht [11]) and the Earth [12]. A solid line for $Ro = 1$ is shown for reference. The dotted line indicates the equatorial jet instability regime as observed by Wicht. The dashed line indicates the maximum torque line for a smooth inner sphere observed in the present work and in Zimmerman et al. [4] | 55 |
| 3.6 | | 57 |
| 3.7 | Same for Figure 3.6 but we extrapolate the power laws of the 40-cm experiment to higher Reynolds numbers in order to compare with 3-m experiment torque data from Zimmerman et al. [4] (stars). Dotted, dashed and solid curves indicate no baffles, 10% and 5% baffle height designs respectively. For clarity, we only show error bars for smooth in 40-cm and for the 3-m experiment. | 59 |

| | | |
|------|--|----|
| 3.8 | Rossby number dependence of the measured inner sphere torque. The magnitude of the torque at a given Ro and Re is normalized by $G_\infty(Re)$, the torque expected at that Reynolds number if the outer sphere were not rotating. Error bars for straight 10% are shown in the range of bistable states are representative for all baffles $Ro^{-1} > 0.6$. The dashed line indicates the location of the peak for maximum relative dimensionless torque in the 40-cm experiment with smooth inner sphere. | 62 |
| 3.9 | Radial velocity in the equatorial plane for all baffle designs. In color map: azimuthal average of the velocity in the radial direction, normalized by the tangential velocity at the inner sphere equator, as a function of the normalized radius (left vertical axis) for different Rossby number (horizontal axis). Warm colors mean velocity in the direction outward from the inner sphere and cool colors inward. The symbols show the radial average of each of the columns in the color plot (indicated in the right vertical axis) as a function of Ro^{-1} . The vertical dashed lines indicate the location of the maximum relative torque G/G_∞ for each baffle design. | 66 |
| 3.10 | Azimuthal velocity in the equatorial plane for all baffle designs. In color map: azimuthal average of the velocity in the azimuthal direction, normalized by the tangential velocity at the inner sphere equator, as a function of the normalized radius (left vertical axis) for different Rossby number (horizontal axis). Cool colors mean velocity in the opposite direction of the rotation of the inner sphere and warm colors mean moving in the same direction. The symbols show the radial average of each of the columns in the color plot (indicated in the right vertical axis) as a function of Ro^{-1} . The vertical dashed lines indicate the location of the maximum relative torque G/G_∞ for each baffle design. | 68 |
| 3.11 | Spherical radial component of the velocity field (u_r) in the meridional plane ($r/r_o, \theta$) normalized by the tangential speed in the inner sphere at the equator, for different baffle designs and modes. We normalize the radial coordinate by the radius of the outer sphere r/r_o . Warm colors are outward radial flows, and cold colors are inward radial flows. | 72 |
| 3.12 | Meridional component of the velocity field (u_θ) in the meridional plane ($r/r_o, \theta$) normalized by the tangential speed in the inner sphere at the equator, for different baffle designs and modes. We normalize the radial coordinate by the radius of the outer sphere r/r_o . Warm color are flows from the north pole toward the equatorial plane, and cold colors are toward the pole. | 74 |
| 3.13 | Local time average azimuthal vorticity normalized by the inner angular frequency in the meridional plane ($r/r_o, \theta$) for different baffle designs and modes. We normalize the radial coordinate by the radius of the outer sphere r/r_o . Negative values point out of the page. | 76 |

| | | |
|------|--|-----|
| 4.1 | Vessel cross section with the inner sphere and shaft. On top section view: Detail of the shaft and its attachment to the lid. The inner race of the main top bearing is free to slide axially on the lid shaft, allowing for thermal expansion of the vessel. The locknut on the shaft, above the top shaft bearing, holds the entire weight of the inner sphere and shaft. Two lip seals prevent fluid from leaking into the bearing. On bottom section view: Detail of shaft and the bayonet coupler. The bottom end of the shaft can move axially on the bayonet. Individual drawings taken from Triana [13] and compiled by this author. | 79 |
| 4.2 | Diagram of the transfer plan before the insertion of the dip tube. | 81 |
| 4.3 | Aerial picture of the storage tank. | 82 |
| 4.4 | Oil lines connection diagram to the storage tank and the sphere. In red are the parts we added and in black the preexisting. | 84 |
| 4.5 | Cross section of the insertion diagram including the dip tube, the extraction flange, the lid, the inner sphere and shaft | 86 |
| 4.6 | Collection of dip tubes for tank and sphere. | 87 |
| 4.7 | Extraction flange diagram: (a) Port to valve flange connector. (b) Ball valve. (c) Lip seal to valve connector. (d) Lip seal. (e) Lip seal holder. (f) O-ring. (g) O-ring holder. (h) During insertion. (k) After insertion. | 88 |
| 4.8 | Spacer to support the dip tube and transfer line. | 90 |
| 4.9 | Picture of the final installation of the transfer line (indicated by red arrows). On the right the tip of the sphere installation. On the left, the tank installation. | 90 |
| 4.10 | Picture of the ports installation procedure. (a) Extraction flange port to be installed. (b) Jacks used to lift the ports that had gotten stuck by solidified sodium. (c) Cleaning tools used to degrease the surface. (d) Visualization port already installed. (e) Artur. | 93 |
| 4.11 | Diagram of the transfer plan after the insertion of the dip tube. | 94 |
| 4.12 | Visualization window on one of the ports of the experiment. Liquid sodium can be spotted from the window. | 95 |
| 4.13 | Flying inner sphere-shaft-lid combo. In the picture you can see the pink sodium covering the combo. | 96 |
| 4.14 | Installation used to release the top inner bearing from the shaft. Left arrow points at the liquid nitrogen hose pouring liquid inside the shaft aperture. Right arrow points at the heat tape used to heat up the bearing. | 97 |
| 4.15 | Left: Bottom view of the inner bottom bearing and the bayonet coupler after the bearing retainer and lip seals were removed. The dirty bearing can be spotted. Right: the new stainless steel bayonet coupler (front) and the old one (back), oiled infused brass alloy. A layer of oxide (white color) can still be seen after many wet cleans. | 99 |
| 4.16 | Left: Smooth inner sphere. Right: Rough inner sphere with alpha baffles installed. | 100 |
| 4.17 | Diagram of new baffled inner sphere. A full version with measures can be found in the Appendices. | 101 |
| 4.18 | Diagram of the transfer plan from tank to sphere. Sodium refilling. | 103 |
| 4.19 | Finger probes. Top: the old one. Bottom: the new one. | 104 |

| | | |
|-----|---|-----|
| 5.1 | The 3-m experiment vessel. (a) The three-meter outer sphere vessel. Half pipe oil jacket surround the 1-inch thickness vessel for heating. (b) Smooth one-meter diameter inner sphere, before remodeling. (c) Arrange of 31 magnetic Hall probes. (d) Pair of electromagnets to apply quadrupole and dipole external magnetic field. (e) Instrumentation ports with pressure sensors, temperature sensors and a set of magnetic probes. | 106 |
| 5.2 | Dimensionless torque from the inner motor versus Reynolds number with stationary outer sphere ($Ro = \infty$) for all baffle designs in the 3-m experiment. A power law of the form $G_\infty = bRe^a + c$ was fitted to each data set. Values a , b and c are listed in Table 5.1 | 109 |
| 5.3 | Rossby number dependence of the measured inner sphere torque. The magnitude of the torque at a given Ro and Re is normalized by $G_\infty(Re)$, the torque expected at that Reynolds number if the outer sphere were not rotating. The dashed line indicates the location of the peak for maximum relative dimensionless torque for smooth and rough inner sphere. | 113 |
| 5.4 | Possible bistability regime for rough inner sphere in the 3-m experiment. Time series in outer sphere rotation units of the dimensionless normalized torque (top) and azimuthal magnetic field induced (bottom) for $Ro^{-1} = 0.49$. A running average of 10 seconds has been applied to remove the high frequency oscillations. Compare with Zimmerman et al. [4, Figure 10]. | 115 |
| 5.5 | Compensated plots of the dimensionless torque as a function of Reynolds number for different Rossby numbers, for smooth (left) and rough (right) inner sphere in the 3-m experiment. Dashed lines are taken in the absence of an external magnetic field, solid lines are taken with an external dipolar field of $B_{ext} \sim 20$ G. Runs for scoop mode are indicated with " ∇ " and for wedge mode with " Δ ". The torque for stationary outer sphere for both cases scales close to $G_\infty \sim Re^{1.85}$ which implies that the curves in this plot with a power law less than one (curving downward like the cases for $Ro^{-1} < 0$) implies a torque higher than G_∞ | 117 |
| 5.6 | Magnetic field amplification with stationary outer sphere ($Ro^{-1} = 0$) as a function of the magnetic Reynolds number for one pair of Hall probes in Port B of the experiment (see Section 5.1) in the cylindrical radial direction (B_r) and in the azimuthal direction (B_ϕ) for the two types of boundaries and their respective modes (scoop[$<$] and wedge[$>$]). During this run, there is no externally applied magnetic field from the coils. | 121 |
| 5.7 | Magnetic field amplification in the external Hall probes array, express in spherical Harmonics decomposition (dimensional Gauss coefficients) with stationary outer sphere ($Ro^{-1} = 0$) as a function of the magnetic Reynolds number for the two types of boundaries and their respective modes (scoop[$<$] and wedge[$>$]). During this run, there is no externally applied magnetic field from the coils. | 122 |

| | | |
|------|--|-----|
| 5.8 | Magnetic field amplification for counter-rotating spheres ($Ro^{-1} < 0$) around the maximum torque regime for one pair of Hall probes in Port B of the experiment (see Section 5.1) in the cylindrical radial direction (B_r) and in the azimuthal direction (B_ϕ) for the two types of boundaries and their respective modes (scoop[<] and wedge[>]) for constant $Rm \sim 220$. Horizontal dashed line indicates the maximum gain reported in the smooth case in the internal probes (azimuthal [-.] and radial [-]) around the same Rossby number for comparison. | 124 |
| 5.9 | Magnetic field amplification in the external Hall probes array, express in spherical Harmonics decomposition (dimensional Gauss coefficients) with counter-rotating spheres ($Ro^{-1} < 0$) as a function of the magnetic Reynolds number for the two types of boundaries and their respective modes (scoop[<] and wedge[>]). The horizontal dashed line indicates the maximum gain reported in the smooth case in the external probes. During these runs, there is no externally applied magnetic field from the coils. | 125 |
| 5.10 | Timeline of the voltage in some of the experiment probes in seconds since midnight (ssm). HLS: High Latitude South. HLN: High Latitude North. MLS: Mid Latitude South. EQ: Equator. Brad: Internal Probe in the radial direction. Bphi: Internal Probe in the azimuthal direction. This run takes place for solid body rotation at 0.1 Hz and with no applied external magnetic field. | 126 |
| 5.11 | Magnetic field amplification around the maximum torque regime as a function of the Rossby number for one pair of Hall probes in Port B of the experiment (see Section 5.1) in the cylindrical radial direction (B_r) and in the azimuthal direction (B_ϕ) for the two types of boundaries and their respective modes (scoop[<] and wedge[>]) for different sets of Reynolds numbers. The maximum torque regime is indicated with a dashed vertical line for each boundary type. A constant external dipolar magnetic field of 20 G in the center of the experiment was present during all the runs. | 127 |
| 5.12 | Magnetic field amplification around the maximum torque regime as a function of the Rossby number for the 31 Hall probes array in the spherical radial direction (see Section 5.1) in the form $B_l^m = l(l+1)g_l^m$ (where g_j^m are the Gauss coefficients of the spherical harmonics decomposition) for the two types of boundaries and their respective modes (scoop[<] and wedge[>]) for a constant Reynolds number: $Rm = 950$ for smooth, $Rm = 220$ for rough boundary. These Rossby ramps are taken around the maximum torque regime indicated with a dashed vertical line for each boundary type. A constant external dipolar magnetic field of 20 G in the center of the experiment was present during all the runs. | 130 |
| 5.13 | Hammer-Aitoff projection of the spherical radial magnetic field measured by the 31 Hall probe array for the Rough Scoop mode in Figure 5.11 (center) for three parameter space points: (a) $Ro^{-1} = -0.22$; (b) $Ro^{-1} = -0.21$, at the torque peak and (c) $Ro^{-1} = -0.20$ | 131 |

| | | |
|------|---|-----|
| 5.14 | Magnetic field amplification at the maximum torque regime (smooth $Ro^{-1} = 0.055$, rough $Ro^{-1} = 0.21$) as a function of the magnetic Reynolds number for one pair of Hall probes in Port B of the experiment (see Section 5.1) in the cylindrical radial direction (B_r) and in the azimuthal direction (B_ϕ) for the two types of boundaries and their respective modes (scoop[<] and wedge[>]). A constant external dipolar magnetic field of 20 G in the center of the experiment was present during all the runs. | 132 |
| 5.15 | Magnetic field amplification at the maximum torque regime as a function of the magnetic Reynolds number for the 31 Hall probes array in the spherical radial direction (see Section 5.1) in the form $B_l^m = l(l + 1)g_l^m$ (where g_l^m are the Gauss coefficients of the spherical harmonics decomposition) for the two types of boundaries and their respective modes (scoop[<] and wedge[>]). A constant external dipolar magnetic field of 20 G in the center of the experiment was present during all the runs. | 133 |
| 5.16 | Hammer-Aitoff projection of the spherical radial magnetic field measured by the 31 Hall probe array for the Rough wedge mode in Figure 5.11 (right) for three parameter space points: (a) $Rm = 50$; (b) $Rm = 120$ and (c) $Rm = 220$ | 134 |
| 5.17 | Magnetic field generation at the experiment probes as a function of the balanced power in the inner motor in kilowatts at the maximum torque state for a 20 G externally applied magnetic field. The power limit in each motor is 260kW at 1800 rpm. The absolute upper bound on the mechanical power input of the 3-m experiment is 320 kW based on the motor torque and the allowable boundary speed [14]. | 136 |
| 5.18 | Power Spectrum of the internal probe magnetic field signal in the cylindrical radial direction (B_r) at the maximum torque regime (smooth $Ro^{-1} = 0.055$, rough $Ro^{-1} = 0.21$) as a function of the magnetic Reynolds number for the two types of boundaries and their respective modes (scoop[<] and wedge[>]). Dashed lines indicate power laws for comparison. The frequencies are normalized by the outer sphere angular frequency and shifted one decade away with each different Reynolds number. A constant external dipolar magnetic field of 20 G in the center of the experiment was present during all the runs. | 137 |
| 5.19 | Power Spectrum of the internal magnetic field probe signal in the cylindrical radial direction (left) at the maximum torque regime versus the power spectrum of an external probe located at the equator (right), for different baffle configurations. Dashed lines indicate power laws for comparison. The frequencies are normalized by the outer sphere angular frequency. A constant external dipolar magnetic field of 20 G in the center of the experiment was present during all the runs. | 139 |
| 5.20 | Power Spectrum of the internal probe magnetic field signal in the cylindrical radial direction (B_r) for the Scoop Mode of the rough inner sphere in their respective modes with corotating and counter-rotating regimes for different Rossby numbers. The frequencies are normalized by the outer sphere angular frequency and shifted one decade away with each different Rossby number. A constant external dipolar magnetic field of 20 G in the center of the experiment was present during the runs with positive Rossby number. | 141 |

| | | |
|------|---|-----|
| 5.21 | Power Spectrum of the internal probe magnetic field signal in the cylindrical radial direction (B_r) for the Wedge Mode of the rough inner sphere with corotating and counterrotating regimes for different Rossby numbers. The frequencies are normalized by the outer sphere angular frequency and shifted one decade away with each different Rossby number. A constant external dipolar magnetic field of 20 G in the center of the experiment was present during the runs with a positive Rossby number. | 143 |
| 5.22 | Power Spectrum of the internal probe magnetic field signal in the cylindrical radial direction (B_r) around the maximum torque regime (smooth $Ro^{-1} = 0.055$, rough $Ro^{-1} = 0.21$) for a constant magnetic Reynolds number ($Rm \sim 950$ for Smooth and $Rm \sim 220$ for Rough) for the two types of boundaries and their respective modes (scoop[<] and wedge[>]). Dashed lines indicate power laws for comparison. The frequencies are normalized by the outer sphere angular frequency and shifted one decade away with each different Reynolds number. A constant external dipolar magnetic field of 20 G in the center of the experiment was present during all the runs. | 144 |
| 5.23 | Probability distribution function for the internal probe in the cylindrical radial direction for different Rossby numbers around the maximum torque regime for smooth and rough inner sphere in their two modes runs of Figure 5.12 with an externally applied field of 20G. Dotted lines indicate Gaussian to guide the eye. | 145 |
| 5.24 | Standard deviation from the mean for the internal magnetic field probe in the cylindrical radial direction as a function of the centered Rossby number (left) around the maximum torque regime and as a function of the magnetic Reynolds number (right). | 146 |
| 5.25 | Probability distribution function for the internal probe in the cylindrical radial and azimuthal direction for different Rossby numbers around the maximum torque regime for the rough inner sphere in the scoop mode if the runs in Figure 5.9 with no external field applied . Dotted lines indicate Gaussians to guide the eye. | 147 |

List of Abbreviations

| | |
|------------------|---|
| Ek | Ekman Number |
| Re | Reynolds Number |
| Rm | Magnetic Reynolds Number |
| Ro | Rossby Number |
| Pm | Magnetic Prandtl Number |
| \mathbf{u} | Fluid Velocity |
| \mathbf{B} | Magnetic Field |
| ν | Kinematic Viscosity |
| η | Magnetic diffusivity |
| σ | Conductivity |
| ρ | Density |
| p | Pressure |
| S | Power spectral density |
| ω | Velocity/Magnetic field angular frequency |
| Ω | Containers angular frequency |
| ℓ | Degree of the Spherical Harmonics |
| m | Order of the Spherical Harmonics |
| T | Temperature |
| α | Thermal diffusivity |
| h | Helicity |
| δ | Boundary Layer length scale |
| τ | Dipole diffusion time scale / Dimensional torque. |
| G | Dimensionless torque |
| G_∞ | Dimensionless torque at $Ro = \infty$ |
| \mathbf{t}_l^m | Toroidal vector spherical harmonics |
| \mathbf{s}_l^m | Poloidal vector spherical harmonics |
| Y_ℓ^m | Scalar spherical harmonics |
| \mathcal{E} | Electromotive force |
| MHD | Magnetohydrodynamics |
| 3-m | The three meter experiment |
| 40-cm | The Forty centimeter experiment |
| IREAP | Institute for Research in Electronics and Applied Physics |

Chapter 1: Introduction

1.1 Motivation

Perhaps one of the most important physical phenomena for the livelihood of humankind on Earth is the existence of a magnetic field surrounding the planet. This magnetic field protects life from the deadly solar radiation, and acts as a shield against the accelerated charged particles constantly launched from the Sun. It was believed that the origin of the field was due to a permanent magnet inside the Earth; however, the inside of the Earth is at much higher temperatures than the Curie temperature of the iron core, which is the point where all ferromagnetism is lost. In 1919, Joseph Larmor hypothesized that the magnetic field of the Sun was due to the motion of conductive liquid fluid inside. This was the first time that the notion of conductive flows sustaining a magnetic field was considered.

The origin of the Earth's magnetic field is also a topic that continues to generate discussion throughout the scientific community. Though, there is a consensus about where it is generated: the outer core - an ocean of an iron-nickel alloy between the solid inner core and the solid mantle. The liquid composition of the outer core was hypothesized by Danish seismologist Inge Lehman in 1929, and it has been later corroborated by seismic measurements. It constitutes our current model of study. However, the inaccessibility of this region on Earth makes us completely reliant on remote observation and sensing for further and deepening the existent knowledge about the

core's composition and dynamics, leaving us with relatively limited data.

The theoretical problem of the Earth's magnetic field generation is also of high difficulty to solve. The Navier-Stokes equation that governs the fluid motion in the outer core is known to have no analytical solution, particularly for planetary, and even laboratory scales. Additionally, due to the wide range of spatial scales involved, the numerical approach is one of limited scope. Although progress has been made, we are still a few orders of magnitude away from resolving the problem for these scales. The major barrier is the existence of a threshold for the generation of the magnetic field. This threshold is, ironically, in the nonlinearities of the system; meaning that we need more turbulent flows (more complex and difficult to resolve) in order to generate a self-sustained magnetic field similar to the Earth's. This is the same complexity that makes numerical resolution difficult. Hence, the arrival of the experiments.

The first attempts to generate a magnetic field in the laboratory due to conductive flows started with very limited geometries: twisted pipe flows were used to generate the topologies required to sustain a magnetic field Benton [15]. More complex, and less restricted geometries followed up with cylinder-like type of flows Gailitis et al. [16], Bourgoin et al. [17]. The ultimate desired geometry for experiments is perhaps a spherical one, that resembles more accurately the Earth's dynamics. Unfortunately, with less constraints and less controlled flows, comes greater experimental difficulties.

This process of a self-sustained magnetic field generation seen in many planets, stars and galaxies, due to rotating turbulence of their conductive constituents, is formally known as the *dynamo action*. It can be thought of as a competition between Faraday induction and dissipation due to electrical resistance. The former drags, stretches, twists, and amplifies the magnetic field, while the latter transforms the electric currents into heat at smaller scales. They are determined

respectively by the momentum diffusivity ν (kinematic viscosity) and the magnetic diffusivity η (inversely proportional to the electrical conductivity). The ratio of these two numbers is known as the magnetic Prandtl number $Pr_m = \nu/\eta$, and is small for all liquid metals.

Despite the numerical difficulties, dynamos have been simulated before [18, 19, 20, 21, 22]. However, the parameters involved in these simulations are very different from those of the Earth or even the experiments. For instance, simulations tweak the conductivity of the flows to ease dynamo action. This is observed in the magnetic Prandtl number P_m (defined in more details in Section 3.5): simulations run at $P_m = 1$ whilst Earth's Prandtl number is closer to 10^{-5} . Another dimension that we cannot match, not even in experiments, is the length scale. This affects significantly the Coriolis forces observed in the system, which are known to be one of the most important drivers of planetary dynamics. The effect of Coriolis forces is indicated by the dimensionless Ekman number Ek (the ratio of viscous to Coriolis forces. See section 3.5). This number in simulations and experiments is as much as nine orders of magnitude greater than that of the Earth.

All these mismatches of the parameters between the simulation and the real astronomical bodies, motivate a global attempt to bridge this gap using experiments. In particular, there is an ongoing global attempt to replicate Earth-like magnetic field dynamos in the laboratory [4, 23, 24, 25] with realistic turbulence that cannot be achieved by current simulations.

Spherical Couette flows are flows between two concentric spheres that rotate differentially. They are a useful model to study rotating turbulence, particularly, in the context of planetary dynamics [26, 27, 28], given the resemblance of the geometry in the cores. The solid inner sphere mimics the inner core boundary, whilst the outer sphere mimics the mantle-core boundary. Shear forces at the surfaces, and Coriolis forces due to the global rotation, drive and shape the

motion of the fluid between the spheres, similarly to the more widely explored cylindrical Taylor-Couette flows [27, 29, 30, 31, 32, 33]. However, there is another important mismatch: the Earth's inner core does not rotate significantly with respect to the outer core. The driven mechanism for dynamo generation in the core is known to be a combination of the following: convection, due to thermal gradients; buoyancy, due to constant solidification of the inner core (and a sort of inverse rain from the outer core towards the mantle) and Coriolis forces due to global rotation (check for instance Merrill et al. [34]). However, there is an analogy between thermal convection and shear turbulence which has been studied in the context of Taylor-Couette versus Rayleigh-Bénard convection that has been extensively reported in the bibliography [35, 36, 37]. See for instance Prigent et al. [38] for an overall summary. The analogy, in simple words, states that at high Reynolds numbers (very turbulent flows) the nature of the turbulence of Taylor-Couette and Rayleigh-Bénard flows is statistically equivalent. This comes in handy for the experimentalists who now see rotating flows as a suitable candidate to replace thermal convection with shear flows as the dynamo driving force. Spherical Couette dynamos have also been found extensively in numeric simulations, and the parameter range exploration continues to grow every day [9, 11, 18, 19, 20, 21, 22, 39, 40].

1.2 Background and Prior Work

Experimental dynamos have been found in the laboratory in restricted geometries such as the ones of Riga [16] and Karlsruhe [41]. These successes proved theoretical predictions about a self-excitation in the magnetic field due to a well organized flow, and motivated the search of dynamos in less confined, more Earth-like geometries and turbulence like in spherical Couette

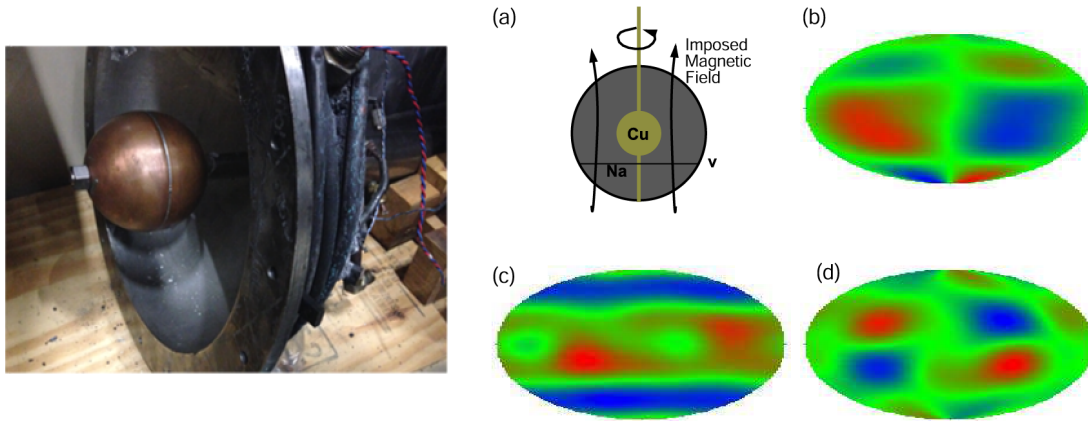


Figure 1.1: The spherical 30 cm diameter apparatus and characteristic induced magnetic field instability patterns. The device (a) consists of a thin stainless spherical outer vessel, a rotating inner copper sphere, and liquid sodium in between. The resulting dynamics change character under the influence of an externally applied magnetic field coaxial with the rotation are shown in (b-c). From [2].

flows. Spherical experiments attempting Earth-like dynamos and exploring magneto-turbulence include the one in Madison at the University of Wisconsin, USA [23] and the DTS spherical Couette flow in Grenoble, France [24, 25]. Other experiments, like the Von Karman sodium experiment [42] and the DRESHDYN experiment in Dresden, Germany [43] use a cylindrical geometry. The former successfully achieved a dynamo using ferromagnetic impellers as main driver of the flow.

At the University of Maryland we have built a series of different spherical Couette Flows experiments during almost 30 years, with the intention of studying magnetohydrodynamics (MHD) and eventually generate a dynamo in this Earth-like configuration. This is why all our experiments are intended to mimic the aspect ratio of the Earth's core of $\Gamma = r_i/r_o = 0.35$. We use liquid sodium as the conductive flow since it is the liquid metal with the highest conductivity and it melts at 97 C which is a reasonably achieved temperature for experimental purposes. However, handling sodium is extremely dangerous due to its reactive, toxic, corrosive and inflammatory

properties. Sodium needs to be kept in a neutral atmosphere, for which we used nitrogen as an inert gas. Sodium oxidizes rapidly, the oxidation can be observed in real time. The reaction takes the oxygen in the air and leaves behind different types of sodium oxides which are toxic, corrosive, and irritating to the skin and eyes. The reaction of sodium and water is particularly dangerous; it leaves behind hydrogen gas in high concentrations, which is volatile, and the reaction is exothermic. The consequence could be a detonation that sends into the air liquid sodium and oxide traces. Hence, extreme measures are constantly being taken to guarantee the optimal performance of the experiment and the safety of the team.

The first experiment of this series had 30 cm in diameter [2] and was able to reach a magnetic Reynolds number of $Rm \sim 25$. By that time, that parameter space was relatively unexplored. This experiment reported the first experimental observation of Magnetorotational Instability (see for instance Chandrasekhar [35]) but did not shield a dynamo.

The second experiment of the series is a 60 cm outer diameter spherical Couette. This experiment observed inertial modes [44] in a spherical geometry. The setup was also used to study thermal convection in spherical Couette geometries, but it did not succeed in generating the necessary velocity scales for dynamo action. However, it showed very interesting results. [45].

Finally we arrive at the 3-meter diameter spherical Couette experiment (3-m) [4, 46, 47]. It is, like its predecessors, intended to mimic the aspect ratio of the Earth's core of $\Gamma = r_i/r_o = 0.35$, where $r_i = 0.51$ m and $r_o = 1.46$ m are the inner and outer sphere radii of the experiment. The boundaries of both spheres were originally smooth with only a characteristic roughness due to the unpolished stainless steel material from fabrication. The 3-m experiment approximately matches Earth's magnetic Reynolds numbers of $Rm \approx 900$, $Re \approx 10^9$, and works with liquid sodium, which has a $Pr_m \approx 10^{-5}$. An external dipolar or quadrupolar magnetic field can be

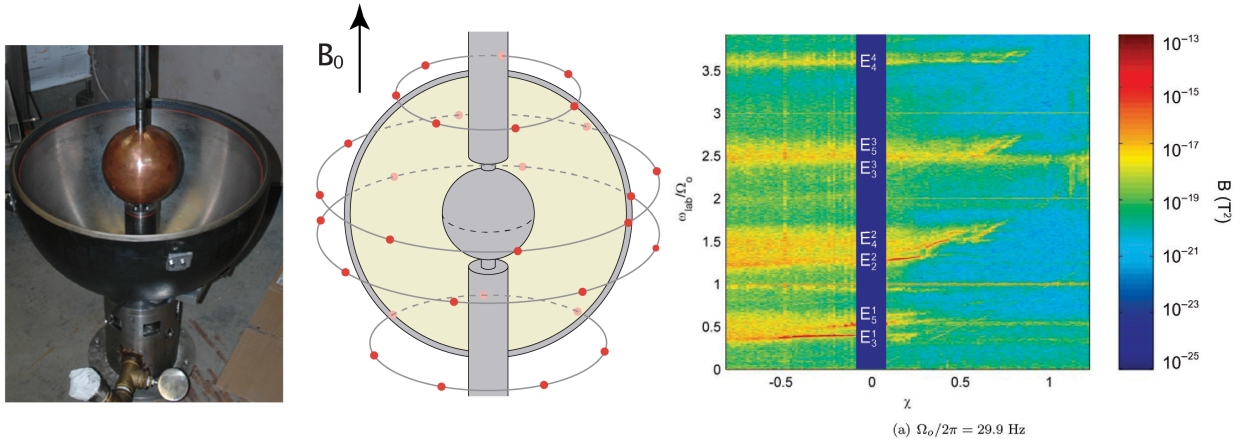


Figure 1.2: The spherical 60 cm diameter apparatus and characteristic induced inertial modes spectrograms. From [3].

applied by electromagnets in the axial direction, with an intensity up to 200 Gauss at the center of the experiment.

This is the biggest rotating liquid sodium experiment in the world to date, which despite matching many parameters of the Earth’s core, has not yielded a magnetic dynamo. However, the experiment has shown very interesting phenomena for the geophysics community such as inertial modes [48] and precessional states [47]. Additionally, phenomena of significant interest for the non-linear and astrophysics community such as the bi-stability states [46] have been reported for the first time in this geometry.

The 3-m experiment experiment has shown an significant amplification of the magnetic field in the azimuthal direction up to 8 times the externally applied magnetic fields (see Figure 1.3 and work by Zimmerman et al. [4]). It has, additionally, shown amplification of 10 – 30% in the internal radial direction [4]. These results, especially the latter, are significant for dynamo in the laboratory. In order to understand their importance, we need to elaborate on the mechanism of its generation.

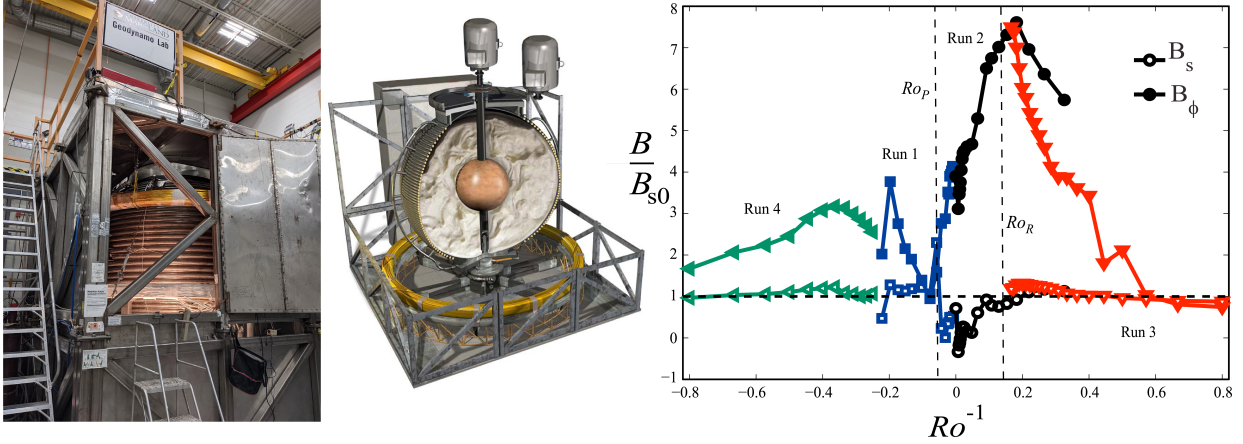


Figure 1.3: The spherical 3-m diameter apparatus. Real (left) and schematic (center). On the right we see results from Zimmerman et al. [4] where amplification of the internal fields (B/b_{s0}) is shown for different runs.

Theoretical dynamo studies [8, 49] indicate that electrically conductive flows can drag and stretch the external magnetic field lines. The general idea behind the dynamo action is that a seeded (generally weak) magnetic field is stretched and amplified by the conductive flows in such a way that can be fed back into the original applied direction. This process closes the loop for a somewhat feedback process.

One fundamental model for this process is known as the $\alpha\omega$ -dynamo [50, 51, 52] shown schematically in Fig 1.4: a magnetic field applied in the axial direction is stretched in the azimuthal direction due to shear forces in the form of differential rotation (Ω -effect) and then twisted back into the meridional directions due to the helical component of the turbulence (α -effect). For the purpose of this dissertation, we interpret meridional flows as an indicator of the strength of the three-dimensional *poloidal* flows. The turbulence responsible for the α -effect can be connected with the vorticity of the meridional flows, which combined with the azimuthal flows responsible for the Ω -effect, give rise to helicity (defined more carefully in section 2.1.3). In the $\alpha\omega$ -dynamo then, the helicity is dominated by vorticity from the poloidal/meridional flows:

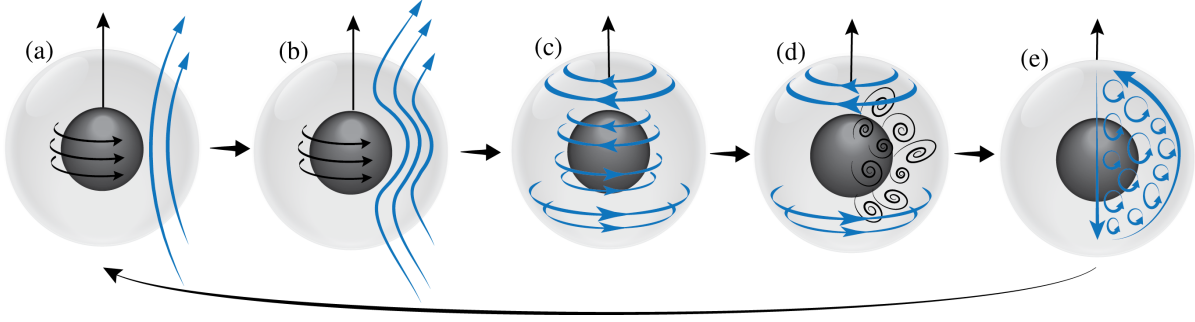


Figure 1.4: Schematic representation of the alpha-omega dynamo. An applied external magnetic field (blue arrows) (a) gets stretched by a differential rotation (b) in the azimuthal direction of the experiment (c), then turbulent and helical flows (d) twist the magnetic field lines back in the direction of a dipole (e), which is the direction of the original applied magnetic field (a), closing the cycle for the amplification process. Adapted from a diagram in [5]

$$H \approx \int_V \mathbf{u}_\varphi \cdot (\nabla \times \mathbf{u}_m) dV = \int_V u_\varphi \omega_\varphi dV, \quad (1.1)$$

where the subindexes φ and m stands for azimuthal direction and the meridional plane respectively, and $\boldsymbol{\omega} = \nabla \times \mathbf{u}$ is the vorticity.

Many authors have elaborated on the key role played by helicity in dynamo action. In particular, Nakajima and Kono [53] proposed that maximizing helicity is strongly correlated with the efficiency of a flow in producing dynamo action. Love and Gubbins [54] and Khalzov et al. [55] commented on the connection between helicity and the ratio of poloidal to rotational motion and its influence on dynamo instability. Further studies support these notions in different flows and geometries [56, 57, 58, 59, 60, 61]. The relative small amplification of the field observed in the 3-m experiment in the radial direction is evidence of this effect. Flows in the meridional directions $((r, \theta))$ of the experiment may be responsible for dragging the field into this direction (see Figure 1.4) completing the loop for the feedback process. These results indicated then a substantial Ω -effect but a limited α -effect [4]. Hence, increasing the meridional flows and their

vorticity, together with the azimuthal flows, would be an effective way of achieving more helical flows in the experiment, thus enhancing the α -effect.

In Couette flows, energy and angular momentum are injected into the fluid through the boundary layers. Many recent works have tested the roughness in the boundaries of rotating experiments, mainly Taylor-Couette flows. Adding roughness to the inner boundary changes the boundary layer from *viscous-coupling* to fully *pressure-dominated* [10, 62, 63], which provides a more effective transfer of angular momentum to the fluid and could favor injection of flow in the meridional directions. Numerical work by Finke and Tilgner [10] examines this directly in the context of Spherical-Couette flows. In their work, a rough inner sphere, modeled using a body force, was simulated numerically. They found that such body force increases the coupling between the inner sphere and the fluid, resulting in a stronger equatorial jet, therefore increasing the poloidal flows. This new configuration lowers the threshold in the parameter space for achieving dynamo action by a factor of approximately five.

In order to better examine this process before performing long-lasting modifications in the 3-m experiment, we decided to work in a smaller water experiment to study for the first time the hydrodynamical properties of spherical Couette flows with rough boundaries. One of the goals was to extrapolate these results into the parameter space of the 3-m experiment to guide its redesign; however, we found important properties in the dynamics of rough spherical Couette flows and compared them with previous numerical simulations and experiments, including in Taylor-Couette flows. The results obtained with the 40-cm experiment allowed us to plan modifications in our 3-m experimental setup, not only regarding inner motor power specifications but also final baffle design.

With that information in hand, we would be better prepared towards modifying the 3-m

experiments to induce more helical flows that would take us closer to achieve dynamo action. These two experiments would be the first ever experimental measurements of rough boundary spherical Couette flows, both in the context of hydrodynamics and magnetohydrodynamics.

1.3 Outline of this dissertation

We start by lining up the most fundamental theoretical notion required to understand the motivation behind this dissertation. We begin the section with some basic hydrodynamics concepts, then the basics of magnetohydrodynamics. Finally, we address the problem of the dynamo action, specifically in spherical geometries.

In chapter 3 we describe the 40-centimeter diameter spherical Couette experiment. This experiment was initially assembled by Till Zurner with the collaboration of this author. The inner motor and electronics, including data acquisitions instruments, were installed by the author of this dissertation. To add roughness we test baffles attached to the inner sphere from pole to pole, in a similar way as done previously in Taylor-Couette flows [31, 63]. Additionally, we try several heights and shapes of baffles to contrast their different effects on the dynamics of the flows. Results include torque measurements from the inner motor as a function of Reynolds and Rossby numbers (Section 3.2.1), and velocimetry using particle tracers and Particle Image Velocimetry (PIV) in both the equatorial and meridional planes (Section 3.2.2).

Chapter 4 is then a story line of the steps and decisions taken during the remodeling stage of the 3-m experiment. This chapter is motivated, not only as a record of the goals achieved in the present dissertation, but also as a written journal for the incoming graduate student who might face themselves with similar challenging situations. We hope that this chapter serves as a guide

to address some of these difficulties.

In chapter 5 we finally show preliminary results of the remodeled baffled 3-m experiment and compare them with previous data with smooth inner sphere taken by Daniel Zimmerman, Santiago Triana, Matthew Adams and Doug Stone. These results include torque data, as in the 40-cm experiment, and magnetic data. We divide the latter in Mean Measurement and Time Dependent Measurements. One particular difference with previous results that we implemented, was to try to perform ramps in the parameter space changing only one of the dimensionless group while leaving the other one constant. It is known that the dynamics of the rotational experiments could be separated into Rossby number dependence and Reynolds number dependence. Although other numbers can be used, these are the main two we use throughout this dissertation.

Finally, we summarized the main results and proposed steps for the immediate future of this research project. Even though this doctoral dissertation work left important results towards a dynamo generation in spherical Couette flows, perhaps the most important contribution for the next generation of students is that, for the time these lines are being written, the experiment is working finally after 5 years of modifications and repairs.

Chapter 2: Theory Fundamentals

2.1 Hydrodynamics

2.1.1 Navier-Stokes equation

Let us begin with the well known Navier-Stokes Equation 2.1 that governs the fluid's motion:

$$\frac{\partial \mathbf{u}}{\partial t} + (\mathbf{u} \cdot \nabla) \mathbf{u} = -\nabla(p/\rho) + \nu \nabla^2 \mathbf{u}, \quad (2.1)$$

where \mathbf{u} is the velocity field, p is the pressure, ρ is the density of the fluid and ν its kinematic viscosity. A derivation can be found in any fluid mechanics book, see for instance [64, 65, 66].

We will also use, for the rest of this dissertation, the no-slip boundary condition for the velocity field at the boundaries ($\mathbf{u}|_S = 0$), and the assumption that the fluid is incompressible, the so called continuity equation (because its incompressibility implies mass conservation):

$$\nabla \cdot \mathbf{u} = 0.$$

From left to right the terms in the Navier-Stokes equation describe: 1) the change in time of the velocity field \mathbf{u} , 2) the acceleration of the fluid element by the spatial rate of change of its

velocity field (advection), 3) the acceleration due to the spatial change in the pressure, and 4) the diffusion into thermal energy due to the viscous forces in the fluid. Additionally, if there is any external force applied to the fluid, it will appear balanced into the Navier-Stokes equation as we will see later on.

2.1.2 Vorticity

Apart for the treatment of the fluid by its streamlines, or lines of constant modulus of the velocity $|\mathbf{u}|$. It is useful for the sake of this dissertation to talk about the vorticity of the fluid flow. This is defined as the curl of the velocity field:

$$\boldsymbol{\omega} = \nabla \times \mathbf{u}. \quad (2.2)$$

Vorticity is understood as how much a vector field (in this case a velocity field \mathbf{u}) will tend to make a particle rotate about a central point that is moving with the flow as well. It is illustrative to imagine the case of planar velocity field, i.e.,

$$\mathbf{u}(x, y) = (u_x, u_y, 0), \quad \boldsymbol{\omega} = (0, 0, \omega_z).$$

In the case of a whirlpool-like flow, where all the particles rotate around a central point with the same angular velocity Ω , it is easy to prove [50, 64] that the vorticity is $\omega_z = 2\Omega$. If we now use the identity

$$\nabla(u^2/2) = (\mathbf{u} \cdot \nabla)\mathbf{u} + \mathbf{u} \times \nabla \times \mathbf{u}.$$

into the Navier-Stokes equation 2.1, together with the definition of vorticity, we obtain:

$$\frac{\partial \mathbf{u}}{\partial t} = \mathbf{u} \times \boldsymbol{\omega} - \nabla(p/\rho + u^2/2) + \nu \nabla^2 \mathbf{u}. \quad (2.3)$$

Taking the curl of 2.3 and remembering that the curl of a gradient is zero, we obtain the *vorticity equation*:

$$\frac{\partial \boldsymbol{\omega}}{\partial t} = \nabla \times [\mathbf{u} \times \boldsymbol{\omega}] + \nu \nabla^2 \boldsymbol{\omega}. \quad (2.4)$$

This equation is fundamental in the context of magnetohydrodynamics (MHD). Perhaps one of its more pedagogical interpretations comes to light when we again consider planar flows, i.e., $\boldsymbol{\omega} = \omega_z$. In this case, the equation 2.4 takes the form

$$\frac{D\omega}{Dt} = \nu \nabla^2 \omega,$$

where the operator

$$\frac{D\omega}{Dt} = \frac{\partial \omega}{\partial t} + (\boldsymbol{\omega} \cdot \nabla)\omega, \quad (2.5)$$

is the so-called *convective derivative* of a vector field.

This equation is equivalent to an advection-diffusion heat equation for the temperature in a fluid: if we replace ω by T and ν by α (the thermal diffusivity). The overall picture is fascinating: the vorticity is created at boundary layer by pressure gradients only [67], then it is diffused into the interior of the fluid in the *exact* same way that the temperature is diffused from a heated surface. Vorticity cannot be created or destroyed within the bulk of the fluid. Due to its conservation properties, it is merely spread into the fluid by diffusion [50].

2.1.3 Helicity

Another important quantity for fluid dynamics and magnetohydrodynamics is *helicity*, defined as

$$h = \int_V (\mathbf{u} \cdot \boldsymbol{\omega}) dV, \quad (2.6)$$

where V stands for a volume composed of always the same particles, which is called *material volume*.

We can additionally state that helicity is a conserved quantity. To see this, let us apply the convective derivative 2.5 to the vector product $\mathbf{u} \cdot \boldsymbol{\omega}$:

$$\frac{D(\mathbf{u} \cdot \boldsymbol{\omega})}{Dt} = \frac{D\mathbf{u}}{Dt} \cdot \boldsymbol{\omega} + \frac{D\boldsymbol{\omega}}{Dt} \cdot \mathbf{u}.$$

Using the vorticity equation and the Navier-Stokes equation we notice that the crossed diffusion terms cancel each other and we end up with

$$\frac{D(\mathbf{u} \cdot \boldsymbol{\omega})}{Dt} = \nabla \cdot [(u^2/2 - p/\rho)\boldsymbol{\omega}],$$

where we have used the fact that $\boldsymbol{\omega}$ is solenoidal, i.e., $\nabla \cdot \boldsymbol{\omega} = 0$.

We now integrate for an infinitesimal volume δV , and since the fluid is incompressible, the convective derivative commute with δV ($D(\delta V)/Dt=0$) and we obtain:

$$\frac{d}{dt} \int_V (\mathbf{u} \cdot \boldsymbol{\omega}) dV = \int_V \nabla \cdot [(u^2/2 - p/\rho)\boldsymbol{\omega}] dV,$$

$$\frac{d}{dt} \int_V (\mathbf{u} \cdot \boldsymbol{\omega}) dV = \int_S [(u^2/2 - p/\rho)\boldsymbol{\omega}] dS,$$

where we used the Stokes Theorem and, again, since $\boldsymbol{\omega}$ is solenoidal, its integral on a closed surface is zero. Therefore we obtain the conservation of helicity

$$\frac{d}{dt} \int_V (\mathbf{u} \cdot \boldsymbol{\omega}) dV = 0. \quad (2.7)$$

2.1.4 Boundary Layers

In this section we will go over a brief description of the concept of boundary layers. This subject is of extreme relevance in almost all branches of fluid dynamics. It was first presented by Prandtl in 1904, but it took many more years for his ideas to finally detach to their full potential.

The concept of boundary layer starts imagining a fluid very close to a boundary. If we consider the stationary Navier-Stokes equation

$$(\mathbf{u} \cdot \nabla)\mathbf{u} = -\nabla(p/\rho) + \nu \nabla^2 \mathbf{u}, \quad (2.8)$$

subject to the inviscid boundary condition $\mathbf{u} \cdot d\mathbf{S} = 0$, where $d\mathbf{S}$ is an infinitesimal vector normal to the boundary. We know that the velocity not only needs to be normal to the surface but it must obey the non-slip boundary condition, meaning that it must be zero in the boundary. Therefore, as we get closer to the surface, the only mechanical forces available to slow down the velocity are the viscous forces, because the pressure cannot have a gradient in the transversal direction in the limit near the surface, since the tangential velocity must be zero. This leave us with the viscous

forces balancing the advection at the boundary layer as

$$(\mathbf{u} \cdot \nabla)\mathbf{u} \sim \nu \nabla^2 \mathbf{u}. \quad (2.9)$$

Then, the length scales of the Laplacian (δ) in equation 2.9, which are the length scales of the boundary layer, need to be of the order

$$\delta \sim \sqrt{\nu L/u} \sim Re^{-1/2}, \quad (2.10)$$

where L is the length scale outside the boundary layer and Re is the well-known *Reynolds number* (see section 2.4).

There is a phenomenon that takes place around the boundary layer known as *separation*. When the fluid outside of the boundary layer decelerates, so does the fluid inside the boundary layer, due to the pressure gradient formed across the layer. However, the fluid inside the boundary has less kinetic energy than the fluid outside; hence, sometimes it can start reversing. When this happens, a wake is created and then ejected in the form of eddies outside the boundary layer. This separation of the flow from its surface can be achieved more effectively if the surface is irregular. This is crucial for the present work as we will see in further sections.

2.1.5 Kolmogorov Scaling Law

*“Big whirls have little whirls, that feed on their velocity;
and little whirls have lesser whirls, and so on to viscosity.”*

— Lewis Fry Richardson.

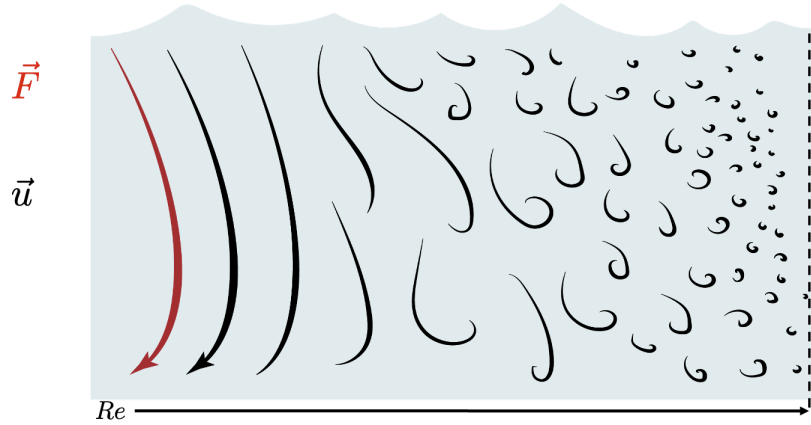


Figure 2.1: Schematic of the energy cascade to small scales in a viscous flow. Re , the Reynolds number, represents the ratio of the forcing and the viscous forces.

The objective of this section is to give a brief description and quantification of one of the most beautiful and also most experimentally demonstrated laws in fluid mechanics. The general idea can be interpreted as follows: when a flow is perturbed by some force F , eddies are formed, first at the scale of the perturbing force. Then, these eddies are transformed by strain (shear) into smaller and smaller scales until the viscosity dissipates these eddies to thermal energy. This notion can be observed schematically in Figure 2.1.

The Reynolds number is defined as

$$Re = UL/\nu, \tag{2.11}$$

and represent the ratio between the scales of the forcing and the scale of the dissipation due viscosity, where ν is the kinematic viscosity and U and L are the characteristic velocity and distance of the large-scales, i.e., the forcing scale, the scale at which the turbulence starts to form, so the bigger eddies are generated. These bigger eddies are then transformed to smaller eddies by means of the strain tensor and so on and so on, until the viscosity dissipates them. The

range in which the energy is dissipated to smaller scales is called the *inertial subrange*.

It can be proved that if the Reynolds number is big enough, the energy dissipation in the inertial subrange is independent of the large scale and of the viscous scales (where the viscosity starts taking part in the dissipation). This is not a trivial result, but a very interesting one. For a light explanation see Davidson [50], and for a more detailed interpretation the book of Tennekes and Lumley [68] is highly recommended.

Let ϵ be the rate of mechanical energy dissipation due viscosity per unit mass. This rate must be equal to the rate at which the energy is fed to the turbulence from the mean flow. If not, the energy in the turbulence will diverge. Moreover, this has to happen across the entire range of the cascade, otherwise eddies of a particular size would grow more than others. In other words, the cascade to smaller scales has to be uniform: ϵ must be constant throughout the cascade.

With these two previous statements, we can construct a dimensional group of units for the mechanical energy of the eddies of size r . Let us call this energy $(\Delta v)^2$, for the inertial subrange. Since it will not depend on either u or l (the large scales) nor on ν , the viscosity (the small scales), then the remaining dimensional groups are ϵ and r and with these two numbers the only way we can form units of energy is

$$(\Delta v)^2 \sim \epsilon^{2/3} r^{3/2}. \quad (2.12)$$

This equation is called the *Kolmogorov and Obukhov's two-thirds law*. However, this equation is often represented in units of the *wave number* $k \sim 1/r$. Let us define $E(k)dk$ as

the energy contained in eddies whose size lies in the range $k \rightarrow k + dk$. Then

$$(\Delta v)^2 \sim \int_k^\infty E(k) dk,$$

and

$$E(k) \sim \epsilon^{2/3} k^{-5/3}. \quad (2.13)$$

This is the famous *Kolmogorov's five-thirds law*. It says that the energy in the eddies as a function of their wavenumber follows a power law for the inertial subrange. This power spectrum has been found in numerous experiments, including the present work as we will see in further sections.

2.1.6 Taylor's Frozen Turbulence Hypothesis

To finish this section on theory fundamentals in hydrodynamics, we will talk about the Taylor Hypothesis, which is more like an "experimental fundamental". It provides a basis for the measurements of streamwise derivatives of flow variables. Taylor proposed that for short time intervals, turbulence can be assumed to be frozen as it convects past a probe fixed at a point in the space [69]. This statement can be expressed mathematically as

$$\frac{du_x}{dx} = -\frac{1}{U_c} \frac{du_x}{dt}.$$

Where U_c is the convection speed of the frozen turbulence and u_x the velocity in the spatial direction x as measured by the probe.

Practically, this means that the *spatial spectrum* (k) can be connected with the *temporal*

spectrum (ω) given by the relation

$$k_x \approx \omega/u_x.$$

This relation will allow us to obtain the one-dimensional streamwise spectra from the temporal frequency spectra.

2.2 Magnetohydrodynamics (MHD)

In this section we start introducing the effects of electromagnetic fields into the fluid equations.

2.2.1 Maxwell's Equations for MHD

Let us start by introducing the reduced form of the Maxwell's equations for MHD:

$$\nabla \times \mathbf{E} = -\frac{\partial \mathbf{B}}{\partial t}, \quad (2.14)$$

$$\nabla \times \mathbf{B} = \mu \mathbf{J}, \quad (2.15)$$

$$\nabla \cdot \mathbf{B} = 0, \quad (2.16)$$

$$\nabla \cdot \mathbf{J} = 0. \quad (2.17)$$

A few statements have been assumed for these equations. First, we have neglected the displacement currents in the Ampere-Maxwell equation because the velocity scales are much smaller than c , the speed of light. Additionally, for the purpose of MHD, the charge density plays no significant role in comparison to the current density \mathbf{J} , since $|\rho \mathbf{E}_0|/|\mathbf{J} \times \mathbf{B}_0| \ll U^2/c^2 \ll 1$,

where U is the velocity scale and we have used $E_0 \sim UB_0$. We have also included the modified Ohm's Law for a conducting fluid in the moving frame of the flow velocity field \mathbf{u} ,

$$\mathbf{J} = \sigma(\mathbf{E} + \mathbf{u} \times \mathbf{B}). \quad (2.18)$$

With this, the Lorentz force is:

$$\mathbf{F} = \mathbf{J} \times \mathbf{B}, \quad (2.19)$$

where we have neglected again the current density. With these equations in hand, we have all the tools that we need to start developing dynamo theory.

2.2.2 Induction Equation

The fundamental equation for dynamo theory is the *induction equation*. Taking the curl of the Ohm's law 2.18 and dividing by σ we obtain:

$$\nabla \times \frac{\mathbf{J}}{\sigma} = \nabla \times \mathbf{E} + \nabla \times (\mathbf{u} \times \mathbf{B}).$$

Now, using equations 2.15 and 2.14 we obtain:

$$\nabla \times \left(\frac{1}{\mu\sigma} \nabla \times \mathbf{B} \right) = -\frac{\partial \mathbf{B}}{\partial t} + \nabla \times (\mathbf{u} \times \mathbf{B}).$$

Where $1/\mu\sigma$ is the *magnetic diffusivity* η which we will assume is constant. Now, using the vector identity $\nabla \times (\nabla \times \mathbf{B}) = -\nabla^2 \mathbf{B}$, where we have used equation 2.16, we finally obtain the induction equation

$$\boxed{\frac{\partial \mathbf{B}}{\partial t} = \nabla \times (\mathbf{u} \times \mathbf{B}) + \eta \nabla^2 \mathbf{B}.} \quad (2.20)$$

There are two basic limits of the induction equation that can help us to understand its implications. The first limit is the case where no velocity field exists; so, $\mathbf{u} = 0$ and

$$\frac{\partial \mathbf{B}}{\partial t} = \eta \nabla^2 \mathbf{B}.$$

This is just a diffusion equation for the magnetic field. If a conductor is immersed in an uniform magnetic field, the field in the conductor eventually becomes uniform. Let us consider a sinusoidal plus constant field in the Cartesian z direction applied into a conductor of the form $B_z = B_0 + B_1 \sin(kz)$. Here k will be the wave number of the applied field. If we plug this into the diffusion equation we obtain $B_z = B_0 \sin(kz) \exp(-\nu k^2 t) + B_1$. Hence, the mean life of a magnetic field in a stationary conductor is of the order

$$\tau = 1/k^2 \eta.$$

This is also called the *dipole diffusion timescale*. For liquid sodium as the conductor and a scale of 1 meter, which is typical for dynamo experiments, the decay time is on the order of 3 seconds. For the Earth, on the other hand, it is of the order of 20000 years! This is longer than a human lifetime but much shorter than Earth's lifetime. This, for instance, rules out the possibility that the remnant of an extinct permanent dipole is the origin of Earth's magnetic field.

The other limit of the induction equation takes place when a perfect conductor is assumed.

This is $\sigma \rightarrow \infty$ or $\eta = 0$. With this, the induction equation takes the form

$$\frac{\partial \mathbf{B}}{\partial t} = \nabla \times (\mathbf{u} \times \mathbf{B}).$$

This is the so called *frozen flux limit* or *Alfvén's theorem*, which can be better interpreted if we consider the surface integral around a material surface S (composed of the same particles)

$$\int_S \frac{\partial \mathbf{B}}{\partial t} \cdot d\mathbf{S} - \int_S \nabla \times (\mathbf{u} \times \mathbf{B}) \cdot d\mathbf{S} = 0,$$

and by the Stoke's theorem this is the same as:

$$\int_S \frac{\partial \mathbf{B}}{\partial t} \cdot d\mathbf{S} + \oint_C \mathbf{u} \times \mathbf{B} \cdot d\mathbf{l} = 0,$$

where C is the closed contour of the material surface S . We can think of the relation between the surface and the line differentials on the previous integral as linked by the fluid velocity *only if* we are talking of a material surface, i.e., moving with the particles of the fluid. This is now

$$d\mathbf{S} = (\mathbf{u} \times d\mathbf{l})\delta t.$$

Therefore, we get back to a surface integral of the magnetic field, by using the cyclic properties of the scalar triple product to rearrange the terms on the line integral, and then simply added to the first integral on the equation. Hence,

$$\frac{d}{dt} \int_S \mathbf{B} \cdot d\mathbf{S} = 0.$$

This equation is the *frozen flux limit* for a material surface S , because it says that the magnetic flux through a material surface does not change in time, i.e., the magnetic field lines are frozen with the fluid velocity lines. This is no longer true if diffusion is included, because diffusion allows the field lines to slip through the fluid, quoting C.A. Jones in [70]. Even though we have omitted most of the mathematical rigor, this is an attempt to sketch an idea of the proof that it is explained in more detail by Davidson [50] for instance.

We would like to conclude this section by restating the induction equation but now using the dimensionless units. By deciding on a typical length scale L (that could be the size of the experiment, or the planet) and a typical velocity U (that could be the angular velocity of the boundaries of the experiment) we can write down the induction equation in its dimensionless form as

$$\boxed{\frac{\partial \mathbf{B}}{\partial t} = \nabla \times (\mathbf{u} \times \mathbf{B}) + \frac{1}{Rm} \nabla^2 \mathbf{B}.} \quad (2.21)$$

Where the derivatives are taken with respect to the new dimensionless coordinates and where Rm is the *magnetic Reynolds number* defined as

$$Rm = \frac{UL}{\nu}. \quad (2.22)$$

It basically measures the ratio of inertial forces to magnetic diffusivity. In other words, it tells us whether we are close to the diffusion limit or to the frozen flux limit. See the section 2.4 for a detailed explanation in the context of this dissertation's experimental work and the Figure 2.2 for a schematic representation of the physical interpretation of the Reynolds numbers.

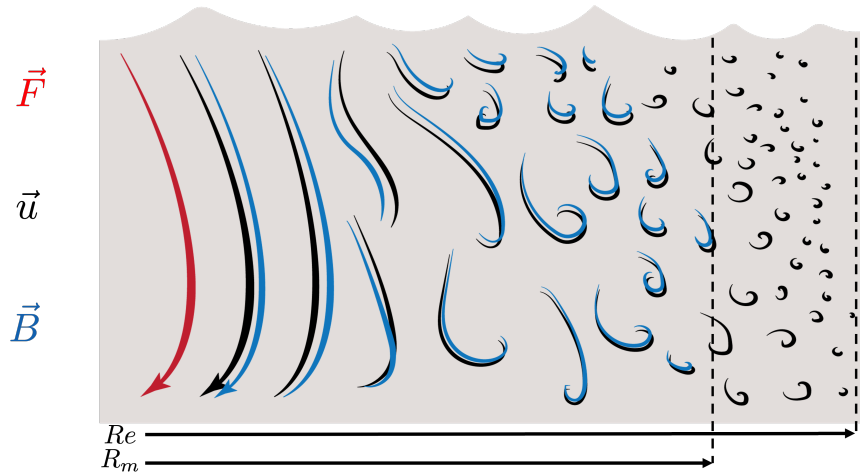


Figure 2.2: Schematic of the energy cascade to small scales in a viscous conductive flow. Re , the Reynolds number, represents the ratio of the forcing and the viscous forces and Rm , the magnetic Reynolds number, represents the ratio of the forcing and the magnetic diffusivity. The magnetic field lines in blue are dragged by the velocity field until the magnetic diffusivity, due to the non-infinite conductivity, dissipates them into currents.

2.3 Dynamo Theory

In the next section let us use the formalism and equations learned in the previous sections to address the dynamo problem. In plain words, we are looking for a velocity field that is capable of enhancing the magnetic field in a certain way that creates a self-sustained magnetic field. The dynamo problem is a two way street: one side where the velocity field stretches and amplifies the magnetic field lines, and the other side, where the magnetic field lines are capable of modifying the velocity field lines. In the next section, and for the majority of this dissertation, we will drive on one side of the road: a steady (or turbulent) velocity field capable of amplifying the magnetic field lines. This is called the *kinematic dynamo problem*.

2.3.1 Kinematic Dynamo Problem

Let $\mathbf{u}(\mathbf{x}, t)$ be a velocity field defined on a bounded volume V with surface S of a conductive fluid which has an uniform constant magnetic diffusivity η and density ρ . With this, we can define the total kinetic energy as

$$E(t) = \frac{1}{2} \int_V \rho \mathbf{u}^2 dV < E_0.$$

Here, we also assume that the mechanical energy is bounded.

Concerning the magnetic field $\mathbf{B}(\mathbf{x}, t)$, we shall assume, as we did in previous sections, that this magnetic field is generated entirely by the current distribution \mathbf{J} . The magnetic field will evolve then inside V with the induction equation 2.21, outside V with the Maxwell equations 2.15 and 2.16, and will be continuous across the boundary S , assuming (as it is normally assumed in fluids or solids of constant conductivity) that there are no surface currents: $\mathbf{J}_S = 0$. Additionally, the magnetic field is assumed to converge to 0 at infinity like a dipole field: $\mathbf{B} = O(r^{-3})$ as $r \rightarrow \infty$, and it is subject to the initial condition

$$\mathbf{B}(\mathbf{x}, 0) = \mathbf{B}_0(\mathbf{x})$$

With this, we can define the magnetic energy as

$$M(t) = \frac{1}{2\mu_0} \int_{V_\infty} \mathbf{B}^2 dV. \tag{2.23}$$

where V_∞ is understood as the whole space.

With these previous statements, a natural definition of the dynamo problem is as follows:

Given V and η , a velocity field $\mathbf{u}(\mathbf{x}, t)$ acts as a dynamo if $M(t) \not\rightarrow 0$ as $t \rightarrow \infty$ [51].

In other words, $\mathbf{u}(\mathbf{x}, t)$ successfully counteracts the erosive action of the ohmic dissipation. The magnetic energy M could tend to a constant nonzero value, or could oscillate either periodically or chaotically. It may also increase without limit which implies that the Lorentz forces need to be taken into account and we are no longer in the kinematic dynamo regime [51]. The velocity field $\mathbf{u}(\mathbf{x}, t)$ may also act as a dynamo for some, but not all, initial conditions \mathbf{B}_0 , or magnetic diffusivities η .

The simpler kinematic dynamo problem is linear in \mathbf{B} and with a constant flow $\mathbf{u}(\mathbf{x})$. Then, we look for solutions of the form

$$\mathbf{B}(\mathbf{x}, t) = \mathbf{B}_0(x, y, z)e^{pt}. \quad (2.24)$$

Here, we seek for eigenmodes \mathbf{B}_0 , each one with a set of complex eigenvalues

$$p = \lambda + i\omega,$$

where λ is the growth rate and ω the frequency of the dynamo wave.

Even with this simplification, the kinematic dynamo is a difficult problem. There are a few working kinematic dynamo models that have been proved successfully. Among them we have the *Faraday Disk Dynamo Models* that consists of rotating disks in the presence of a magnetic field, capable of generating currents capable of sustaining a magnetic field. See figure 2.3. There are a few working disk dynamos like this, check for instance [70].

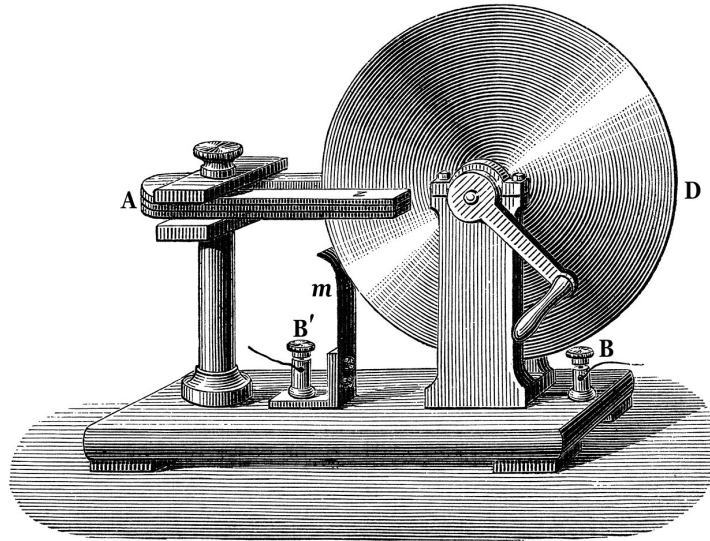


Figure 2.3: Drawing of Faraday disk, the first electromagnetic generator, invented by British scientist Michael Faraday in 1831. The copper disk (D) rotated between the poles of a horseshoe shaped magnet (A), creating a potential difference between the axis and rim due to Faraday's law of induction. If an electrical circuit such as a galvanometer was connected between the binding posts (B) and (B') the motion induced a radial flow of current in the disk, from the axle toward the edge. The current flows into the spring contact (m) sliding along the edge of the disk, out of binding post (B') through the external circuit to binding post (B), and back into the disk through the axle. From Alglave and Boulard [6]

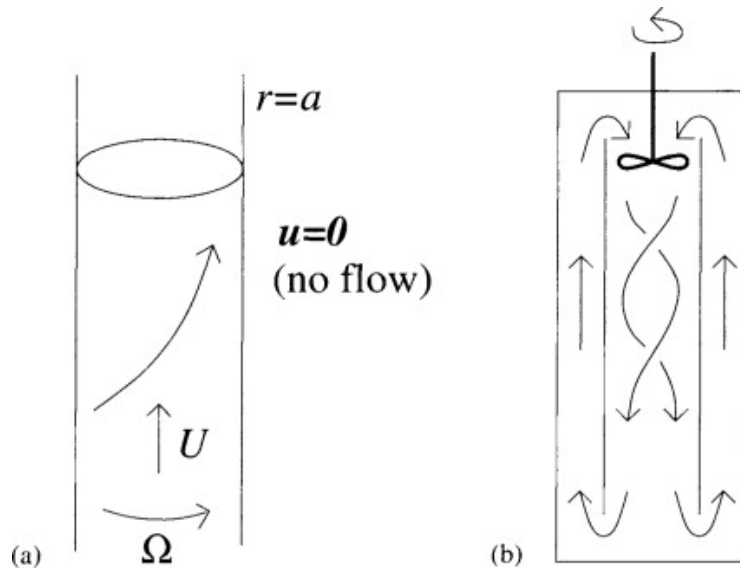


Figure 2.4: Sketches of the Ponomarenko Dynamo model (a) and the Riga dynamo experiment (b). From Gilbert [7].

We also have flow dynamos in restricted geometries like the *Ponomarenko dynamo* illustrated in Figure 2.4 (a): a simple helical flow in a cylindrical container. For all these models an analysis can be made in terms of the minimum magnetic Reynolds number capable of sustaining dynamo action by assuming a solution of the form 2.24 in the respective system of reference (cylindrical, spherical, etc) into the induction equation. See for instance [7, 71, 72]. A detailed analysis escapes the scope of this dissertation but a good summary, for which the majority of this section was inspired, can be found in Course 2 of Cardin et al. [70]. Check also Childress and Gilbert [52] for a detailed study of the dynamo action in the context of chaos theory.

For the rest of the dissertation we will focus on kinematic dynamo models in the context of spherical geometries. In order to do so, we will introduce new mathematical formulations in the next section.

2.3.2 Spherical Dynamos

When there is no current in a region of space, the magnetic field satisfies $\nabla \times \mathbf{B} = 0$, which implies the existence of a scalar potential V such that $\mathbf{B} = \nabla V$ and

$$\nabla^2 V = 0.$$

This is Laplace's Equation. When $V \rightarrow 0$ at infinity, the solution of this equation can be expressed in the form:

$$V = \frac{a}{\mu} \sum_{\ell=1}^{\infty} \sum_{m=0}^{\ell} \left(\frac{a}{r}\right)^{\ell+1} P_{\ell}^m(\cos \theta) (g_{\ell}^m \cos(m\phi) + h_{\ell}^m \sin(m\phi)), \quad (2.25)$$

where we have spherical coordinates. Here, P_ℓ^m are the Schmidt normalized Legendre functions, a is the radius of the Earth, and g_ℓ^m and h_ℓ^m are the *Gauss coefficients*.

From here we can obtain the magnetic field by means of $\mathbf{B} = \nabla V$. For this dissertation in particular it will be convenient to express the magnetic field projected onto the sphere surface where the currents are contained in the space. This could be the Earth's Core-Mantle boundary or the vessel of the experiment. In this case the radial component of the magnetic field in the surface takes the form:

$$\hat{\mathbf{r}} \cdot \mathbf{B}(r, \theta, \phi) = \sum_{\ell=1}^{\infty} \sum_{m=0}^{\ell} \ell(\ell + 1) \left(\frac{a}{r}\right)^{\ell+2} P_\ell^m(\cos \theta) (g_\ell^m \cos(m\phi) + h_\ell^m \sin(m\phi)). \quad (2.26)$$

With this, the quantity

$$B_\ell^m = \ell(\ell + 1) \left(\frac{a}{r}\right)^{\ell+2} g_\ell^m, \quad (2.27)$$

(or h_ℓ^m) will be the peak field strength of the radial magnetic field at the spherical boundary associated with the mode (l, m) . For instance the mode $(1, 0)$ corresponds to an axial dipole field, the mode $(2, 0)$ with a quadrupole field, the mode $(1, 1)$ to a rotating equatorial dipole field, and so on.

Together with the spherical harmonics decomposition, we can decompose the magnetic field in spherical geometry into poloidal and toroidal components. By means of $\nabla \cdot \mathbf{B} = 0$, only two independent scalar fields are needed to specify the magnetic field \mathbf{B} :

$$\mathbf{B} = \mathbf{B}_T + \mathbf{B}_P,$$

where

$$\mathbf{B}_T = \nabla \times (\mathbf{r}T(\mathbf{r}, t)), \quad (2.28)$$

$$\mathbf{B}_P = \nabla \times \nabla(\mathbf{r}P(\mathbf{r}, t)). \quad (2.29)$$

Each one of the scalar fields T and P can be decomposed in surface spherical harmonics by means of 2.26.

Another common field decomposition is in the symmetric and axisymmetric parts. This is standard for rotational experiments in which the dynamics are considerably symmetric, given the existence of a preferable direction of movement. The formalism is used theoretically by Braginskii (see for instance Chapter 8 of Moffatt [51]) to study weak departures from axial symmetry in dynamo systems.

To continue with our study of dynamos in spherical geometry, let us now introduce the work and formalism of Bullard and Gellman (1954) [49]. They decomposed the magnetic and velocity field in toroidal and poloidal spherical harmonics:

$$\mathbf{B} = \sum_{l,m} \mathbf{T}_\ell^m + \mathbf{S}_\ell^m,$$

$$\mathbf{u} = \sum_{l,m} \mathbf{t}_\ell^m + \mathbf{s}_\ell^m.$$

Where

$$\mathbf{t}_\ell^m = \nabla \times \hat{\mathbf{r}}t_\ell^m(r, t)Y_\ell^m(\theta, \phi), \quad \mathbf{s}_\ell^m = \nabla \times \nabla \times \hat{\mathbf{r}}s_\ell^m(r, t)Y_\ell^m(\theta, \phi), \quad (2.30)$$

where $Y_\ell^m(\theta, \phi)$ are the scalar spherical harmonics. The previous equations can be similarly written for S_ℓ^m and T_ℓ^m .

Bullard and Gellman (1954) used this notation to study kinematic dynamos in a spherical geometry. A proposed velocity fields \mathbf{u} , in terms of t_ℓ^m and s_ℓ^m , could modify an existent magnetic fields, expressed in toroidal and poloidal parts as well, to generate a self sustained dynamo. The angular part of the field is contained in the (l, m) pair, and the radial part is expressed as polynomials on r . For instance, they proposed a velocity field of the form:

$$\mathbf{u} = \epsilon t_1^0 + s_2^2,$$

with a stationary radial dependence on the toroidal and poloidal components: $t_1^0(r) = r^2(1 - r)$ and $s_2^2(r) = r^3(1 - r)^2$. In their calculations this field was capable of generating a dynamo, however, posterior numerical runs showed that they were actually not dynamos.

One of the main results of Bullard and Gellman [49] was a list of selection rules that showed which interaction between magnetic fields and velocity fields were allowed by expressing the induction equation in toroidal and poloidal spherical harmonics components. They expressed the allowed interactions in triads. For instance

$$(S_\alpha, T_\beta, T_\gamma)$$

can be read as: a poloidal magnetic field of order α ($l = \alpha$) and wave number m_α , is advected by a toroidal velocity field T_β , to create a toroidal magnetic field T_γ . This interaction is only possible if the triad α, β and γ satisfy a series of selection rules. We will not list them all, but they can be

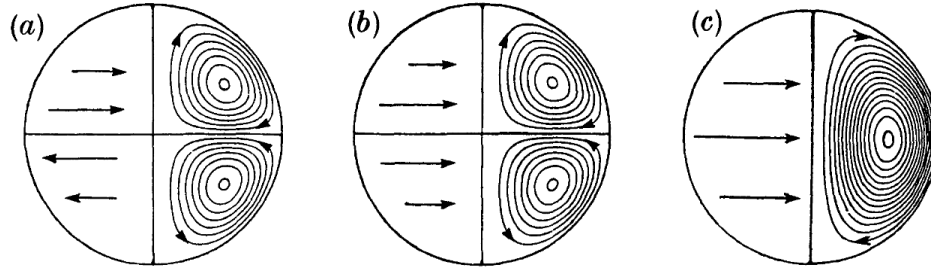


Figure 2.5: Sketches of the flows proposed by Dudley and James to generate dynamos and shown respectively in equation 2.31. On the right, the meridional sections, on the left the azimuthal flow direction. From Dudley M. L. et al. [8]

found in Bullard and Gellman [49], section 6. One of them is, for instance, that $\alpha + \beta + \gamma$ must be even and must form the sides of a triangle.

Following the Bullard and Gellman formalism, Dudley and James [8] proposed a series of new velocity fields that could lead to dynamo action. These flows are of the form

$$\mathbf{u} = \epsilon \mathbf{s}_2^0 + \mathbf{t}_2^0, \quad \mathbf{u} = \epsilon \mathbf{s}_2^0 + \mathbf{t}_1^0, \quad \mathbf{u} = \epsilon \mathbf{s}_1^0 + \mathbf{t}_1^0. \quad (2.31)$$

with $t_1^0(r) = s_1^0 = r \sin \pi r$ and $t_2^0(r) = s_2^0 = r^2 \sin \pi r$. These fields are illustrated in Figure 2.5. They generated dynamo for selected values of ϵ , each one of them with its respective critical magnetic Reynolds number of order $Rm \sim 100$. In all three cases the meridional and poloidal flows are of similar intensity and the main generated field is an oscillatory equatorial dipole that rotates in time, so $(l = 1, m = 1)$ [70].

There are more of these flows proposed to generate a dynamo, one of particular interest is the Kumar-Roberts flow, which is similar to the ones in Figure 2.5 but more complex, with one term intended to mimic thermal convection rolls in the core:

$$\mathbf{u} = \epsilon_0 \mathbf{t}_1^0 + \epsilon_1 \mathbf{s}_2^{2c} + \epsilon_2 \mathbf{s}_2^{2c} + \epsilon_3 \mathbf{s}_2^{2s}, \quad (2.32)$$

where the $2s$ ($2c$) stands for the sine (cosine) Gauss coefficient of equation 2.26 [70].

Gubbins et al. [9] studied in more detail these flows for a diverse range of ϵ and radial dependences. They defined the relative energy as divided in the differential rotation energy D governed by ϵ_0 , the meridional circulation energy M governed by ϵ_1 , and the convection energy C governed by ϵ_3 and ϵ_4 . Therefore,

$$D + M + C = 1$$

They found a relation between the helicity of the flows and the critical Reynolds number for dynamo action. Additionally, they found some regions, in terms of proportion between M and D , in which dynamos were not possible. They summarize it in the so-called Love diamonds (Love is one of the authors of [9]) shown in Figure 2.6. There you can see that the widest area with the lower critical magnetic Reynolds number in the upper diamond coincides with an area of high helicity in the lower diamond.

2.3.3 Mean field dynamo theory

In this section we will introduce a conventional approach taken also in fluid dynamics to study turbulence models, the *mean field approximation*. This will allow us to understand the role of the fluctuations in the behavior of the mean flows, and thus, the importance of the turbulence in

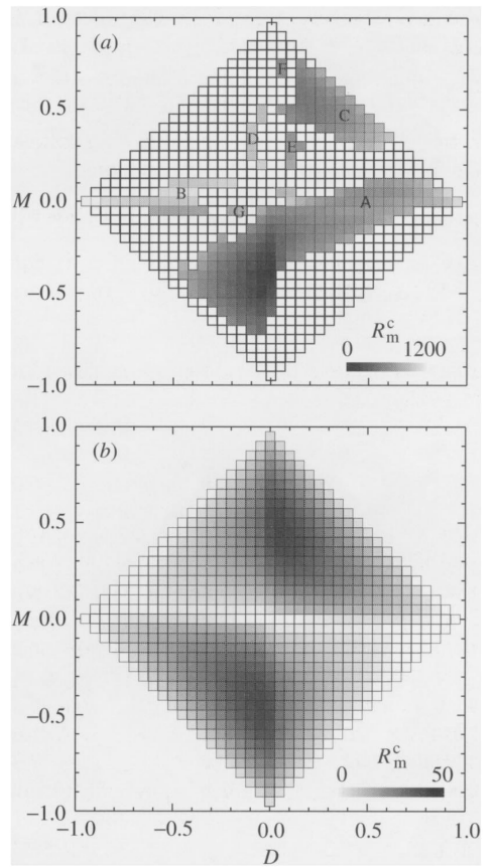


Figure 2.6: The Love diamonds. The upper diamonds indicated the regions of the map (D, M) where dynamos occur and at which critical magnetic Reynolds number. Lower dynamo is the helicity of the flows. From Gubbins et al. [9]

the dynamo mechanism. In particular this section will help us to understand the relation between the helicity and the dynamo action, and hence, allows us to connect the water experiments with the sodium experiments which is the main storyline of the present dissertation. The discussion in this chapter is guided mostly from the notes of C. A. Jones in the book by Cardin et al. [70].

We start with a very simple approach: we split the magnetic and velocity field into mean and fluctuating parts:

$$\mathbf{B} = \overline{\mathbf{B}} + \mathbf{B}', \quad \mathbf{u} = \overline{\mathbf{u}} + \mathbf{u}'. \quad (2.33)$$

With the so called, *Reynolds averaging rules*:

$$\overline{\mathbf{B}_1 + \mathbf{B}_2} = \overline{\mathbf{B}_1} + \overline{\mathbf{B}_2}; \quad \overline{\overline{\mathbf{B}}} = \overline{\mathbf{B}}; \quad \overline{\mathbf{B}'} = 0, \quad (2.34)$$

$$\overline{\mathbf{u}_1 + \mathbf{u}_2} = \overline{\mathbf{u}_1} + \overline{\mathbf{u}_2}; \quad \overline{\overline{\mathbf{u}}} = \overline{\mathbf{u}}; \quad \overline{\mathbf{u}'} = 0. \quad (2.35)$$

We will also assume that averaging commutes with differentiation.

$$\frac{\partial \overline{\mathbf{B}}}{\partial t} = \overline{\frac{\partial \mathbf{B}}{\partial t}} \quad \nabla \overline{\mathbf{B}} = \overline{\nabla \mathbf{B}}. \quad (2.36)$$

With all this, we now average the induction equation 2.21 resulting in

$$\frac{\partial \overline{\mathbf{B}}}{\partial t} = \nabla \times (\overline{\mathbf{u} \times \mathbf{B}}) + \eta \nabla^2 \overline{\mathbf{B}}. \quad (2.37)$$

Now, we use the Reynolds Averaging rules on the first term on the right side of 2.37 and we obtain:

$$\frac{\partial \overline{\mathbf{B}}}{\partial t} = \nabla \times (\overline{\mathbf{u}} \times \overline{\mathbf{B}}) + \nabla \times \mathcal{E} + \eta \nabla^2 \overline{\mathbf{B}}, \quad (2.38)$$

where $\mathcal{E} = \overline{\mathbf{u}' \times \mathbf{B}'}$. The term \mathcal{E} is called the e.m.f. (electromotive force).

The direct consequence is fairly simple but powerful in concept: there is a new fluctuating term in the mean induction equation. In other words, the turbulent magnetic and velocity fields are interacting in such a way that, if they satisfy the averaging rules, they modify the mean magnetic fields.

We can subtract equation 2.38 from the induction equation 2.21 to obtain the induction equation of the turbulent magnetic field \mathbf{B}' :

$$\frac{\partial \overline{\mathbf{B}'}}{\partial t} = \nabla \times (\overline{\mathbf{u}} \times \mathbf{B}') + \nabla \times (\mathbf{u}' \times \overline{\mathbf{B}}) + \nabla \times \mathcal{G} + \eta \nabla^2 \mathbf{B}', \quad (2.39)$$

where $\mathcal{G} = \mathbf{u}' \times \mathbf{B}' - \overline{\mathbf{u}' \times \mathbf{B}'}$.

If we assume that at a starting time there is only an external applied field $\mathbf{B}_0 = \overline{\mathbf{B}}$, The equation 2.39 guarantees that the field \mathbf{B}' and $\overline{\mathbf{B}}$ are linearly related [51]. This allows us to express the term \mathcal{E} as a convergent series in the form:

$$\mathcal{E}_i = \alpha_{ij} B_{0j} + \beta_{ijk} \frac{\partial B_{0j}}{\partial x_k} + \dots \quad (2.40)$$

Here, α_{ij} and β_{ijk} are pseudo tensors and we have only expanded up to the first order terms.

If we assume that the turbulence is isotropic and homogeneous, the statistical properties of \mathbf{u} are invariant under rotation and translation, ergo, α_{ij} and β_{ijk} must be isotropic tensors as well:

$$\alpha_{ij} = \alpha(\mathbf{x})\delta_{ij}, \quad \beta_{ijk} = -\beta(\mathbf{x})\epsilon_{ijk}. \quad (2.41)$$

Plugging this back into 2.38 we obtain the main equation of the mean field dynamo theory,

$$\boxed{\frac{\partial \bar{\mathbf{B}}}{\partial t} = \nabla \times (\bar{\mathbf{u}} \times \bar{\mathbf{B}}) + \nabla \times \alpha \bar{\mathbf{B}} - \nabla \times (\beta \nabla \times \bar{\mathbf{B}}) + \eta \nabla^2 \bar{\mathbf{B}}.} \quad (2.42)$$

In particular, if α and β are constant, the term $\nabla \times (\beta \nabla \times \bar{\mathbf{B}}) = -\beta \nabla^2 \bar{\mathbf{B}}$, so it acts as an enhanced diffusivity. This is known as the *beta effect*. From now on, we will focus on the α term, known in the literature as the *alpha effect*. This term is directly connected with the helicity of the velocity fields as we will see next.

The implications of the alpha effect can be better understood if we use the Ohm's law 2.18.

If $\alpha_{ij} = \alpha \delta_{ij}$, then to order zero

$$\mathcal{E} = \alpha \bar{\mathbf{B}},$$

and by Ohm's law we have

$$\mathbf{J} = \sigma \mathcal{E} = \sigma \alpha \bar{\mathbf{B}}. \quad (2.43)$$

This equation might not seem relevant at first, but it implies that the electrical current generated by the turbulent fluctuations is *parallel* to the magnetic field lines. This, in contrast, with Ampere's law 2.15. As mentioned by Moffatt [51], this is the heart of the dynamo theory. It provides an obvious means whereby the dynamo cycle might be completed, i.e., the toroidal field can be transformed back to poloidal field. With this new term in equation 2.42 the Cowling's Theorem no longer applies and we can have dynamos with simple axisymmetric fields.

If we express the magnetic field into poloidal (\mathbf{B}_p) and azimuthal component (\mathbf{B}_θ), equation 2.42 (neglecting the β -effect) for the poloidal fields becomes:

$$\frac{\partial \mathbf{B}_p}{\partial t} = \nabla \times (\mathbf{u}_p \times \mathbf{B}_p) + \nabla \times \alpha \mathbf{B}_\theta + \eta \nabla^2 \overline{\mathbf{B}_p}.$$

And so, the α -effect is the only way to generate poloidal fields from entirely azimuthal fields.

To better understand the implications of the alpha effect, let us consider just the fluctuating induction equation, and let us make a change of reference frame to one moving with the mean velocity field, so $\overline{\mathbf{u}} = 0$. Additionally, for the sake of the calculation, we assume that the magnetic Reynolds number associated with the fluctuating scale ($Rm = u'l/\eta$) is small, so equation 2.39 becomes

$$\frac{\partial \overline{\mathbf{B}'}}{\partial t} = (\overline{\mathbf{B}} \cdot \nabla) \mathbf{u}' + \eta \nabla^2 \mathbf{B}'. \quad (2.44)$$

If we know assume a fluctuating magnetic field as a superposition of random waves of the form $\mathbf{u}' = \text{Re}[\mathbf{u} \exp i(\mathbf{k} \cdot \mathbf{x} - \omega t)]$, and we plug it into the equation 2.44, we obtain

$$\mathbf{B}' = \text{Re} \left[\frac{i(\mathbf{k} \cdot \overline{\mathbf{B}}) \mathbf{u}}{\eta k^2 - i\omega} \exp i(\mathbf{k} \cdot \mathbf{x} - \omega t) \right]. \quad (2.45)$$

Now we evaluate $\mathcal{E} = \overline{\mathbf{u}' \times \mathbf{B}'}$ and we obtain

$$\overline{\mathbf{u}' \times \mathbf{B}'} = \frac{1}{2} \frac{i\eta k^2 (\mathbf{k} \cdot \overline{\mathbf{B}})}{\eta^2 k^4 + \omega^2} (\mathbf{u}^* \times \mathbf{u}).$$

Here the $*$ stands for the complex conjugate. On the other hand, we can calculate also the helicity

of the turbulent fields H as

$$H = \overline{\mathbf{u}' \cdot \nabla \times \mathbf{u}'} = -\frac{1}{2}i\mathbf{k} \cdot (\mathbf{u}^* \times \mathbf{u}).$$

Therefore, comparing this calculation of H with the one for $\overline{\mathbf{u}' \times \mathbf{B}'}$, we can see that if $\mathcal{E} = \overline{\mathbf{u}' \times \mathbf{B}'} = \alpha \overline{\mathbf{B}}$, then in fact α is going to be proportional to the helicity H .

A more detailed calculation can be found in Moffatt [51], but also an analysis based on dimensionless groups can be made as suggested by Davidson [50]. We might expect α to depend only on $|\mathbf{u}'|$ (the velocity of the eddies), η and ℓ (the size of the eddies). At high magnetic Reynolds numbers we can expect α to be independent of η , and so the only dimensional group that we can create suggests that $\alpha \sim \mathbf{u}'$. But α is a pseudo-scalar, and so is helicity. So, alternatively, we can construct the same dimensional group by

$$\alpha \sim \overline{[\mathbf{u}' \cdot \nabla \times \mathbf{u}']} \ell / |\mathbf{u}'|.$$

This kind of arguments implies, but does not prove, that helicity is a key component of the α -effect for high Rm . A similar argument can be made for a low magnetic Reynolds number, where the helicity also acts as the pseudo-scalar that we need to include to match the dimensional group. See for instance Davidson [50] for an introductory discussion, and Moffatt [51] for a more rigorous approach.

2.3.4 Dynamo Models: The α^2 and $\alpha\omega$ dynamo

The existence of α -effect allows us to have axisymmetric dynamos. With asymmetric fields of the form

$$\mathbf{u} = s\omega(s, z)\hat{\phi} + \mathbf{u}_\theta; \quad \mathbf{B} = sB(s, z)\hat{\phi} + \mathbf{B}_\theta, \quad (2.46)$$

where s stands for the cylindrical radius and with $\mathbf{B}_\theta = \nabla \times A(s, z)\hat{\phi}$. With this, the induction equations become

$$\partial B/\partial t + s(\mathbf{u}_\theta \cdot \nabla)(B/s) = s(\mathbf{B}_\theta \cdot \nabla)\omega + \nabla \times (\alpha\mathbf{B}_\theta) + (\beta + \eta)(\nabla^2 - s^{-2})B, \quad (2.47)$$

$$\partial A/\partial t + s^{-1}(\mathbf{u}_\theta \cdot \nabla)(sA) = \alpha B + (\beta + \eta)(\nabla^2 - s^{-2})A. \quad (2.48)$$

There are two main source terms involving the poloidal magnetic field \mathbf{B}_θ on the right of equation 2.47. The ratio of these two source terms is of the order

$$\frac{s(\mathbf{B}_\theta \cdot \nabla)\omega}{\nabla \times (\alpha\mathbf{B}_\theta)} = O\left(\frac{L^2|\nabla\omega_0|}{\alpha_0}\right). \quad (2.49)$$

Where L is a characteristic length and the sub-index 0 indicates a typical value for α and the gradient of vorticity.

We have then two situations. The first one is when $L^2|\nabla\omega_0| \ll \alpha_0$. In this case the differential rotation term in equation 2.47 is negligible, and we have a dominating α -effect acting as both sources of poloidal and toroidal field. This model is called the α^2 dynamo. The second

situation is when $L^2|\nabla\omega_0| \gg \alpha_0$ where the differential rotation term dominates. Now, the toroidal field is generated by differential rotation and the poloidal field is generated by the α -effect. Dynamos generated this way are called $\alpha\omega$ -dynamos.

2.3.5 Kolmogorov Scaling Law for Magnetic Fields

There is an analog to the five-thirds Kolmogorov scaling law of section 2.1.5 but for magnetic field lines. As discussed briefly in that section, the viscous range is the scale at which the viscosity starts being relevant for the dynamics. This viscous scale is characterized by a viscous cut-off wave number k_η , i.e., the size of the eddies that starts being dissipated by viscosity. The same happens for the magnetic field lines: there is a scale at which the magnetic diffusion starts dominating the dynamics of the magnetic field, and it starts to diffuse into electrical currents in the flow. This range is characterized by the conduction cut-off k_σ .

Following the discussion by Moffatt [73], Nornberg et al. [74] and the discussion in the previous section, if we take $\mathbf{B} = \overline{\mathbf{B}} + \mathbf{B}'$ into the induction equation, assume a fluctuating magnetic field as a superposition of random waves of the form $\mathbf{u}' = \text{Re}[\mathbf{u} \exp i(\mathbf{k} \cdot \mathbf{x} - \omega t)]$, and plug it into the equation 2.44 we obtain equation 2.21. We now assume Taylor's hypothesis (see section 2.1.6), i.e., the magnetic fluctuations are primarily due to advection of eddies by the mean flow [74] and so the dispersion relation is approximately $\omega \sim ku_0$ (where u_0 is associated with the estimation of the magnetic Reynolds number). We now divide equation 2.45 by the dispersion relation and obtain that

$$\left(\frac{i\omega}{ku_0} + \frac{k\eta}{u_0} B' \right) \sim i \frac{u}{u_0} \overline{B}.$$

If we now consider the case where $k \ll k_\sigma$, then by definition this conduction cut-off is related with the magnetic Reynolds number in the form $k_\sigma \equiv u_0/\eta = Rm/a$ where a is a characteristic length associated with u_0 . This will let us approximate

$$B'^2/\overline{B}^2 \sim u^2/u_0^2,$$

and from equation 2.13 we have that $E(k) = u^2/k \sim k^{-5/3}$, and so the magnetic energy spectrum is

$$E_M(k) = B'^2/k^2 \sim k^{-5/3}.$$

If, on the other hand, $k_\sigma \ll k$ we obtain the scaling

$$B'^2/\overline{B}^2 \sim u^2/(\eta k)^2,$$

and then

$$E_M(k) \sim k^{-2}E(k) \sim k^{-11/3}.$$

This is the Kolmogorov scaling law for magnetic fields under turbulent diffusion, assuming Taylor's hypothesis. It has been found experimentally in many situations, including in the Madison experiment [74]. However, it was not found in the VKS experiment [75] where it was attributed to a spatial filtering due to the dimension of the tube containing the probe.

2.4 Dimensionless Parameters

In this last section of the theory framework, we summarize the main dimensionless numbers used and defined in the present dissertation for the particular control parameters of our experiments, i.e., spherical Couette flows.

We define the fluid and magnetic Reynolds numbers as:

$$Re = \frac{|\Omega_i - \Omega_o|(r_i - r_o)^2}{\nu}, \quad Rm = \frac{|\Omega_i - \Omega_o|(r_i - r_o)^2}{\eta} \quad (2.50)$$

where Ω_i is the angular frequency of the inner sphere, Ω_o is the angular frequency of the outer sphere, and r_i and r_o are the inner and outer radii respectively. The value for r_i does not include the baffles height. The kinematic viscosity ν is taken as $1.1 \times 10^{-6} \text{ m}^2/\text{s}$ for water [76] and $0.71 \times 10^{-6} \text{ m}^2/\text{s}$ for liquid sodium [77]. The magnetic diffusivity η is $0.079 \text{ m}^2/\text{s}$ for sodium [77].

The dimensionless parameter used to characterize the differential rotation is the Rossby number:

$$Ro = \frac{(\Omega_i - \Omega_o)}{\Omega_o}. \quad (2.51)$$

This also indicates the ratio of inertial to Coriolis forces.

We also define the Ekman number as:

$$E = \frac{\nu}{\Omega_o(r_i - r_o)^2}. \quad (2.52)$$

This indicates the ratio of viscous to Coriolis forces. For the 3-m experiment we achieve $E \approx$

10^{-9} , a relatively small number for a laboratory experiment, though still larger than that for the Earth's $E \approx 10^{-15}$ [12].

Chapter 3: The 40-cm experiment: Hydrodynamics Studies

In this chapter we will discuss the results on the 40-cm water experiment. This experiment serves as a model of the 3-m spherical Couette Flows experiment with the same sphere's radius ratio of $\Gamma = 0.35$. As mentioned before, the idea was to perform velocimetry measurement to test scaled models of different baffles configurations to test the dynamics and topology of the flows generated, and, if possible, give an estimate of the helicity improvement that the flows could develop under different baffles design. We will describe first, the experimental setup and the parameter space; then, we will continue with the main results, starting from torque scaling, equatorial velocimetry and meridional velocimetry. The latter performed in the only region we could anticipate by the equatorial velocimetry results as we will see. The next section follows mostly our publication Rojas et al. [78] in Physical Review Fluids but we have adapted it to follow this dissertation outline.

3.1 Experimental Set-up

The experiment shown in Figure 3.1 consists of two independently rotating spheres with $\Gamma = r_i/r_o = 0.35$. The 40-cm diameter outer sphere is made of two 5-mm thick acrylic shells bolted together at the equator using a rubber gasket seal, and is rotated by a motor using a gear belt. The 14-cm diameter inner sphere is connected directly to a motor using a shaft that sits on

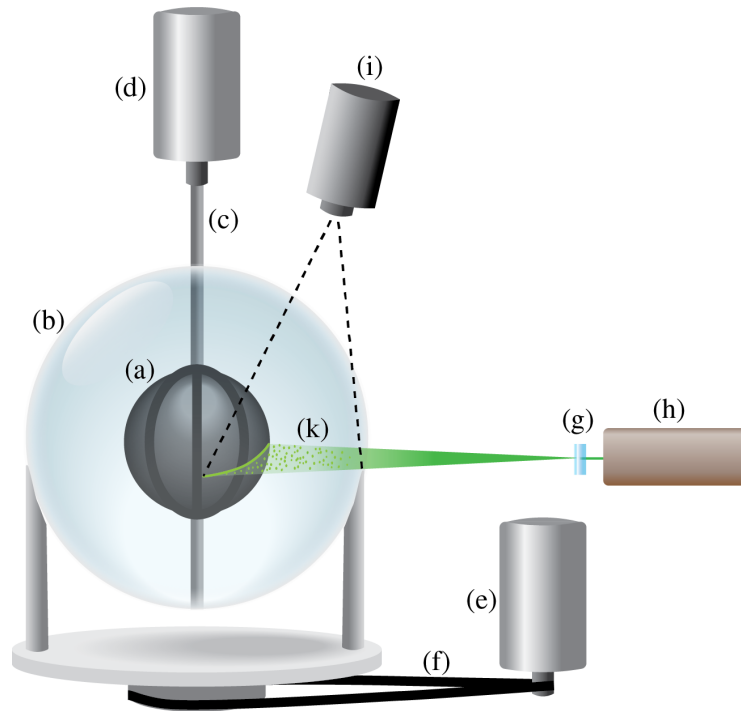


Figure 3.1: Schematic of the 40-cm experiment. (a) 12 cm diameter inner sphere with straight baffles. The baffle height adds 5% or 10% to the inner sphere radius. (b) 40 cm diameter acrylic outer sphere filled with water. (c) 1 cm diameter inner shaft. (d) 3 kW inner motor. (e) 2.23 kW outer motor. (f) Gear belt. (g) Cylindrical lens for laser sheet. (h) 6 W NdYVO₄ continuous laser. (i) High-speed camera positioned for measurements in the equatorial plane. (k) Polystyrene particles dispersed in the water.

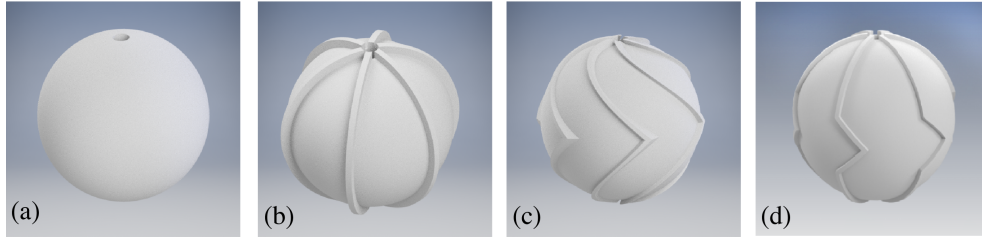


Figure 3.2: Four types of inner spheres were tested in the 40-cm experiment. (a) Smooth, (b) Straight, (c) Chevron and (d) Alpha. The two rotation directions for (c) and (d) are called wedge mode and scoop mode.

a bearing in the bottom of the outer sphere. This motor was taken from a broken treadmill and adapted for the experiment. It was connected to an external power supply. Once the experiment is assembled, the outer sphere is filled with water at about 20°C. Very extended running times are avoided to reduce changes in temperature: only $\pm 2^\circ\text{C}$ were detected, which implies around 0.5% change in kinematic viscosity of the water. This is negligible compared to the experiment systematic uncertainty associated with the friction in the motor (see section 3.2.1).

The inner spheres with baffles were 3D-printed from Polylactic Acid (PLA) with baffles whose height was 5% and 10% of the inner sphere radius. Three baffle designs are tested in both heights: straight baffles from pole to pole (Figure 3.2), chevron shaped baffles with a curve given by $\theta = \varphi$ in spherical coordinates on the surface of the sphere (Figure 3.2) and a hybrid of straight and chevron baffles as shown in Figure 3.2, which will be called *alpha* baffles for the rest of this work. The motivation for this design is to test an asymmetric baffle model more amenable to fabrication than the chevron shaped baffles. With these chevron and alpha designs we aim to break one symmetry of the experiment ($\varphi \rightarrow -\varphi$). For smooth and straight design, reversing the rotation direction of both spheres gives the same flow states, whereas reversing both for chevron and alpha designs should yield distinct states. We call these two different modes of operation for each of the asymmetric designs *wedge* and *scoop*. This causes an effective doubling of the

parameter space as we will discuss in section 2.4.

For the smooth inner sphere, the maximum rotation rate was 50 Hz for the inner sphere and 5 Hz for the outer sphere. We record the current and voltage in the inner motor, calculate the power with these two values and use the rotation rate to derive the power and torque: $P_i = \Omega_i \cdot \tau_i$, where P_i is the power, Ω_i is the inner sphere angular velocity and τ_i is the torque from the inner motor. Optical sensors are used to measure the frequency for both motors. The main source of torque error is the friction from the bearings and in the motors. Runs at very low rotation rate are performed to estimate the friction error in the experiment. A run with air instead of water was also performed to examine the error in the torque at high rotation rates.

For the velocimetry measurements a 6 W laser, stationary in the laboratory frame of reference, passes through a cylindrical lens to create a laser sheet. When measurements of the equatorial plane are performed the laser sheet hits the sphere in a parallel plane to the equator a few millimeters above it to avoid being occluded by the flange and gasket seal. Polyethylene fluorescent particles of 75-106 μm diameter are added to the water to allow particle image velocimetry (PIV) techniques [79]. High speed videos at 1000 frames per second (fps) are used to record the particle motions in 1-s intervals. Several videos of the same parameters are performed and averaged.

To compensate for the spherical aberration due to the change in the refraction index between water and air, a calibration measurement is done as follows: (i) with the camera in the same position as it was for the measurements, a metallic square mesh of known spacing is placed in the equatorial and meridional planes respectively. (ii) The sphere is filled with water and pictures of both planes are taken. (iii) A non-linear calibration curve is fitted to the data, which allows us to transform from pixel position in the videos, to radial and angular position in spherical coordinates. In spite of this calibration, spherical aberration makes measurements unavailable

near the outer sphere boundary as well as near the shaft and inner sphere boundary due to laser reflections which locally saturate the camera. More details about the velocity measurements will be discussed in section [3.2.2](#).

The control system for the experiment is shown in Figure [3.3](#). Everything is controlled by a Data Acquisition System (DAQ) which is programmed to talk to the driver of the outer motor and with the power supply that powers the inner motor. It also collects the data from the system in form of voltages across key segments of the system. A resistive load is situated between the power supply and the inner motor; the voltage drop across this known resistor was used to compute the current in the inner motor. This voltage corresponded to the inputs AI3 and AI1 on the DAQ. Additionally, the voltage in the motor was acquired by measuring the voltage drop across the inputs AI2 and AI1. With this two values, we were able to measure the power in the inner motor.

A set of two optical gates were used to compute the rotation rates in the inner and the outer motors. At the first stages of the experiment an oscilloscope was used to manually measure the frequency in both motor, but later this was upgraded to be detected directly by the program that runs the motors. This stage was crucial for improving the control feedback with the experiment: given the lack of a driver for the inner motor, the voltage input had to be constantly adjusted to overcome the torque demands of the system and keep the rotation rate at the requested value. This demanded a constant read of the rotation rates of the systems and a set of calibrations curves to better estimate the initial voltage demands.

In Figure [3.4](#) we see a representation of the differences in the parameter space due to an asymmetric baffle design like the chevron or alpha baffles (see Figure [3.2](#)). Changing the rotation direction of the inner sphere Ω_i , changes the leading edge shape of the baffles that engages with

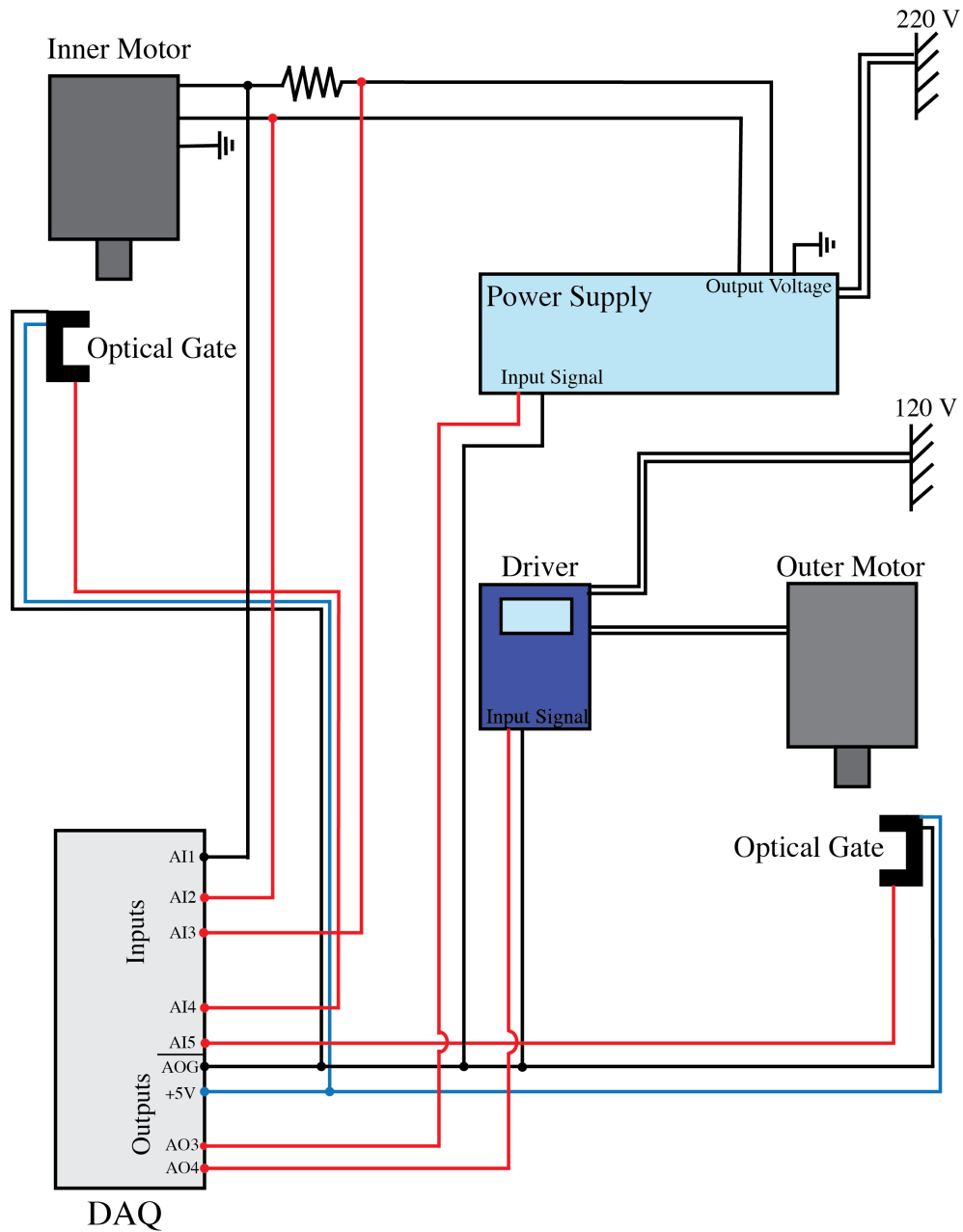


Figure 3.3: Schematics of the 40-cm experiment control system. A Data Acquisition System (DAQ) communicates with a DC external power supply and with the outer motor driver. The power supply then control directly the inner motor by a series of logic inputs by the DAQ. The outer motor is controlled by its own driver who is controlled by the DAQ. A resistive load is located between the inner motor and the power supply to measure the current in the system.

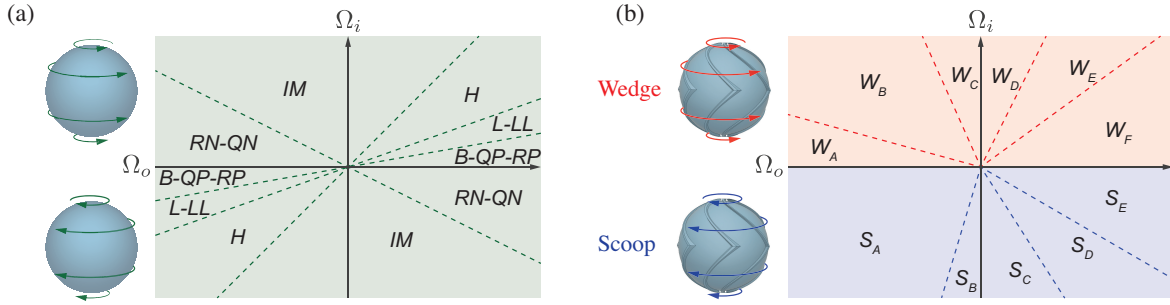


Figure 3.4: Schematic of the doubling of the parameter space (Ω_o, Ω_i) by breaking the symmetry of the inner sphere with respect to the rotation direction. The Finke and Tilgner [10] parameter space corresponds to the vertical axis. In (a) an inversion with respect to the origin results in the same states, making this plane to be symmetric to inversion through the origin. In (b), an inversion results in different, yet unknown, states. State labels for (a) come from prior studies in the 3-m system [4]. State labels in (b) are for illustrative purposes only.

the fluid. We called these two different directions wedge mode and scoop mode, as indicated in Figure 3.4. These two modes are expected to change the hydrodynamics of the resulting flows, hence giving rise to different states, in a similar way that changes in the angle of attack in aerodynamics result in different lift and drag forces for planes [80]. Doubling the parameter space and creating different types of spherical Couette flows may result in increasing our ability to find a dynamo in the 3-m experiment. An initial understanding of the effects of these two modes and its comparison with symmetric baffle designs is then a crucial goal of the present work.

In Fig. 3.5 we compare the parameter space for the 40-cm, 3-m experiment and a numerical simulation by Wicht [11]. The simulation by Finke and Tilgner [10] is performed with a stationary outer sphere so $Ro = \infty$ or $E^{-1} = 0$, and does not appear in this figure.

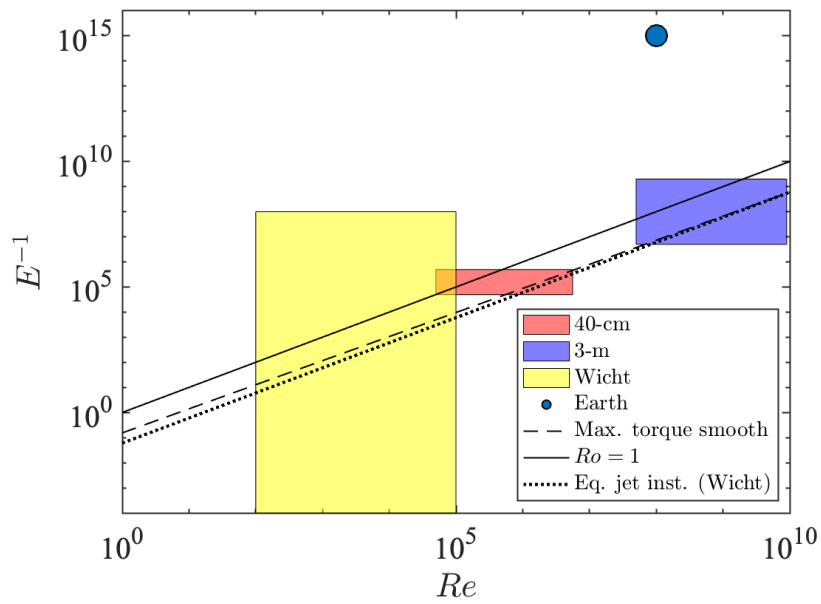


Figure 3.5: Inverse Ekman and Reynolds number parameter space for experiments (40-cm, 3-m), simulations (Wicht [11]) and the Earth [12]. A solid line for $Ro = 1$ is shown for reference. The dotted line indicates the equatorial jet instability regime as observed by Wicht. The dashed line indicates the maximum torque line for a smooth inner sphere observed in the present work and in Zimmerman et al. [4]

3.2 Results

The basic driving mechanisms in the experiment are the rotation rates of the inner and outer spheres. Equivalently, we can use Reynolds and Rossby numbers as independent control parameters: the former is a measure of how turbulent in the flow, induced by the differential rotation, and the latter measures the importance of the overall rotation. These parameters have been previously used to map the dynamics of Taylor and spherical Couette flows [1, 4].

We separate the results in two sections: first, we show torque as a function of Reynolds and Rossby numbers. Then, we show particle image velocimetry (PIV) results performed in both the equatorial and meridional planes to examine flow differences for each baffle design.

3.2.1 Torque Measurements

We define the dimensionless torque as:

$$G = \frac{\tau}{\rho\nu^2 r_i}, \quad (3.1)$$

where τ is the dimensional torque, ρ the fluid density, ν the kinematic viscosity and r_i the inner sphere radius. Similarly, we define G_∞ as the dimensionless torque when $Ro = \infty$; i.e., when the outer sphere is stationary. This parameter will be important later when we use it to normalize the dimensionless torque as a function of differential rotation.

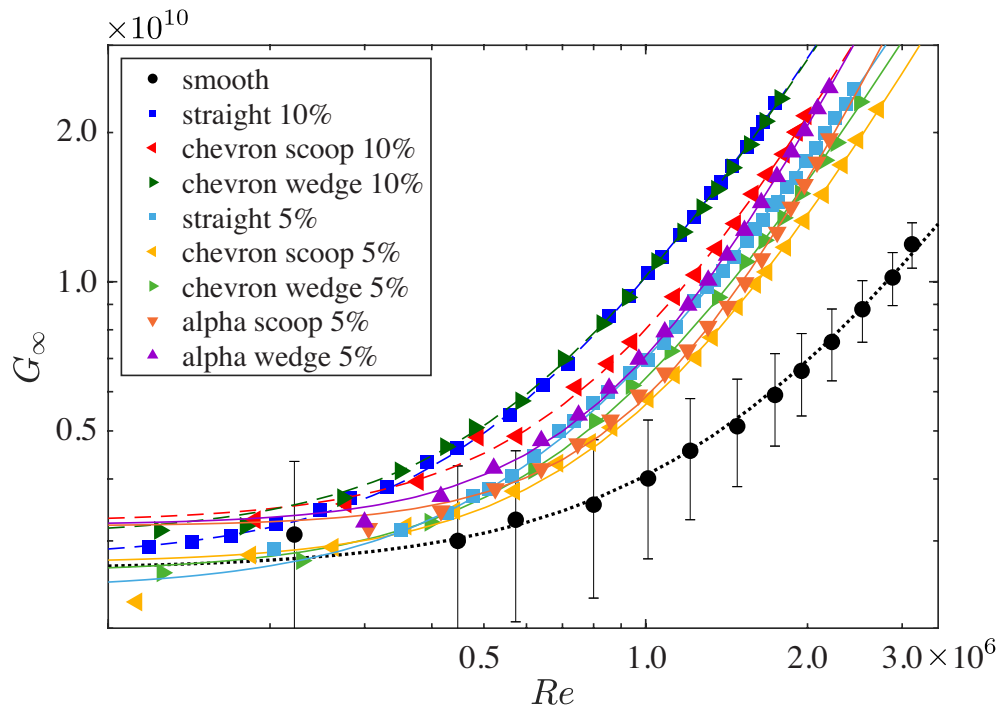


Figure 3.6: Dimensionless torque from the inner motor versus Reynolds number with stationary outer sphere ($Ro = \infty$) for all baffle designs. A power law of the form $G_\infty = bRe^a + c$ was fitted to each data set. Values a , b and c are listed in Table 3.1. Dotted, dashed and solid curves indicate no baffle, 10% and 5% baffle height designs respectively. Smooth design error bars are shown for reference and apply for all curves.

3.2.1.1 Reynolds number dependence

The Reynolds number dependence of the dimensionless torque with a stationary outer sphere ($G_\infty(Re)$) is shown in Figure 3.6 for all three baffle designs (as well as no baffles: smooth) and two baffle heights in the 40-cm experiment. We distinguished between scoop and wedge modes in both the chevron and alpha designs. As expected, the 10% baffles present a higher torque than the 5% ones. Additionally, we see that wedge mode (see Figure 3.4b) generates more torque than scoop for both baffle heights and both asymmetric designs (chevron and alpha). The reason for this will become clearer when we examine the velocimetry data in section 3.2.2.2.

We have fitted a power law of the form $G_\infty = bRe^a + c$ to the dimensionless torque over the entire range of Reynolds numbers measured. The resulting coefficients are shown in Table 3.1. We interpret the constant c as a torque due to friction in the shaft's contacts, the motors and the bearings. As it was done for previous works in 3-m [4], this value c was used as total length of the error bars for each plot since at higher rotation rates it does not change significantly and it is still the biggest source of uncertainty.

Table 3.1: Power law fit of the form $G_\infty = bRe^a + c$ of the plots in Figs. 3.6 and 3.7 and Taylor-Couette flows in [1].

| Experiment | a | b | c |
|--|------|---------|----------------------|
| 3-m ($\Gamma = 0.35$)[4] | 1.89 | 0.003 | 3.3×10^{10} |
| Smooth | 1.58 | 0.044 | 2.6×10^9 |
| Straight 10% | 1.77 | 0.18 | 2.8×10^9 |
| Chevron scoop 10% | 1.80 | 0.11 | 3.1×10^9 |
| Chevron wedge 10% | 1.95 | 0.0093 | 3.3×10^9 |
| Straight 5% | 1.74 | 0.16 | 2.4×10^9 |
| Chevron scoop 5% | 1.81 | 0.047 | 2.6×10^9 |
| Chevron wedge 5% | 1.89 | 0.012 | 2.7×10^9 |
| Alpha scoop 5% | 2.11 | 0.00068 | 2.7×10^9 |
| Alpha wedge 5% | 2.17 | 0.00035 | 3.2×10^9 |
| Taylor-Couette ($\Gamma = 0.72$) [1] | 1.85 | 0.03 | 1.0×10^8 |

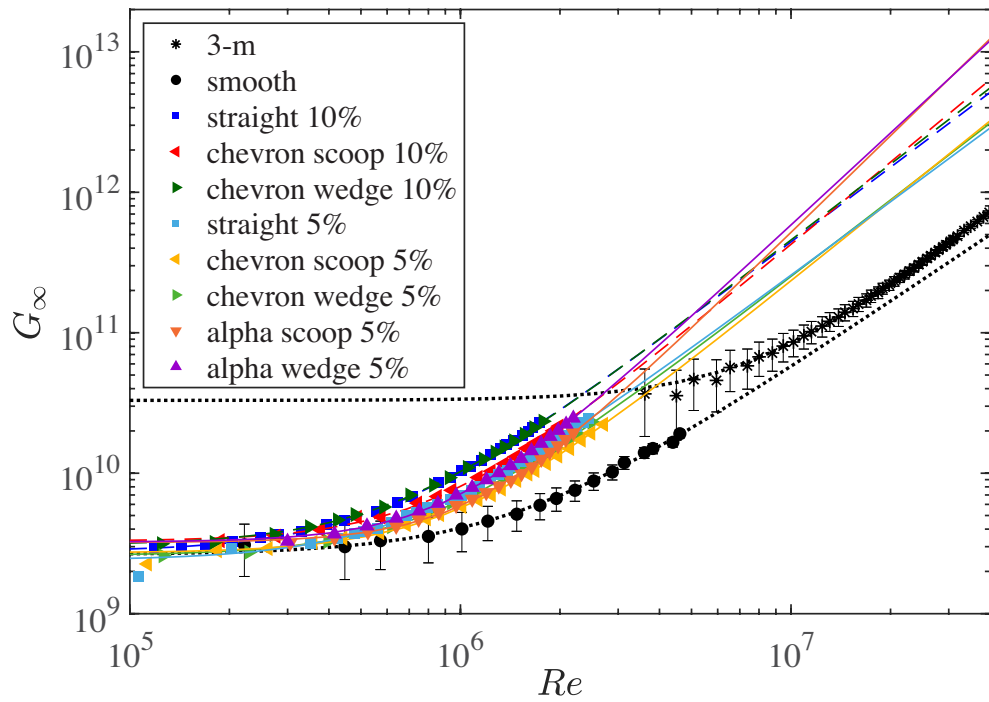


Figure 3.7: Same for Figure 3.6 but we extrapolate the power laws of the 40-cm experiment to higher Reynolds numbers in order to compare with 3-m experiment torque data from Zimmerman et al. [4] (stars). Dotted, dashed and solid curves indicate no baffles, 10% and 5% baffle height designs respectively. For clarity, we only show error bars for smooth in 40-cm and for the 3-m experiment.

The exponent a , approaches $a = 2$ (the Kolmogorov scaling) asymptotically for increasing Reynolds number in shear-driven turbulence, as shown in [30, 31]. In Table 3.1 we observe that for the 40-cm experiment, runs with baffles have higher exponents a than the smooth design, indicating that a tripped boundary layer and pressure drop across the baffles are improving the angular momentum transport. This is well documented by van den Berg et al. [31] and Zhu et al. [62] in which they showed in a Taylor-Couette experiment how wall roughness facilitates transport until the Kolmogorov scaling (in which viscosity dependence is eliminated) is reached, leading to purely pressure drop dominated flows. It is also important to mention that before the Kolmogorov scaling regime where the exponent converges to 2, there is a transition region where the exponent could be higher than 2 for an intermediate range of Reynolds numbers as is well known in boundary layer theory for the case for rough boundary pipe flows. See for instance [81].

The prefactor b in Table 3.1 is a geometry-dependent friction factor associated with the gap between the sphere boundaries as indicated by [4] and it is expected to be lower for wider gaps. The radius ratio for Earth-like spherical Couette is $\Gamma = r_i/r_o = 0.35$ and for Taylor-Couette used in [1] $\Gamma = 0.7245$. We would expect the prefactors b in the 40-cm experiment to be of the same order of 3-m, since the radius ratio is the same, but this is not the case. They all vary between the values of 3-m and Taylor-Couette, straight being higher than scoop, and scoop higher than wedge in each baffle configuration and size. Also, the prefactors in 10% baffles are higher on average than the 5% baffles (except for wedge 10%), which is consistent with [4].

We extrapolate these power laws into the parameter space of the 3-m experiment, (Figure 3.7) to estimate torque and power demands from these baffle designs, which are important design data. First, we notice that the power law for the smooth case seems to align with that of the

3-m experiment at high Re ; although the slope is smaller, the magnitude is very close relative to the other projections. This might indicate that the inner sphere of the 3-m experiment is already affected by its slight roughness that is higher than that of the smooth sphere of the 40-cm. It might also indicate that for the parameters in the 40-cm experiment we have not reached the same regime observed in the power law for 3-m. [4]. This is consistent with the fact that the exponent a is the lowest among all the designs in 40-cm.

We can see in Figure 3.7 that the extrapolated torque for all 10% baffles is approximately 8 times bigger than 3-m at $Re \approx 3.0 \times 10^7$, which is the highest Re recorded for this measurement in 3-m. Also, the extrapolated torque for the chevron and straight 5% baffles at this Re is 4 times bigger than 3-m. Nevertheless, the 5% height alpha baffles show the highest torque projection among all of them, even compared to the 10% baffles. Since the fitting exponent a is greater than 2 at the 40-cm Reynolds number, it is expected that the projection into 3-m parameter space may be overestimated.

Even though we only have three data points, there seems to be linear proportionality between the torque and the height of the baffles at high Re . This is not the case for Taylor-Couette flows discussed in [63] where the relation between these two parameter seems to be closer to quadratic. A linear dependence is consistent with the increase of surface area of the baffles. However, more measurements for different heights of baffles would be required for a better understanding of the dependence in spherical Couette flows.

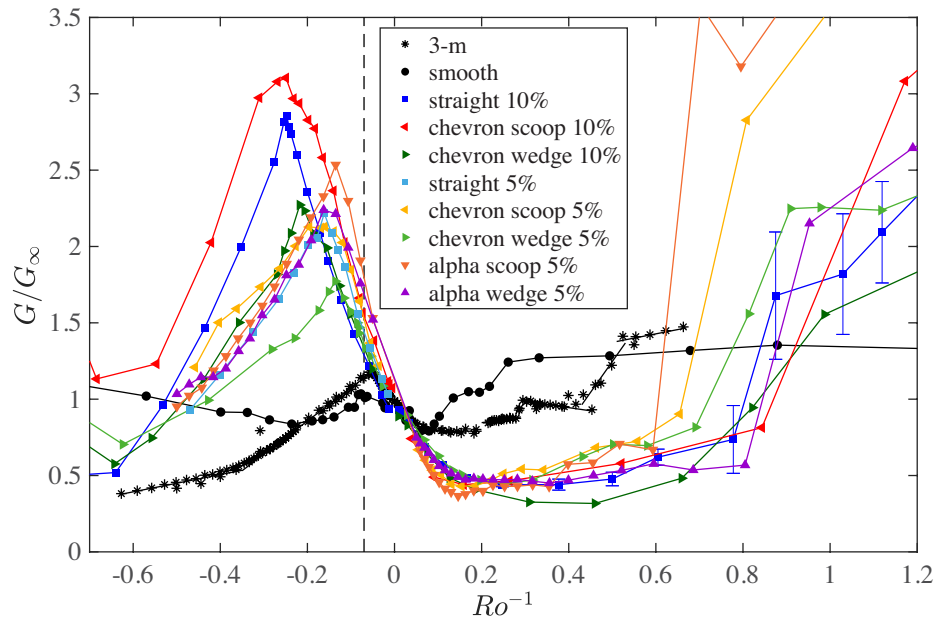


Figure 3.8: Rossby number dependence of the measured inner sphere torque. The magnitude of the torque at a given Ro and Re is normalized by $G_\infty(Re)$, the torque expected at that Reynolds number if the outer sphere were not rotating. Error bars for straight 10% in the range of bistable states are representative for all baffles $Ro^{-1} > 0.6$. The dashed line indicates the location of the peak for maximum relative dimensionless torque in the 40-cm experiment with smooth inner sphere.

3.2.1.2 Rossby number dependence

When we differentially rotate both spheres, the Coriolis forces shape the flow, significantly changing the states. The Rossby number (defined in section 2.4) characterizes the differential rotation and from past work determines which dynamical state is observed. In order to isolate the dependence of the dynamics on the Rossby number, we normalize the dimensionless torque by G_∞ . Previous work by Zimmerman et al. [4] and Paoletti and Lathrop [1] found that the torque, for both Taylor-Couette and spherical Couette flows, can be factorized at high Reynolds number ($Re \approx 10^6$) as

$$G(Ro, Re) = f(Ro)G_\infty(Re), \quad (3.2)$$

where $G_\infty(Re)$ is the torque with outer sphere stationary, i.e. $Ro = \infty$. Then G/G_∞ is a function of Ro only, and the torque G scales like $G_\infty(Re)$ for a fixed $Ro \neq \infty$.

The form of $G/G_\infty(Re)$ in Figure 3.8 is similar to the one in 3-m [4] and in Taylor-Couette flows [1]. The main difference is the amplitude and location of the peaks for maximum relative torque. For 10% chevron scoop and 10% straight baffles the amplitude is more than three times the scaled peak torque in the 3-m system (see Table 3.2 for actual values). This shows a much stronger forcing for differential rotation relative to a stationary outer sphere and indicates that the coupling between the spheres is significantly higher with baffles. We can also see that the amplitude of the peak for chevron wedge is the lowest of the 10% baffle designs. This same proportion between these designs prevails for straight and chevron 5%; however, the amplitude changes. This indicates a lower coupling with lower baffle height, a similar result to that of Taylor-Couette flows [62]. Less obvious are the reasons for the difference in torque between

wedge and scoop modes for the same baffle design: the peak amplitude for scoop mode is higher than wedge mode. The same behavior happens for alpha baffles of 5% height, but if compared to the other 5% models, it is higher than all of them. Additionally, alpha scoop 5% is even higher than chevron wedge 10%. This suggests a more effective coupling at the expense of less absolute torque, i.e., a smaller G_∞ for the case of alpha baffles.

Another interesting feature is the location of the relative torque maxima, as can be seen in Table 3.2. It moves to lower inverse Rossby numbers as we increase baffle height. This is expected as indicated in [4, 82] where a reduction in the gap would imply an amplification of the fluid engagement, or coupling between the boundaries. With this, a lower rotation rate in the inner boundary is required to match the fluid drag and angular momentum transferred to the fluid from the outer boundary, corresponding to a reduction in the inverse Rossby number. This reduction of the gap also explains why this maximum is located at lower values for spherical Couette versus Taylor-Couette flows. The location of the maximum also changes for wedge versus scoop modes. All of these differences suggest a very rich dynamics happening for different models of baffles that required more than global measurements (like torque) to be described, and that motivated the velocimetry studies in section 3.2.2.

For $Ro > 0$ we observed bistable states that happen between $0.6 < Ro^{-1} < 1$ in Figure 3.8 in the region that also sees a large increase torque. The same behavior happens for all baffle designs. These results are similar in location and amplitude to bistable states in the 3-m experiment that are characterized in more detail in [46]. The time dynamics can be described as a spontaneous jump between two torque values: a slow decay into the lower torque state (named L) followed by a jump into a higher torque state (H). The timing between these states, and the time spent in each one of them, as reported in [4, 46], depends highly on the Rossby number. This

Table 3.2: Location and amplitude of the maxima in Figure 3.8 and Taylor-Couette flows in [1].

| Experiment | G/G_∞ | Ro^{-1} |
|--|--------------|-----------|
| 3-m ($\Gamma = 0.35$) [4] | 1.20 | -0.05 |
| Smooth | 1.04 | -0.07 |
| Straight 10% | 2.86 | -0.25 |
| Chevron scoop 10% | 3.10 | -0.25 |
| Chevron wedge 10% | 2.27 | -0.21 |
| Straight 5% | 2.21 | -0.16 |
| Chevron scoop 5% | 2.13 | -0.16 |
| Chevron wedge 5% | 1.77 | -0.14 |
| Alpha scoop 5% | 2.53 | -0.14 |
| Alpha wedge 5% | 2.23 | -0.16 |
| Taylor-Couette ($\Gamma = 0.72$) [1] | 1.25 | -0.25 |

bi-stability was more evident in torque fluctuations with baffles relative to the smooth design, presumably because the engagement of the boundaries with the flow is higher.

3.2.2 Velocimetry

In this section we will show results of the velocimetry measurements performed using PIV techniques in the equatorial and meridional plane of our 40-cm spherical Couette apparatus. For the velocimetry in the equatorial plane, we focused on the dependence of the velocity as a function of radius since, by symmetry, we expect certain invariance of the velocity field as a function of the azimuthal angle φ . For our study, we only focused on time averages, so wave motion was not analyzed in our measurements, although the presence of waves in spherical Couette setup is well known (see for example [3, 48, 83]). For the meridional plane we inspected the dynamics at constant Rossby numbers corresponding to the maximum G/G_∞ for reasons we will explain in the next section.

Recordings of 1 s of duration were performed using a high speed camera at 1000 Hz. The rotation rate of the inner sphere is between 10-15 Hz around the maximum torque area for all the

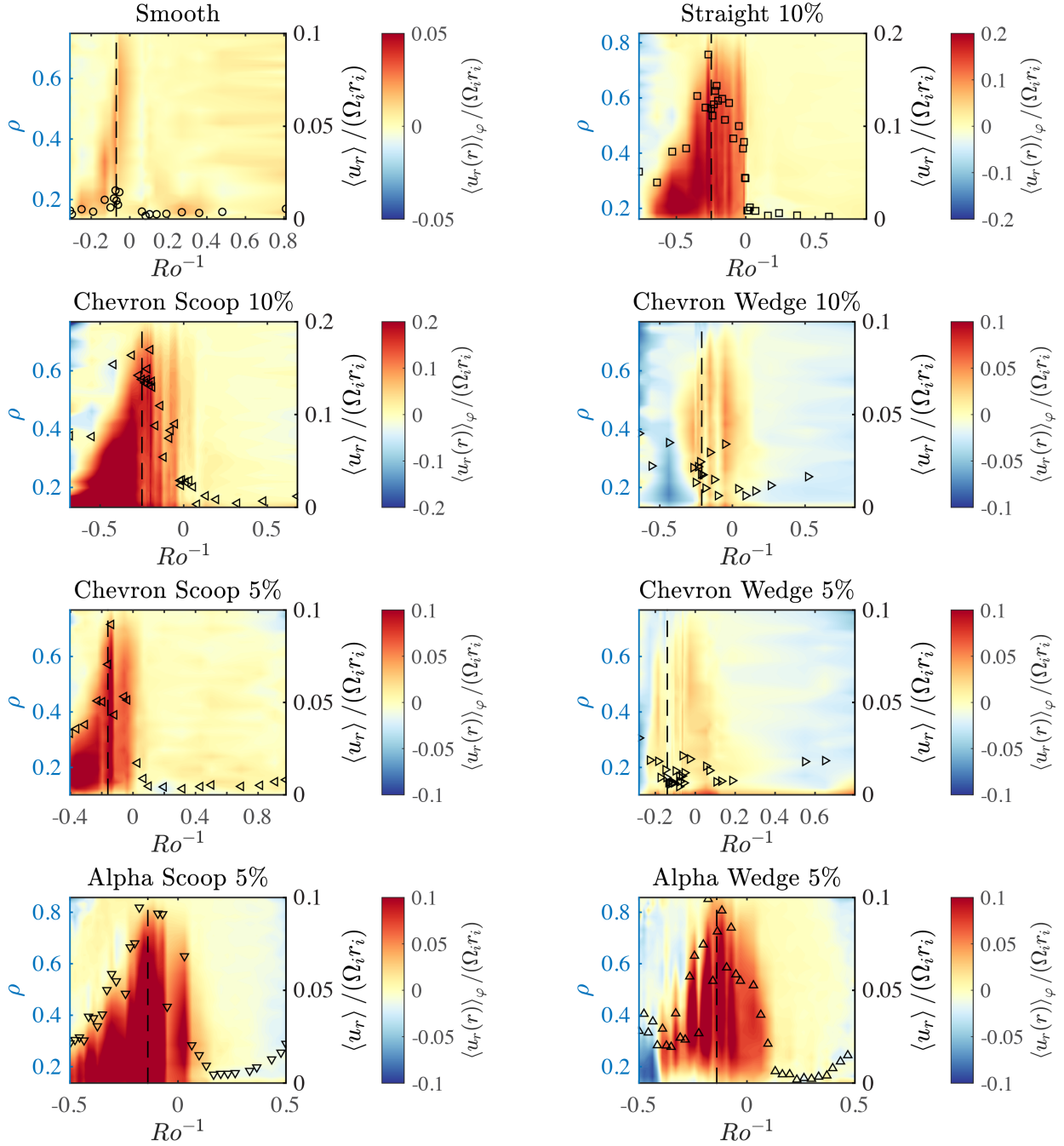


Figure 3.9: Radial velocity in the equatorial plane for all baffle designs. In color map: azimuthal average of the velocity in the radial direction, normalized by the tangential velocity at the inner sphere equator, as a function of the normalized radius (left vertical axis) for different Rossby number (horizontal axis). Warm colors mean velocity in the direction outward from the inner sphere and cool colors inward. The symbols show the radial average of each of the columns in the color plot (indicated in the right vertical axis) as a function of Ro^{-1} . The vertical dashed lines indicate the location of the maximum relative torque G/G_∞ for each baffle design.

baffle designs, which means 10-15 rotations of the inner sphere per each 1-s movie taken.

3.2.2.1 Equatorial Plane

The dimensionless torque measurements in section 3.2.1 show very different dynamics for each design as a function of Ro^{-1} , mainly by the location and amplitude of the maximum relative torque peak (see Figure 3.8). This point of maximum relative torque has shown the highest amplification of magnetic field in the cylindrical radial direction [4] for the liquid sodium flows. We performed velocimetry for a range of Ro values around the peak with $Re \approx 10^6$. We normalized the velocities by the tangential velocity of the inner sphere at the equator, $\Omega_i r_i$, where r_i is the radius of the inner sphere, and Ω_i its angular frequency. We also define the normalized radius as $\rho = (r - r_i)/l$, where $l = r_o - r_i = 12$ cm is the gap between the spheres.

In Figure 3.9 and Figure 3.10 we show color plots of the normalized radial velocity as a function of the normalized radius $u_r(\rho)$ and the normalized azimuthal velocity as a function of the normalized radius $u_\varphi(\rho)$. We have also shown in each graph the average velocity only as a function of Ro^{-1} . Additionally, the location of the maxima relative torque for each baffle design (shown in Figure 3.8 and listed in Table 3.2) is indicated with a dashed line on each of the plots. Since on average the bistable states occur on a time scale bigger than the camera recording time lapse, we have omitted velocity measurements for the Ro where bistability occurs.

Looking at the smooth case first, we notice that the velocity in the azimuthal direction (see Figure 3.10) is much higher on average than the radial velocity (see Figure 3.9). Near the region of maximum torque the azimuthal velocity reaches a minimum and there is an equatorial jet radially outward. This equatorial jet strengthens as we approach to the maximum torque peak.

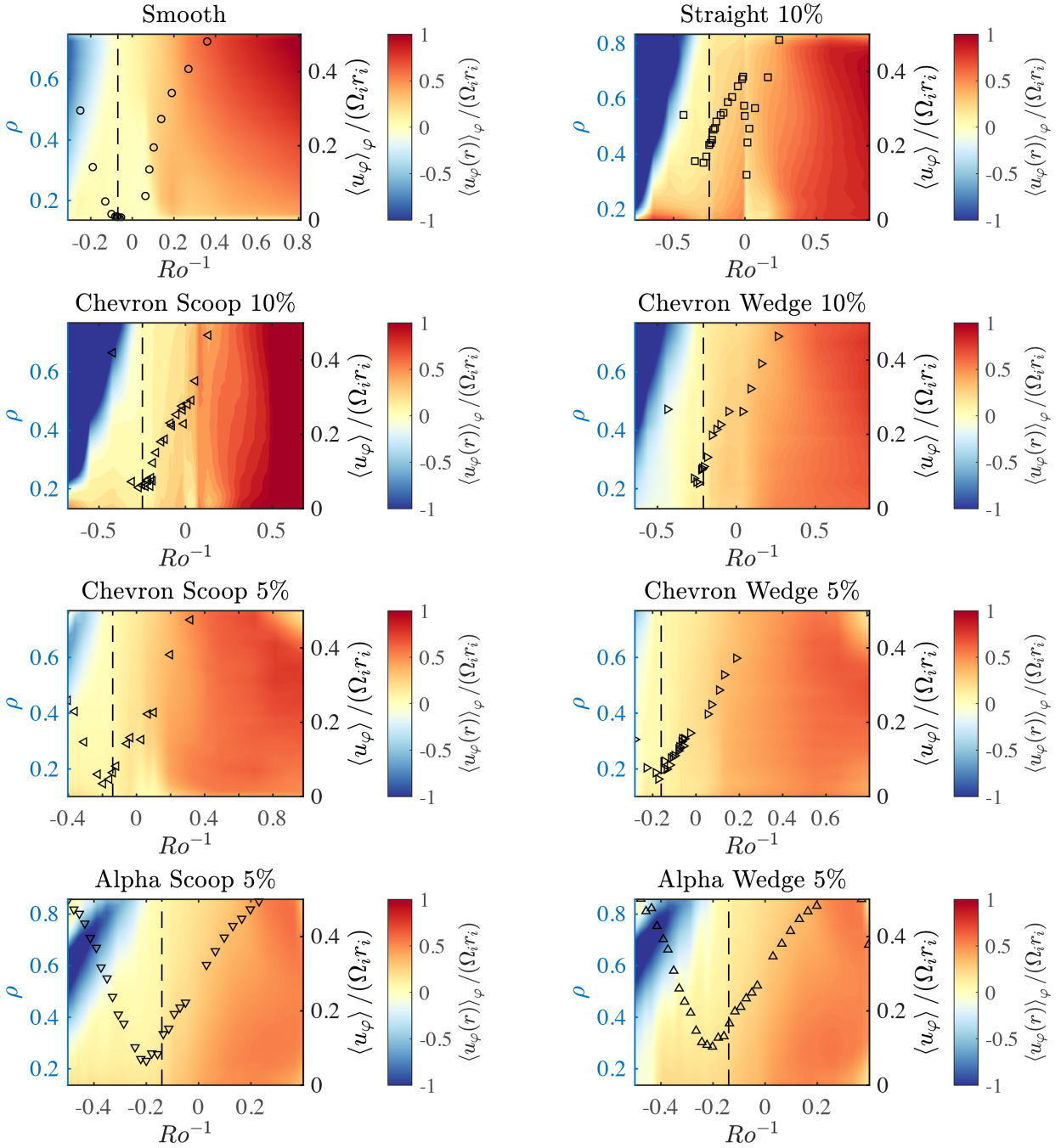


Figure 3.10: Azimuthal velocity in the equatorial plane for all baffle designs. In color map: azimuthal average of the velocity in the azimuthal direction, normalized by the tangential velocity at the inner sphere equator, as a function of the normalized radius (left vertical axis) for different Rossby number (horizontal axis). Cool colors mean velocity in the opposite direction of the rotation of the inner sphere and warm colors mean moving in the same direction. The symbols show the radial average of each of the columns in the color plot (indicated in the right vertical axis) as a function of Ro^{-1} . The vertical dashed lines indicate the location of the maximum relative torque G/G_∞ for each baffle design.

The radial velocity seems irregular and fluctuating in comparison to the azimuthal component. This could be due to the low values of the radial velocities compared to the azimuthal velocities, or because of dynamics that are longer term than our 1 s measurements. The Rossby number for the formation of this jet coincides with the Rossby number for the peak of highest amplification of the radial magnetic field in the 3-m system, which reinforces the importance of the mean flows in the amplification process [10].

For the straight 10% baffles, we see a significant increase in the maximum relative radial velocity with respect to the smooth design. This is by itself a very important result: baffles have increased the coupling between the inner sphere and the fluid, resulting in a better radial transfer of angular momentum. We reiterate that the normalization is by the tangential velocity of the inner sphere at the equator, so this increase is not related to the angular velocity of the spheres, rather to the interaction between its boundary and the flow. The equatorial jet seems more stable and uniform here than in the smooth design, and we can see that it spreads out through the entire radius at the peak of maximum torque.

If we compare this last result with Wicht [11] in Figure 3.5, we see that the Rossby number for the equatorial jet instability (dotted line) coincides with the Rossby number of maximum torque (dashed line) in the parameter space. We show one Reynolds number in the color plots of this section. Measurements done for different Re confirm that the Rossby number for the maximum torque peak does not change significantly with Re for any of the baffle designs.

For the chevron scoop mode with 10% baffle height, we see that the general behavior and intensities are very similar to straight 10% baffles although the equatorial jet seems more uniform when changing Rossby numbers around the maximum torque peak. This might be due to the baffle orientation: if you see Figure 3.4, scoop mode orientation pushes the fluid into the

equatorial plane due to the inclination of the baffles. Additional data in favor of this hypothesis will be shown in section 3.2.2.2. A similar result as in the previous plots is seen for the azimuthal velocity: a lower u_φ for the maximum G/G_∞ and an inner-sphere-dominated dynamics in this region.

For the chevron wedge mode with 10% baffle height, we can see (Figure 3.9) that now the radial profile is different from previous ones: the equatorial jet has very low intensity and has spread in the radial direction. It also looks non-uniform and there is a negative inward flow around $Ro^{-1} \approx -0.5$. This shows a different dynamics for this mode, with a less stable equatorial jet and time scales slower than 1 s for this regime.

A possible explanation for the lower radial amplitudes is again the orientation of the baffles that now, in wedge mode, push the velocity upward from the equator in the direction of the poles, causing a narrower and weaker equatorial jet. This might be the reason that the absolute torque of the wedge mode is higher than scoop mode (Figure 3.6): the orientation of the blades pulls the fluid in the negative radial direction at the equator, creating pressure gradient unfavorable for the equatorial jet that happens due to centrifugal forces. This competition between a centrifugal force and a negative pressure gradient requires more torque in the inner motor, causing the difference in the absolute torque plots.

We now proceed to compare specifically 10% baffles with 5% for the chevron shape, in the second to last row of Figure 3.9 and Figure 3.10. There the velocity profiles are very similar between both baffles heights but the amplitudes are smaller for the 5% height; hence, the coupling has reduced with respect to the 10% baffle design as expected. For wedge mode, the negative circulation and irregularity in the radial flow is again present, and for chevron scoop 5% we also see a well formed and stable equatorial jet around the maximum torque region.

Finally for alpha baffles, the results have the same characteristic peak at maximum torque for the radial velocity with similar amplitudes to the chevron 5% cases, except for the wedge mode, where we can see now a clear jet being formed. Although it seems to be more unstable than the alpha scoop mode, which is consistent with previous wedge baffle results. We can also observe an inward flow in the radial plot around $Ro^{-1} = -0.5$ as it was observed for chevron wedge 10%. For the azimuthal velocity similar behavior to the other baffles and modes is observed, although now the values near the maximum torque, i.e. at the minimum azimuthal velocity, seem to be greater than previous chevron 5% cases, implying that the coupling with the inner sphere is stronger. There seems to be a mismatch between the torque peak (dashed vertical line) and the minimum for azimuthal velocity for alpha baffles. A similar phenomenon was reported by Zimmerman et al. [4] in the 3-m experiment, where they noticed that the minimum of Ω -effect, i.e., a minimum on the gradient of azimuthal velocity, is offset from the torque maximum peak.

Besides the different dynamics observed for wedge and scoop mode in both chevron and alpha designs, the aforementioned features inspired the results obtained in the next section: near this maximum torque region, the azimuthal velocity reaches a minimum. According to Holme [56] the poloidal shear is at a maximum where the toroidal shear is close to zero, which is consistent with our observations. This motivated us to perform measurements in the meridional plane; a task we thought would be very difficult to achieve due to the the high velocities that rotating fluid experiments normally have in the azimuthal direction, i.e. the direction of rotation. With these low azimuthal velocities at the maximum torque region, a laser sheet in the meridional plane could illuminate particles for enough time to be captured by the high speed camera.

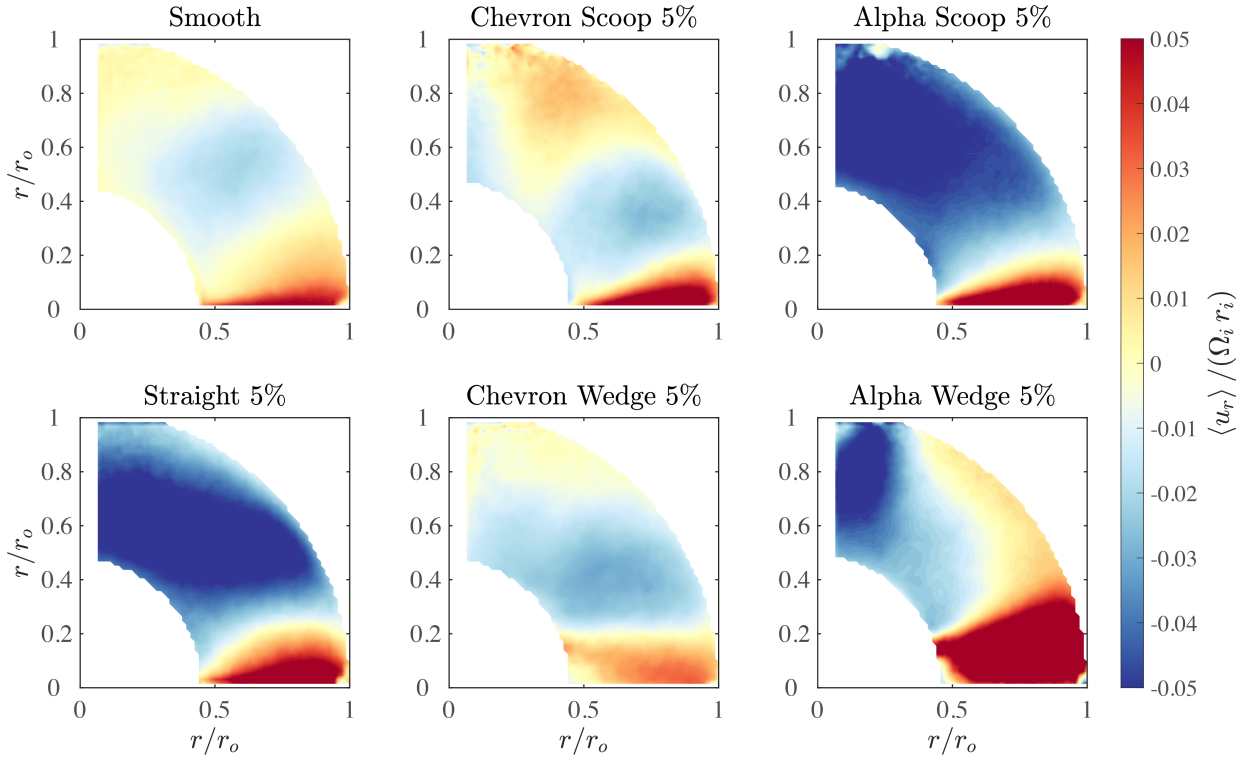


Figure 3.11: Spherical radial component of the velocity field (u_r) in the meridional plane ($r/r_o, \theta$) normalized by the tangential speed in the inner sphere at the equator, for different baffle designs and modes. We normalize the radial coordinate by the radius of the outer sphere r/r_o . Warm colors are outward radial flows, and cold colors are inward radial flows.

3.2.2.2 Meridional Plane

We now present results of the velocity field in the meridional plane ($\varphi = \text{const.}$) at a fixed Rossby number equal to the corresponding maximum torque for each baffle design (refer to Table 3.2). Due to the low velocities in the azimuthal direction at this particular region, as shown in the previous section, we could have particle tracks long enough to be detected by the high speed camera. It is important to mention that this still brings a cutoff for the maximum velocity we can measure: assuming the width of the laser is 3 mm, the camera records at 1000 fps and that we discard tracks shorter than 4 frames, the maximum speed we can detect is around 1 m/s, which is close to the maximum speed we measured on the meridional plane but high enough to not saturate the plots.

Since we fixed Ro , we did a sweep for different Reynolds numbers to compare the difference in the dynamics. Averages between different Reynolds numbers were performed over the normalized velocity fields only for those states in which the dynamics was similar enough; in our case, for $1 \times 10^6 < Re < 2 \times 10^6$. Although we only show results for the 5% baffle height designs in this section, we expect 10% meridional plots to behave similarly but with higher relative velocities given our results comparing 5% and 10% torque and equatorial velocity measurements in previous sections.

In Figure 3.11 we can see the spherical radial component of the velocity field (u_r) in the meridional plane, as a function of r and θ , for each baffle design. First, we notice a clear increase in the velocities with straight baffles, the equatorial jet is stronger by a factor of approximately 2 in the bulk of the jet, and there is a broader area of inward flow, or recirculation, above it. The main kinetic energy is stored at the equatorial jet [10, 84], so this increase is by itself a

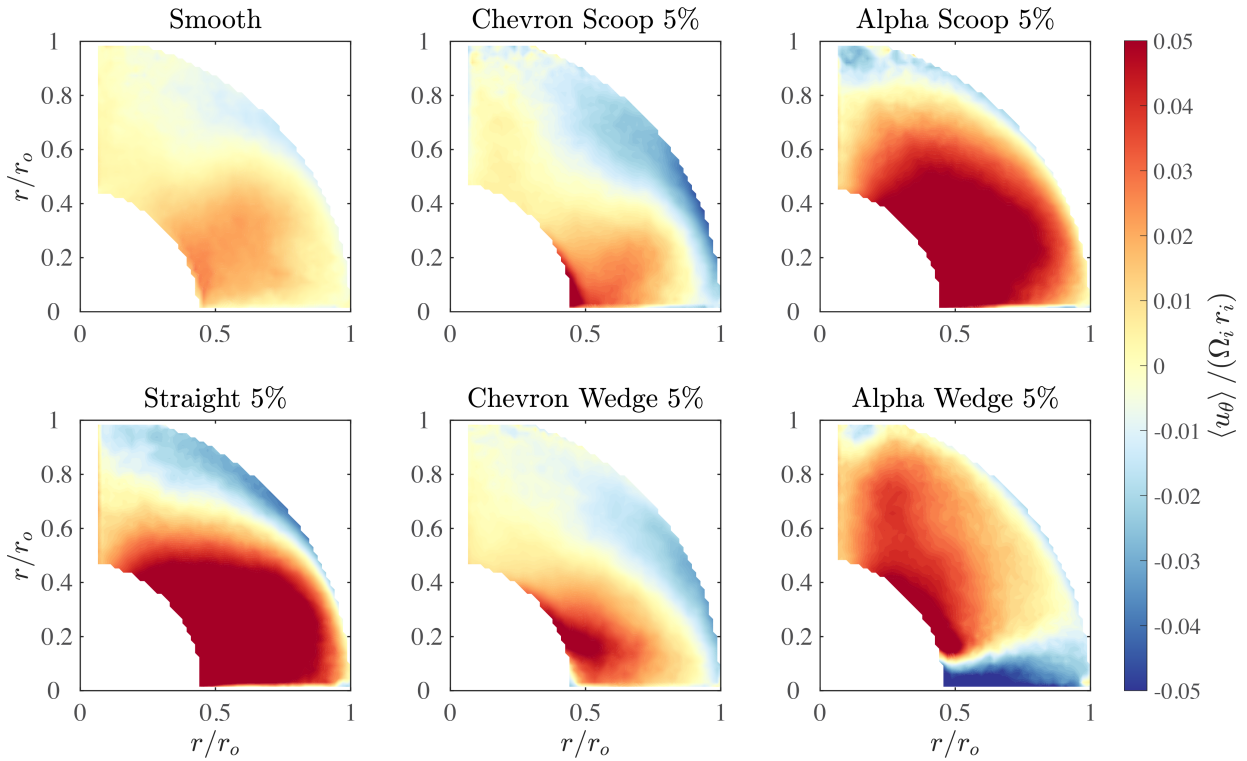


Figure 3.12: Meridional component of the velocity field (u_θ) in the meridional plane ($r/r_o, \theta$) normalized by the tangential speed in the inner sphere at the equator, for different baffle designs and modes. We normalize the radial coordinate by the radius of the outer sphere r/r_o . Warm color are flows from the north pole toward the equatorial plane, and cold colors are toward the pole.

favorable result for dynamo action. If we now take a look at the results for the chevron design, we notice that scoop and wedge mode show different topologies. The radial flows in the chevron scoop mode are similar to smooth and straight with an equatorial jet that is more intense than the smooth case but with less meridional circulation than the straight case. If we now take a look at the chevron wedge mode, we notice the equatorial jet is much weaker here, even weaker than the smooth case, but there is more inward flow above the equatorial jet. This is consistent with the torque plots in Figure 3.8 where chevron wedge 5% requires less torque to run at constant speed at maximum Rossby than chevron scoop 5%. It also agrees with the equatorial plots in Figure 3.9 that show this difference in the equatorial plane intensities. A very similar result can be observed for the meridional component of the velocity field of the baffle designs mentioned above (smooth, straight and chevron) in Figure 3.12: an increase of the intensities when baffles are added specially with straight baffles and a different topology in the flows for chevron scoop and wedge.

Alpha baffles combine the stronger coupling observed in the straight baffles case, with the change in the topologies due to an asymmetric design (see Figure ??). The results are very promising: we can see that the topology and intensities of the scoop mode are very similar to the straight baffles case. For the wedge mode now the equatorial jet in Figure 3.11 is much wider and intense than the chevron wedge mode, with values that are on the same order of magnitude as the scoop mode, with a stronger recirculation. For the meridional flows we now notice a negative region above the equatorial planes, which indicates that the flow is going upward in the bulk of the jet, creating a different topology than the scoop mode. We also notice a thinner recirculation layer near the outer sphere boundary and the shaft. Those recirculation layers likely extend into the region outside the measurement volume. These topologies in the flows

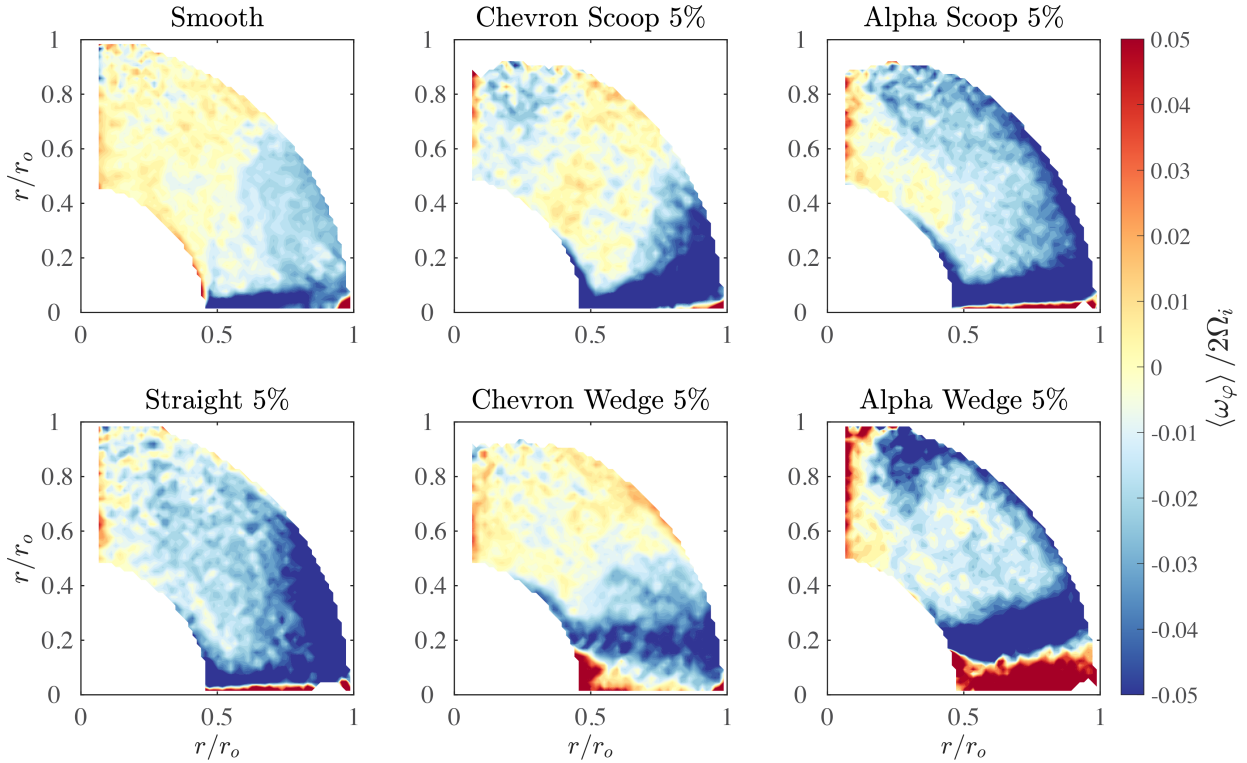


Figure 3.13: Local time average azimuthal vorticity normalized by the inner angular frequency in the meridional plane ($r/r_o, \theta$) for different baffle designs and modes. We normalize the radial coordinate by the radius of the outer sphere r/r_o . Negative values point out of the page.

are consistent with the interpretation given before about the orientation of the blades and the direction of the flow transported: scoop modes push the flow in the direction of the equatorial plane, amplifying its intensity; however, wedge mode takes it out of the equatorial plane and together with the centrifugal forces, transfers the energy into the meridional directions. With the alpha baffle designs, we will gain similar coupling as with straight baffles while doubling the parameter space like with chevron baffles. This is important for future design considerations in the 3-m experiment.

As mentioned before, the vorticity in the meridional plane, combined with the flows in the azimuthal direction indicate the helicity of the flows in the meridional planes. Figure 3.13 shows the local vorticity of the flows in the meridional plane for all the baffle designs. The region around

the equator for straight, chevron scoop and alpha scoop with respect to the smooth design, shows a significant increase compared to other regions of the meridional plane. Additionally, the region of high vorticity is wider for chevron wedge and alpha wedge and it is located now at a latitude above the equator, showing even a positive vorticity in the region adjacent to the inner sphere at the equator level. This positive vorticity region is more evident for alpha wedge mode, and is consistent with the meridional flows in Figure 3.12 that show a negative meridional velocity in this region. Such redistribution of the vorticity can be favorable for dynamo action [53], by increasing the α -effect in the 3-m experiment and hence reducing the critical magnetic Reynolds number for dynamo action [54, 57, 58]. Additionally, according to some authors [85] having a gradient of helicity is an important ingredient for dynamo generation. With alpha wedge baffles we would have a configuration that allows us to explore this effect in the 3-m experiment.

The properties for the vorticity generated by alpha baffles, combined with the highest values for the averaged azimuthal velocity shown in section 3.2.2.1, suggest that the alpha design generates the most promising flows for achieving an enhancement of the helicity in the 3-m experiment.

Chapter 4: The 3-m Upgrade

In this chapter we will discuss the modification performed to the 3-m experiment. This is the main contribution of this doctoral dissertation. Given the results for the 40-cm water experiment, we decided to weld 5% alpha baffles (see discussion section in chapter 3) into the inner sphere of the experiment. Additionally, the experiment was failing: the inner motor was not able to provide enough torque to reach the requested rotation rates, which is an indication that something might have been wrong with the bottom inner bearing. In Figure 4.1 we provide cross sections of the vessel taken from Triana [13] about the schematics of the 3-m experiment. Detailed sections views of the top and bottom bearing arrangements are particularly important for the disassembling and assembling of the experiment. We encourage anyone interested in the engineering of these arrangements (this author hopes there is no need to open the experiment in the near future) to check in detail Triana [13] and Zimmerman [14].

In order to open the experiment and safely extract the inner sphere to weld the baffles, we needed first to drain the 12 tons of sodium contained in the outer vessel. Given the considerable dangers that could arise during this process, a carefully planned, studied and reviewed Standard Operation Procedure (SOP) was written (See Appendices) in collaboration with Artur Perevalov, Heidi Myers, Don Martin, Nolan Ballew and Daniel Lathrop. The idea was to extract the sodium in a single day operation, store it in a storage tank while the modification took place

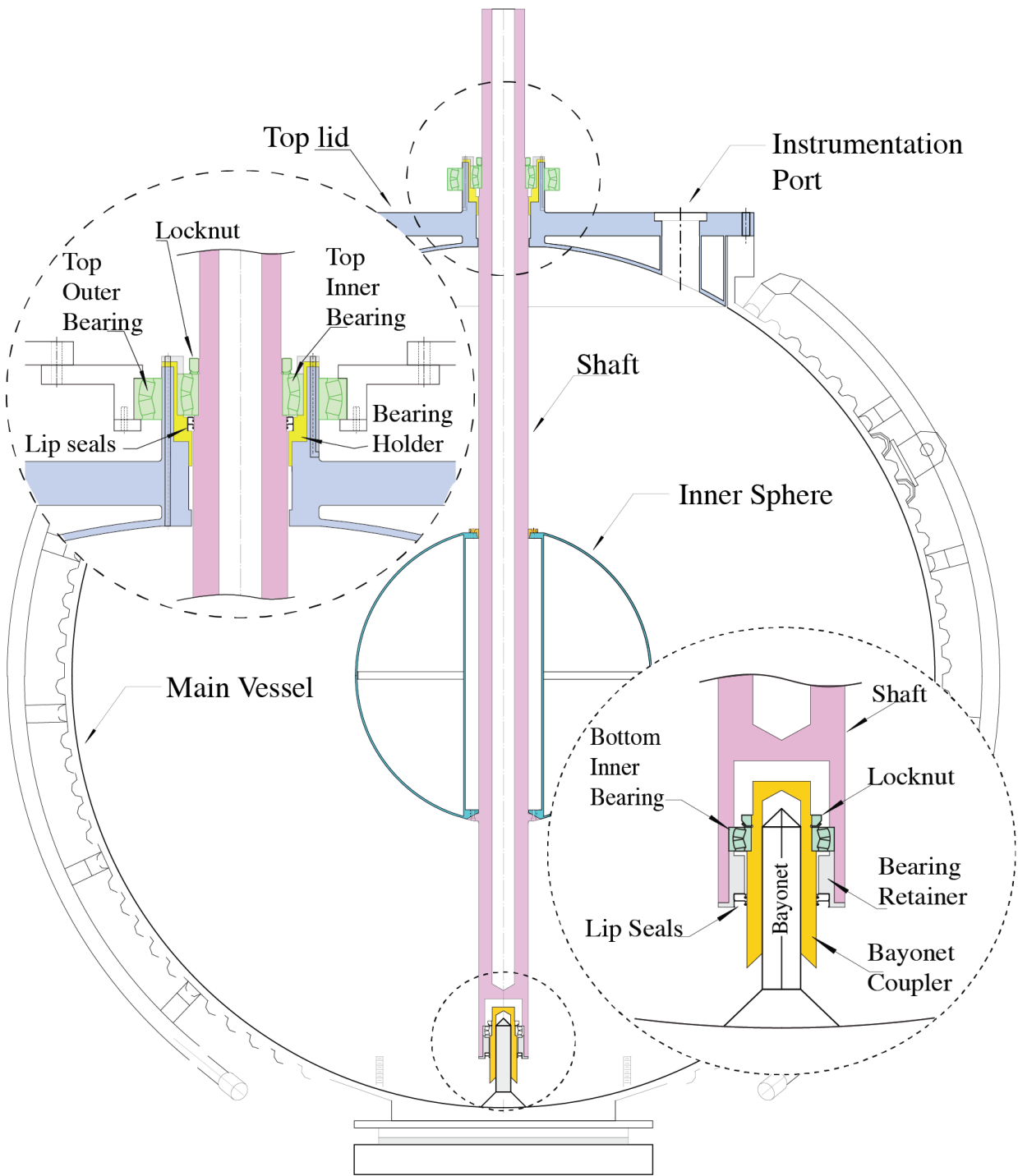


Figure 4.1: Vessel cross section with the inner sphere and shaft. On top section view: Detail of the shaft and its attachment to the lid. The inner race of the main top bearing is free to slide axially on the lid shaft, allowing for thermal expansion of the vessel. The locknut on the shaft, above the top shaft bearing, holds the entire weight of the inner sphere and shaft. Two lip seals prevent fluid from leaking into the bearing. On bottom section view: Detail of shaft and the bayonet coupler. The bottom end of the shaft can move axially on the bayonet. Individual drawings taken from Triana [13] and compiled by this author.

and, after the experiment was partially assembled, put the sodium back (also in a single day operation), finishing up the remaining details of the assembly, and run the experiment. Given the extreme importance of the draining day, we separate this chapter in two sections: before and after the transfer. The first section includes the design of the SOP, the transfer operation, the sodium plumbing, and the storage tank design. The second section includes the sodium cleaning operation, the disassembly of the inner sphere, the baffles design and construction, and the final sodium transfer.

4.1 Before Transfer

4.1.1 SOP Overview

After careful consideration of many possible plans for extraction, and after long discussion with many colleagues, in particular with Don Martin and Nolan Ballew, we came up with a plan that we will narrate in the present section.

The idea was to design a curved dip tube that would go through one of the port of the experiment in a *hot insertion* (with the sodium molten) and sit on the bottom of the outer sphere, as close as possible to the bottom part of the inner sphere shaft (see Figure 4.1 and diagram on Figure 4.2). Once there, we would connect the dip tube to a heated transfer line that would be connected to the storage tank. Once the connection was made, we would raise the pressure on the sphere vessel and after the goal pressure is reached, we would open a valve on top of the dip tube that would allow the sodium to flow from the sphere to the storage tank, kept at a lower pressure. The refilling process, of sodium from the tank to the experiment, involved a similar technique but with the dip tube already in place in the storage tank, so no hot insertion was necessary. We will

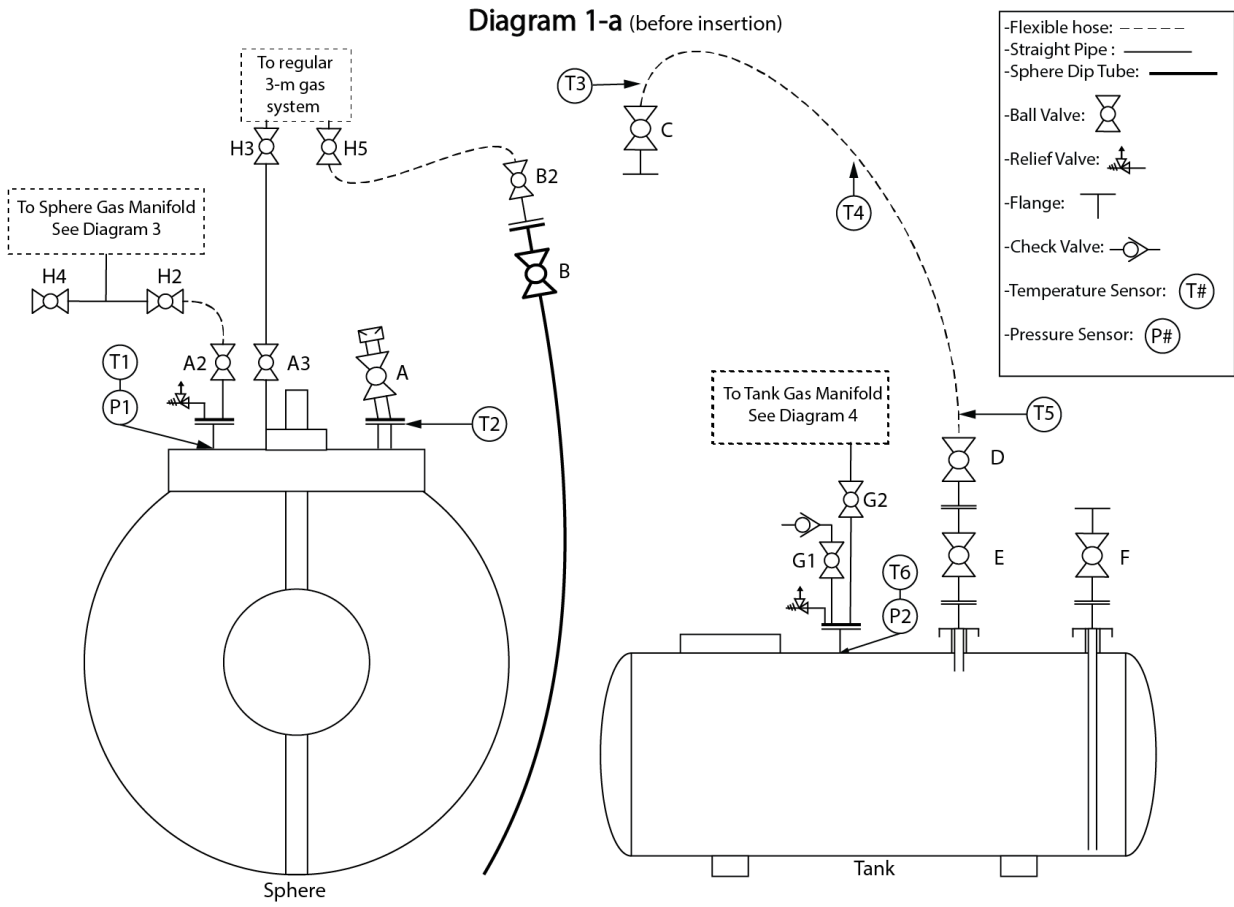


Figure 4.2: Diagram of the transfer plan before the insertion of the dip tube.



Figure 4.3: Aerial picture of the storage tank.

discuss this in more detail in the next section.

The scheme described above involved the design and construction of different parts, pieces, and piping that we can separate into three broad groups: the sodium plumbing, the storage tank and the gas injection system. The author of this dissertation was in charge of the sodium plumbing system entirely, took part in the installation and design of the oil lines for the storage tank, and assisted in the installation and design of the Gas Injection System which Artur Perevalov took charge of. In the upcoming subsection we will detail the construction and design process of these three items with special consideration for the upcoming graduate students that will take charge of this project.

4.1.2 Storage Tank

A picture of the storage tank can be seen in Figure 4.3 and a detailed drawing can be found in the Appendices. It was designed and built by Central Fabricators Inc. It is a 3450 gallons cylindrical vessel with semi-spherical ends. Is made of a carbon steel alloy (SA 516 Gr. 70) of 1/4" thickness to improve thermal conductivity, and designed for 15 psig of internal pressure at 400 F. It includes two dimple jackets used to heat the interior of the container. The dimple jacket was designed to cover a sufficient area that would allow the sodium to melt in a reasonable time (less than two days, which is the normal time it takes for melting the sodium in the 3-m experiment). The jacket sections provide a coverage of 30 ft² on the bottom section of the tank. It includes four nozzles, three on top and one on the bottom. The top three nozzles were used for instrumentation, gas injection, and for the two insertion tubes: a short one for transferring the sodium from the sphere to the tank, and a long one that sits on the tank's bottom nozzle (the fourth one). The whole tank was installed over steel blocks, to provide an inclination that would guarantee that most of the molten sodium would accumulate in the flanged bottom nozzle, where the long dip tube was sitting for the final transfer from tank to sphere. Additionally, the tank included a manway for future cleaning and disposal. The vessel and jackets were built, tested and stamped per the ASME code. The vessel exterior received a DTM Epoxy Mastic for preventing rust.

The dimple jackets needed to be connected to the experiment heater exchangers and needed to be able to work in parallel with the experiment. Careful calculations (done by Artur Perevalov) were performed to determine if the dimple jacket should be connected in series or in parallel. We decided to use parallel connections since it provided a more uniform heat distribution (refer to

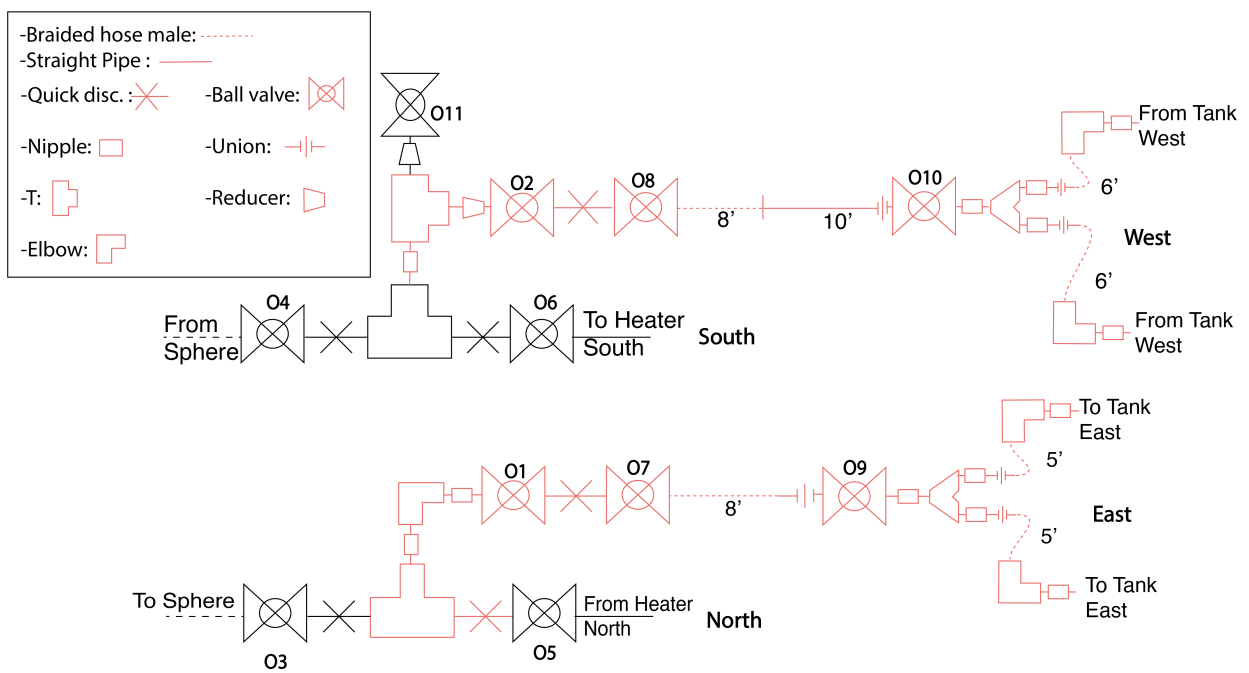


Figure 4.4: Oil lines connection diagram to the storage tank and the sphere. In red are the parts we added and in black the preexisting.

his dissertation for detailed calculations). The design and plumbing system used is indicated in Figure 4.4. We carefully designed these oil lines in anticipation of the most possible scenarios. For instance, the quick connectors were added in the section closer to the wall, so all the remaining oil in the pipes will stay with the tank after the draining process. The idea was to store the tank outside the building after the transfer was done. Additionally, many valves were added to guarantee that the sections of the piping could be taken apart without a significant oil spilling in the process. This pipe configuration allows to independently or simultaneously heat the tank and sphere. For example: closing valves O4 and O3 and opening valves O1 and O1 will heat only the tank (see the SOP in the Appendices). Finally, we filled out the dimple jackets and oil pipes with heating oil, trying to prevent the presence of air bubbles inside which could potentially damage the pump. This was accomplished by lifting one side of the end oil line of the tank at a higher altitude than the dimple jacket, while pumping the oil manually from a barrel to the other end of the tank's oil line. Several heating tests were performed to ensure the functionality of the system and to inspect for oil leaks.

4.1.3 Sodium Plumbing

The next section to consider is the sodium plumbing system which involves the design and construction of the sphere dip tube, the extraction flange (which includes all the lip seal installation for inserting the dip tube) and the transfer line (to connect the sphere with the tank).

A sketch of the dip tube can be seen in Figure 4.5 and a full mechanical drawing with dimensions in the Appendices. After careful consideration we decided to go with a curved version of the dip tube. Other designs included a sectioned one, straight at first and curving at the end.

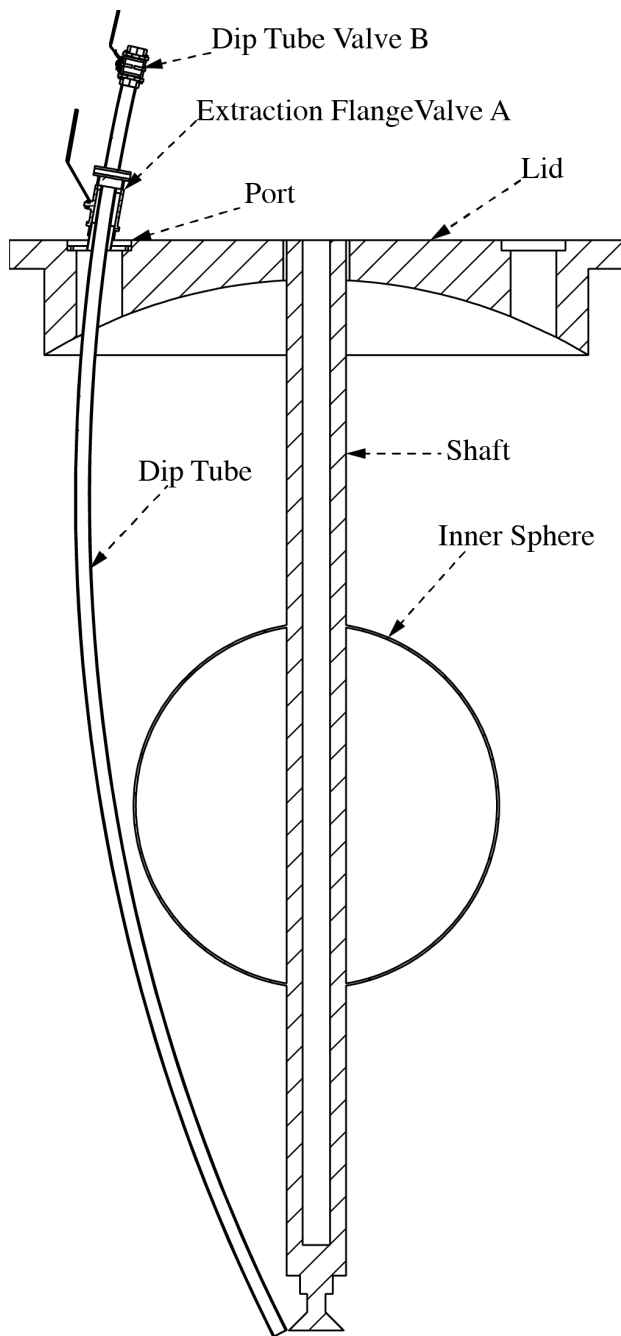


Figure 4.5: Cross section of the insertion diagram including the dip tube, the extraction flange, the lid, the inner sphere and shaft

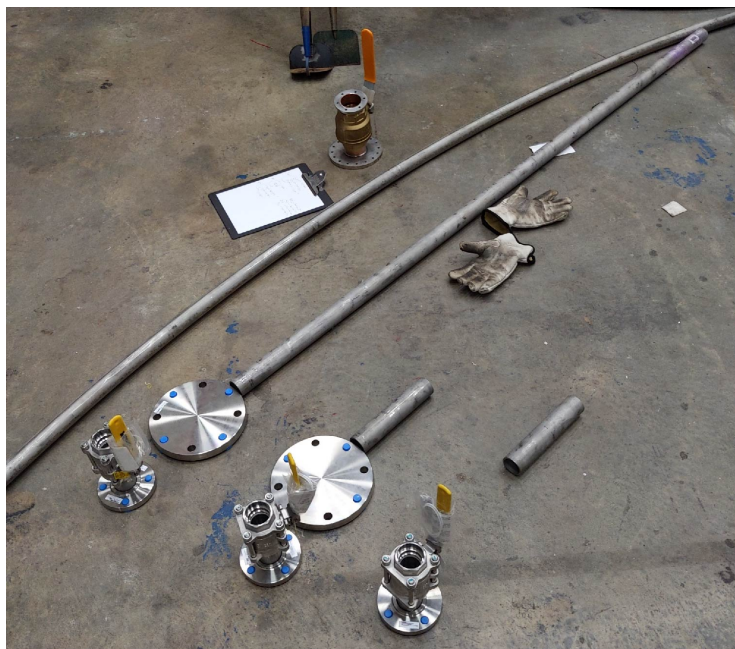


Figure 4.6: Collection of dip tubes for tank and sphere.

This design was discarded and replaced with the curved one because it would make the insertion process smoother, which was the most critical step in the whole transfer process. With that in mind, careful consideration was taken to ensure the curvature radius of the dip tube could pass through the port's aperture at such an angle that would reach the base of the shaft in the outer sphere vessel. This ensured that the least amount of sodium possible was left behind in the outer vessel. The radius of curvature of the dip tube ended up being 520 cm (with this we mean that the dip tube is just a section of a circle of radius of 520 cm) and with a length of 355 cm. Finally, a ball valve was welded at the end of the dip tube. This was the crucial valve, the one that was going to be opened to start the sodium flow to the tank.

Another set of straight dip tubes were designed: two for the tank, one short (for putting the sodium into the tank), another long (for extracting the sodium from the tank to the sphere), and one last short one for the sphere, for putting the sodium back to the experiment. A picture can be seen in Figure 4.6. The straight dip tubes were cut from a single pipe and were welded

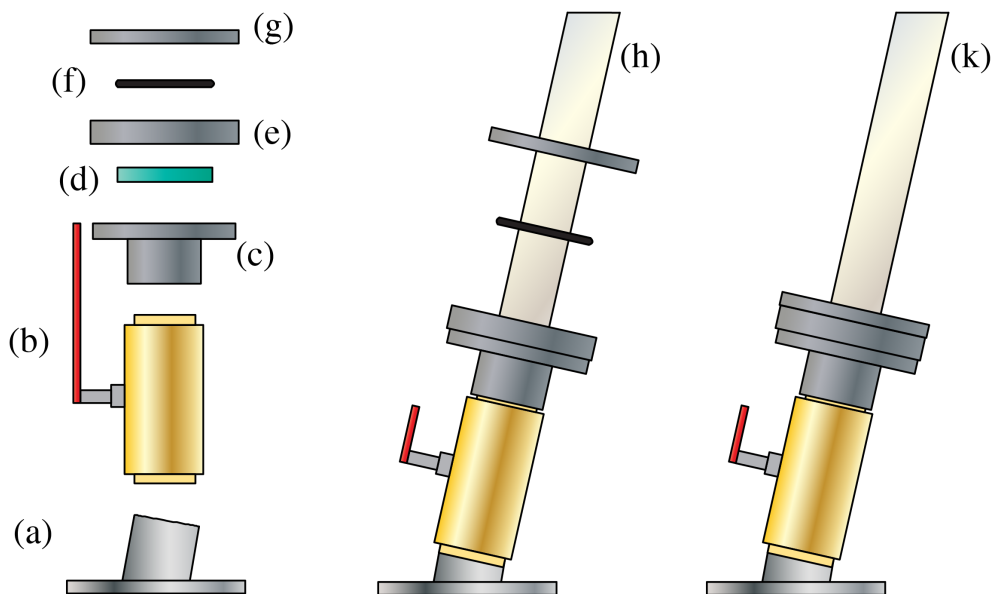


Figure 4.7: Extraction flange diagram: (a) Port to valve flange connector. (b) Ball valve. (c) Lip seal to valve connector. (d) Lip seal. (e) Lip seal holder. (f) O-ring. (g) O-ring holder. (h) During insertion. (k) After insertion.

to the flanges, seen in the picture, by Nolan Ballew. The dip tubes and flanges were all made of stainless steel 304.

The extraction flange is the assemblage of different components shown in Figure 4.7. The purpose of this flange is to allow the hot insertion of the dip tube while preventing the air from entering into the experiment. In order to achieve this the flange included a lip seal and an o-ring. The lip seal will allow the movement of the dip tube while being able to hold around 1 psi of pressure in the sphere, and the o-ring secures the dip tube to the flange and provides a better sealing when the pressure needs to be raised to 10 psi for the extraction, after it has reach the bottom of the outer sphere. The process goes as indicated in Figure 4.7: First, the port to valve flange connector, the ball valve and the lip seal to valve connector are welded together and installed on the Port A of the experiment (ports' labels are indicated on the lid of the experiment). Then, the lip seal holder with the lip seal installed inside is bolted into the lip seal to the valve

connector. At this stage, with the valve A closed of course, the extraction flange is ready to receive the dip tube. When the insertion is going to take place, the o-ring and the o-ring holder are placed in the dip tube. Once the tip of the dip tube has gone through the lip seals, the valve A can be opened safely, and the insertion can proceed until the tube has reached the bottom. Once secured against the bottom, the o-ring holder can be bolted into the lip seal holder, and this will squeeze the o-ring against the dip tube, securing a better seal for the rest of the transfer. Finally, a spacer is situated between the o-ring holder and the valve B of the dip tube, as shown in Figure 4.8. This serves as a better support of the dip tube and the transfer line (that will be bolted into the end of the dip tube later on) to prevent the dip tube from pushing against the lip seals and damaging them (even though the insertion is ready and most of the pressure in the experiment is held by the o-ring, keeping the integrity of the lip seals is important when the dip tube is removed after transfer). After the transfer takes place, this spacer will be used to lift the dip tube to prevent it from being in contact with the remaining sodium left behind in the bottom of the vessel that could cause the dip tube to get stuck when the sodium solidifies. Detailed drawings of each one of these parts can be found in the Appendix section. Additionally, the SOP provides a much detailed and rigorous description of the insertion process.

The final part of the sodium plumbing arrangement is the transfer line. It is a heated, 28-foot-long, 1.5” of internal diameter, stainless steel flexible hose, with a maintenance temperature of 120 C and three standard round pin thermocouple plugs for monitoring (one in each end and another in the center of the line). It was connected to a rotary potentiometer and then to a wall plug to regulate the input voltage. A picture of the final installation of the hose during transfer can be seen in Figure 4.9.



Figure 4.8: Spacer to support the dip tube and transfer line.

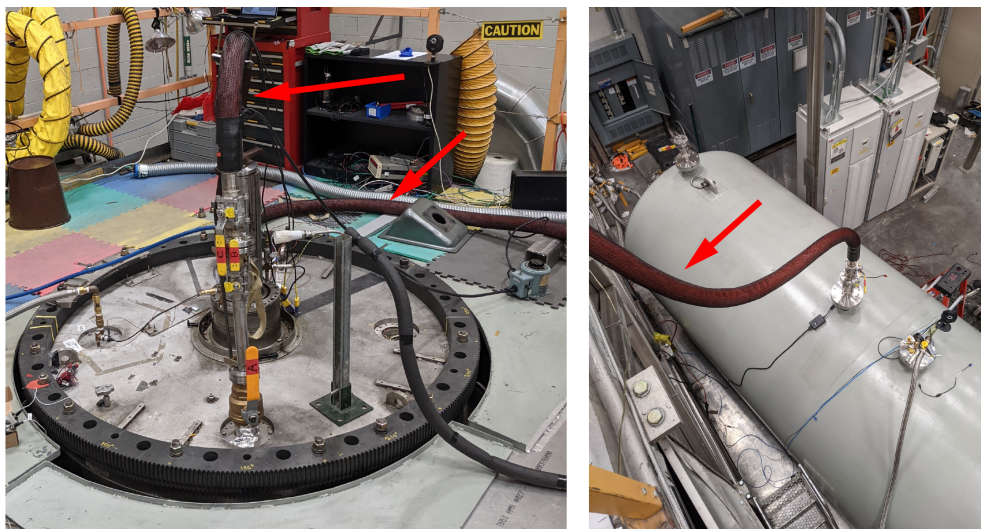


Figure 4.9: Picture of the final installation of the transfer line (indicated by red arrows). On the right the tip of the sphere installation. On the left, the tank installation.

4.1.4 Gas Injection System

As you can see on the diagram in Figure 4.2, the gas injection system is a very important part of the transfer process. Both the tank and the sphere need to be pressurized at 10-15 psi. Additionally, this pressurization process needed to be sustained at high flow-rates. This is because the estimated time for draining was around 2 hours which implied that 12 tons of sodium, equivalent to approximately 12000 liters (3500 gallons), needed to be drained at a rate of 2-5 liters per second. This is why 5 nitrogen cylinders were used to provide the flow rates needed. We needed to provide enough nitrogen to replace the sodium leaving the sphere (or tank, when putting the sodium back) to replace the space and keep the same pressure of 10 psi required to keep the sodium flowing. For a detailed discussion on the gas handling system refer to Artur Pervalov PhD dissertation, and also to the Appendices section to see the diagrams for the different gas manifolds in the SOP.

One important function of the gas injection system was to inert the container and pipes prior to the sodium transfer. It is important to remove most of the oxygen (less than 2% of oxygen content is desired) in both the sphere and the tank. In order to do that, we pressurized both containers over several cycles: we raised the pressure to 5 psi, then released the air inside, then we pressurized again, and drained, over and over until the oxygen content of the output gas was less than 2%. To accomplish that we used a digital oxygen sensor installed in one of the exhaust hoses (see the center nozzle in the tank picture in Figure 4.3). The transfer line was also purged of oxygen in a similar way and the dip tube was purged before insertion as indicated in the SOP.

4.1.5 Initial Disassembly

With all the parts of the transfer system explained in the sections above, we proceeded to remove the parts of the experiment that were in the way and needed to be removed to guarantee the safety of the procedure. First, we dismantled the outer motor and outer motor frame of the experiment. Then we proceeded to remove the inner motor with its frame. We used the 5-ton crane located in the high bay of the IREAP building where the experiment is located. Then we removed most of the instrumentation and left in place the temperature sensors and the pressure sensors. Most of these instruments were located in a new port that we designed and built. A total of 3 ports were installed in the sphere after this stage: the visualization windows, the gas port and the extraction flange. In the gas port we installed a pressure sensor and a thermocouple to measure the temperature of the sodium. Another gas port was installed in the tank top nozzle as indicated in the diagram in Figure 4.11.

The installation of these ports on the lid of the experiment were performed following an SOP inherited from the previous 3-m graduate student team, and modified accordingly by us. It involved a gloved bag to make sure the least amount of oxygen entered the experiment while exposing the interior of the experiment when replacing the ports, two jacks and some threaded rods bolted into the port. A picture of the procedure is shown in Figure 4.10.

The diagram in Figure 4.11 shows the schematic of the transfer during the extraction process after the dip tube is inserted. With this configuration the sodium was safely extracted from the sphere into the storage tank. During the transfer we monitored the process by measuring the height of the sodium with a laser distance meter through a visualization window installed in one of the ports of the experiment as can be seen in Figure 4.12. Based on the change of height

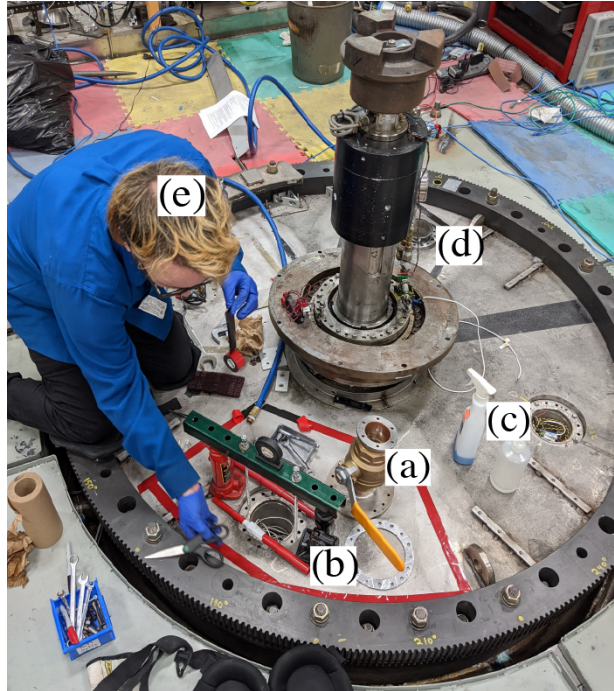


Figure 4.10: Picture of the ports installation procedure. (a) Extraction flange port to be installed. (b) Jacks used to lift the ports that had gotten stuck by solidified sodium. (c) Cleaning tools used to degrease the surface. (d) Visualization port already installed. (e) Artur.

per unit time, an estimation of the flow speed and draining time were performed. Additionally, a flow meter was installed in one of the nozzles in the tank to corroborate the flow rate estimates. Artur Perevalov developed a software to perform these estimates in real time.

The presence of this visualization windows was crucial to overcome one of the difficulties that we encountered during the initial transfer operation: by the end of the first day of heating, we noticed that the liquid sodium level was rising above the beginning of the port, right at the sphere boundary (see Figure 4.1 and appendixes). This should have not been happening since the window port was supposed to be sealed, so a bubble must have formed between the glass surface and the sphere vessel boundary. This could only be happening because there was a leak on the windows port. We could remediate the situation by simply reducing the heating and hence stop the expansion of the liquid metal. We did not fix the leak because it was small compared to the

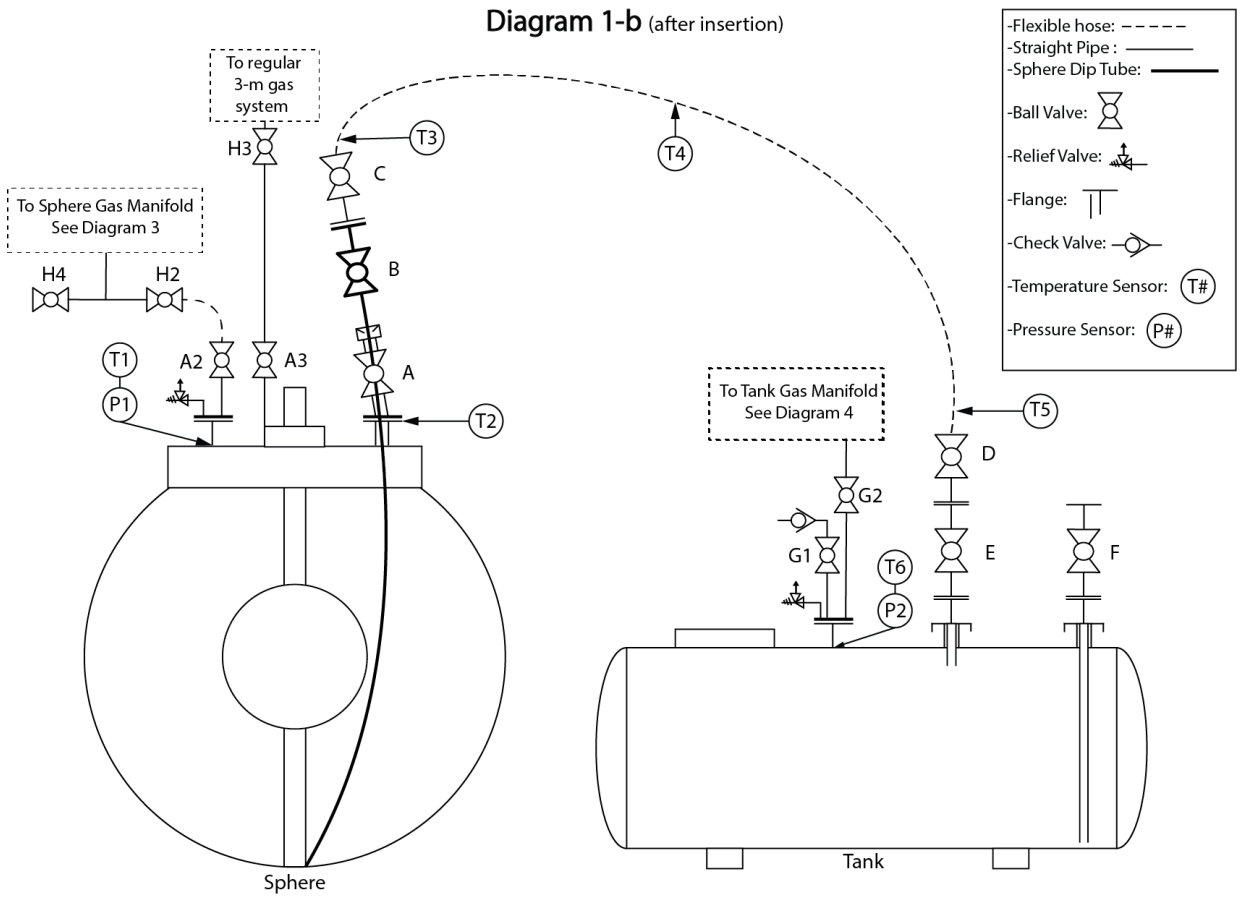


Figure 4.11: Diagram of the transfer plan after the insertion of the dip tube.



Figure 4.12: Visualization window on one of the ports of the experiment. Liquid sodium can be spotted from the window.

amount of gas that we would inject on the next day. We just needed to be careful that the sodium level did not reach the windows, to prevent leaks.

4.2 After Transfer

4.2.1 Final Disassembly

After the sodium was transferred and the system cooled down, we proceeded to disassemble the remaining parts of the experiment. Previously, most of the electronics had been removed, leaving in place only the instrumentation for monitoring the transfer, like the pressure sensors and temperature sensors. The top outer bearing (see diagram in Figure 4.1) was removed at this stage prior to the transfer. It was removed after the inner frame. The next step was to remove the dip tube that was still inserted. This was performed in a similar way as the insertions, with the support of the crane. Since the sphere was slightly pressurized (~ 1 psi) there was no major risk, and the seals could get damaged during the extraction of the dip tube. With the ball valve A closed after the dip tube was removed, the vessel was sealed. By removing the gear belt and the bolts



Figure 4.13: Flying inner sphere-shaft-lid combo. In the picture you can see the pink sodium covering the combo.

that secured the lid to the sphere vessel (see diagram in Figure 4.1), the inner sphere-shaft-lid combo was safe to fly, as shown in Figure 4.13.

Once the inner sphere and shaft was extracted, we removed the top locknut (see diagram in Figure 4.1) which in theory would release the lid to move upward but that was not the case. The reason was that the tight fit between the top inner bearing and the shaft was not allowing the lid to slide upward and decouple from the shaft. In the diagram 4.1 it can be seen that the lid is bolted to the Bearing Holder (in yellow) which pushes the bearing upward when lifting the lid. After careful consideration, the solution we came up with was to cool down the shaft and heat the bearing in such a way that a thermal gradient is maintained across both objects, hopefully releasing the bearing. We had to additionally secure the inner sphere to the ground to prevent it from lifting. For this we used some chains to tighten the inner sphere to the frame of the cube



Figure 4.14: Installation used to release the top inner bearing from the shaft. Left arrow points at the liquid nitrogen hose pouring liquid inside the shaft aperture. Right arrow points at the heat tape used to heat up the bearing.

(the metal frame that contains the 3-m experiment). After a few hours heating the inner bearing with some heat tapes, and applying liquid nitrogen to the interior of the shaft, the lid finally got released (not without a scary "pop"). In Figure 4.14 you can see the arrangement that we used in this process.

Once the lid and the shaft were disassembled, we proceeded to carefully clean each one of the parts, starting with a solution of isopropyl alcohol with 10% water to remove the bigger layers of sodium and letting it oxidize overnight. Repeated applications of these solutions worked to remove the excess of sodium but we recommend transitioning to 100% water once there is total certainty that the sodium was either oxidized or removed. Alcohol is not very effective at removing the last layer of sodium oxides. Prior to this cleaning stage, we had many practice

sessions cleaning old containers of sodium, including a barrel with almost 100 pounds of sodium. We hired a cleaning company to take care of the inside of the outer vessel, given the lack of equipment required for the safety of this operation, including respiration masks and full hazmat suits. The cleaning took place in a two-day operation. After removing most of the sodium chunks from the bottom, they proceeded to seal the vessel and spray water vapor. The remaining water and sodium hydroxide solution leftovers were removed the next day and the interior mopped and cleaned by us the day after.

4.2.2 Fixing the Outer-Inner Sphere Coupler

When the inner sphere was set horizontally for cleaning we could, for the first time, take a look at the inner bottom bearing (see Figure 4.15 and compare with the section view in Figure 4.1). There was clear evidence of sodium in the bearing which might have been the reason for failure. Additionally the chromium sleeve that was added to improve the sealing and reduce the damage on the lip seal due to the friction, was peeled off from the bayonet coupler. That could have also damaged the bearing, maybe even more likely than the sodium itself, because ball bearings like these have been reported to work submerged in liquid metal before (with considerable lifespan reduction).

This bearing also happened to be stuck, so a bearing remover was built by the IREAP machinist Tom Weimar. Once the whole combo of bearing and bayonet coupler was removed, taken apart and cleaned, we proceeded to inspect their condition. As you can see in Figure 4.15, even after being cleaned many times, the bayonet coupler continued to generate an oxide layer. The reason for this was the alloy chosen for its construction: an oiled infused brass alloy. The



Figure 4.15: Left: Bottom view of the inner bottom bearing and the bayonet coupler after the bearing retainer and lip seals were removed. The dirty bearing can be spotted. Right: the new stainless steel bayonet coupler (front) and the old one (back), oiled infused brass alloy. A layer of oxide (white color) can still be seen after many wet cleans.

original idea was that the different alloys of brass and steel would prevent a cold weld between the bayonet, bayonet coupler and copper pins (see drawing in Figure 4.1). However, this oiled infused brass could have also influenced the damage on the bearing by absorbing the sodium and damaging the sleeve. The actual reason for failure of the bearing is uncertain; however, too many factors together seem to add up enough motives to decide to replace the bayonet coupler for a new one. We decided to go with stainless steel 316 as the material of the coupler, and brass for the pins. In this way, the brass pins between the two stainless steel pieces (the bayonet and the coupler) would still prevent a cold weld. The detailed drawings can be found in the Appendices section and were made by this author; however, due to the high precision required for the construction of this piece, Tom was in charge of its fabrication.



Figure 4.16: Left: Smooth inner sphere. Right: Rough inner sphere with alpha baffles installed.

4.2.3 Baffles design and construction

After the shaft was removed from the inner sphere for deep cleaning and to ensure there was no sodium left in the bolt holes, threads and corners; it was assembled again and shipped to Central Fabricators Inc. where a set of six alpha baffles of 1/2 inches thickness and one inch height (corresponding to a 5% radius height as in the water experiment in section 3) were welded on. A set of detailed drawings can be seen in the Appendices. After the welding took place, the new inner sphere and shaft were taken to House of Balance for a dynamical balancing at 900 rpm, even though the experiment will not reach such speeds. A comparative picture can be seen in Figure 4.16.

Once the sphere arrived back from the balancing house, it was lifted vertically and a new set of top inner and top outer bearing were assembled into the shaft-lid-inner sphere combo. When installing the top inner bearing, we had to use liquid nitrogen again and heat tapes to install it. In this case, the weight of the lid (almost 4000 lbs) was enough to push the bearing into its final position. Once again, refer to Figure 4.1. The next step was to install the combo into the outer sphere. We added Teflon sealing tape between the outer sphere vessel and the lid to ensure the

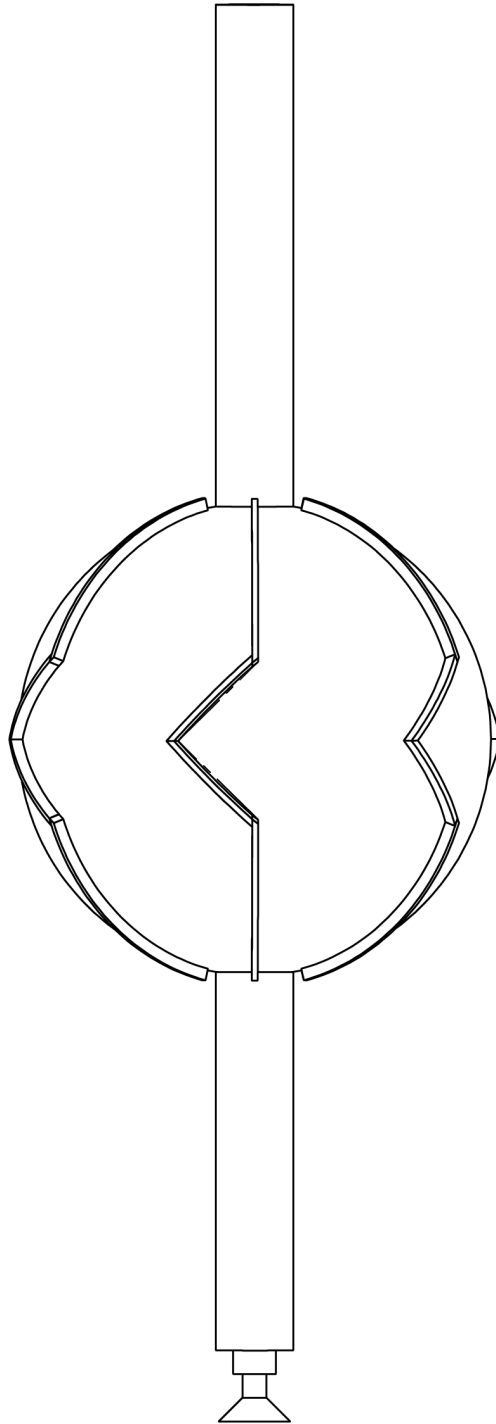


Figure 4.17: Diagram of new baffled inner sphere. A full version with measures can be found in the Appendices.

sealing. Then, the lid was bolted into the outer vessel. At this point we were ready to transfer the sodium back from the tank. Once the sphere was inert we started the sodium insertion SOP (see Appendices) which follows the same idea as the extraction SOP (from sphere to tank): the tank is heated, the sodium molten, then the pressure is raised to 10 psi and the sodium will flow between tank and sphere. In this case there was no necessity of a dip tube hot insertion, since it was already installed in the tank prior to being filled with sodium. See diagram in Figure 4.18. However, the sodium flow did not start immediately as expected. A solid sodium chunk presumably was not molten in the inside of the tank dip tube by the moment of the transfer. It took a couple more hours than estimated, and some heat blankets around the presumed location of the chunk (we noticed the possible chunk location because the valve F of the tank was not closing) to finally melted down and trigger the sodium flow.

Finally, the rest of the parts of the experiment were installed in the following order: the instrumentation ports, the gear belt, the inner frame and the inner motor and the outer motor and outer motor frame. One last section remains.

4.2.4 New Probe Installation

Our main contribution regarding instrumentation probes consisted in the design of another finger probe. This is the name that was given to the set of two hall probes inserted in a stainless steel tube, 30 cm into the sodium. These two probes are oriented 90 degrees inclined from each other. The construction of this piece was made based on the preexisting one with the idea of having two internal measurements that were diametrically opposed to study spatial correlations between them. See Figure 4.19 and also the Appendices for a detailed description of the probe.

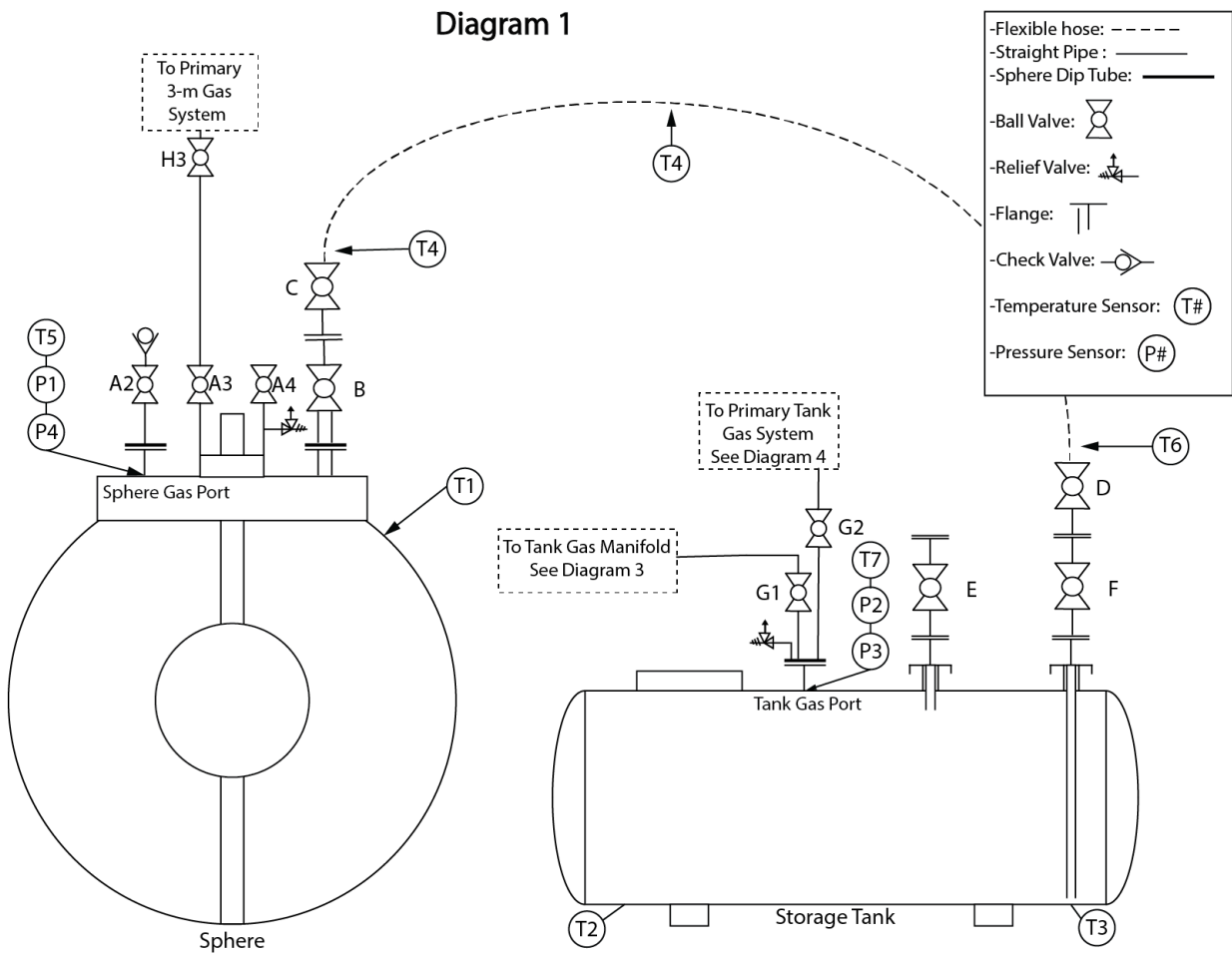


Figure 4.18: Diagram of the transfer plan from tank to sphere. Sodium refilling.



Figure 4.19: Finger probes. Top: the old one. Bottom: the new one.

These probes were inserted and calibrated with the magnets to test the proper orientation. We turned the magnets on and rotated the probe until we measured a minimum (or maximum) of voltage in the radial probe. This was an indication that we reached the desired alignment in the cylindrical radial direction because the magnets are not expected to have azimuthal components. Different intensities were used to corroborate the original alignment. During some of the runs the new finger probe got loose and rotated. The data was later rotated as well and the results were consistent. After this incident, the probes were secured in a better way to prevent it from happening again.

This concludes the journey to the center of the 3-m experiment. In the next section we will present the formal experimental set up with the new upgrades and the results of what we called Magneto-hydrodynamic studies. Last but not least, we wanted to add that, for time constraints, there were many events and tasks performed during the progress of this project that we did not list in this section. The big ones, that we think are worth at least mentioning in this dissertation, were the magnet wires repair and the scrubber repair, which were technical difficulties that we had to overcome for the successful outcome of this project. We ask the reader to refer to the authors and/or to Don H. Martin, for further information.

Chapter 5: The 3-m Experiment: Magnetohydrodynamic Studies

5.1 Experimental Set-up

In this section we will describe the experimental set-up of the 3-m diameter spherical-Couette sodium experiment including part of the design and instrumentation. This experiment was designed and built by previous graduate students in this laboratory, Daniel Zimmerman and Santiago Triana. We will describe the instrumentation installed by them that is used for our measurements. For a more detailed experimental description, check their respective dissertations [13, 14]. In the next section, we will show the results from the upgrade, and we will focus on the new instrumentation added by me and my coworker Artur Perevalov during the completion of this Ph.D.

In Figure 5.1 we can see a schematic of the 3-m experimental vessel. It has the same radii ratio as the 40-cm experiment $\Gamma = r_i/r_o = 0.35$. The outer vessel is a 3-m diameter spheroid, with an opening of approximately 1.6 meters in diameter at the top, where the lid with the instruments is located. The bottom of the lid is also spherical so the system of lid and outer sphere forms a spherical vessel (see Figure 4.1). The inner sphere is a 1 meter diameter stainless steel. A 6 inches diameter cylindrical shaft, that extends almost 4 meters, connects the outer and the inner sphere together. A bearing sits in the bottom of the outer sphere with a coupler that allows both spheres to independently rotate. This bayonet coupler was modified by us, as

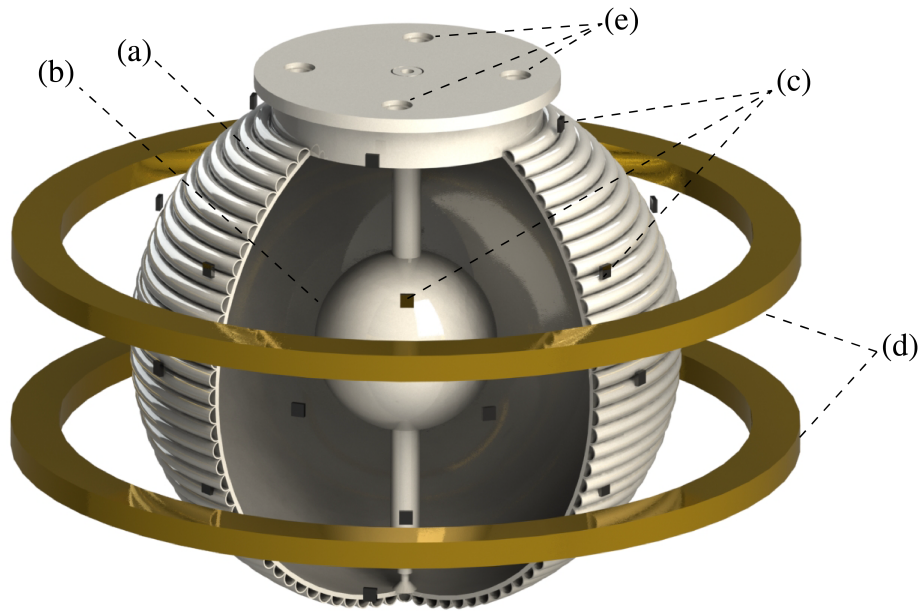


Figure 5.1: The 3-m experiment vessel. (a) The three-meter outer sphere vessel. Half pipe oil jacket surround the 1-inch thickness vessel for heating. (b) Smooth one-meter diameter inner sphere, before remodeling. (c) Arrange of 31 magnetic Hall probes. (d) Pair of electromagnets to apply quadrupole and dipole external magnetic field. (e) Instrumentation ports with pressure sensors, temperature sensors and a set of magnetic probes.

indicated in the previous section (see section 4.2.2). Additional sets of bearings in the top and bottom, hold the shaft and lid with the frame of the experiment and allow the differential rotation of the spheres.

Two 260 kW motors drive the inner sphere and the outer sphere. The inner motor is connected and directly aligned with the shaft. A torque sensor (Futek TFF-600), and an adapting coupler, join the motor and the shaft together. The outer motor is geared to the outer sphere by a belt with 400 teeth in a reduction gear on the lid of the experiment. The lid is where most of the instrumentation is located. A desktop computer, with a PCI-DAS6402-16 acquisition card, collects the data from mostly the magnetic and pressure probes. The temperature is acquired directly by an Omega Wireless thermocouples in selected locations in the experiment: one in contact with the sodium through one of the instrumentation ports, two on the outer shell on the

side of the experiment and on the bottom. The last one is located on one of the magnets to prevent overheating when running at high currents. Three 9 Volts lead batteries are located on the lid to power up the instrumentation when rotating. A set of two electromagnets are aligned with the axis of the experiment. They are capable of applying a dipole or quadrupole field for up to 200 G in the center of the configuration.

A total of 33 Hall Probes (Honeywell SS94A1F) were located initially in the experiment. This allows us to measure magnetic fields in various critical locations in the experiment. A set of 2 Hall probes is located in one of the ports in the cylindrical radial and the azimuthal direction at 30 cm into the sodium and 120 cm from the center. The remaining 31 probes are located around the outer sphere vessel in the spherical radial direction in an arrangement that allows us to extract the spherical harmonics decomposition of the field up to $l = 4$ (see section 2.3.2). After upgrading the experiment we designed and constructed a new set of probes identical to the 2 internal ones (for a total of 35 Hall probes) but we placed them axially opposed to the first set. This was done with the proposed study of spatial correlations, axial symmetry of the internal fields, and as a backup plan - in case of failure or misalignment of the original set of internal probes, which has been reported previously.

5.2 Results

In this chapter we will present the results of the 3-m experiment. We will include the analysis of previous measurements taken by Santiago Triana and Daniel Zimmerman (some of them published [4, 46, 47, 48] others not published) with the smooth inner sphere boundary. The goal is to compare them with the results in the presence of the rough inner sphere boundary that

we designed [78], installed and test during the completion of this PhD.

Similar to the 40-cm experiment, we will start analyzing the torque and its dependence primarily on the Reynolds number Re and the Rossby number Ro . For the 3-m experiment we will use the magnetic Reynolds number Rm instead of the Reynolds Number (or *Fluid* Reynolds Number) as is conventional when the presence of magnetic fields is relevant for the dynamics (see section 2.4). We will continue with the analysis of the mean magnetic field amplification in the different probes: the internal probes and the Hall array (see section 5.1). The former gives a close look into the internal topology of the magnetic fields in the flow. It will, in particular, indicate the presence or not of a radial magnetic field, whose importance for the dynamo mechanism we have stated in section 2.3. For the Hall array probes we will use Gauss coefficients decomposition (see section 2.3.2) and use it to also infer about the internal dynamics of the flow and magnetic field. Finally, we perform time dependent analysis of both Hall array and internal probes' time traces of the amplified magnetic field, and compare them with the expected results from the literature. These studies include, for example, spectrum analysis and probability distribution as a function of Reynolds and Rossby numbers.

5.2.1 Torque Scaling

5.2.1.1 Reynolds number dependence

The torque dependence on the Reynolds number for a stationary outer sphere and for the 3 inner sphere modes (smooth, scoop and wedge) is shown in Figure 5.2. In the same way we did for the 40-cm experiment, this curve will be used to normalize the torque for the runs with changing Rossby number since the total hydrodynamic torque factorizes as

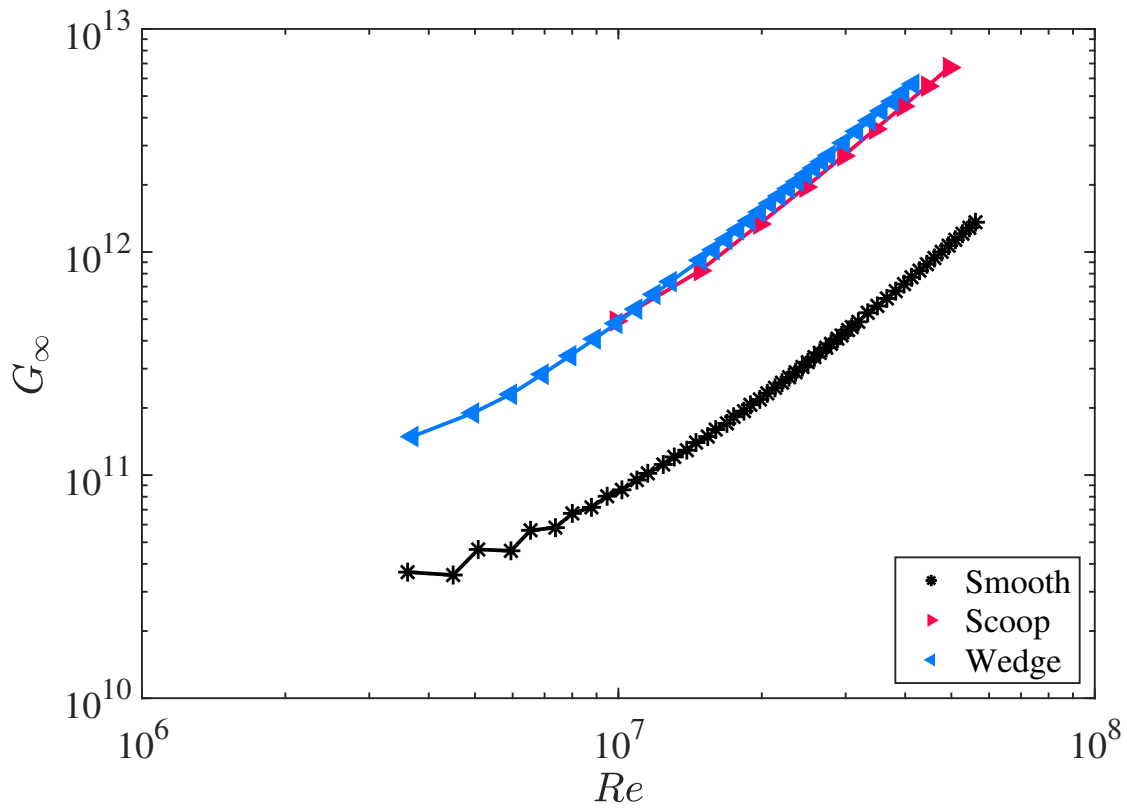


Figure 5.2: Dimensionless torque from the inner motor versus Reynolds number with stationary outer sphere ($Ro = \infty$) for all baffle designs in the 3-m experiment. A power law of the form $G_\infty = bRe^a + c$ was fitted to each data set. Values a , b and c are listed in Table 5.1

Table 5.1: Power law fit of the form $G_\infty = bRe^a + c$ of the plots in Figure 3.7 and Taylor-Couette flows in [1].

| Experiment | a | b | c |
|-----------------------------------|------|-------|----------------------|
| 3-m Smooth ($\Gamma = 0.35$)[4] | 1.83 | 0.009 | 2.3×10^{10} |
| 3-m Scoop | 1.85 | 0.042 | 1.3×10^{11} |
| 3- Wedge | 1.84 | 0.053 | 8.4×10^{10} |

$$G(Ro, Re) = f(Ro)G_\infty(Re), \quad (5.1)$$

as reported by Paoletti and Lathrop [1], Zimmerman et al. [4], Dubrulle et al. [82].

The first we notice is the clear increment in the torque generated by the motor for the same Reynolds number. This difference increases slightly as we increase the Reynolds number from 4.2 at the smallest Reynolds number, to 5.2 times more, approximately at the maximum Reynolds number. In fact, the slope of this curve saturates to its final value faster for a rough inner sphere. For the runs with baffles on the inner sphere the motors reached their torque limit, sometimes they even overheated and shut down. This means that with the baffles installed we are able to put all the torque capacity of the inner motor into the flow and magnetic field generation, something that never happened with the smooth inner sphere where the only limitations for spinning the inner sphere were the resonance mode of the cube and the frame that hold the motors. If we compared the extrapolation to higher Reynolds numbers done for the water experiment in Figure 3.7, we were expecting a net dimensionless torque of $G_\infty 10^{13}$ for a $Re \sim 3 \times 10^7$ which is less than 1% difference from the real value that we measured of $G_\infty = 7 \times 10^{12}$.

In table 5.1 we can see the results of a power law fit of the form $G_\infty = bRe^a + c$ to the dimensionless torque as a function of the Reynolds number. The main differences are in the coefficient b and c , being both higher with baffles than without them. The coefficient c is

a measure of the torque at low Reynolds numbers when the inner sphere rotates slowly, hence we would expect that its main contribution is due to the seals and bearings friction. The baffles clearly increase torque on the inner sphere, even at slow rotation rates. It is important to mention that the current set of motors is not intended to operate at frequencies below 1 Hz, and the baffles have a significant effect on torque at those frequencies. Figure 5.2 shows that the curve for smooth inner sphere converges to a constant value as $Re \rightarrow 0$ whereas the same is less clear for the rough inner sphere cases.

The coefficient b is a geometry-dependent factor. In Taylor-Couette flows, it is expected to grow as we reduce the gap between the cylinders [1, 4, 82]. More specifically, in Taylor-Couette, this prefactor is expected to be inversely dependent on the critical Reynolds number for self-sustained turbulence (see Dubrulle and Hersant [32]). In fact, for Taylor-Couette in the subcritical regime with fully developed turbulence,

$$G \sim \gamma^{sub} Re^2,$$

where

$$\gamma^{sub} = \delta/R_g,$$

being R_g the critical Reynolds number for self-sustained turbulence and δ a factor that depends entirely on the gap between cylinders.

Because of the dynamical similarities between the Spherical and Taylor-Couette flows we can expect these relations to hold to a certain extent, which is the case shown in Table 5.1. Both prefactors b for baffles added to the inner sphere are higher than with the smooth boundary

Table 5.2: Location and amplitude of the maxima in Figure 5.3

| Experiment | G/G_∞ | Ro^{-1} |
|--------------------|--------------|-----------|
| 3-m Smooth [4] | 1.20 | -0.05 |
| 3-m Alpha scoop 5% | 2.19 | -0.21 |
| 3-m Alpha wedge 5% | 2.06 | -0.21 |

case, which indicates that we are effectively reducing the gap. Additionally, as mentioned in the literature [10, 62, 63, 78], the presence of the baffles changes the nature of the boundary layer to a pressure-dominated one, having additional effects on the angular momentum transfer; hence, in the torque.

The coefficient a for the rough boundary case is surprisingly similar to the smooth boundary. Although it is greater for both baffle modes, from the 40-cm water experiment and from Taylor-Couette (see [31, table I]) we expected this value to be much closer to 2. This might indicate that the flows are actually not significantly more turbulent than the smooth case, presumably due to the fact that the inner motor is incapable of reaching the same rotations rates as with the smooth sphere.

5.2.1.2 Rossby number dependence

For the Rossby number dependence we can see Figure 5.3, where we have also plotted the 3-m smooth case for comparison, in the same way we did for the water experiment (see Figure 3.8). Additionally, we can see the list of the location and amplitude of the maximum torque peak in Table 5.2. The first we notice is a clear increment on the normalized dimensionless torque with baffles, although only for negative Rossby numbers. Let us talk about the region $Ro^{-1} < 0$ where the maximum torque peak is located. When compared with Figure 3.8 we can see that the amplitudes of the torque at the maximum torque peak are only approximately 10% lower

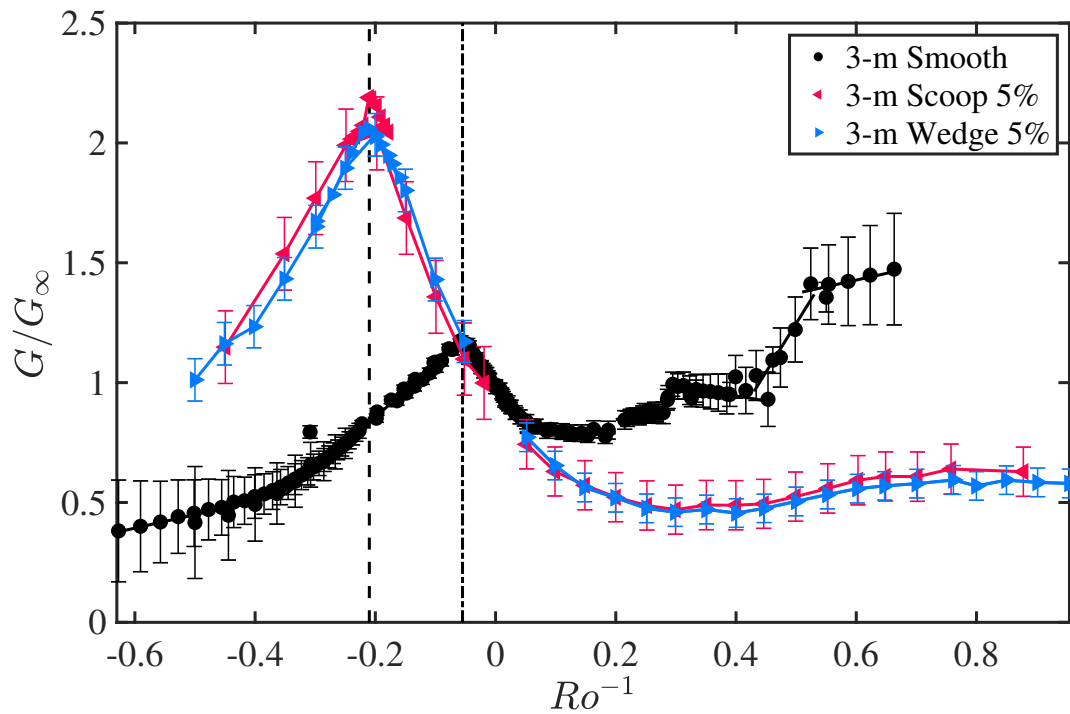


Figure 5.3: Rossby number dependence of the measured inner sphere torque. The magnitude of the torque at a given Ro and Re is normalized by $G_\infty(Re)$, the torque expected at that Reynolds number if the outer sphere were not rotating. The dashed line indicates the location of the peak for maximum relative dimensionless torque for smooth and rough inner sphere.

than what we expected from the water experiment, with scoop torque being higher than wedge at the peak. Additionally, the location of the torque peak moved to more negative inverse Rossby numbers as expected as well. What this actually implies is that we have increased the effect that the inner sphere has on controlling the dynamics of the system, and the rotation rate of the inner sphere required for a state to happen is now lowered, shifting everything to higher inverse Rossby numbers in absolute value.

Even though the location of the maximum torque peak shifted, it moved to a higher Rossby number than we were expecting. From the 40-cm experiment, the location for 5% height alpha baffles was around $Ro^{-1} \sim -0.15$ and for the 3-m experiment we obtained a location of the peak closer to -0.21 ± 0.01 independently of the mode (scoop or wedge). This change in the location of the peak to more negative inverse Rossby numbers is the equivalent of having taller baffles on the sphere, as seen in Figure 3.8 and 3.2. This was certainly unexpected given the good agreement for the torque as function of Reynolds number discussed in the previous section. One possibility could be that the baffles thickness (as opposed to height) was not the same ratio as tested in the water experiment. For engineering purposes of the baffles construction, the thickness of the baffles was set to half of their height, whereas in the water experiment where this ratio was one to one. This might have had an effect on the generation on the flow separation at the baffles [62]. Another possibility is that the viscosity takes a more important role now that we have changed the coupling in the boundary layer and the difference of the 30% between the viscosity of the water and liquid sodium has a more significant effect in the generation of this new pressure-dominated boundary layer. A more detailed analysis of this difference is out of the scope of the present dissertation; however, it is left as a possible research topic for which the 40-cm experimental setup could be used in the near future.

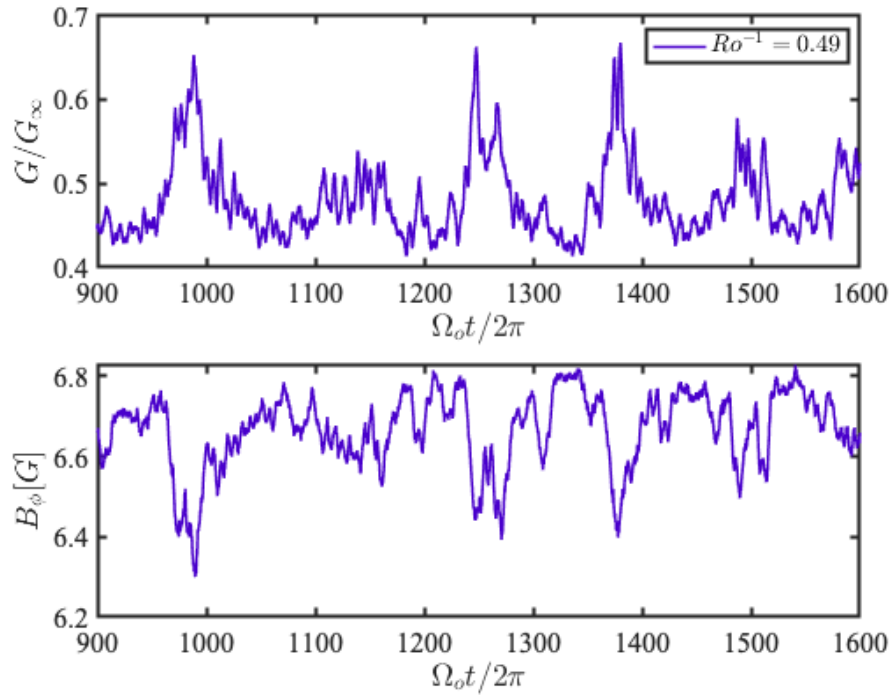


Figure 5.4: Possible bistability regime for rough inner sphere in the 3-m experiment. Time series in outer sphere rotation units of the dimensionless normalized torque (top) and azimuthal magnetic field induced (bottom) for $Ro^{-1} = 0.49$. A running average of 10 seconds has been applied to remove the high frequency oscillations. Compare with Zimmerman et al. [4, Figure 10].

For the region where $Ro^{-1} > 0$ we observed also a similarity with the 40-cm experiment. The torque is lower than the smooth case for increasing Rossby number until bistability takes place. However, there does not seem to be a region where the torque jumps to some higher torque state like with a smooth inner sphere [46]. This could mean that we have not yet reached the High Torque State region observed and explored by Zimmerman et al. [4, 46] where the normalized torque reaches values higher than the torque peak around negative Rossby numbers. When compared to the 40-cm experiment we see that the jump to high torque state (H) happens at values higher than $Ro^{-1} \sim 0.8$ which we have only partially studied. However, we did observe some instability in the torque time traces that start taking place for $Ro^{-1} > 0.5$ as we can see in Figure 5.4. The behavior of these time traces is similar to the ones reported by Zimmerman et al. [46]: an increase in the torque accompanied by a decrease in the azimuthal magnetic field. However, the torque fluctuations are only of 10% of G_∞ , compared with the smooth case where the fluctuations are between 50 – 100% of G_∞ . The correlation between torque fluctuations and magnetic field fluctuation, and the bursting dynamic, might be a strong indication that we are in the onset of a dynamo generation as reported in [86, 87].

We have yet to explore regions where the bistability may be stronger, presumably for $Ro^{-1} > 1$ given the results in the 40-cm experiment. However, we might need to evaluate the fact that the baffles have a significant effect on the bistability regime. According to Zimmerman et al. [46], this regime is linked to the appearance of a strong shear along the inner tangent cylinder. By adding baffles, we not only strengthened the equatorial jet, but made it present for most of the rotation rate regimes. An equatorial jet for the strong corotation regime, that would not be there with a smooth inner sphere, would destroy the inner tangent cylinder, preventing the bistability regime to take place.

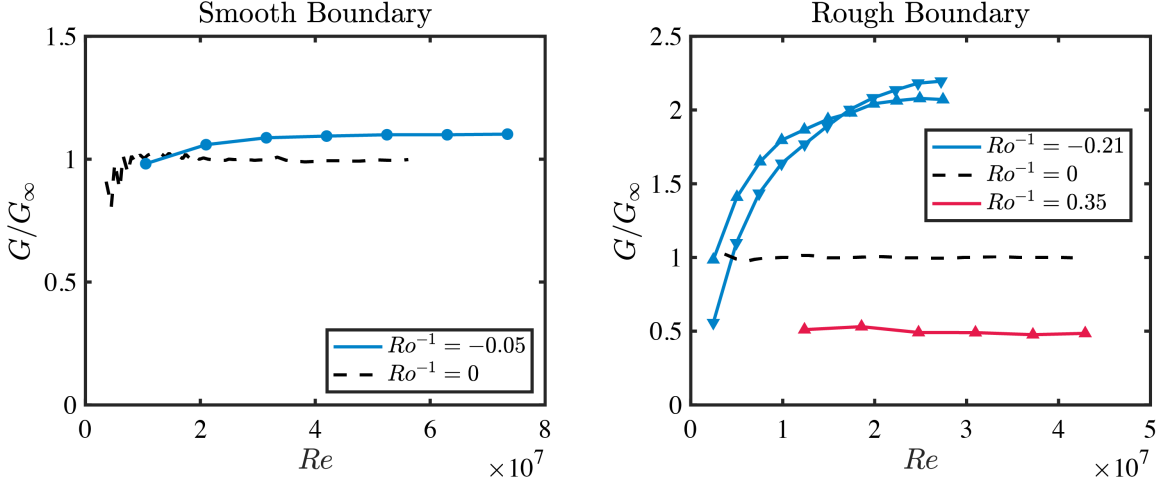


Figure 5.5: Compensated plots of the dimensionless torque as a function of Reynolds number for different Rossby numbers, for smooth (left) and rough (right) inner sphere in the 3-m experiment. Dashed lines are taken in the absence of an external magnetic field, solid lines are taken with an external dipolar field of $B_{\text{ext}} \sim 20$ G. Runs for scoop mode are indicated with "▽" and for wedge mode with "△". The torque for stationary outer sphere for both cases scales close to $G_{\infty} \sim Re^{1.85}$ which implies that the curves in this plot with a power law less than one (curving downward like the cases for $Ro^{-1} < 0$) implies a torque higher than G_{∞} .

In section 5.2.1.1 we considered runs in the parameter space where the Reynolds number was changing while the inverse Rossby number was kept constant at a value of zero; meaning, the outer sphere was stationary. These runs, where the only parameter we change is the Reynolds number, are called *Reynolds ramps*. Respectively with the rest of parameters (Rossby ramps and magnetic ramps). Let us now study a few sets of Reynolds ramps but with a different Rossby number.

In the Taylor-Couette experiments [1, 82] it is well-known that the Reynolds number dependence on the dimensionless torque is the same independently of the Rossby number (see equation 5.1). Something similar was obtained previously for Spherical Couette flows [4]. In Figure 5.5 we plotted the normalized dimensionless torque for five Reynolds ramps with different Rossby numbers and for both configurations of smooth and rough inner sphere. The normalized

Table 5.3: Power law fit of the form $G_\infty = bRe^a + c$ of the plots in Figures 3.7 and 5.5

| Experiment | Ro^{-1} | a | b | c |
|------------|-----------|------|-------|----------------------|
| 3-m Smooth | 0 | 1.83 | 0.009 | 2.3×10^{10} |
| 3-m Smooth | -0.05 | 1.84 | 0.008 | 3.2×10^{10} |
| 3-m Scoop | 0 | 1.85 | 0.042 | 1.3×10^{11} |
| 3-m Scoop | -0.21 | 1.89 | 0.041 | 3.1×10^{10} |
| 3-m Wedge | 0 | 1.84 | 0.053 | 8.4×10^{10} |
| 3-m Wedge | -0.21 | 1.87 | 0.067 | 3.4×10^{10} |
| 3-m Wedge | 0.35 | 1.85 | 0.022 | 8.6×10^{10} |

dimensionless torque is just a compensated plot of the form $G/(bRe^a + c)$ where a, b and c are given for every inner sphere configuration by the values on the table 5.1. For the smooth boundary case, for a Rossby number near to the maximum torque regime and with a applied magnetic field, we can see a curve that converges in a few steps to $G/G_\infty = 1.2$ which is the corresponding value for that particular Rossby number as indicated in Table 5.2. For the rough boundary case however, the curve with $Ro^{-1} = -0.21$ (around the maximum torque regime) converge slowly compared to the smooth case. For the rough case we have also plotted another Reynolds ramps for a positive Rossby number near the minimum torque peak, in the corotation regime (see red curve on Figure 5.5). This curve is almost constant as a function of Reynolds number as we would expect if the power law was the same regardless of the Rossby number. A compensated plot (G/G_∞) curving downwards like the one for $Ro^{-1} = -0.21$ implies that the non normalized torque (G) has an exponent higher than the exponent of G_∞ .

As we can see in Table 5.3, we have extended Table 5.1 by adding the coefficients of a power law fit of the dimensionless torque for the Reynolds ramps taken at Rossby number different than zero, some of them plotted in Figure 5.5. The two runs at maximum torque regime for rough inner sphere are the ones with a higher exponent a indicating that turbulence is probably more fully developed for this configuration. Remember that the Kolmogorov turbulence scales

as Re^2 and it has been shown for Taylor Couette flows [31, 62] that baffles make this transition to ultimate turbulence regime faster, facilitating the transport of angular momentum across the boundary layer.

Another possibility for this increment in the exponents a at the maximum torque regime for rough inner sphere is that in this region we are also obtaining a significant amplification of the magnetic field, as we will see in the next section, and that increment is directly due to the fact that there is more energy demand due to the generation of the magnetic field. The increment in the torque demands before and after the onset are one of the indications of a possible dynamo generation, as reported by Monchaux et al. [75] and Gailitis et al. [16].

5.2.2 Mean Field Amplification

We will now discuss the magnetic measurement by the 35 Hall probes, including the two new ones that we installed during the remodeling stage. In this section in particular we will focus on the time average of the magnetic probes for different sets of parameters. Like with torque data, we will divide the section in Reynolds and Rossby numbers dependence and additionally we will add a subsection about the dependence of the dynamics on the externally applied magnetic field. We will divide our magnetic measurements in two types: internal measurements given by the four probes submerged in sodium; and external measurements, given by the 31 external Hall probes distributed around the outside of the outer sphere. We will use these 31 signals to generate the spherical harmonics decomposition in the form of Gauss coefficients, as explained in Section 2.3.2 and using Equation 2.27. In the case of modes with $m \neq 0$ we will add the $\pm m$ modes in quadrature: $B_l^m = \sqrt{(B_l^{+m})^2 + (B_l^{-m})^2}$. We will mostly show results taken on the negative

Rossby number region, particularly around the maximum torque regime, since it is in this region where the highest amplification of the magnetic field was found. We will address results on the corotation regime or with the stationary outer sphere when it is relevant for the discussion.

The process of debiasing the magnetic field signal was critical for the accuracy of the results. First, we performed a calibration curve for the magnetic field in the Hall probes as a function of the current in the coils of the electromagnets that generated the external magnetic field: with the experiment cold, and solid sodium inside, the outer sphere was set to rotate at around 0.1 Hz. Then, a ramp in the external field was applied in steps of 20 Amps in the coils, for 10 revolutions of the outer per step in the magnetic field. This curve measures the contribution of the external magnets in every magnetic probe without the effect of the liquid sodium. Second; before every run and with the sodium molten, the experiment was set to rotate in solid body configuration (the outer and the inner sphere rotating at the same frequency). Magnetic data was acquired for around 10 revolutions of the outer sphere with the external magnetic field off. This will give the base level of every Hall probe which depends on its temperature and ambient magnetic field which fluctuates daily. Finally, after the desired runs were performed, to debias the data we subtracted the base level voltage in the probes taken right before the run (or sometimes after the run) with no magnetic field applied, and the respective value of the magnetic field contribution of the coils. In this way, the remaining value of the magnetic field will only be the contribution of the magnetic field generated by the advection of the liquid sodium only.

In the next section we will show preliminary results without an externally applied magnetic field as a function of Reynolds and Rossby number for the internal and external probes. This will allow us to study the generation and amplification of the ambient magnetic field: the Earth's and the laboratory field which is inherent to the building. After this study, we will present results

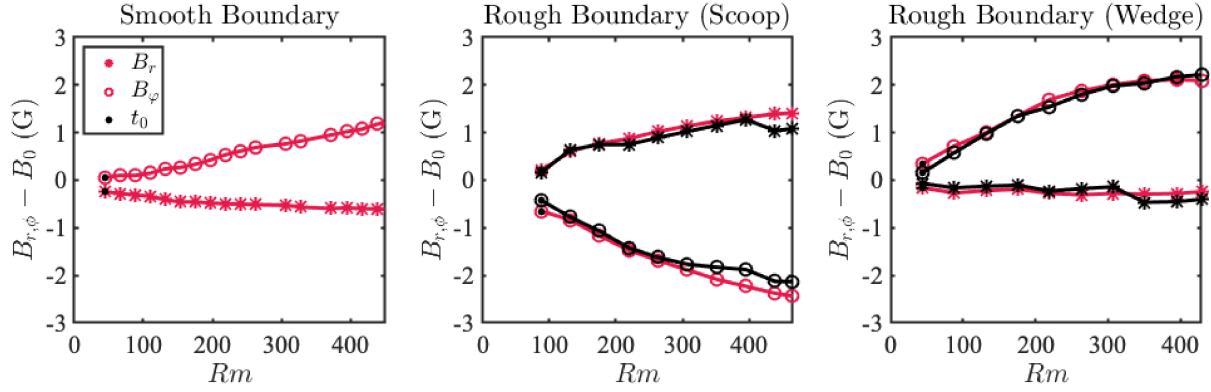


Figure 5.6: Magnetic field amplification with stationary outer sphere ($Ro^{-1} = 0$) as a function of the magnetic Reynolds number for one pair of Hall probes in Port B of the experiment (see Section 5.1) in the cylindrical radial direction (B_r) and in the azimuthal direction (B_ϕ) for the two types of boundaries and their respective modes (scoop[<] and wedge[>]). During this run, there is no externally applied magnetic field from the coils.

with a weekly imposed magnetic field to fix the topology of the external fields, particularly in the dipole configuration. Within each section we will try to separate the discussion in the internal and external field as a function of Rossby and Reynolds number as the controlling parameters for this experiment.

5.2.2.1 No applied magnetic field

As the first exploratory measurements in our new rough boundary experiment, we performed runs with stationary outer sphere and increased the inner sphere angular frequency in both directions (so, both modes: scoop and wedge). For these initial sets of runs we did not apply an external magnetic field. In Figure 5.11 we can see the magnetic amplification for the finger probes in both the azimuthal and cylindrical radial direction of the experiment with no externally applied magnetic field and with stationary outer sphere as a function of the magnetic Reynolds number. The three cases are up for comparison: smooth inner sphere and both modes of rough inner

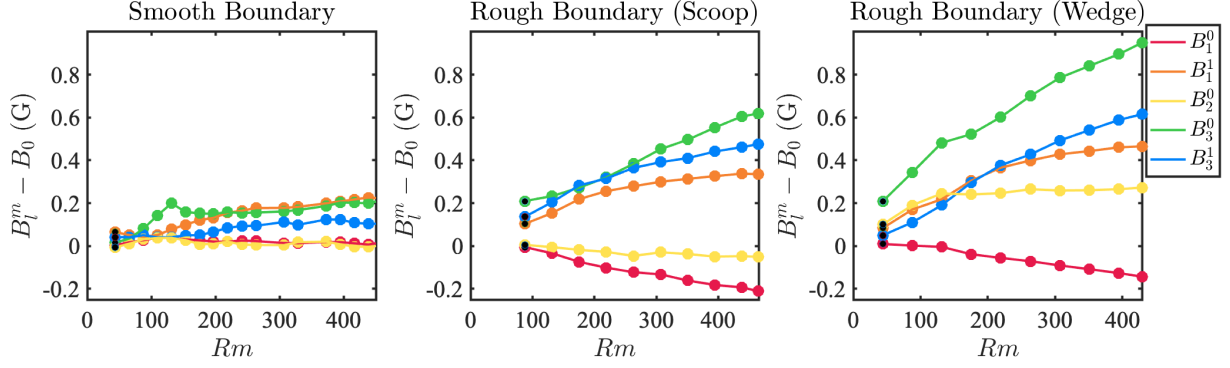


Figure 5.7: Magnetic field amplification in the external Hall probes array, express in spherical Harmonics decomposition (dimensional Gauss coefficients) with stationary outer sphere ($Ro^{-1} = 0$) as a function of the magnetic Reynolds number for the two types of boundaries and their respective modes (scoop[<] and wedge[>]). During this run, there is no externally applied magnetic field from the coils.

sphere (scoop and wedge). The additional probes that we installed are shown in black. The main observation of these plots is the increase of the amplified field for the rough inner sphere as a function of magnetic Reynolds number. Especially for low magnetic Reynolds number the amplification is significant compared to the smooth case. The azimuthal magnetic field is the one that shows the highest amplification, and changes sign in the presence of baffles as we will discuss in more detail in the section 5.2.2.2. The radial component of the internal magnetic field has also increased, although for the wedge case it seems to have a similar magnitude as the smooth case.

In Figure 5.7 we can see the Gauss decomposition of the magnetic field in the Hall probe array of the same runs in Figure 5.6. We can see a dominant B_3^0 mode through all the regimes as well as an B_1^1 and B_3^1 . The presence of the $m = 1$ modes could indicate the presence of a possible equatorial rotating dipole which is the most common expected configuration as reported in numerical simulation like the one from Gubbins et al. [9] and Nornberg et al. [74]. The fact that we have stronger fields in the external array than in the smooth case could point towards an

increase of the flux expulsion as proposed by Moffatt [51] due to closed streamlines of flow now thanks to the baffles. It is also interesting to notice that the dipole field is growing with a negative value with respect to most of the other modes. Also, the change in sign for some of the even modes, like B_2^0 for scoop versus wedge modes. It is hard to determine the existence of a dynamo just by these plots. Ideally we would expect a significant amplification of the external fields, although there is no well-known estimation of the intensity that we should be expecting for these Reynolds numbers. Our only reference of experimental dynamos achieved in the laboratories [42, 88] suggest values of the order of tens of Gauss, although for very different geometries. Another possible evidence of the presence of a dynamo is the presence of a threshold for the amplification of the fields as reported in the VKS and Riga experiments [42, 88]. However, there is no clear threshold for the field reported here, unless it is hidden at lower magnetic Reynolds number than the ones that we reached in these runs. There is neither a clear geometry, like a strong dipole or quadrupole, which are the most possible dynamo configurations. The presence of strong $m = 1$ modes is promising but not conclusive enough. The B_3^0 mode suggest the presence of a $l = 2$ fluid mode, as will be more clear in the next section, which seems to be positive for a dynamo action in this geometry as reported by Bullard and Gellman [49].

The next exploratory runs that we performed were in the counter-rotation regime with no applied field. These runs were performed as a first swipe to locate the maximum torque peak, which we found to be around $Ro^{-1} \sim -0.21$ for either scoop or wedge mode. The torque measurements for these runs are also reported in Figure 3.8. In Figure 5.8 we can see the two internal probes for both modes of the rough inner sphere. For this parameter space we did not have a similar run for the smooth case with no applied field, but we did find a set of runs where we turned off the magnetic field while changing parameters. We used those values to get the average

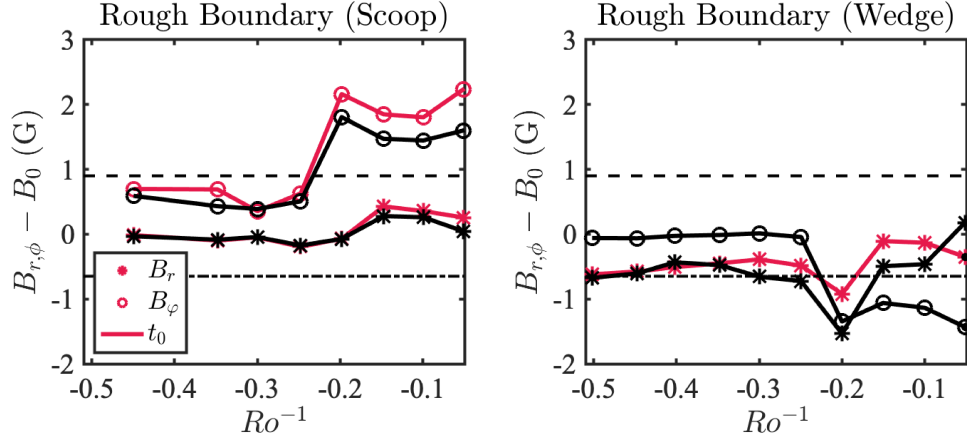


Figure 5.8: Magnetic field amplification for counter-rotating spheres ($Ro^{-1} < 0$) around the maximum torque regime for one pair of Hall probes in Port B of the experiment (see Section 5.1) in the cylindrical radial direction (B_r) and in the azimuthal direction (B_ϕ) for the two types of boundaries and their respective modes (scoop[<] and wedge[>]) for constant $Rm \sim 220$. Horizontal dashed line indicates the maximum gain reported in the smooth case in the internal probes (azimuthal [-.] and radial [-]) around the same Rossby number for comparison.

amplification with the smooth inner sphere at the maximum torque regime ($Ro^{-1} \sim -0.055$ for smooth) that are shown in the plots as dashed lines. The location of the peak, and the amplification at that particular point in the parameter space for both azimuthal and radial field is evident. Although, the radial field for scoop is not as strong as it is for wedge mode. The direction of the amplification is consistent with Figure 5.6 and for the peak, the amplified field surpasses the values of the smooth inner sphere for all except the radial direction in the scoop mode.

In Figure 5.9 we can see the external Hall probe array results for the runs in Figure 5.8. Two modes are dominant: the B_3^0 and the axial dipole mode B_1^0 . Both peak for the maximum torque. The B_3^0 mode is flatter for inverse Rossby numbers to the right of the peak (more negative Rossby numbers), the dipole mode however is sharp just around that peak and decreases for values on the sides of the peak. It is also inverse with respect to the B_3^0 mode similar to the stationary outer sphere. The amplification is significantly greater than for the smooth case; however, these values are still below 1 Gauss which is close to the inherent fluctuation associated with the building.

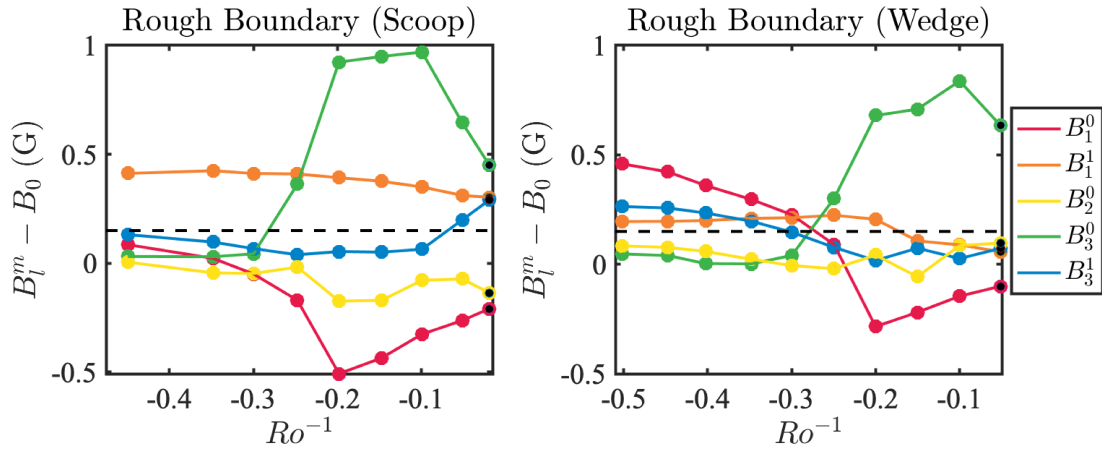


Figure 5.9: Magnetic field amplification in the external Hall probes array, express in spherical Harmonics decomposition (dimensional Gauss coefficients) with counter-rotating spheres ($Ro^{-1} < 0$) as a function of the magnetic Reynolds number for the two types of boundaries and their respective modes (scoop[<] and wedge[>]). The horizontal dashed line indicates the maximum gain reported in the smooth case in the external probes. During these runs, there is no externally applied magnetic field from the coils.

During the bias measurements, where we performed solid body rotations (inner and outer at the same rotation frequency), the fluctuating ambient magnetic fields oscillate between 0.5 G in the probes near the equator and almost 2 G for probes on the poles. This ambient magnetic field is expected to be greater at the poles, especially the north pole, since this is where most of the electronics equipment is located. The Figure 5.10 shows a timeline of the voltage in some of the probes at different latitudes for solid body rotation without applied external magnetic fields. The sensitivity of the probes is 31 mV per Gauss, so oscillations of 0.1 V are equivalent to a couple of Gauss which is already in the same order of magnitude of the amplification that we are measuring.

There are two possible solutions to overcome this difficulty. One is to somehow cancel, or reduce, the ambient (mostly the building's) magnetic field. At the time this section was written, this was a work in progress by one of our most recent graduate students Elaine Jaross and Shiyi

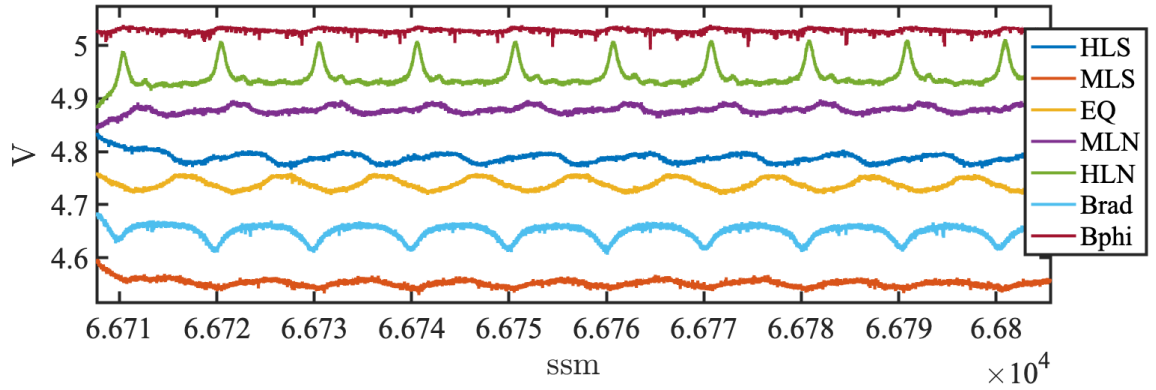


Figure 5.10: Timeline of the voltage in some of the experiment probes in seconds since midnight (ssm). HLS: High Latitude South. HLN: High Latitude North. MLS: Mid Latitude South. EQ: Equator. Brad: Internal Probe in the radial direction. Bphi: Internal Probe in the azimuthal direction. This run takes place for solid body rotation at 0.1 Hz and with no applied external magnetic field.

Wang. Additionally, we could run the experiment with an applied external field, which was already in the goals of this dissertation. This will allow us to interpret the new amplified fields with the, well-known, geometry of the field that we are applying (either dipole or quadrupole) to infer properties of the fluid states inside the experiment. These results can be compared with the 40-cm experiment results of the previous section, especially in the maximum torque region where we were able to measure meridional velocity profiles.

5.2.2.2 Applied magnetic field

In the next section we will present the results of the mean magnetic fields of the internal and external probes as a function of Rossby number first and then as a function of magnetic Reynolds number for a constant magnetic field applied of 20 G in the center of the experiment in a dipole configuration. We will focus the Rossby number dependence in regions with negative Rossby numbers around the peak torque.

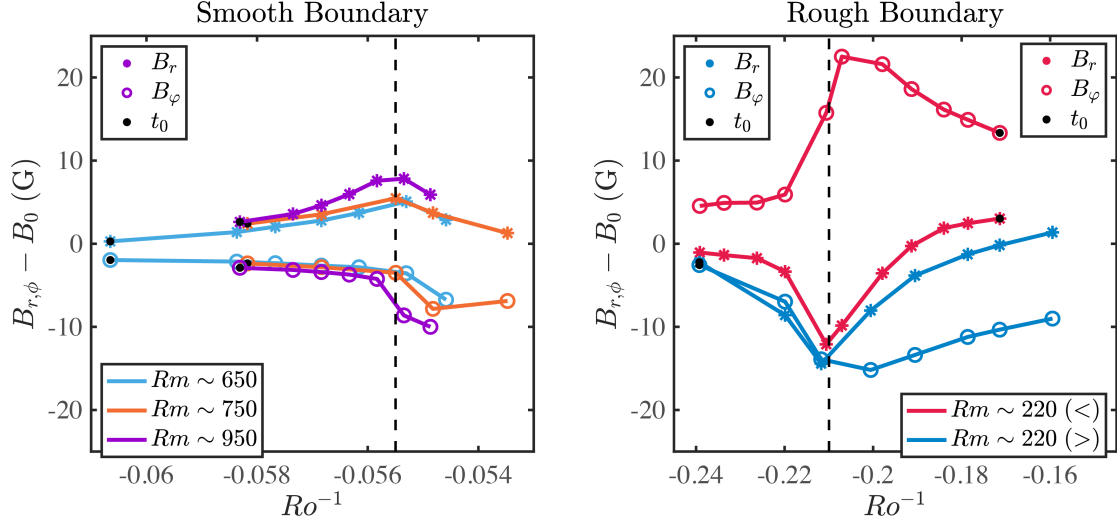


Figure 5.11: Magnetic field amplification around the maximum torque regime as a function of the Rossby number for one pair of Hall probes in Port B of the experiment (see Section 5.1) in the cylindrical radial direction (B_r) and in the azimuthal direction (B_ϕ) for the two types of boundaries and their respective modes (scoop[<] and wedge[>]) for different sets of Reynolds numbers. The maximum torque regime is indicated with a dashed vertical line for each boundary type. A constant external dipolar magnetic field of 20 G in the center of the experiment was present during all the runs.

In Figure 5.11 we can see the magnetic amplification for the finger probes in both the azimuthal and cylindrical radial direction of the experiment. A magnetic field of 20 G in the center of the experiment is applied for all the runs. For the smooth case we can see that the induced magnetic field reaches a local maximum near the maximum torque peak (indicated with a vertical dashed line) regardless of the Reynolds number. As observed by Zimmerman et al. [4] the maximum radial field is offset from the maximum azimuthal field. The former one being centered with the maximum torque peak. This same result was observed for the 40-cm water experiment and reported in [78], where the minimum for the azimuthal velocity in the equatorial plane was offset from the torque peak. The fact that this minimum of azimuthal speed near the equator coincides with a maximum in the azimuthal field generation is an evidence of the importance of the shear: the geostrophic constraints due to rotation vanish, which allows a more efficient

transport of angular momentum in the radial direction [89]. In other words, the global rotation in the experiment vanishes at this point, as the drag forces due to each boundary equate each other in the opposite direction, hence maximizing the torque in the inner motor. This cancellation of the global rotation comes with a broader shear region in between the spheres which maximizes the azimuthal amplification of the magnetic field.

For the rough boundary case we notice a significant increment of the induced field with respect to the smooth boundary case even with a much lower Reynolds number. This is a clear indication of the effectiveness of the baffles in transferring angular momentum and coupling the inner boundary with the fluid. The amplification takes place for both internal directions measured. It is stronger in the azimuthal direction for the scoop mode ($<$) than for the wedge mode ($>$) for $Ro^{-1} < -0.21$, whereas the radial field appears stronger for the wedge mode.

The direction of the amplified field changes with the rotation direction of the outer: for smooth and scoop mode the outer sphere has a positive angular velocity (right-hand rule) but the direction of the amplified field changes. For wedge mode in the negative Rossby region, the outer sphere was rotated in the negative direction, that is why the azimuthal field changes sign with respect to the scoop case. Remember that the probes are fixed with the outer sphere. With a smooth inner sphere the direction of the amplified internal azimuthal field is in *opposite* direction of the inner sphere's tangential velocity. With baffles, the amplified internal azimuthal field is in the direction of the inner sphere's tangential velocity. This change of direction of the amplified field in the azimuthal direction is intriguing and not well understood yet. Verschoof et al. [63] showed that for rough Taylor Couette flows, the contribution to the torque due to skin friction (shear) near the wall decreased with roughness. This highlights the role of the pressure drag with rough boundaries as mentioned before. The presence of rough elements might then have a

significant impact on the shear forces in the bulk of the fluid (away from the boundaries) which is the origin of the omega effect, a.k.a., the stretching of the magnetic field lines in the azimuthal direction.

The radial field also changes sign, not as a function of the rotation direction of the sphere but as a function of the roughness: with baffles, the amplified radial field is negative (inward, towards the axis of rotation) whereas for smooth boundary it is positive. If we look at Figure 3.11 for the 40-cm experiment, we can notice that the radial velocity field near the pole of the experiment (which is where these probes are located) changes sign for smooth versus rough spheres. More precisely, for no baffles there is a positive radial velocity field at the poles whilst for the alpha baffles is strongly negative, which is a sign of a strong recirculation. This is therefore consistent with the observed induction effect in the finger probes.

We will stress once more the importance of these results: for a Reynolds number of almost 4 times less than the maximum achieved without baffles, we are increasing by 100% the magnitude of the internal magnetic fields generated in the experiment near the maximum torque peak region.

In Figure 5.12 we can see the main spherical harmonics contributions to the total external field measured by the Hall probe array for the same runs as in Figure 5.11. This magnetic field is in the spherical radial direction of the experiment and plotted as a function of the inverse Rossby number. The most relevant feature of this plot is the dominance of the B_3^0 mode over almost the entire span of these runs. This mode is particularly dominant at the max torque peak for the scoop mode where it reaches a value of 20 G, which is equivalent to the externally applied field in the center of the experiment. Notice that at this point, all the other magnetic field modes decrease their intensity as well. For the rough boundary in the wedge mode, the B_3^0 mode is still dominant but all the other modes are more intense compared to the scoop and smooth mode.

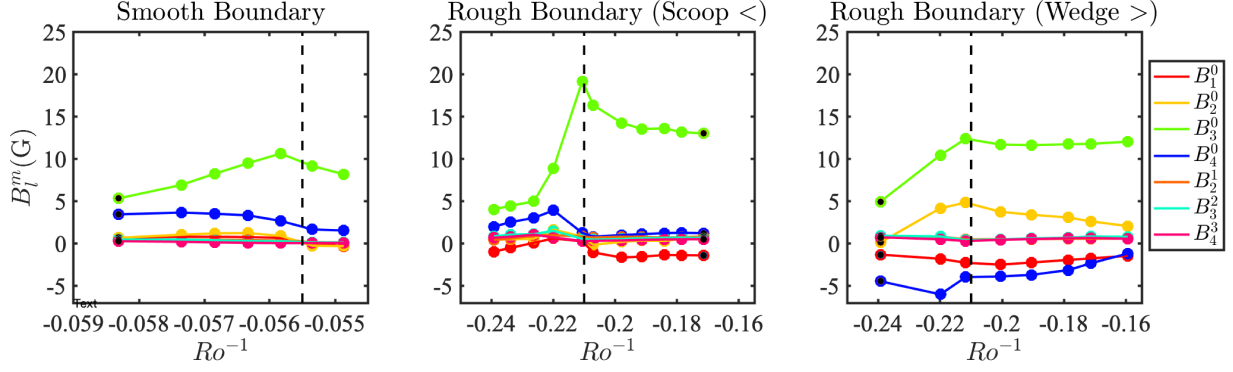


Figure 5.12: Magnetic field amplification around the maximum torque regime as a function of the Rossby number for the 31 Hall probes array in the spherical radial direction (see Section 5.1) in the form $B_l^m = l(l + 1)g_l^m$ (where g_j^m are the Gauss coefficients of the spherical harmonics decomposition) for the two types of boundaries and their respective modes (scoop[<] and wedge[>]) for a constant Reynolds number: $Rm = 950$ for smooth, $Rm = 220$ for rough boundary. These Rossby ramps are taken around the maximum torque regime indicated with a dashed vertical line for each boundary type. A constant external dipolar magnetic field of 20 G in the center of the experiment was present during all the runs.

We can use the results in Chapter 3 to better interpret this data. In Figure 3.11 and in Figure 3.9 we can see that the maximum torque regime is characterized by an equatorial jet stretching all the way to the outer boundary and recirculating towards the poles. This jet has different properties depending on the mode. In particular for the scoop mode it is more intense than the other cases, but narrower. This type of flow topology has order $l = 2$ and let us consider the axisymmetric case where the azimuthal wavenumber $m = 0$ ($S_{l=2}^{m=0}$). The externally applied magnetic field is dipolar, so its main component is of the form $S_{l=1}^{m=0}$. Using the Bullard and Gellman [49] notation, the interaction between an $l = 2$ poloidal velocity field with a $l = 1$ poloidal magnetic field produces a $l = 3$ magnetic field:

$$(B_1^0, S_2^0, B_3^0),$$

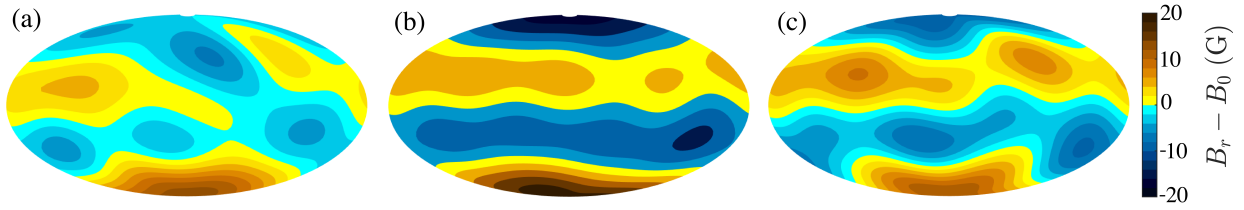


Figure 5.13: Hammer-Aitoff projection of the spherical radial magnetic field measured by the 31 Hall probe array for the Rough Scoop mode in Figure 5.11 (center) for three parameter space points: (a) $Ro^{-1} = -0.22$; (b) $Ro^{-1} = -0.21$, at the torque peak and (c) $Ro^{-1} = -0.20$.

which satisfies the selection rules.

In Figure 5.13 we can see a Hammer-Aitoff projection of all the spherical harmonic modes (not only the ones in Figure 5.12) of the magnetic field for the scoop mode of Figure 5.12. As in previous plots, we have subtracted the external magnetic field contributions. The center graph corresponds to the maximum torque peak at $Ro^{-1} = -0.21$. The other two correspond to Ro^{-1} to both sides of this peak. We can see the $l = 3$ mode very clearly for (b) which also has the highest amplitude. The field for (c) is weaker but still has a visible $l = 3$ topology with more oscillatory behavior and less axial symmetry than (b), and for the plot (a) we have lost most of the $l = 3$ topology. This figure serves as a validation of the results in Figure 5.12.

In Figure 5.14 we can see the magnetic amplification for the finger probes in both the azimuthal and cylindrical radial direction of the experiment as a function of the magnetic Reynolds number for the Rossby number of the maximum torque regime. A magnetic field of 20 G in the center of the experiment is applied for all of the runs in this figure.

In the search of a dynamo, the magnetic Reynolds number dependence is crucial. The previous successful dynamo experiments showed a clear threshold for the dynamo action, with a change in the slope of magnetic energy density as a function of the magnetic Reynolds number (See for instance [16, 42] and for a recent review of all the experimental approaches see [86]).

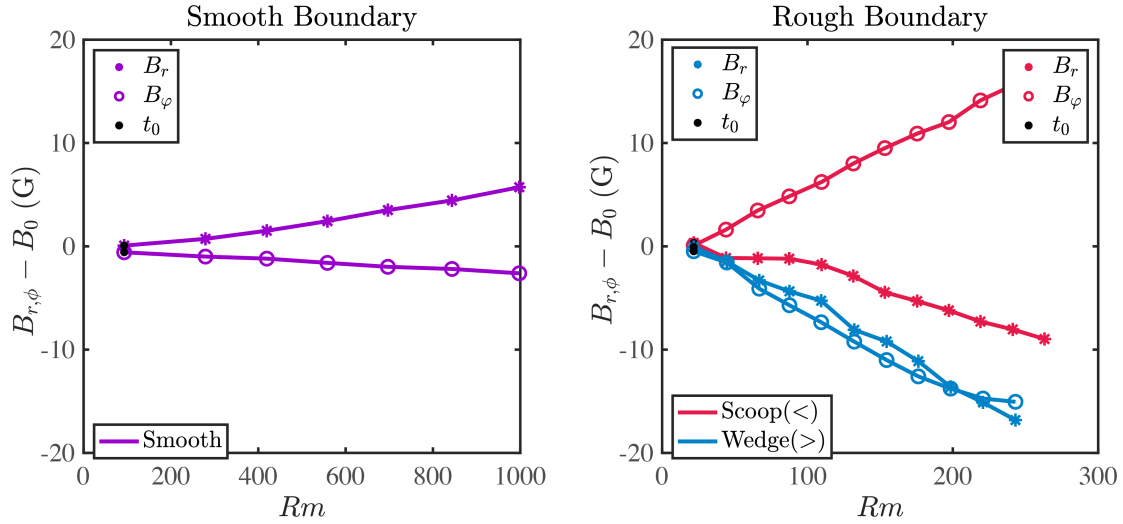


Figure 5.14: Magnetic field amplification at the maximum torque regime (smooth $Ro^{-1} = 0.055$, rough $Ro^{-1} = 0.21$) as a function of the magnetic Reynolds number for one pair of Hall probes in Port B of the experiment (see Section 5.1) in the cylindrical radial direction (B_r) and in the azimuthal direction (B_ϕ) for the two types of boundaries and their respective modes (scoop[<] and wedge[>]). A constant external dipolar magnetic field of 20 G in the center of the experiment was present during all the runs.

For the Smooth boundary case we can see that the amplitude of the amplified signal grows almost linearly as a function of magnetic Reynolds number, with the radial component higher than the azimuthal one. For this Rossby number the amplitude in the radial component is the highest among all the parameter space, which we know is necessary for the dynamo action. However, we do not see a clear bifurcation for this plot.

For the rough boundary we see intensities and directions of the amplification that are consistent with those of Figure 5.11. Both modes have azimuthal amplification of a similar order but in opposite directions as expected. The radial field is negative towards the axis of the experiment, contrary to the smooth case. We want to stress the fact that the maximum Reynolds number for the rough boundary case is $Rm = 220$ which is almost four times lower than the smooth case $Rm = 950$, however the amplifications observed are of the order of 18 G which is more than double of the 8 G observed for the smooth case. We can compare these results with

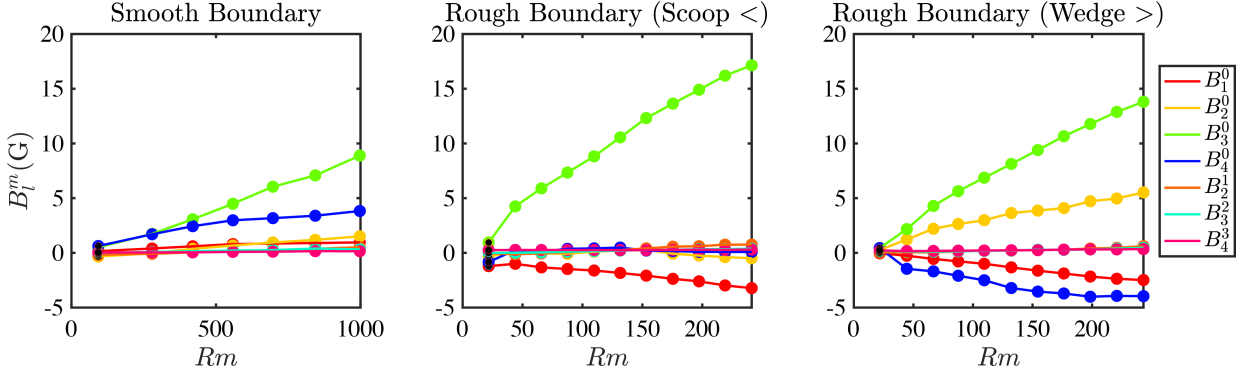


Figure 5.15: Magnetic field amplification at the maximum torque regime as a function of the magnetic Reynolds number for the 31 Hall probes array in the spherical radial direction (see Section 5.1) in the form $B_l^m = l(l + 1)g_l^m$ (where g_j^m are the Gauss coefficients of the spherical harmonics decomposition) for the two types of boundaries and their respective modes (scoop[<] and wedge[>]). A constant external dipolar magnetic field of 20 G in the center of the experiment was present during all the runs.

the Madison Dynamo Experiment [74] where the maximum value measured in the axisymmetric modes was around 20 G for a 50 G transverse field applied. In our new experiment, we are getting modes of the same order as the applied field. Despite the significant increment in the intensity of the induced field, we do not see a clear change in the slope of the curves that could indicate a transition to dynamo action. At least in this range of parameters. We believe that three scenarios are possible: (1) the transition to dynamo is at higher magnetic Reynolds number than the one that our motors can provide; (2) the transition to dynamo takes place at a much lower Rm that we are not sampling with enough precision, for the Riga ([88] and the VKS2 ([42]) experiments, the threshold for dynamo was between 30 to 40 magnetic Reynolds number ; (3) the applied magnetic field is affecting the criticality of the dynamo transition and maybe acting against the dynamo generation. We have performed a few runs to test this hypothesis that we will discuss at the end of this section.

In Figure 5.15 we can see the Gauss decomposition of the magnetic field in the Hall

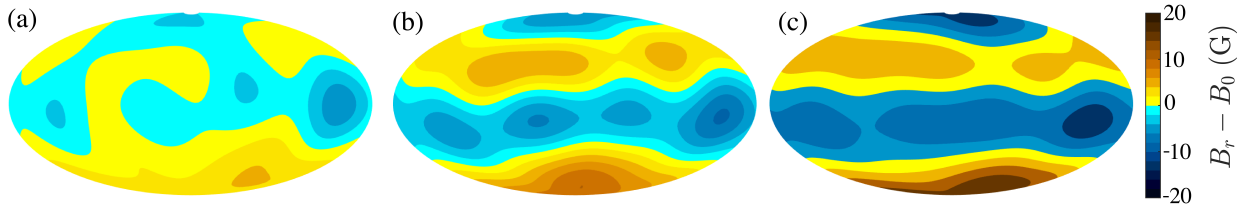


Figure 5.16: Hammer-Aitoff projection of the spherical radial magnetic field measured by the 31 Hall probe array for the Rough wedge mode in Figure 5.11 (right) for three parameter space points: (a) $Rm = 50$; (b) $Rm = 120$ and (c) $Rm = 220$.

probe array of the same runs in Figure 5.14 for the maximum torque regime. The properties are similar to the ones studied for the Rossby number dependence. We can see a dominant B_3^0 mode through all the regimes. This mode is more intense for the scoop configuration. We observe more intense magnetic modes other than B_3^0 for the wedge configuration which is consistent with the Rossby ramps in Figure 5.12. Snapshots of the Hammer-Aitoff projection of all the spherical harmonic modes for the wedge configuration can be observed in Figure 5.16, where we can see the formation of the dominant B_3^0 mode and its clear dependence on the Reynolds number.

If we compare Figure 5.16 (c) with Figure 5.13 (b) we can see that the region of negative magnetic field below the equator in Figure 5.16 (c) is wider than the one in Figure 5.13 (b). These two plots correspond to the same parameter space but one is in the scoop mode and the other one in the wedge mode. This difference is due to the presence of spherical harmonic modes with even order l like B_2^0 and B_4^0 for the wedge mode that cause this asymmetry across the equatorial plane. It can be pictured as if the even modes are pushing the B_3^0 mode out of the equator. Even though these are snapshots for a particular time, the same behavior was observed throughout the run. This is an evidence of the difference in the topology generated by this asymmetric baffles configuration as predicted by the 40-cm water experiment [78].

To finish this section we can evaluate the magnetic field amplification, not as a function of

dimensionless groups like Re or Ro , but instead as a function of more "practical" units that could be better used to analyze the engineering aspects of the experiment. Let us take a look at the amplified external and internal fields but as a function of the kilowatts supplied by the motors. We understand that in general the power is proportional to the cube of the Reynolds number: $P \sim Re^3$. We also know that in a stationary state, there is a balance between the torque in both motors (inner and outer) so the total power in the flow is:

$$\begin{aligned} P_{\text{tot}} &= P_{\text{inn}} + P_{\text{out}} \\ &= \Omega_i \langle \tau_i \rangle + \Omega_o \langle \tau_o \rangle. \end{aligned}$$

But if the torques are in balance, then $\langle \tau_i \rangle = -\langle \tau_o \rangle$ and so we have

$$\begin{aligned} P_{\text{tot}} &= \Omega_i \langle \tau_i \rangle - \Omega_o \langle \tau_i \rangle \\ &= \langle \tau_i \rangle (\Omega_i - \Omega_o) \\ &= \langle \tau_i \rangle \Omega_o Ro. \end{aligned}$$

In Figure 5.17 you can see the magnetic fields both internally and externally amplified. The internally generated was chosen to be the probe in the cylindrical radial direction, and the externally generated is the amplitude of the strongest mode observed during the run, in this case B_3^0 . The rough inner sphere runs are limited by the torque in the inner motor, so that value observed is the highest power that the motor can supply for that particular Rossby Number. This value is 4 times smaller than the corresponding power for the smooth case. However, the amplitude of the fields is almost two times higher. This is evidence of the effect that the baffles

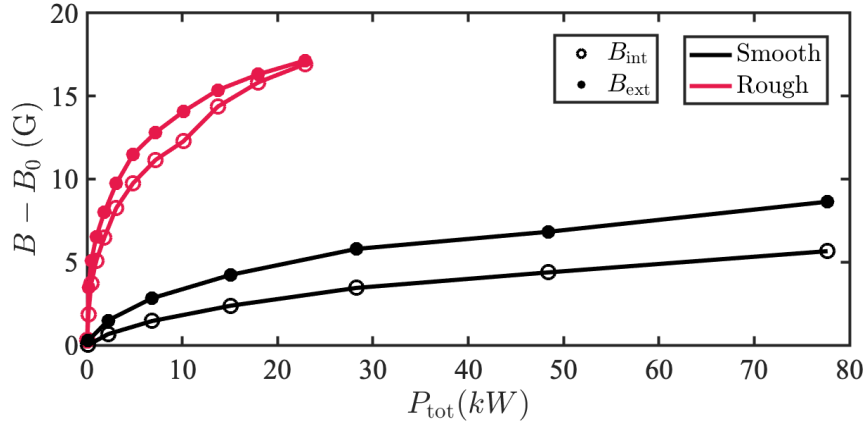


Figure 5.17: Magnetic field generation at the experiment probes as a function of the balanced power in the inner motor in kilowatts at the maximum torque state for a 20 G externally applied magnetic field. The power limit in each motor is 260kW at 1800 rpm. The absolute upper bound on the mechanical power input of the 3-m experiment is 320 kW based on the motor torque and the allowable boundary speed [14].

have in conveying the energy into flows that are capable of amplifying the fields more effectively.

5.2.3 Time-dependent dynamics

We will now proceed to analyze the time dependent dynamics of the amplified fields. This can help provide an insight on the nature of the amplification generated by the flow. We will focus on the comparison with and without baffles, as this is the novel contribution of the present doctoral dissertation, as we did for the main field amplifications. However, whenever the author considers it interesting for the sake of the discussion, we will drift towards other comparison parameters, like Rossby number or applied magnetic field.

5.2.3.1 Power Spectra

We will start the discussion in this section with the power spectral decomposition, and we will focus our attention on the internal probes. These, being in (almost) direct contact with the

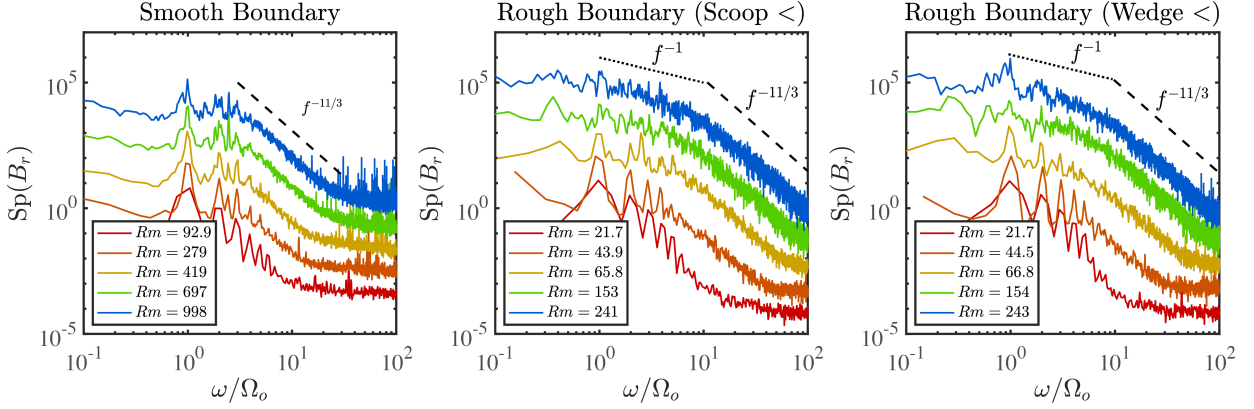


Figure 5.18: Power Spectrum of the internal probe magnetic field signal in the cylindrical radial direction (B_r) at the maximum torque regime (smooth $Ro^{-1} = 0.055$, rough $Ro^{-1} = 0.21$) as a function of the magnetic Reynolds number for the two types of boundaries and their respective modes (scoop[<] and wedge[>]). Dashed lines indicate power laws for comparison. The frequencies are normalized by the outer sphere angular frequency and shifted one decade away with each different Reynolds number. A constant external dipolar magnetic field of 20 G in the center of the experiment was present during all the runs.

sodium, give rise to the richest dynamics because they can depict smaller scales than the probes located on the outside. Let us start with the magnetic Reynolds number dependence for the same runs as in Figures 5.14 and 5.15.

In Figure 5.18 we can see the Power Spectrum Decomposition of the internal probe magnetic field signal in the cylindrical radial direction (B_r) at the maximum torque regime as a function of the magnetic Reynolds number for the two types of boundaries and their respective modes as discussed previously. We can see that rough boundary modes show a higher amplitude than the smooth case for most of the spectrum frequencies. The dissipative scale is not visible for either of the experiments but the inertial range extends towards higher amplitudes with baffles, before the electrical noise signal starts appearing in the graph (for $\omega/2\pi > 60\text{Hz}$). For low magnetic Reynolds numbers the curves are more similar to each other, indicating that the effect of the pressure-dominated boundary layer is more relevant for higher magnetic Reynolds numbers as

expected from [62, 63, 78]. We also observe some low frequency oscillations than get buried for increasing magnetic Reynolds numbers, these frequencies are harmonics of the outer sphere frequency as expected and observed previously [3, 4, 13, 44].

We now discuss the power law regimes for the different configurations. A power law of $f^{-11/3}$ is expected under the Taylor hypothesis [73, 90] which indicates that the turbulence is develop enough that there is a correlation between the spatial and the temporal spectrum, meaning that the power laws scale with same exponent. In other words, it says that the turbulent eddies are frozen in space as they are advected past the sensor, in this case the magnetic probe. Additionally we have to understand the -11/3 exponent. As explained in more details in section 2.3.5, for $k_0 < k < k_\sigma$ the magnetic field lines are advected by the Kolmogorov turbulence giving an energy spectrum that scale in the same way as the kinematic spectrum: $E_m(k) \propto k^{-5/3}$. However, when $k_\sigma < k$, this regime is called the resistive dissipation range, and the magnetic field lines are additionally diffused to smaller scales due to magnetic diffusivity, adding and extra k^{-2} to the power law, hence the magnetic energy spectrum: $E_m(k) \propto k^{-11/3}$.

Going back to Figure 5.18, we notice a power law close to -11/3 for both smooth and rough inner sphere boundaries. For the rough boundary in particular, we see a clearer transition to a steeper slope for $Rm > 44$. For these magnetic Reynolds numbers all the curves seem to converge to the same shape. According to Moffatt [73], we would expect a break in the spectrum, or a so-called knee [74], that indicates the location of the dissipation scale k_σ . We do not think that we have the resolution of the data good enough to accurately locate this breaking in the spectrum; however, this is not due to instrumentation but instead due to a shortage in the duration of these runs in particular. Longer runs are advised for future graduate students to better resolve the dissipation scale. Nevertheless, we could leave the discussion without providing an estimate

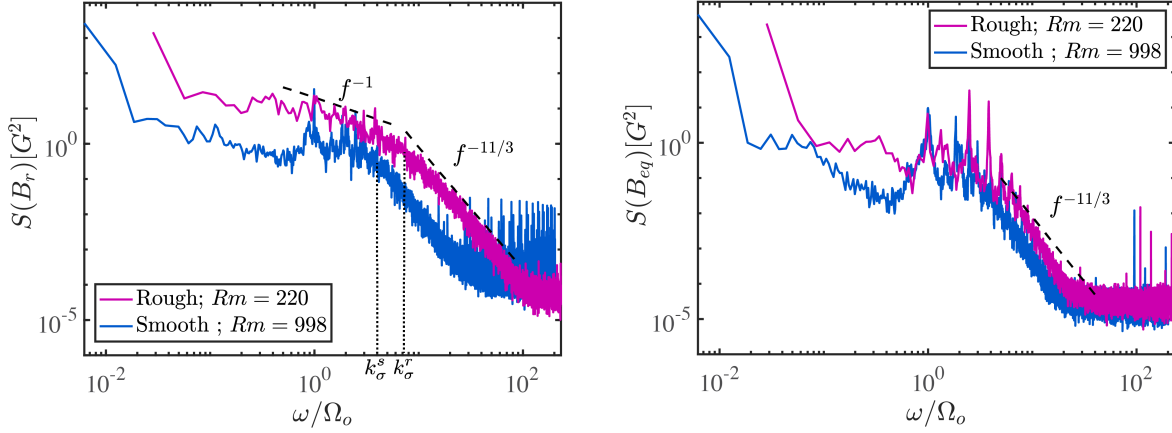


Figure 5.19: Power Spectrum of the internal magnetic field probe signal in the cylindrical radial direction (left) at the maximum torque regime versus the power spectrum of an external probe located at the equator (right), for different baffle configurations. Dashed lines indicate power laws for comparison. The frequencies are normalized by the outer sphere angular frequency. A constant external dipolar magnetic field of 20 G in the center of the experiment was present during all the runs.

for k_σ .

In Figure 5.19, we can see the same plots as in Figure 5.18 but we have only plotted the maximum Reynolds number run for smooth and rough scoop baffles for the internal probes together for comparison, and additionally, for an external probe located at the equator. We notice a steeper slope, indicating a power law with exponent greater than $-11/3$ due to the shielding on the stainless steel vessel, as reported previously by Nornberg et al. [74], Kelley [91]. For the internal probes, we can estimate a power law closer to f^{-1} instead of the $f^{-5/3}$ shown in Figure 5.18 (center) for comparison. This exponent of -1 was reported as well in the VKS experiment and was interpreted as $1/f$ noise due to the presence of several characteristic time scales in the flow [75]. However it was not observed in the Madison experiment [74]. We would like to advise again longer runs for future experiments. Finally, from the spectrum of the internal probe, we could propose an estimate of the dissipative resistive scale for every type of boundary. For the

smooth case have $k_\sigma^s \sim 3\Omega_o(\text{m}^{-1})$ and for the rough boundary (scoop in this case) we have $k_\sigma^r \sim 6\Omega_o(\text{m}^{-1})$. Multiplying by their respective outer sphere angular frequencies and using the relationship $k = 2\pi/\ell$ we obtain the resistive dissipation scales as

$$k_\sigma^s \sim 11 \text{ m}^{-1}, \quad k_\sigma^r \sim 20 \text{ m}^{-1},$$

where the superscript refers to smooth (s) or rough (r) boundary. This shows that the baffles effectively reduce the resistive dissipative scale (because $k \sim 1/\ell$). The dissipative scale with rough boundary are similar to the ones obtained in the Madison experiment which has impellers.

The Rossby number dependence of the Power Spectrum can reveal the presence of different hydrodynamics states in a similar way it was done for water in the 3-m experiment in Zimmerman et al. [4] Figure 4. In Figure 5.20 we can see different power spectrum for a coarse run in Rossby numbers at both sides of the origin: for counter and corotating spheres. The present of different states is evident. For negative Rossby numbers there is a clear transition in the dynamics of the systems for $Ro^{-1} \sim -0.198$ which coincides with the maximum torque peak. The states before the peak (so for $Ro^{-1} > -0.198$, below the green line in the left plot of Figure 5.20) have a less pronounce slope and have less oscillations between 10 and 100 $\omega\Omega_o$. There is only one clear peak at the frequency of the outer sphere, which is expected for a rotating system. For Rossby numbers after the peak ($Ro^{-1} < -0.198$) the slope is steeper and it is actually closer to the -11/3 predicted by Moffatt [73]. These states have broader peaks at the rotation frequency of the outer sphere, with possibly some harmonics present at higher frequencies.

For positive Rossby numbers the picture is very different. The modes show much more activity for frequencies lower than the outer sphere rotation rate. These types of modes, with

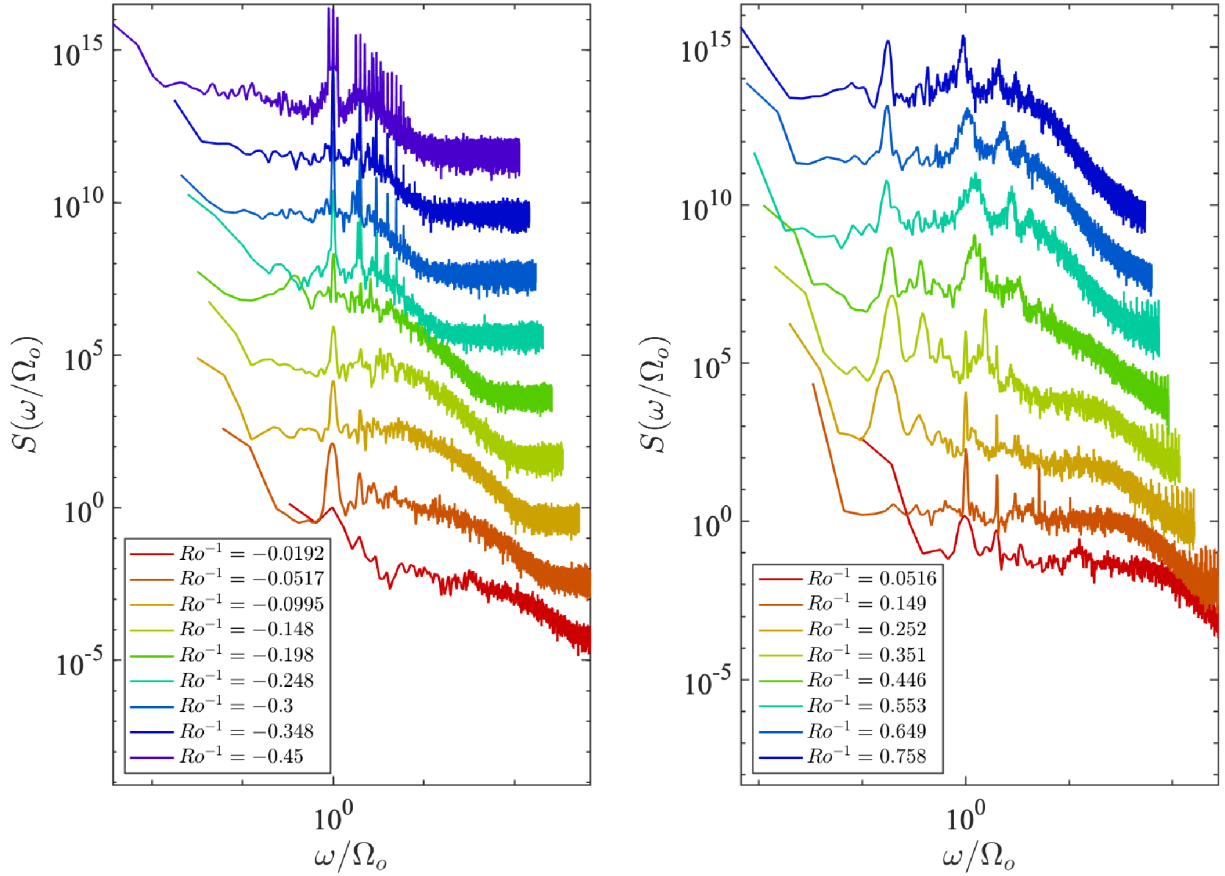


Figure 5.20: Power Spectrum of the internal probe magnetic field signal in the cylindrical radial direction (B_r) for the Scoop Mode of the rough inner sphere in their respective modes with corotating and counter-rotating regimes for different Rossby numbers. The frequencies are normalized by the outer sphere angular frequency and shifted one decade away with each different Rossby number. A constant external dipolar magnetic field of 20 G in the center of the experiment was present during the runs with positive Rossby number.

frequencies approximately $0.12\Omega_o$ are known as cylindrical modes, and have been found repeatedly in spherical Couette simulations and experiments (See for instance Wicht [11]). This cylindrical mode is known to have a strong $m = 1$ component as we observed for the Gauss decomposition of these spectra (not shown here). There is also a transitional state for $Ro^{-1} \sim 0.35$ which coincides with the minimum relative torque in Figure 3.8. There is also a broader peak for the Ω_o angular frequency for $Ro^{-1} > 0.35$ with also some stronger harmonics. The slope is also steeper for these Rossby numbers with values again closer to $-11/3$.

For comparison with the Wedge Mode, we show in Figure 5.21 the power spectrum of very similar runs as the one performed for the Scoop mode in Figure 5.20. The differences are not striking. We could argue that there seem to be stronger subharmonics of the Ω_o peak for the top three curves for both $Ro^{-1} < 0$ and $Ro^{-1} > 0$. This might suggest the presence of more modes as shown in the mean spherical harmonic plots of the external field array in Figures 5.15 and 5.15.

The previous plots were performed in a parameter space in which there was not equivalent data for the smooth inner sphere case. In particular in the absence of an applied external field. However, with a weak applied field there are runs with a fine ramp around the respective torque peaks that show more accurately the transition of state before and after the peak. This is shown in Figure 5.22. The most important feature of these plots is that the transition of states is more clear for rough than for smooth boundary. It can be seen in the gap between yellow and green plots, which is wider for rough boundary. Considering the results from the water experiment, and how this transition is probably related to the development of a full meridional recirculation, these results speaks of how the baffle have, presumably, increased the strength of the flows in this regime making the change of state more evident in the radial amplification of the fields capture

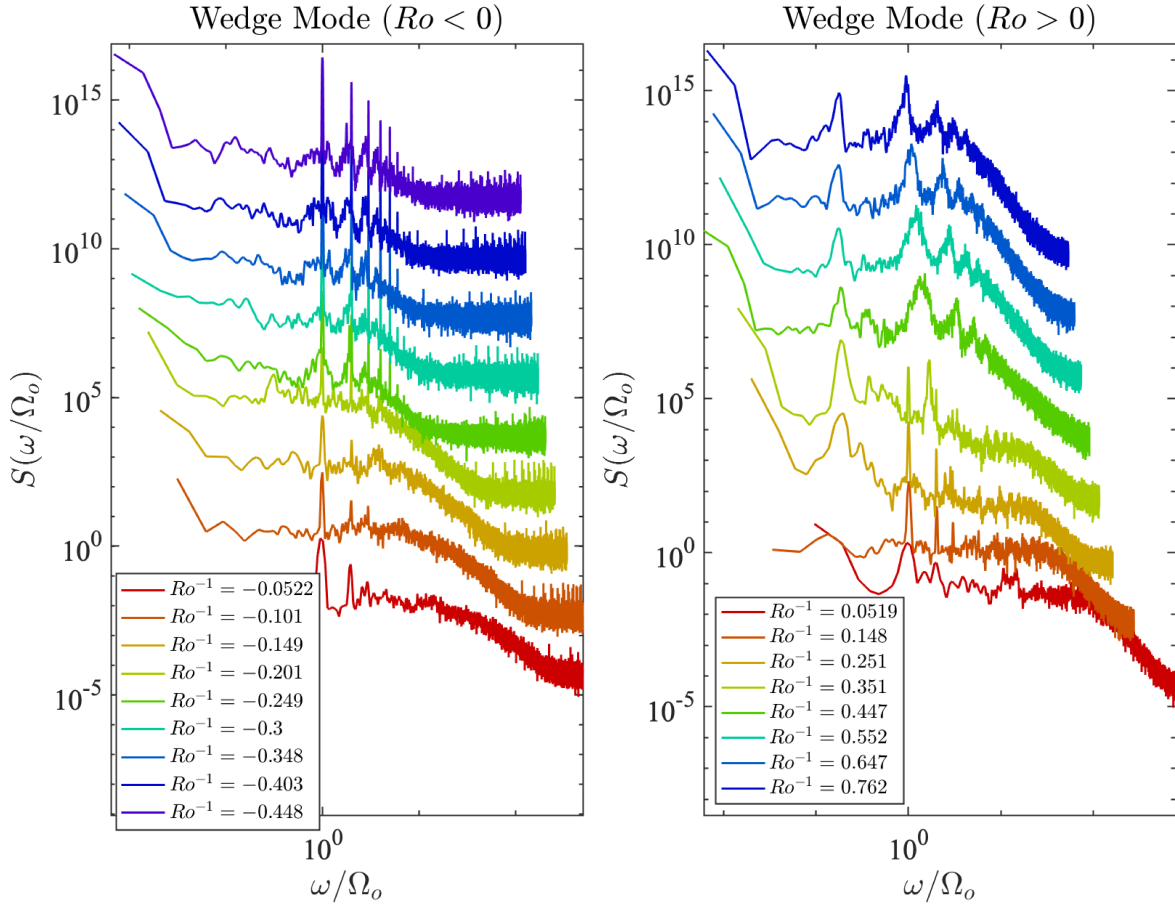


Figure 5.21: Power Spectrum of the internal probe magnetic field signal in the cylindrical radial direction (B_r) for the Wedge Mode of the rough inner sphere with corotating and counterrotating regimes for different Rossby numbers. The frequencies are normalized by the outer sphere angular frequency and shifted one decade away with each different Rossby number. A constant external dipolar magnetic field of 20 G in the center of the experiment was present during the runs with a positive Rossby number.

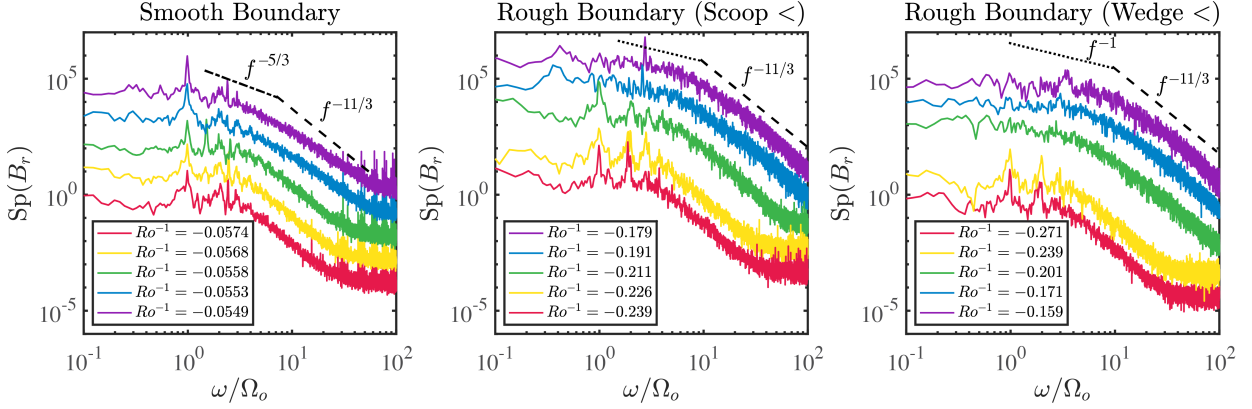


Figure 5.22: Power Spectrum of the internal probe magnetic field signal in the cylindrical radial direction (B_r) around the maximum torque regime (smooth $Ro^{-1} = 0.055$, rough $Ro^{-1} = 0.21$) for a constant magnetic Reynolds number ($Rm \sim 950$ for Smooth and $Rm \sim 220$ for Rough) for the two types of boundaries and their respective modes (scoop[<] and wedge[>]). Dashed lines indicate power laws for comparison. The frequencies are normalized by the outer sphere angular frequency and shifted one decade away with each different Reynolds number. A constant external dipolar magnetic field of 20 G in the center of the experiment was present during all the runs.

by our internal probes.

5.2.3.2 Probability Distributions

Another conventional time dependent analysis performed in turbulent flows is the probability distribution of the data. Let us start with comparing the effect of baffles in the shape on the distribution. We are going to focus on the runs of Figure 5.12 for an applied external magnetic field. The results in this section are very preliminary but we believe there is potential for a deeper study of the magnetohydrodynamics around the maximum torque regime (named optimal transport in some Taylor Couette references [92, 93]).

The Figure 5.23 we can see the normalize Probability Distribution Function (PDF) for different Rossby numbers in the smooth, rough scoop and wedge mode of the 3-m experiment. The results shown are for the internal radial probe, although similar behavior can be observed

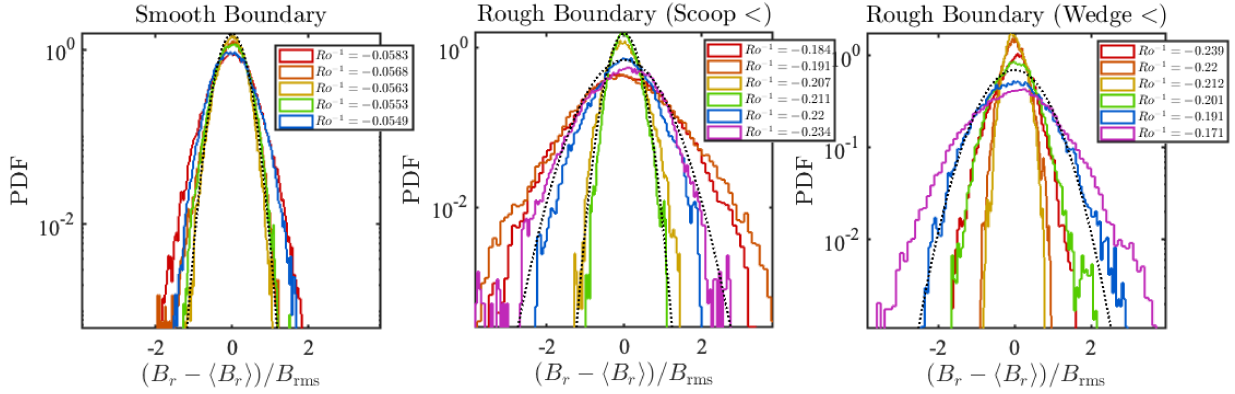


Figure 5.23: Probability distribution function for the internal probe in the cylindrical radial direction for different Rossby numbers around the maximum torque regime for smooth and rough inner sphere in their two modes runs of Figure 5.12 with an externally applied field of $20G$. Dotted lines indicate Gaussian to guide the eye.

for the other probes. The main point we want to address in these figures is the transition for states before and after the torque peak that can be clearly seen in the plots. It is less evident in the smooth boundary case but this is because the standard deviation of the data is less than in the rough boundary case, which is also a remarkable effect of the baffles in the dynamics of the flows. Another important observation is that the standard deviation decreases significantly for values at the peak. In other words, the distributions are much wider for values outside the maximum torque peak indicating the presence of transient behavior of the order of the flow evolution. Gaussians have been plotted to these curves for comparison. There seem to be some small deviations from Gaussians in the tails and some skewness.

In Figure 5.24 we can see the standard deviation for runs around the maximum torque regime as a function of the deviation from the maximum torque peak Rossby number and as a function of the magnetic Reynolds number. One characteristic of the transition to dynamo action reported in Monchaux et al. [75] was the fluctuations of the magnetic field as a function of the Reynolds number. They are expected to jump right at the transition. In Figure 5.24 we tried

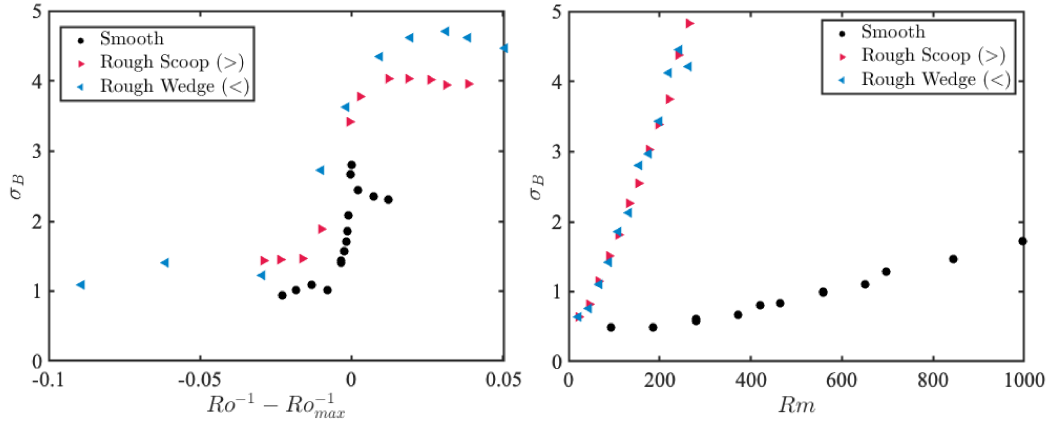


Figure 5.24: Standard deviation from the mean for the internal magnetic field probe in the cylindrical radial direction as a function of the centered Rossby number (left) around the maximum torque regime and as a function of the magnetic Reynolds number (right).

to evaluate this fluctuation for the maximum torque regime without success. Even though the fluctuations increase significantly with baffles, and that we can see the clear change of state after and before the torque peak, the transition for magnetic Reynolds number is not evident from the plots. We believe that we are either before the transition, or we are past the transition, but with the applied field we might be saturating the dynamo state. If there is a transition for lower magnetic Reynolds, it takes place at values below $Rm = 150$ and the resulting geometry of the dynamo is not clear. However, looking at the bright side, we still believe that the increment in the fluctuations is a relevant feature for getting us closer to dynamo action, and it is a clear result of the baffles addition.

In the absence of an applied field, the dynamics around the maximum torque regime are similar in terms of the existence of the transition before and after the peak. However, as we can see in Figure 5.25, the distributions are no longer Gaussian, showing some strong skewness for the radial direction, and even some kurtosis for the azimuthal direction probe. We must mention that these changes are stronger for more negative Rossby numbers than the values for Figure

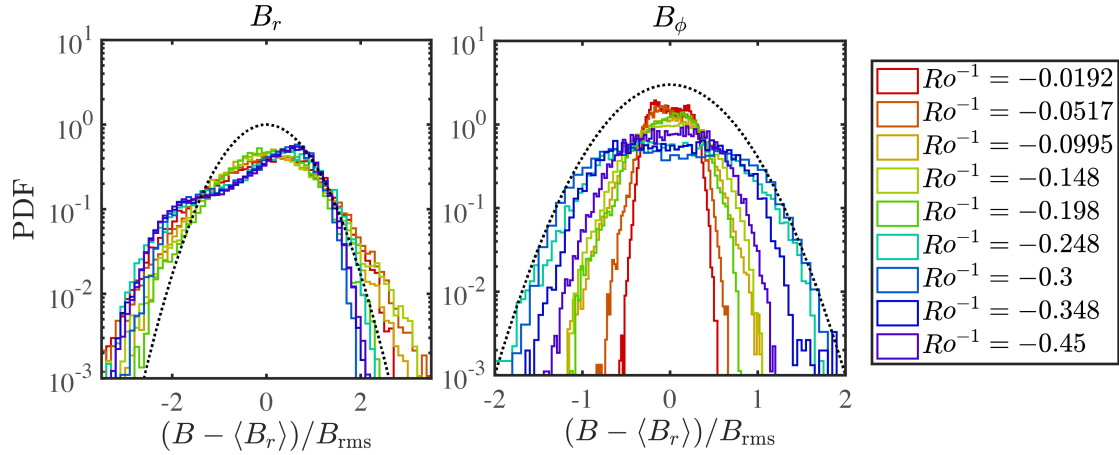


Figure 5.25: Probability distribution function for the internal probe in the cylindrical radial and azimuthal direction for different Rossby numbers around the maximum torque regime for the rough inner sphere in the scoop mode if the runs in Figure 5.9 with no external field applied . Dotted lines indicate Gaussians to guide the eye.

5.23, so we are entering in Inertial Modes territory (see for instance [13]). This could imply the presence of modes that will cause oscillation of the flows between different values, which could explain the shape of the distributions. However, the suppressing effect of the magnetic field could be a reason for the closer to Gaussian behavior of the distributions.

Chapter 6: Conclusions and Recommendations

6.1 Conclusions

We present results on torque scaling and velocimetry of spherical Couette flows with rough boundaries in a hydrodynamics experiment of 40 cm in diameter and compare them with previous work done for smooth boundaries. For roughening the inner sphere boundary we studied four designs of baffles: smooth (no baffles), straight, chevron and alpha baffles (Fig. 3.2) with 5% and 10% of radius height.

We observed different power laws in the dimensionless torque as a function of the Reynolds number (Fig. 3.6) for these different configurations and identified a difference in the torque for counter-clockwise and clockwise rotation of the inner sphere with chevron and alpha baffles due to their asymmetry. Additionally, the torque increases with increased baffle height for three different heights (including smooth case), and it shows a linear dependence rather than a quadratic one, as was reported for Taylor-Couette flows [63].

For the Rossby dependence of the torque, we observed a significant increase in the normalized differential torque when adding baffles, which indicates an increase in the angular momentum transport (Fig. 3.8). The location of the maximum torque peak also changes, not only with the baffle height but also when comparing wedge mode with scoop mode in the case of chevron and alpha baffles. This is evidence of the change in the dynamics of the flows for these two modes.

Velocimetry in the equatorial plane (Fig. 3.9) shows a fully extended equatorial jet that reaches the outer boundary when the torque reaches its maximum relative value. This location in the parameter space matches the equatorial jet instability observed by Wicht [11]. In this region, the azimuthal velocity is at its minimum value throughout all the Rossby numbers measured. This region of maximum normalized torque seems to be a good candidate for the generation of dynamo action in the 3-m experiment, since it has shown maximum radial amplification of the applied magnetic field [4].

Velocimetry measurements of the meridional section at this maximum torque Rossby number showed a significant amplification of the poloidal flows and these results are in agreement with previous equatorial velocimetry measurements (Fig. 3.11 and Fig. 3.12). A difference in the topology of the flows generated was observed in both the equatorial and meridional sections.

We developed a safe and efficient method to transfer 12 tons of liquid sodium from a spherical Couette flow experiment in a single day operation. The procedure was applied twice, for draining and refilling the experiment, showing its effectiveness. Difficulties found along the way were overcome with efficiency, patience and especially teamwork. This standard operation procedure could be adapted to similar experiments and containers. We showed that draining, cleaning and fixing an experimental vessel previously filled with sodium is possible. This task was considered nearly impossible by previous members of this lab: "This is because it would be extremely difficult to take the sodium out and perform fixes; once sodium is in place, it will be there for the life of the experiment."

We disassembled, fixed, and assembled back the 3-m experiment including motors, motor frame, electronics and instrumentation. We designed and installed a new bayonet coupler and replaced the bottom inner bearing, the top inner and outer bearings. We also replaced all the lip

seals in the experiment. We installed a new internal finger probe with 2 magnetic Hall probes. We installed asymmetric baffles in the inner sphere following the results from the 40-cm experiment.

Torque measurements in the new baffled 3-m experiment showed consistency with the estimation based on the 40-cm torque results. However, we did not observe an equivalent change in the dependence of the torque as a function of the Rossby number. The water experiment suggested that there would be a significant difference in the location of the maximum torque peak and this was not the case. According to the water experiment, the shift of the location of the maximum torque peak corresponds to baffles higher than 5%. Nevertheless, the values for the amplitude of the torque in this region was consistent with the results of the water experiment.

We were able to extract all the torque available than the inner motor could supply at those rotation speeds, something that was not possible with a smooth sphere, without pushing the safety constraints on the experiment. In terms of power, we were only able to provide only 1/4 with respect to the smooth inner boundary case, which is only 80 kW of the 260 kW available at full speed. Despite this decrease in the power supplied, we were able to generate magnetic fields with around two times more amplitude, both internally and externally.

Initial runs with stationary outer sphere and no applied field were performed. These showed an increment of amplified fields by a factor of 3-4 for the external fields (in the form of Gauss coefficient decomposition) and a factor of two for the internal fields, although no transition to dynamo was evident. For the dependence on the Rossby number, we performed initial runs with no applied field around the maximum torque regime and observed a significant amplification of the external fields, in particular the dipole mode spiked for the maximum torque peak. The $l = 3, m = 0$ mode was dominant around this regions as well. This might indicate the presence of a strong uniform building field, which together with the $l = 2, m = 0$ velocity field, gave rise

to the $l = 3, m = 0$ magnetic field mode.

We performed runs with a weak externally applied magnetic field in the dipole configuration to fix the geometry of the applied field and to go above the level of the ambient field. These runs allowed us to directly compare toruns with the smooth sphere performed mostly in the same parameter space. The results showed a significant amplification of the internal fields in both the azimuthal and radial directions. The amplification reached almost 20 G in both directions which was the same value as the applied field in the center of the experiment. This is around double the amplitude of the field amplified with the smooth sphere but additionally with a magnetic Reynolds number 4 times smaller. However, no transition to dynamo was evident from the results. The amplification seemed to be linear with magnetic Reynolds number, and a transition to dynamo would show a discontinuity in this parameter as reported in previous successful dynamo experiments. The non-linearity in the external magnetic modes might suggest that a transition is close; however, this could also be just due to temperature changes in the bias level of the probes from the extended rotation periods of the outer sphere. The power spectra measurements of the internal fields revealed a $-1\ 1/3$ slope around the maximum torque peak for the rough inner sphere. This value implies the Taylor-Hypothesis can be applied, and it is also the predicted value of the magnetic cascade for highly turbulent flows for the resistive dissipative range. This power law was found in the Madison experiment (which did not yield a dynamo), but it was not found in the VKS experiment (which did yield a dynamo). The power spectra as a function of Rossby number showed a clear transition between states for both wedge and scoop mode of the rough inner sphere. In particular, changes of state take place at the maximum and minimum torque regime, both characterized by a change in the slope in the dissipative range, and additional oscillations and modes for lower frequencies.

Probability distributions also showed a transition between states and a deviation from Gaussian behaviour in the case of no applied external field. The standard deviation, which is a measure of the fluctuations from the mean in the system, show a significant increment in the presence of roughness for the internal probes. This is another positive factor towards dynamo action as shown in previous successful dynamo experiments.

6.2 Recommendations

For the 40-cm experiment we are deeply interested in using the current hardware and software to perform velocimetry in other locations of the parameter space, targeting possibly bistability states, which internal flow patterns are only hypothesized. Additionally, we propose to perform that velocimetry measurements of planes parallel to the equator, at mid and high latitude. This is with the purpose of having better knowledge of the velocity field in the 3-m experiment. In particular, high latitudes are desired since this is where the internal hall probes are located. We could test the change in the shear direction with and without baffles at this particular location.

More runs in different parameter space are suggested for the 3-m experiment. Given the time constraints during the end of this PhD, we could not have another set of runs based on the results of the first one. For instance, a more detailed set of runs in the positive Rossby number region is always interested, although the preliminary runs did not show a significant amplification of the radial and external fields. However, the correlations between torque and magnetic field in Figure 5.4 are interesting enough to propose more runs in this parameters. Another region in the parameter space that must be explored is the inertial mode regime, which is of great interest for the geophysics community. It is located for smooth inner sphere at $Ro^{-1} < -0.5$ but it could

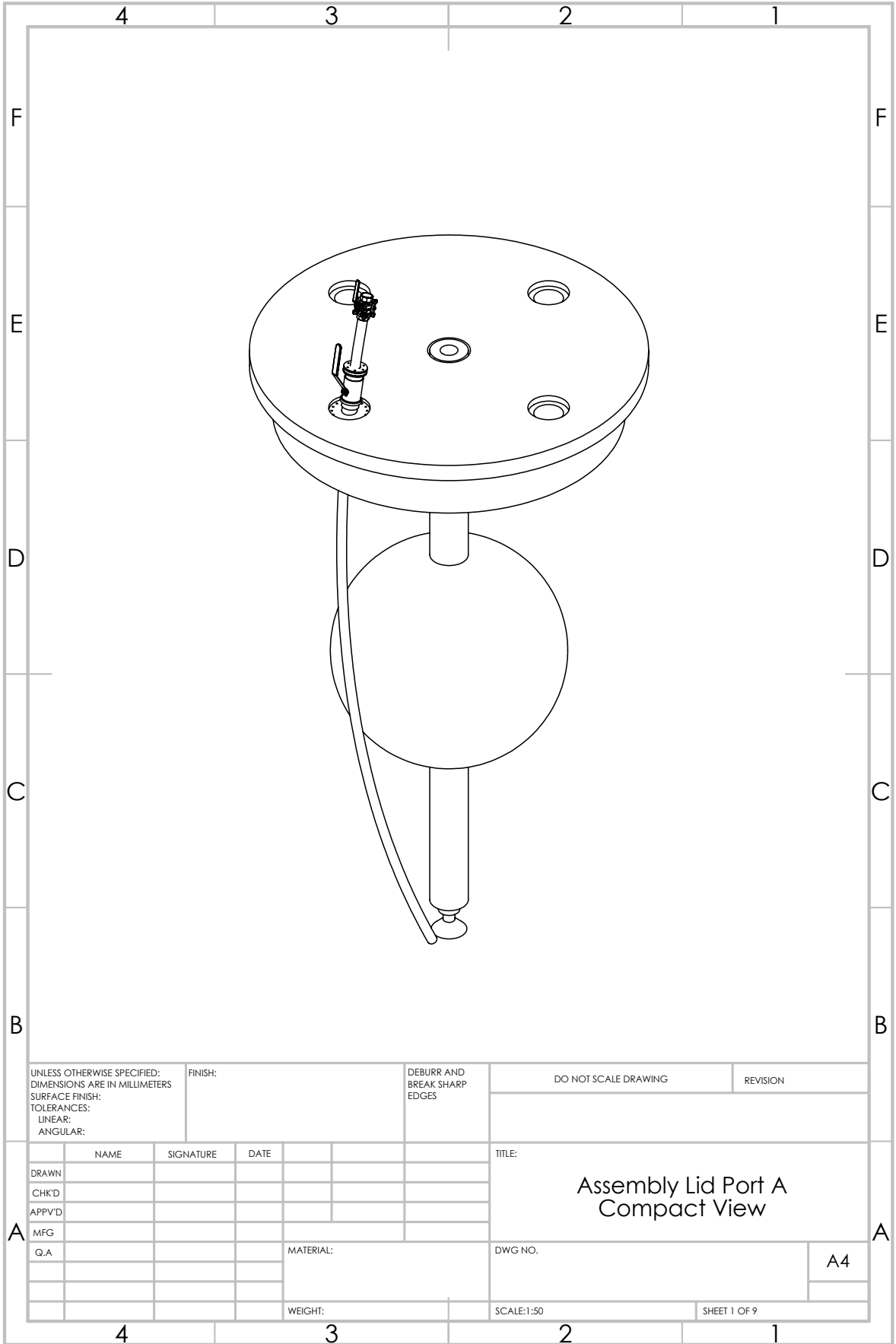
have moved to smaller inverse Rossby numbers in the same way it happened for the maximum torque regime.

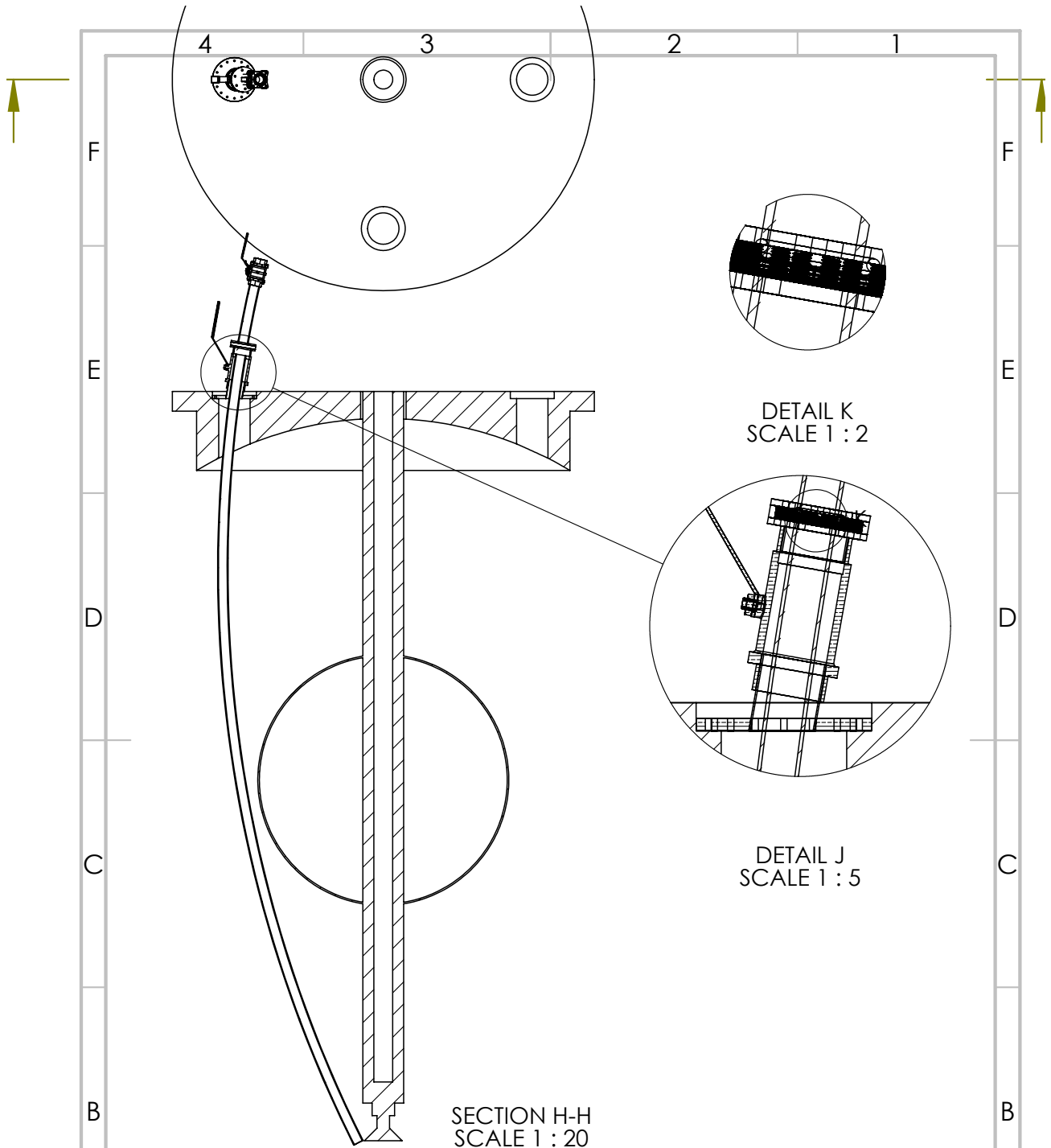
More careful runs to understand the origin of the building field are desired. Additionally, runs to study the effect of temperature fluctuations in the bias value of the voltage in the Hall probes would be of interest. We performed preliminary runs to address this issue but a more detailed analysis of the data is suggested. There are advances in trying to suppress the building field currently taken place, which we considered as an important step in the right direction.

Due to the torque saturation for the inner motor, we suggest that a gearbox be installed. A possibility discussed with Nolan Ballew would be to install a set of gears and belts on the inner motor frame to connect to the shaft. This will require to possibly change the inner motor frame, so this is not a minor step in the research and it could take at least a year of planning, installation, and testing. However, given the significant increment in the magnetic field amplification that we obtained with baffles, which we believe is evidence of the improvement of the flows topology towards dynamo action, exploring higher magnetic Reynolds numbers is an obvious future step.

Appendix A: Mechanical Drawings

We present the mechanical drawings for: the dip tube assembly, the baffles assembly, the bayonet coupler, the new internal finger probe holder and the storage tank (provided by Central Fabricators Inc.).





SECTION H-H
SCALE 1 : 20

DETAIL K
SCALE 1 : 2

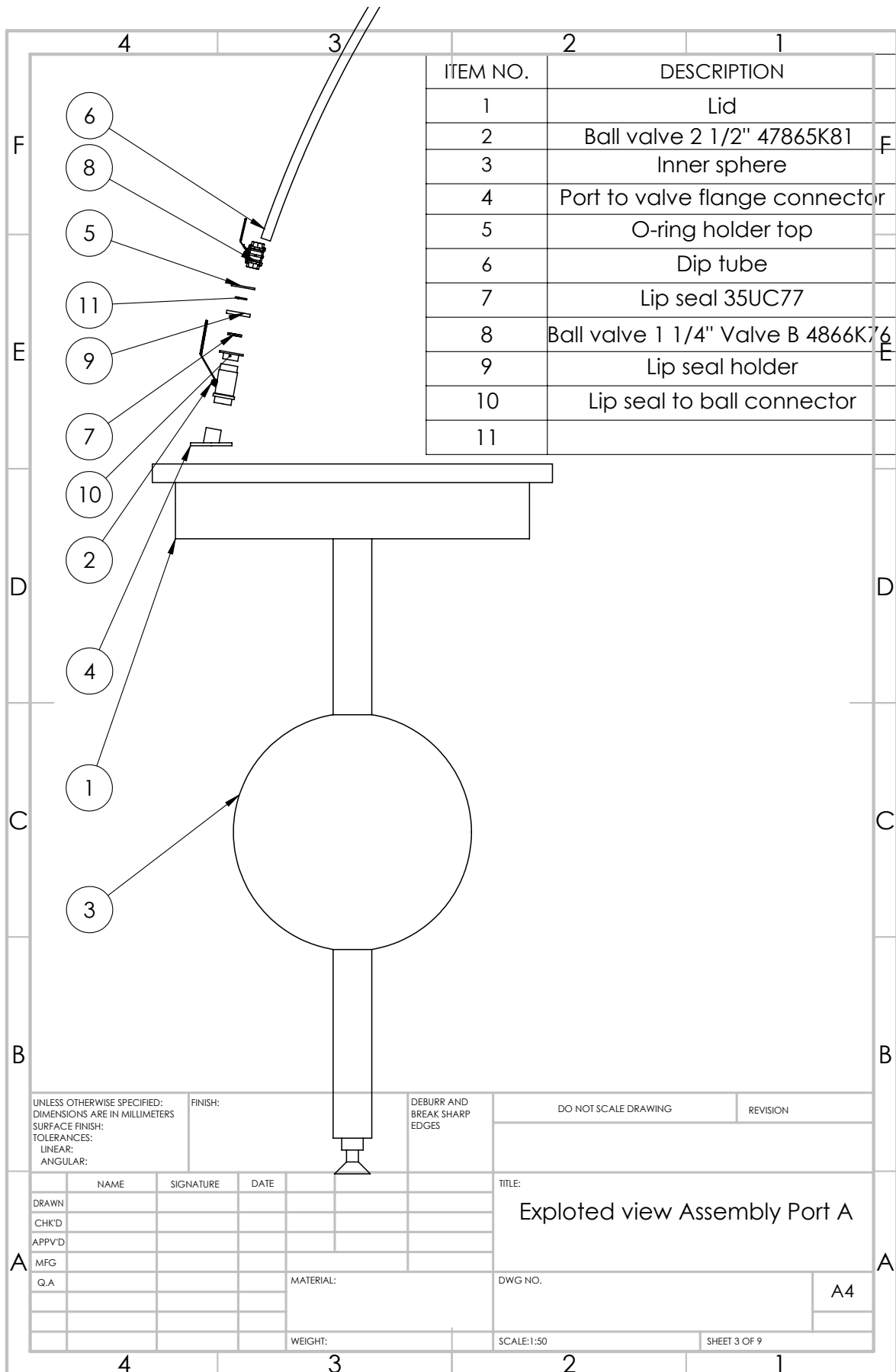
DETAIL J
SCALE 1 : 5

| | | | | | | |
|---|--|---------|------------------------------------|-------------|----------------------|--------------|
| UNLESS OTHERWISE SPECIFIED: DIMENSIONS ARE IN MILLIMETERS SURFACE FINISH: TOLERANCES: LINEAR: ANGULAR: | | FINISH: | DEBURR AND BREAK SHARP EDGES | | DO NOT SCALE DRAWING | REVISION |
| DRAWN | | NAME | | SIGNATURE | | DATE |
| CHK'D | | | | | | |
| APPV'D | | | | | | |
| MFG | | | | | | |
| Q.A | | | | MATERIAL: | | |
| | | | | WEIGHT: | | |
| | | | | SCALE: 1:50 | | SHEET 2 OF 9 |

TITLE:
Section Cut Assembly

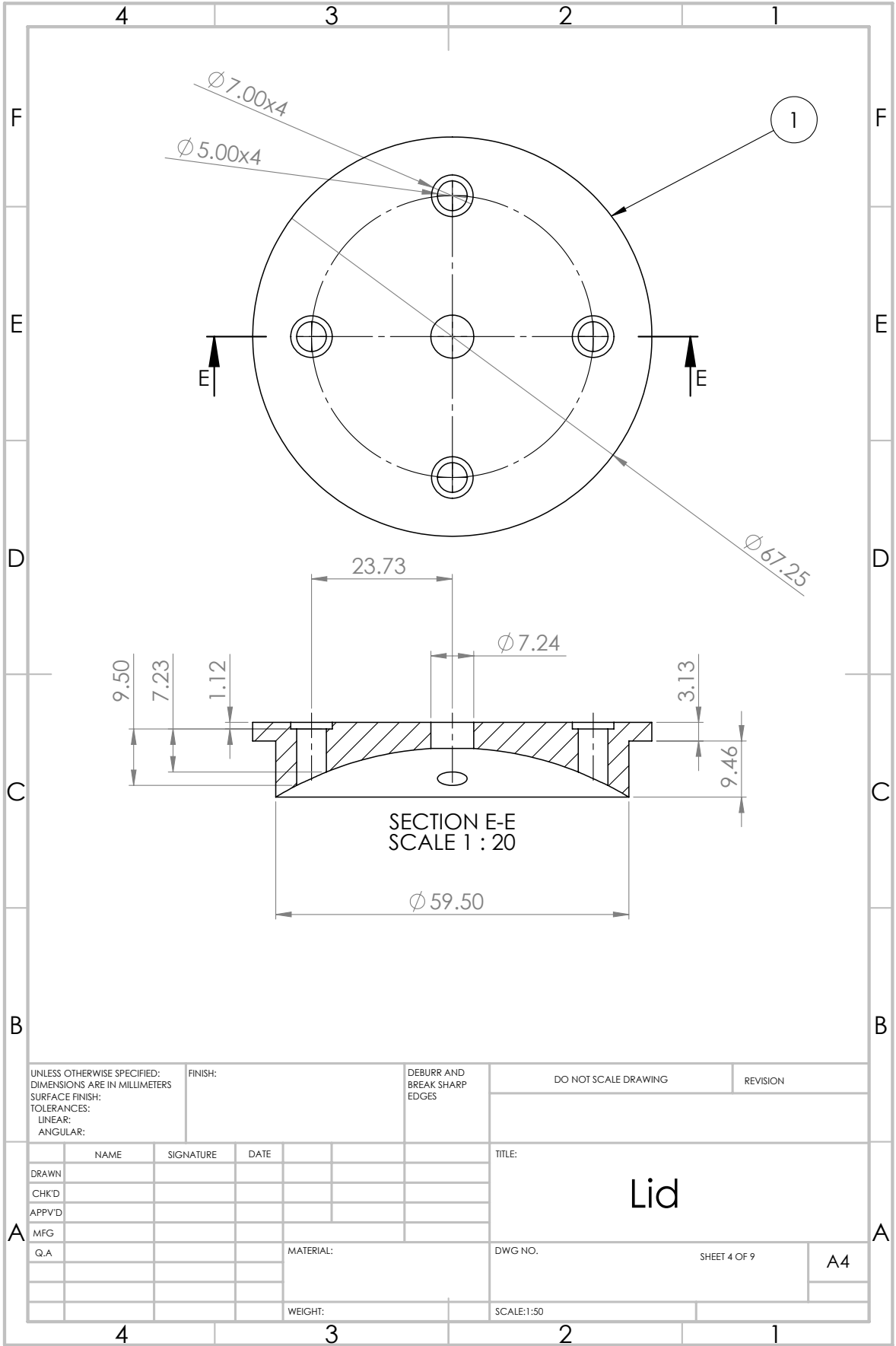
DWG NO.

A4

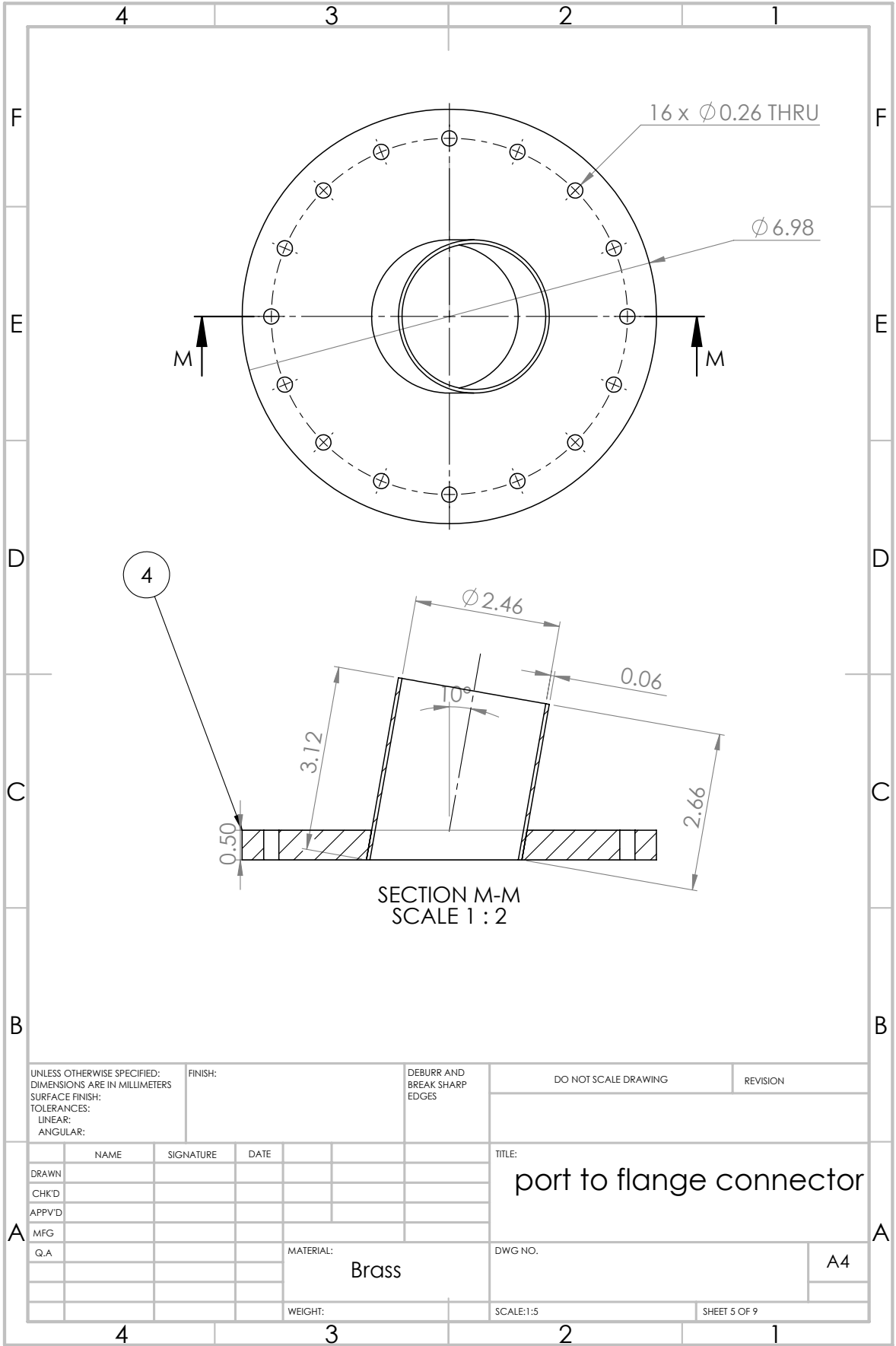


| ITEM NO. | DESCRIPTION |
|----------|-----------------------------------|
| 1 | Lid |
| 2 | Ball valve 2 1/2" 47865K81 |
| 3 | Inner sphere |
| 4 | Port to valve flange connector |
| 5 | O-ring holder top |
| 6 | Dip tube |
| 7 | Lip seal 35UC77 |
| 8 | Ball valve 1 1/4" Valve B 4866K76 |
| 9 | Lip seal holder |
| 10 | Lip seal to ball connector |
| 11 | |

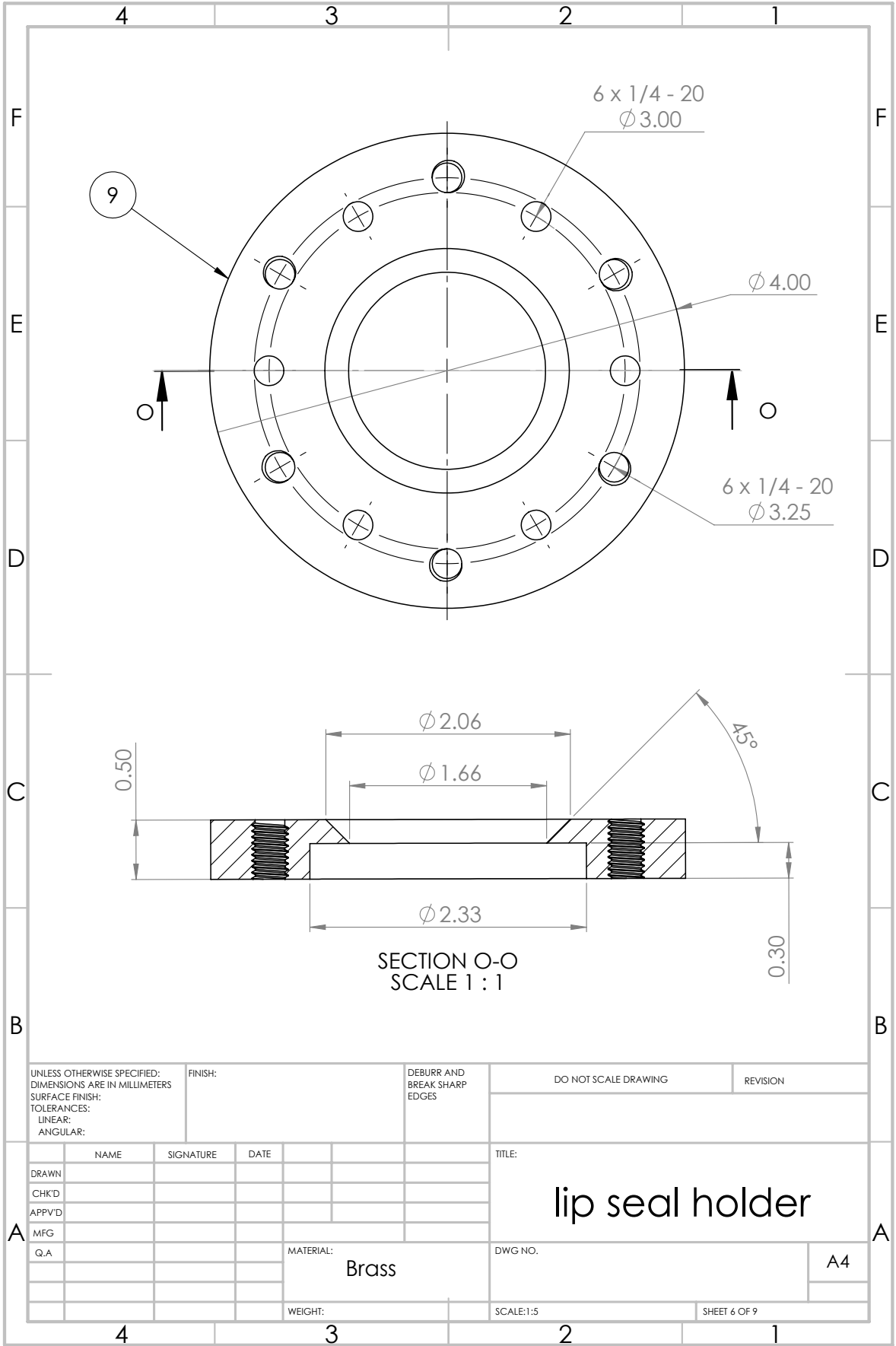
| | | | | | | | | | | | | | | | | | | | | | | | | | | | | | |
|--|--|--|---------|--|------------------------------------|-----------|----------------------|--|----------|--|--|-----------|--|--|--|--|--|-------------------------------|--|--|--|--|--|--------------|--|--|--|--|--|
| UNLESS OTHERWISE SPECIFIED: DIMENSIONS ARE IN MILLIMETERS | | | FINISH: | | DEBURR AND BREAK SHARP EDGES | | DO NOT SCALE DRAWING | | REVISION | | | | | | | | | | | | | | | | | | | | |
| SURFACE FINISH: | | | | | | | | | | | | | | | | | | | | | | | | | | | | | |
| TOLERANCES: | | | | | | | | | | | | | | | | | | | | | | | | | | | | | |
| LINEAR: | | | | | | | | | | | | | | | | | | | | | | | | | | | | | |
| ANGULAR: | | | | | | | | | | | | | | | | | | | | | | | | | | | | | |
| NAME | | | | | | SIGNATURE | | | | | | DATE | | | | | | TITLE: | | | | | | | | | | | |
| DRAWN | | | | | | | | | | | | | | | | | | Exploded view Assembly Port A | | | | | | | | | | | |
| CHK'D | | | | | | | | | | | | | | | | | | | | | | | | | | | | | |
| APP'V'D | | | | | | | | | | | | | | | | | | | | | | | | | | | | | |
| MFG | | | | | | | | | | | | | | | | | | | | | | | | | | | | | |
| Q.A | | | | | | | | | | | | MATERIAL: | | | | | | DWG NO. | | | | | | | | | | | |
| | | | | | | | | | | | | | | | | | | A4 | | | | | | | | | | | |
| | | | | | | | | | | | | WEIGHT: | | | | | | SCALE: 1:50 | | | | | | SHEET 3 OF 9 | | | | | |



| | | | | | | | | | | | |
|---|--|--|-----------|--|------------------------------------|--|------------------------|--|----------|--|--|
| UNLESS OTHERWISE SPECIFIED: DIMENSIONS ARE IN MILLIMETERS SURFACE FINISH: TOLERANCES: LINEAR: ANGULAR: | | | FINISH: | | DEBURR AND BREAK SHARP EDGES | | DO NOT SCALE DRAWING | | REVISION | | |
| DRAWN | | | SIGNATURE | | DATE | | TITLE: <h1>Lid</h1> | | | | |
| CHK'D | | | | | | | DWG. NO. | | | | |
| APPV'D | | | | | | | SHEET 4 OF 9 | | | | |
| MFG | | | | | | | A4 | | | | |
| Q.A | | | | | MATERIAL: | | SCALE: 1:50 | | | | |
| | | | | | WEIGHT: | | | | | | |

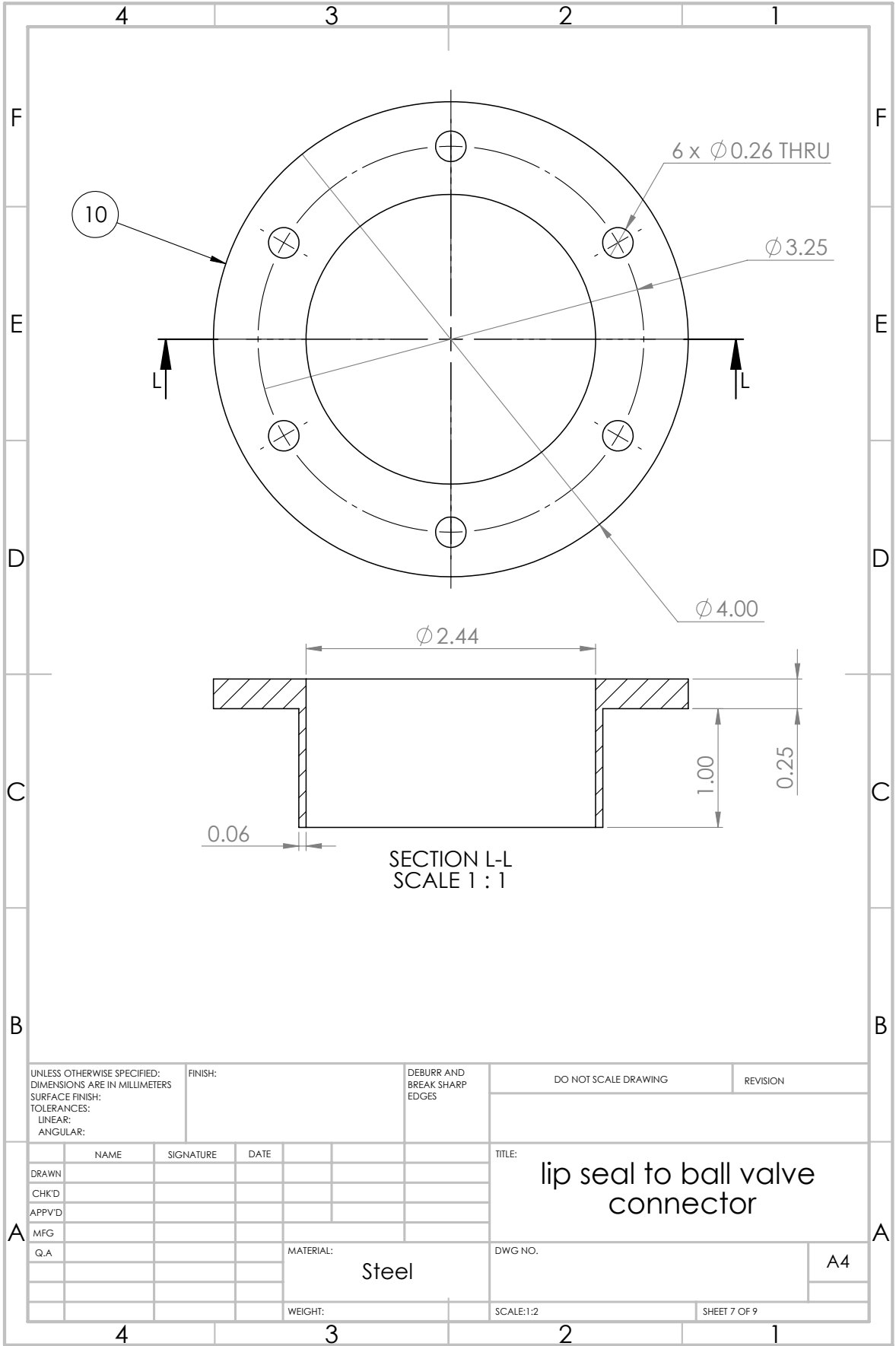


| | | | | | | | | | |
|--|--|-----------|--|------------------------------------|--|--------------------------|--|--------------|--|
| UNLESS OTHERWISE SPECIFIED: DIMENSIONS ARE IN MILLIMETERS | | FINISH: | | DEBURR AND BREAK SHARP EDGES | | DO NOT SCALE DRAWING | | REVISION | |
| SURFACE FINISH: | | | | | | | | | |
| TOLERANCES: | | | | | | | | | |
| LINEAR: | | | | | | | | | |
| ANGULAR: | | | | | | | | | |
| NAME | | SIGNATURE | | DATE | | TITLE: | | | |
| DRAWN | | | | | | port to flange connector | | | |
| CHK'D | | | | | | | | | |
| APPV'D | | | | | | | | | |
| MFG | | | | | | DWG NO. | | | |
| Q.A | | | | | | MATERIAL: | | A4 | |
| | | | | | | Brass | | | |
| | | | | | | WEIGHT: | | SCALE: 1:5 | |
| | | | | | | | | SHEET 5 OF 9 | |



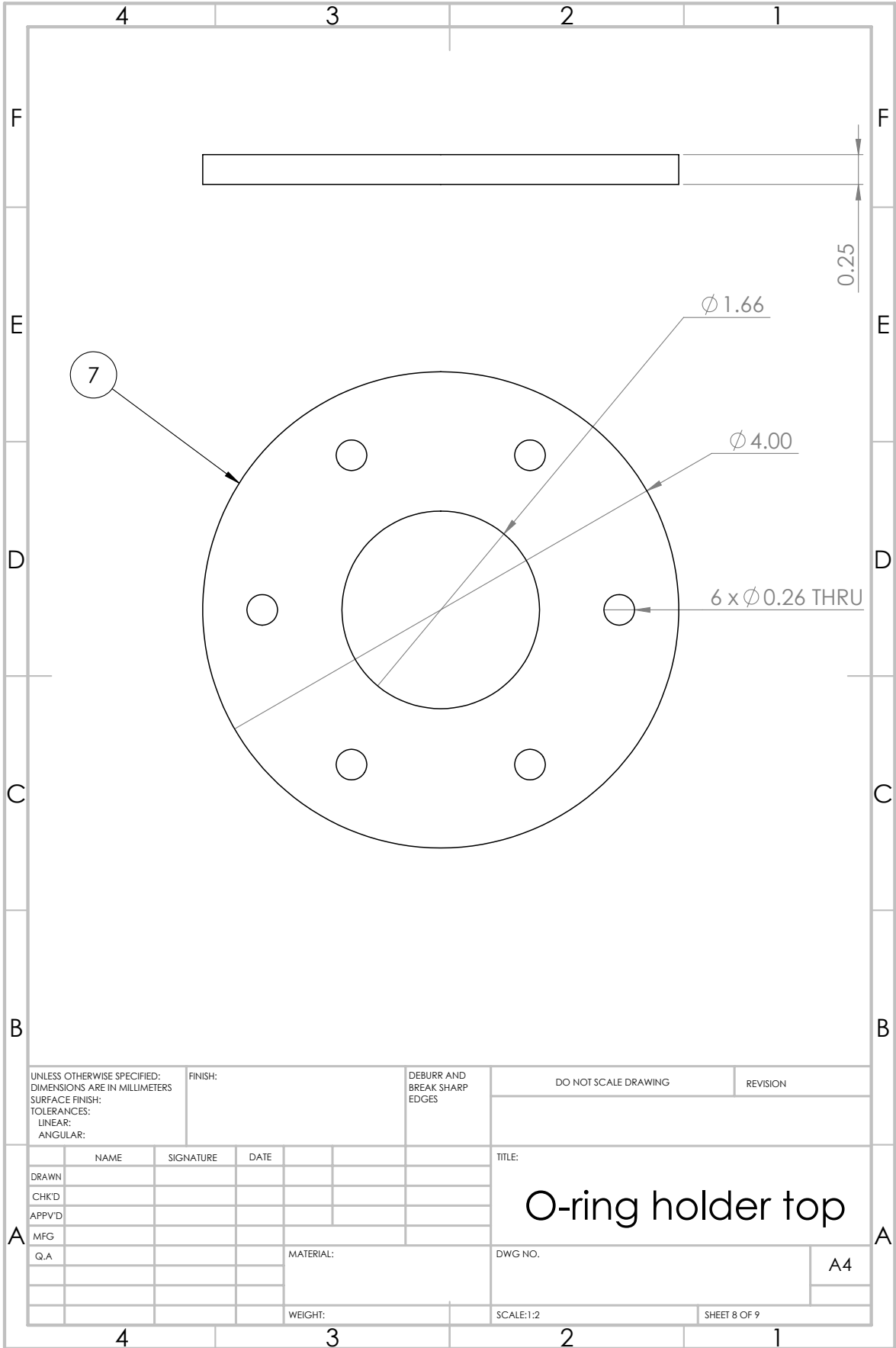
SECTION O-O
SCALE 1 : 1

| | | | | | | | | | |
|--|--|-----------|--|------------------------------------|--|--------------------------|--|--------------|--|
| UNLESS OTHERWISE SPECIFIED: DIMENSIONS ARE IN MILLIMETERS | | FINISH: | | DEBURR AND BREAK SHARP EDGES | | DO NOT SCALE DRAWING | | REVISION | |
| SURFACE FINISH: | | | | | | | | | |
| TOLERANCES: | | | | | | | | | |
| LINEAR: | | | | | | | | | |
| ANGULAR: | | | | | | | | | |
| NAME | | SIGNATURE | | DATE | | TITLE: | | | |
| DRAWN | | | | | | <h1>lip seal holder</h1> | | | |
| CHK'D | | | | | | | | | |
| APP'V'D | | | | | | | | | |
| MFG | | | | | | | | | |
| Q.A | | | | | | | | | |
| | | | | MATERIAL: | | DWG NO. | | A4 | |
| | | | | Brass | | | | | |
| | | | | WEIGHT: | | SCALE: 1:5 | | SHEET 6 OF 9 | |

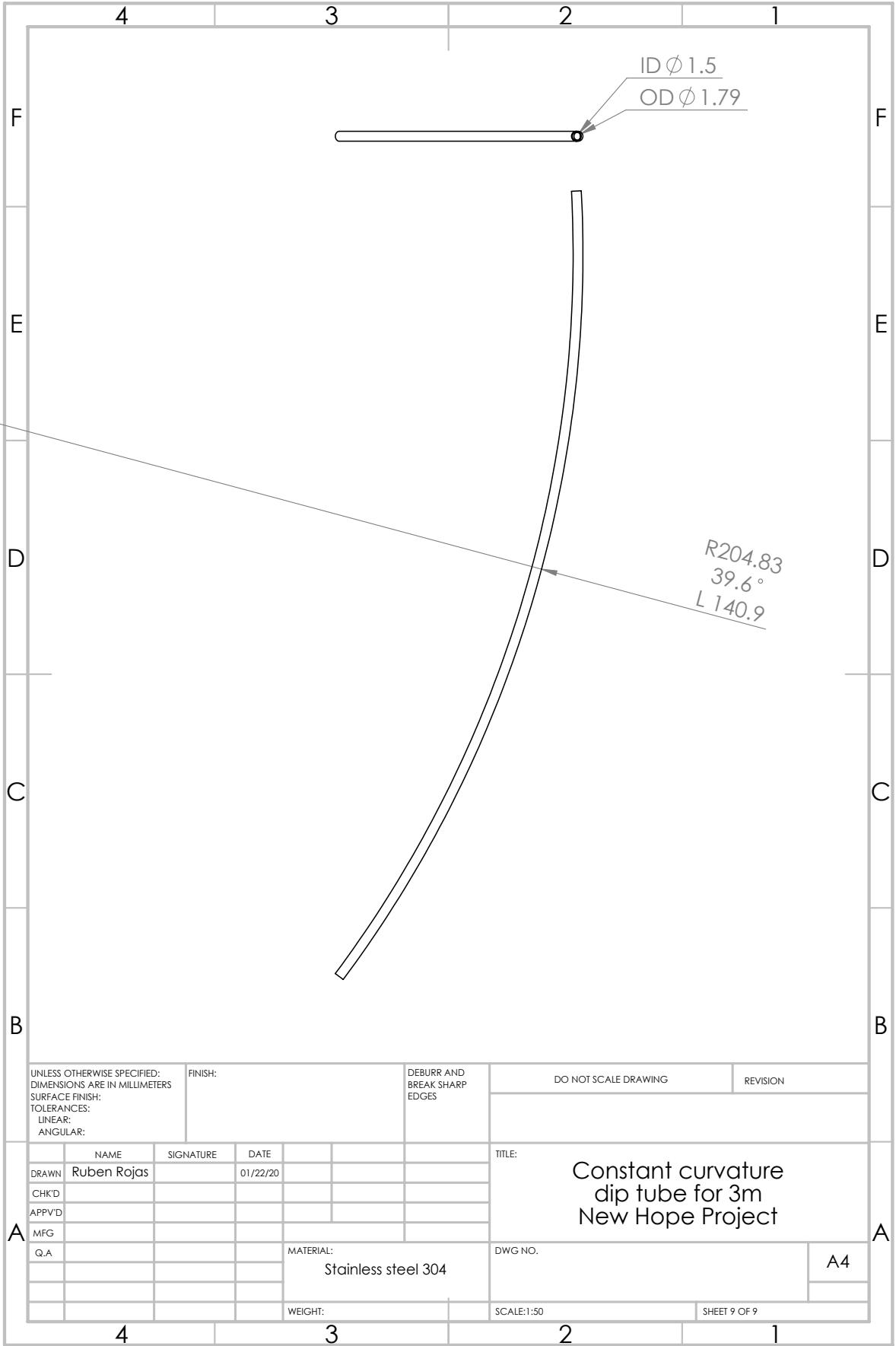


SECTION L-L
SCALE 1 : 1

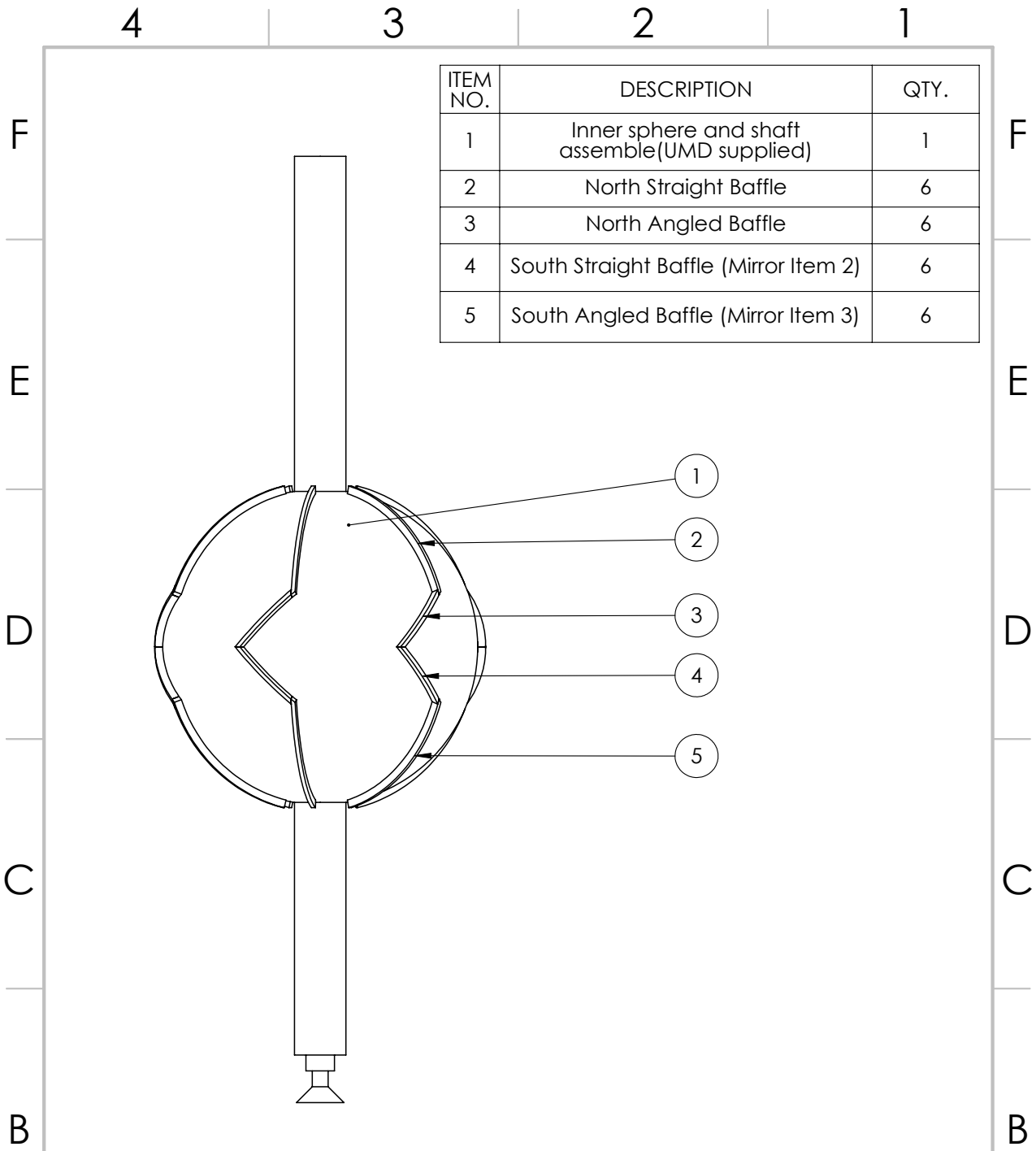
| | | | | | | | | | |
|--|--|-----------|--|------------------------------------|--|-------------------------------------|--|--------------|--|
| UNLESS OTHERWISE SPECIFIED: DIMENSIONS ARE IN MILLIMETERS | | FINISH: | | DEBURR AND BREAK SHARP EDGES | | DO NOT SCALE DRAWING | | REVISION | |
| SURFACE FINISH: | | | | | | | | | |
| TOLERANCES: | | | | | | | | | |
| LINEAR: | | | | | | | | | |
| ANGULAR: | | | | | | | | | |
| NAME | | SIGNATURE | | DATE | | TITLE: | | | |
| DRAWN | | | | | | lip seal to ball valve connector | | | |
| CHK'D | | | | | | | | | |
| APPV'D | | | | | | DWG NO. | | A4 | |
| MFG | | | | | | SCALE: 1:2 | | SHEET 7 OF 9 | |
| Q.A | | | | | | MATERIAL: | | | |
| | | | | | | Steel | | | |
| | | | | | | WEIGHT: | | | |



| | | | | | | | | | | |
|---|--|--|-----------|--|------------------------------------|--|----------------------|--|-------------------|--|
| UNLESS OTHERWISE SPECIFIED: DIMENSIONS ARE IN MILLIMETERS SURFACE FINISH: TOLERANCES: LINEAR: ANGULAR: | | | FINISH: | | DEBURR AND BREAK SHARP EDGES | | DO NOT SCALE DRAWING | | REVISION | |
| DRAWN | | | SIGNATURE | | DATE | | TITLE: | | O-ring holder top | |
| CHK'D | | | | | | | DWG NO. | | A4 | |
| APPV'D | | | | | | | SCALE: 1:2 | | SHEET 8 OF 9 | |
| MFG | | | | | | | WEIGHT: | | | |
| Q.A | | | | | | | | | | |

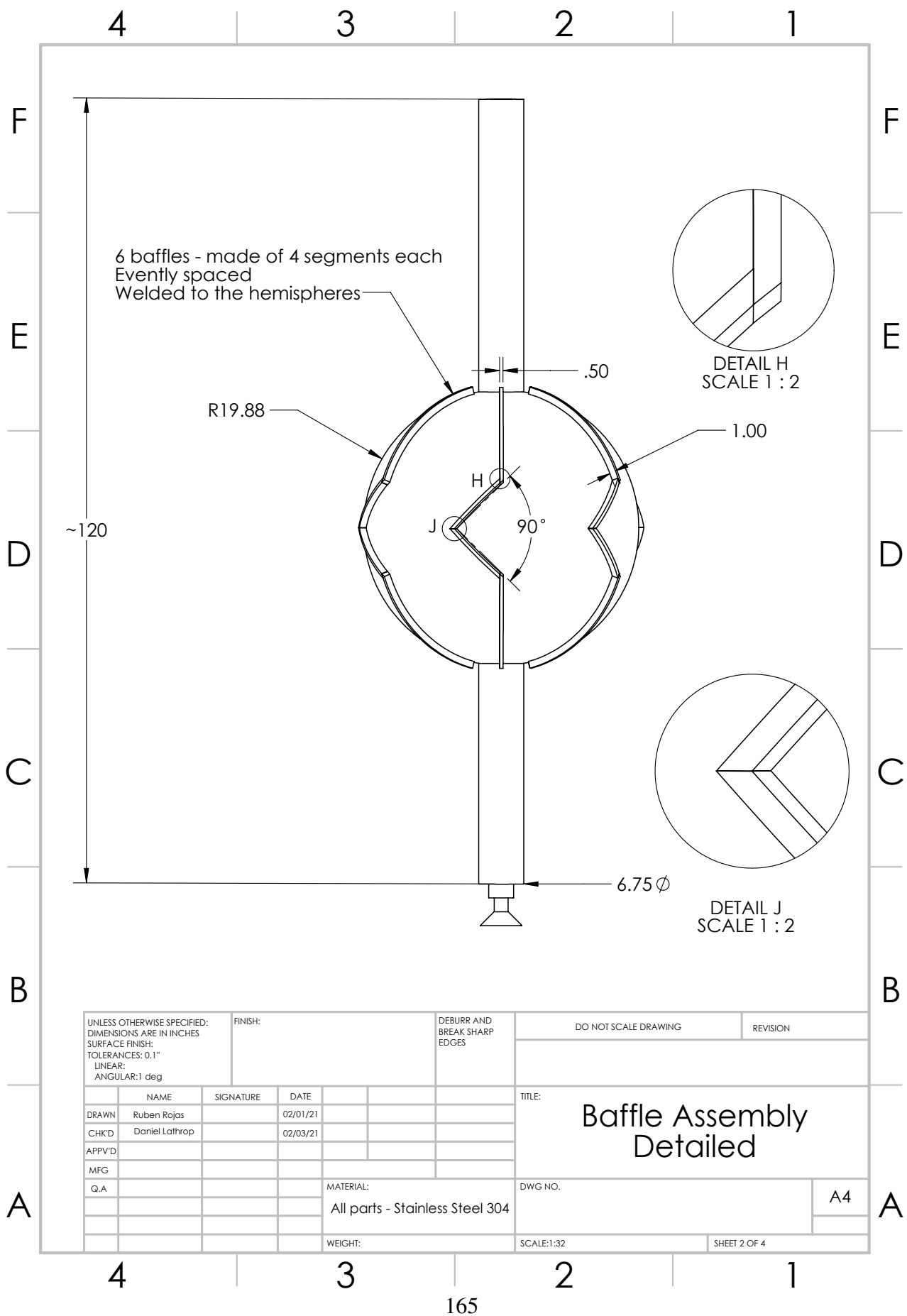


| | | | | | | |
|---|--|--|---------|------------------------------------|--|----------|
| UNLESS OTHERWISE SPECIFIED: DIMENSIONS ARE IN MILLIMETERS SURFACE FINISH: TOLERANCES: LINEAR: ANGULAR: | | | FINISH: | DEBURR AND BREAK SHARP EDGES | DO NOT SCALE DRAWING | REVISION |
| DRAWN: Ruben Rojas | | | | | TITLE: Constant curvature dip tube for 3m New Hope Project | |
| CHK'D: | | | | | DWG NO.: | |
| APP'VD: | | | | | MATERIAL: Stainless steel 304 | |
| MFG: | | | | | WEIGHT: | |
| Q.A: | | | | | SCALE: 1:50 | |
| | | | | | SHEET 9 OF 9 | |

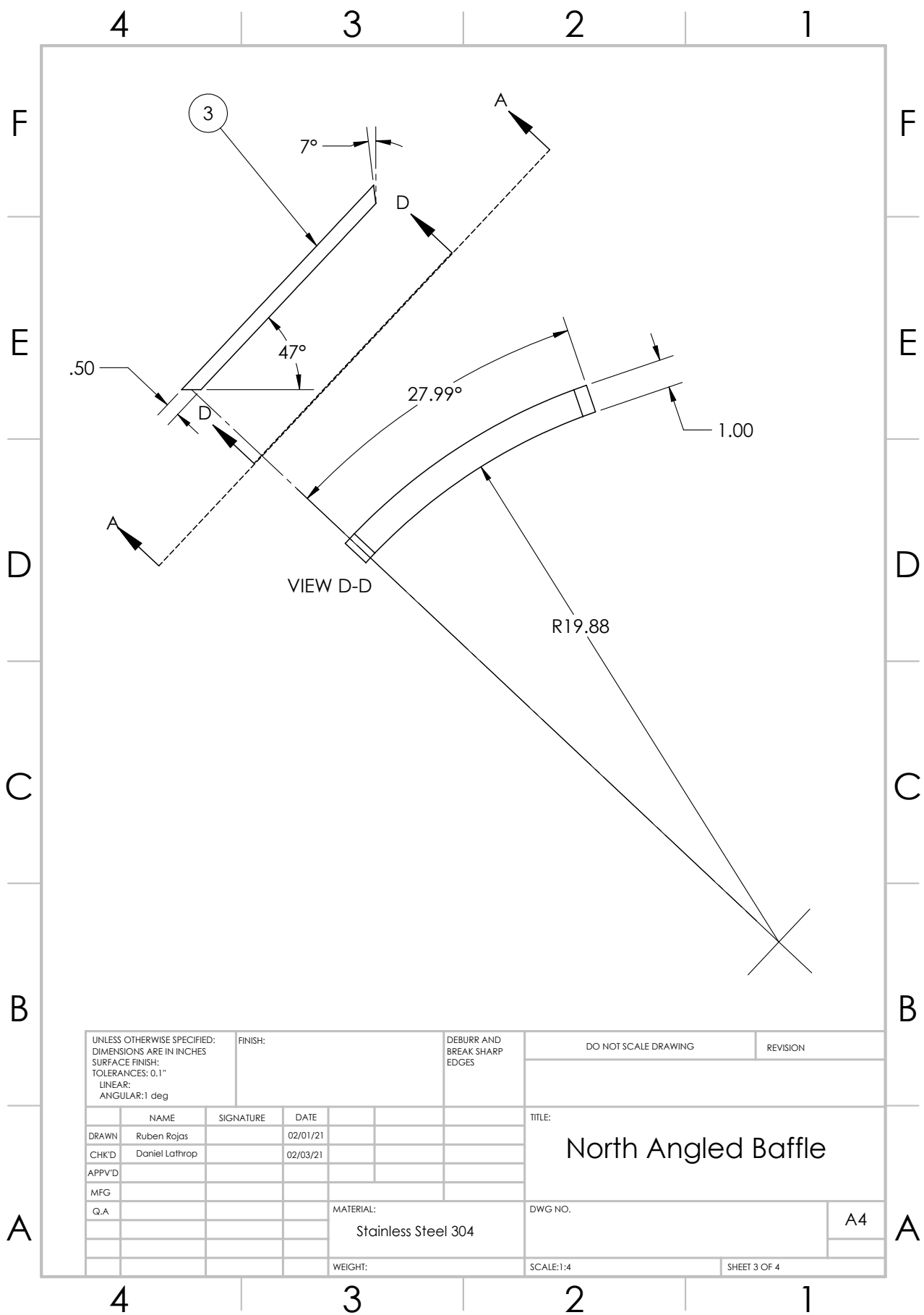


| ITEM NO. | DESCRIPTION | QTY. |
|----------|--|------|
| 1 | Inner sphere and shaft assemble (UMD supplied) | 1 |
| 2 | North Straight Baffle | 6 |
| 3 | North Angled Baffle | 6 |
| 4 | South Straight Baffle (Mirror Item 2) | 6 |
| 5 | South Angled Baffle (Mirror Item 3) | 6 |

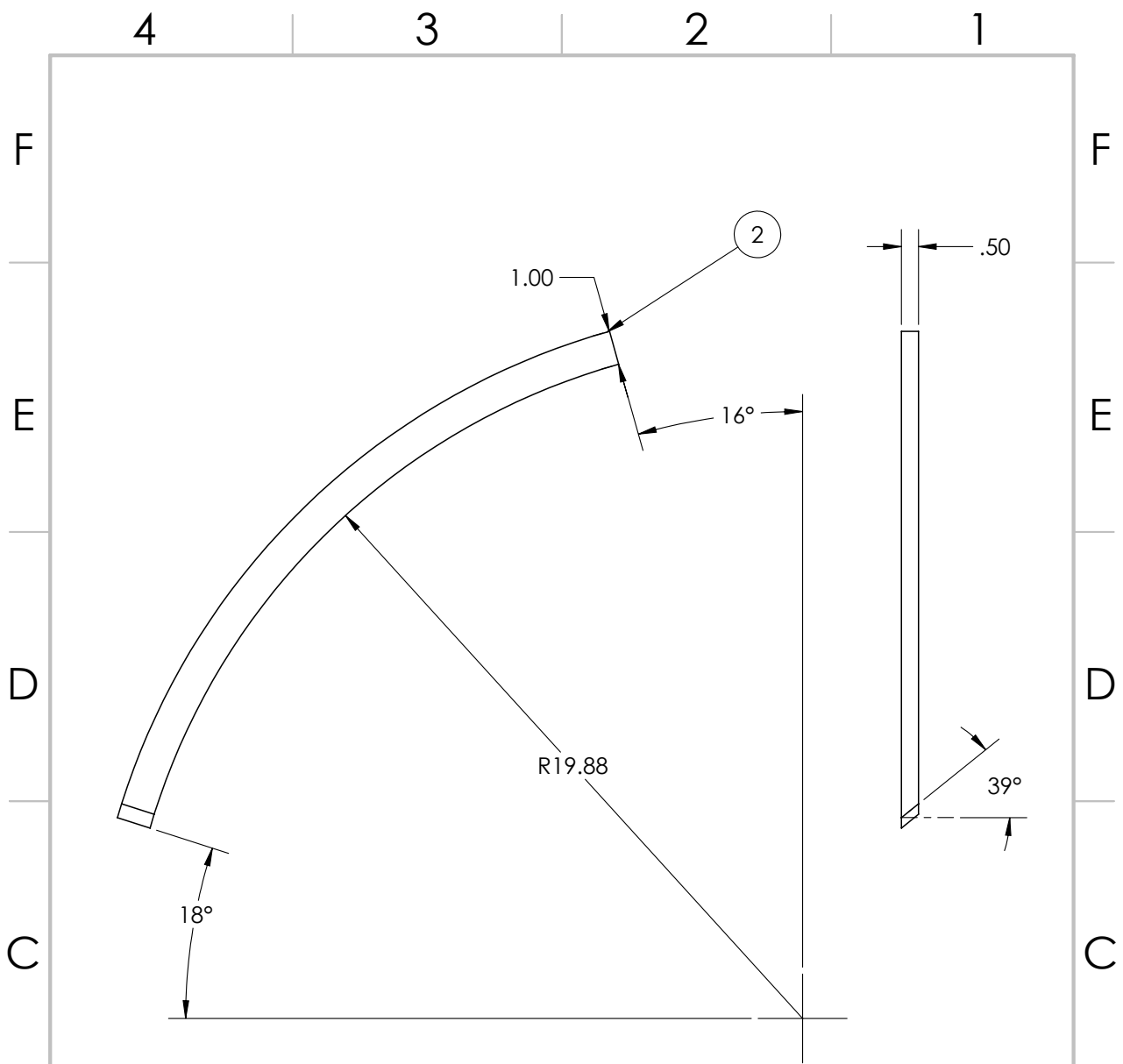
| | | | | | | | | | | | |
|---|--|--|----------------|--|------------------------------------|--|---------------------------------|--|---|--|--------------|
| UNLESS OTHERWISE SPECIFIED: DIMENSIONS ARE IN INCHES SURFACE FINISH: TOLERANCES: 0.1" LINEAR: ANGULAR: 1 deg | | | FINISH: | | DEBURR AND BREAK SHARP EDGES | | DO NOT SCALE DRAWING | | REVISION | | |
| DRAWN | | | NAME | | SIGNATURE | | DATE | | TITLE: | | |
| CHK'D | | | Ruben Rojas | | | | 02/01/21 | | <h2>Baffles Assembly Parts Listing</h2> | | |
| APPV'D | | | Daniel Lothrop | | | | 02/03/21 | | | | |
| MFG | | | | | | | | | | | |
| Q.A | | | | | | | | | | | |
| | | | | | | | MATERIAL: | | DWG NO. | | |
| | | | | | | | All parts - Stainless Steel 304 | | A4 | | |
| | | | | | | | WEIGHT: | | SCALE: 1:32 | | SHEET 1 OF 4 |



| | | | | | | | | | |
|---|--|-----------|--|--|--|---|--|--------------|--|
| UNLESS OTHERWISE SPECIFIED: DIMENSIONS ARE IN INCHES SURFACE FINISH: TOLERANCES: 0.1" LINEAR: ANGULAR: 1 deg | | FINISH: | | DEBURR AND BREAK SHARP EDGES | | DO NOT SCALE DRAWING | | REVISION | |
| DRAWN Ruben Rojas | | SIGNATURE | | DATE 02/01/21 | | TITLE: Baffle Assembly Detailed | | | |
| CHK'D Daniel Lathrop | | | | DATE 02/03/21 | | | | | |
| APP'VD | | | | | | | | | |
| MFG | | | | | | | | | |
| Q.A | | | | | | | | | |
| | | | | MATERIAL: All parts - Stainless Steel 304 | | DWG NO. | | A4 | |
| | | | | WEIGHT: | | SCALE: 1:32 | | SHEET 2 OF 4 | |



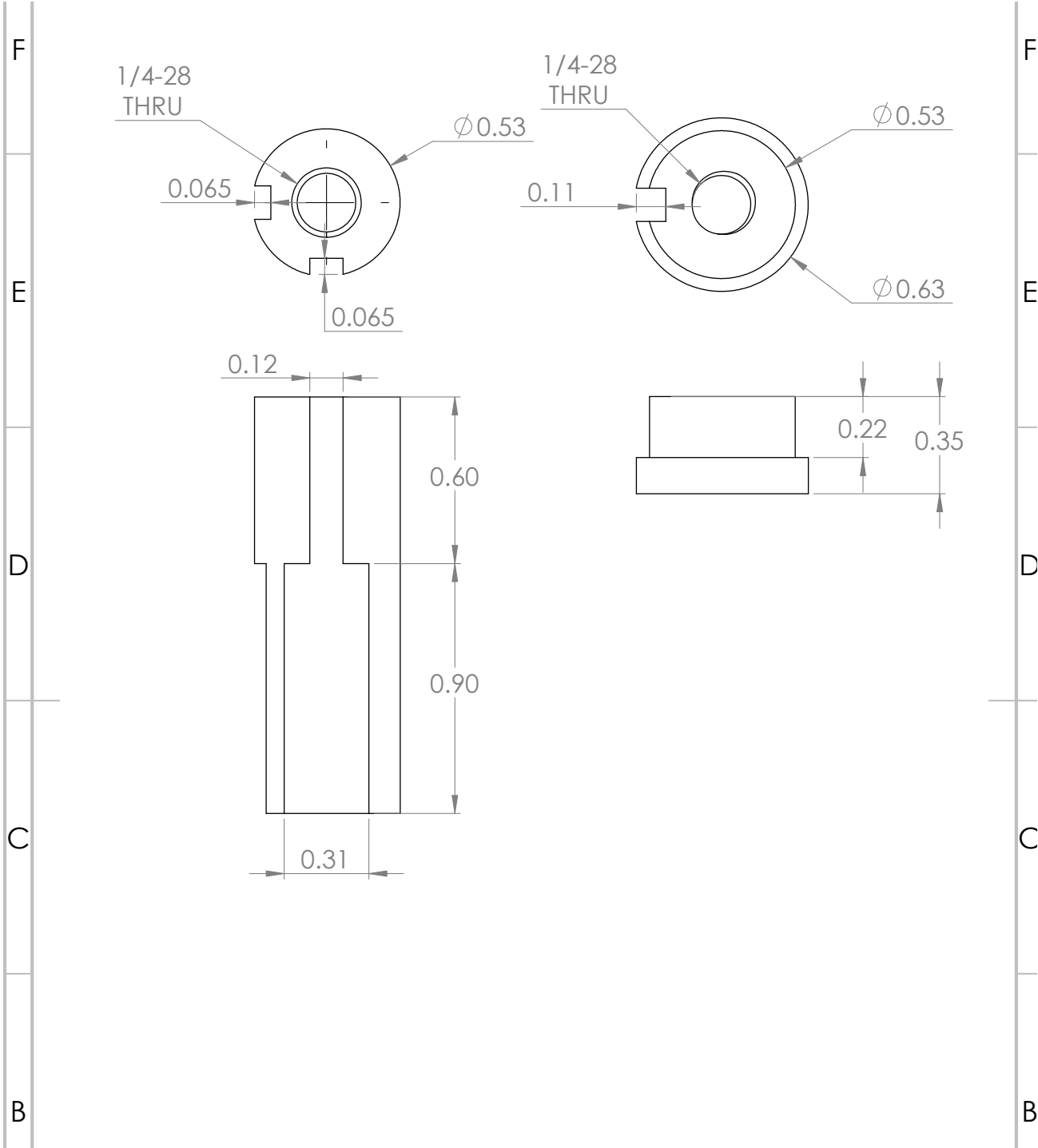
| | | | | | | | | | | | |
|---|--|--|-----------|--|--|------------------------------------|--|----------------------|--------------------------------------|----------|--|
| UNLESS OTHERWISE SPECIFIED: DIMENSIONS ARE IN INCHES SURFACE FINISH: TOLERANCES: 0.1" LINEAR: ANGULAR: 1 deg | | | FINISH: | | | DEBURR AND BREAK SHARP EDGES | | DO NOT SCALE DRAWING | | REVISION | |
| DRAWN Ruben Rojas | | | SIGNATURE | | | DATE 02/01/21 | | | TITLE: North Angled Baffle | | |
| CHK'D Daniel Lathrop | | | SIGNATURE | | | DATE 02/03/21 | | | MATERIAL: Stainless Steel 304 | | |
| APP'V'D | | | SIGNATURE | | | DATE | | | DWG NO. | | |
| MFG | | | SIGNATURE | | | DATE | | | SCALE: 1:4 | | |
| Q.A | | | SIGNATURE | | | DATE | | | SHEET 3 OF 4 | | |
| | | | | | | | | | A4 | | |



| | | | | | | | | | | | |
|---|--|--|--|---------|--|------------------------------------|--|----------------------|--|----------|--|
| UNLESS OTHERWISE SPECIFIED: DIMENSIONS ARE IN INCHES SURFACE FINISH: TOLERANCES: 0.1" LINEAR: ANGULAR: 1 deg | | | | FINISH: | | DEBURR AND BREAK SHARP EDGES | | DO NOT SCALE DRAWING | | REVISION | |
| | | | | | | | | TITLE: | | | |
| | | | | | | | | North Top Baffle | | | |
| | | | | | | | | DWG NO. | | | |
| | | | | | | | | A4 | | | |
| | | | | | | | | SHEET 4 OF 4 | | | |

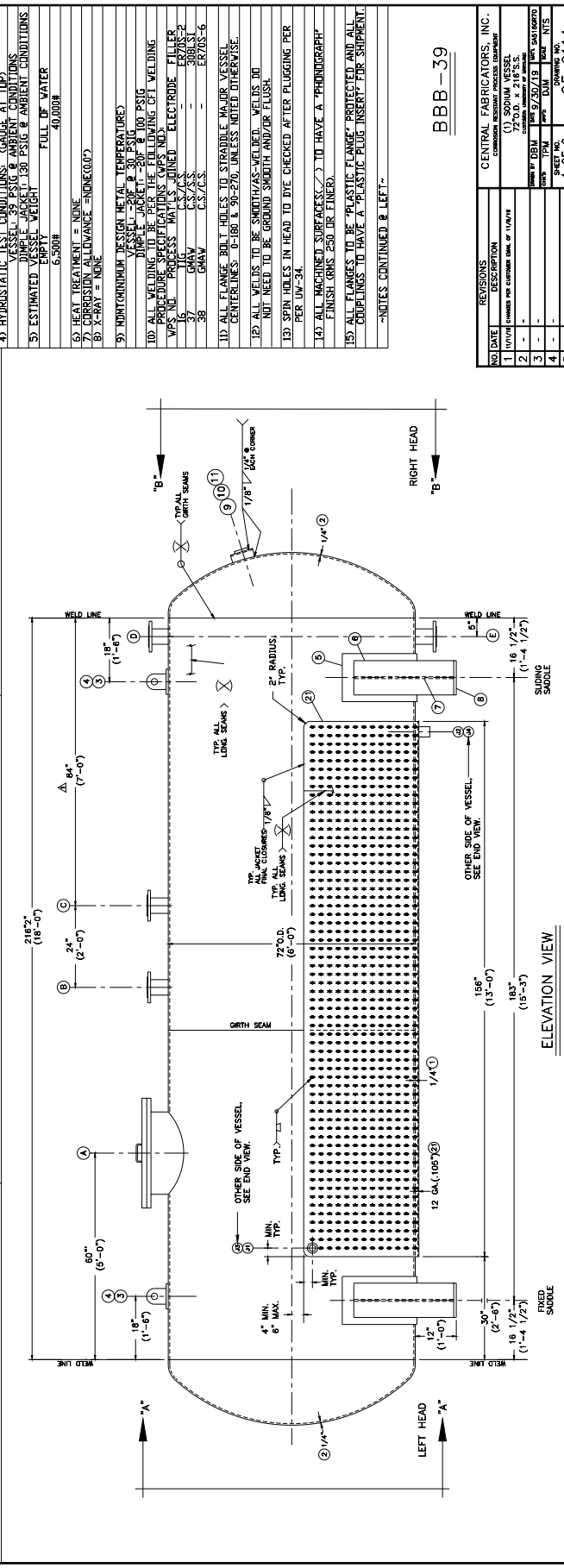
A
B
C
D
E
F

F
E
D
C
B
A



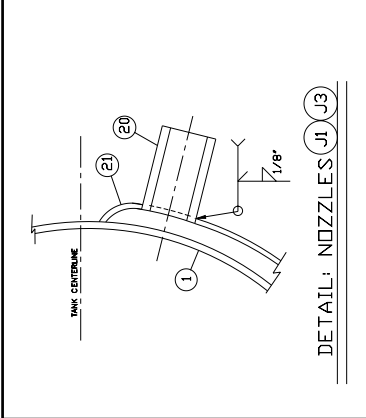
| | | | | | | | | | | | |
|---|--|--|--|-----------|--|------------------------------------|--|--|--|----------|--|
| UNLESS OTHERWISE SPECIFIED: DIMENSIONS ARE IN INCHES SURFACE FINISH: machined TOLERANCES: 0.01" LINEAR: ANGULAR: | | | | FINISH: | | DEBURR AND BREAK SHARP EDGES | | DO NOT SCALE DRAWING | | REVISION | |
| DRAWN Ruben Rojas | | | | SIGNATURE | | DATE 09/13/21 | | TITLE: New Finger Probe Holder | | | |
| CHK'D Tom | | | | | | | | | | | |
| APPV'D Dan Lathrop | | | | | | | | | | | |
| MFG | | | | | | | | | | | |
| Q.A | | | | | | MATERIAL: | | DWG NO. | | A4 | |

| MARKQTY DESCRIPTION | | NOZZLE SCHEDULE | | BILL OF MATERIALS | |
|---------------------|---------------|-----------------|---------------|-------------------|---------------|
| 1 | 1/4" SCH 40 | 1 | 1/4" SCH 40 | 1 | 1/4" SCH 40 |
| 2 | 1/2" SCH 40 | 2 | 1/2" SCH 40 | 2 | 1/2" SCH 40 |
| 3 | 3/4" SCH 40 | 3 | 3/4" SCH 40 | 3 | 3/4" SCH 40 |
| 4 | 1" SCH 40 | 4 | 1" SCH 40 | 4 | 1" SCH 40 |
| 5 | 1 1/2" SCH 40 | 5 | 1 1/2" SCH 40 | 5 | 1 1/2" SCH 40 |
| 6 | 2" SCH 40 | 6 | 2" SCH 40 | 6 | 2" SCH 40 |
| 7 | 3" SCH 40 | 7 | 3" SCH 40 | 7 | 3" SCH 40 |
| 8 | 4" SCH 40 | 8 | 4" SCH 40 | 8 | 4" SCH 40 |
| 9 | 6" SCH 40 | 9 | 6" SCH 40 | 9 | 6" SCH 40 |
| 10 | 8" SCH 40 | 10 | 8" SCH 40 | 10 | 8" SCH 40 |
| 11 | 10" SCH 40 | 11 | 10" SCH 40 | 11 | 10" SCH 40 |
| 12 | 12" SCH 40 | 12 | 12" SCH 40 | 12 | 12" SCH 40 |
| 13 | 14" SCH 40 | 13 | 14" SCH 40 | 13 | 14" SCH 40 |
| 14 | 16" SCH 40 | 14 | 16" SCH 40 | 14 | 16" SCH 40 |
| 15 | 18" SCH 40 | 15 | 18" SCH 40 | 15 | 18" SCH 40 |
| 16 | 20" SCH 40 | 16 | 20" SCH 40 | 16 | 20" SCH 40 |
| 17 | 24" SCH 40 | 17 | 24" SCH 40 | 17 | 24" SCH 40 |
| 18 | 30" SCH 40 | 18 | 30" SCH 40 | 18 | 30" SCH 40 |
| 19 | 36" SCH 40 | 19 | 36" SCH 40 | 19 | 36" SCH 40 |
| 20 | 42" SCH 40 | 20 | 42" SCH 40 | 20 | 42" SCH 40 |
| 21 | 48" SCH 40 | 21 | 48" SCH 40 | 21 | 48" SCH 40 |
| 22 | 54" SCH 40 | 22 | 54" SCH 40 | 22 | 54" SCH 40 |
| 23 | 60" SCH 40 | 23 | 60" SCH 40 | 23 | 60" SCH 40 |
| 24 | 66" SCH 40 | 24 | 66" SCH 40 | 24 | 66" SCH 40 |
| 25 | 72" SCH 40 | 25 | 72" SCH 40 | 25 | 72" SCH 40 |
| 26 | 78" SCH 40 | 26 | 78" SCH 40 | 26 | 78" SCH 40 |
| 27 | 84" SCH 40 | 27 | 84" SCH 40 | 27 | 84" SCH 40 |
| 28 | 90" SCH 40 | 28 | 90" SCH 40 | 28 | 90" SCH 40 |
| 29 | 96" SCH 40 | 29 | 96" SCH 40 | 29 | 96" SCH 40 |
| 30 | 102" SCH 40 | 30 | 102" SCH 40 | 30 | 102" SCH 40 |
| 31 | 108" SCH 40 | 31 | 108" SCH 40 | 31 | 108" SCH 40 |
| 32 | 114" SCH 40 | 32 | 114" SCH 40 | 32 | 114" SCH 40 |
| 33 | 120" SCH 40 | 33 | 120" SCH 40 | 33 | 120" SCH 40 |
| 34 | 126" SCH 40 | 34 | 126" SCH 40 | 34 | 126" SCH 40 |
| 35 | 132" SCH 40 | 35 | 132" SCH 40 | 35 | 132" SCH 40 |
| 36 | 138" SCH 40 | 36 | 138" SCH 40 | 36 | 138" SCH 40 |
| 37 | 144" SCH 40 | 37 | 144" SCH 40 | 37 | 144" SCH 40 |
| 38 | 150" SCH 40 | 38 | 150" SCH 40 | 38 | 150" SCH 40 |
| 39 | 156" SCH 40 | 39 | 156" SCH 40 | 39 | 156" SCH 40 |
| 40 | 162" SCH 40 | 40 | 162" SCH 40 | 40 | 162" SCH 40 |
| 41 | 168" SCH 40 | 41 | 168" SCH 40 | 41 | 168" SCH 40 |
| 42 | 174" SCH 40 | 42 | 174" SCH 40 | 42 | 174" SCH 40 |
| 43 | 180" SCH 40 | 43 | 180" SCH 40 | 43 | 180" SCH 40 |
| 44 | 186" SCH 40 | 44 | 186" SCH 40 | 44 | 186" SCH 40 |
| 45 | 192" SCH 40 | 45 | 192" SCH 40 | 45 | 192" SCH 40 |
| 46 | 198" SCH 40 | 46 | 198" SCH 40 | 46 | 198" SCH 40 |
| 47 | 204" SCH 40 | 47 | 204" SCH 40 | 47 | 204" SCH 40 |
| 48 | 210" SCH 40 | 48 | 210" SCH 40 | 48 | 210" SCH 40 |
| 49 | 216" SCH 40 | 49 | 216" SCH 40 | 49 | 216" SCH 40 |
| 50 | 222" SCH 40 | 50 | 222" SCH 40 | 50 | 222" SCH 40 |
| 51 | 228" SCH 40 | 51 | 228" SCH 40 | 51 | 228" SCH 40 |
| 52 | 234" SCH 40 | 52 | 234" SCH 40 | 52 | 234" SCH 40 |
| 53 | 240" SCH 40 | 53 | 240" SCH 40 | 53 | 240" SCH 40 |
| 54 | 246" SCH 40 | 54 | 246" SCH 40 | 54 | 246" SCH 40 |
| 55 | 252" SCH 40 | 55 | 252" SCH 40 | 55 | 252" SCH 40 |
| 56 | 258" SCH 40 | 56 | 258" SCH 40 | 56 | 258" SCH 40 |
| 57 | 264" SCH 40 | 57 | 264" SCH 40 | 57 | 264" SCH 40 |
| 58 | 270" SCH 40 | 58 | 270" SCH 40 | 58 | 270" SCH 40 |
| 59 | 276" SCH 40 | 59 | 276" SCH 40 | 59 | 276" SCH 40 |
| 60 | 282" SCH 40 | 60 | 282" SCH 40 | 60 | 282" SCH 40 |
| 61 | 288" SCH 40 | 61 | 288" SCH 40 | 61 | 288" SCH 40 |
| 62 | 294" SCH 40 | 62 | 294" SCH 40 | 62 | 294" SCH 40 |
| 63 | 300" SCH 40 | 63 | 300" SCH 40 | 63 | 300" SCH 40 |
| 64 | 306" SCH 40 | 64 | 306" SCH 40 | 64 | 306" SCH 40 |
| 65 | 312" SCH 40 | 65 | 312" SCH 40 | 65 | 312" SCH 40 |
| 66 | 318" SCH 40 | 66 | 318" SCH 40 | 66 | 318" SCH 40 |
| 67 | 324" SCH 40 | 67 | 324" SCH 40 | 67 | 324" SCH 40 |
| 68 | 330" SCH 40 | 68 | 330" SCH 40 | 68 | 330" SCH 40 |
| 69 | 336" SCH 40 | 69 | 336" SCH 40 | 69 | 336" SCH 40 |
| 70 | 342" SCH 40 | 70 | 342" SCH 40 | 70 | 342" SCH 40 |
| 71 | 348" SCH 40 | 71 | 348" SCH 40 | 71 | 348" SCH 40 |
| 72 | 354" SCH 40 | 72 | 354" SCH 40 | 72 | 354" SCH 40 |
| 73 | 360" SCH 40 | 73 | 360" SCH 40 | 73 | 360" SCH 40 |
| 74 | 366" SCH 40 | 74 | 366" SCH 40 | 74 | 366" SCH 40 |
| 75 | 372" SCH 40 | 75 | 372" SCH 40 | 75 | 372" SCH 40 |
| 76 | 378" SCH 40 | 76 | 378" SCH 40 | 76 | 378" SCH 40 |
| 77 | 384" SCH 40 | 77 | 384" SCH 40 | 77 | 384" SCH 40 |
| 78 | 390" SCH 40 | 78 | 390" SCH 40 | 78 | 390" SCH 40 |
| 79 | 396" SCH 40 | 79 | 396" SCH 40 | 79 | 396" SCH 40 |
| 80 | 402" SCH 40 | 80 | 402" SCH 40 | 80 | 402" SCH 40 |
| 81 | 408" SCH 40 | 81 | 408" SCH 40 | 81 | 408" SCH 40 |
| 82 | 414" SCH 40 | 82 | 414" SCH 40 | 82 | 414" SCH 40 |
| 83 | 420" SCH 40 | 83 | 420" SCH 40 | 83 | 420" SCH 40 |
| 84 | 426" SCH 40 | 84 | 426" SCH 40 | 84 | 426" SCH 40 |
| 85 | 432" SCH 40 | 85 | 432" SCH 40 | 85 | 432" SCH 40 |
| 86 | 438" SCH 40 | 86 | 438" SCH 40 | 86 | 438" SCH 40 |
| 87 | 444" SCH 40 | 87 | 444" SCH 40 | 87 | 444" SCH 40 |
| 88 | 450" SCH 40 | 88 | 450" SCH 40 | 88 | 450" SCH 40 |
| 89 | 456" SCH 40 | 89 | 456" SCH 40 | 89 | 456" SCH 40 |
| 90 | 462" SCH 40 | 90 | 462" SCH 40 | 90 | 462" SCH 40 |
| 91 | 468" SCH 40 | 91 | 468" SCH 40 | 91 | 468" SCH 40 |
| 92 | 474" SCH 40 | 92 | 474" SCH 40 | 92 | 474" SCH 40 |
| 93 | 480" SCH 40 | 93 | 480" SCH 40 | 93 | 480" SCH 40 |
| 94 | 486" SCH 40 | 94 | 486" SCH 40 | 94 | 486" SCH 40 |
| 95 | 492" SCH 40 | 95 | 492" SCH 40 | 95 | 492" SCH 40 |
| 96 | 498" SCH 40 | 96 | 498" SCH 40 | 96 | 498" SCH 40 |
| 97 | 504" SCH 40 | 97 | 504" SCH 40 | 97 | 504" SCH 40 |
| 98 | 510" SCH 40 | 98 | 510" SCH 40 | 98 | 510" SCH 40 |
| 99 | 516" SCH 40 | 99 | 516" SCH 40 | 99 | 516" SCH 40 |
| 100 | 522" SCH 40 | 100 | 522" SCH 40 | 100 | 522" SCH 40 |

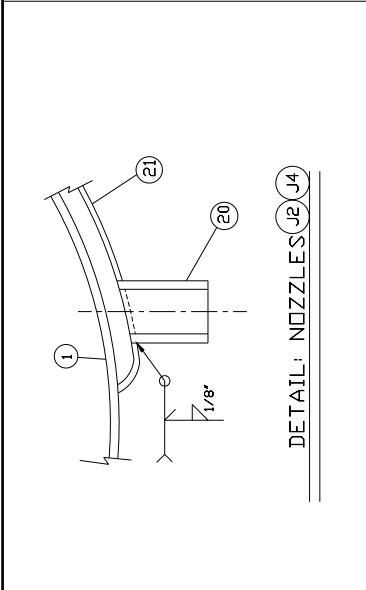


| NO | DATE | DESCRIPTION | REVISIONS |
|----|------|--|-----------|
| 1 | | 1/10/18 CHANGED PER COMPANY DWG OF 1/10/18 | 1 |
| 2 | | | 2 |
| 3 | | | 3 |
| 4 | | | 4 |
| 5 | | | 5 |

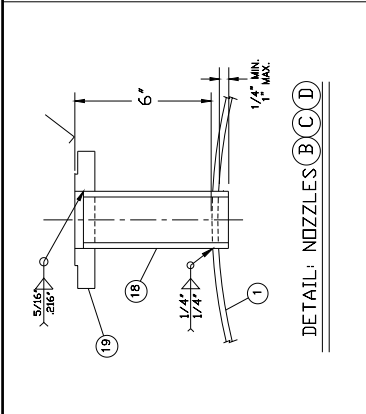
CENTRAL FABRICATORS, INC.
 (1) SODIUM VESSEL
 270.0" x 216" S.S.
 DATE 9/25/18 TIME SAVED
 SHEET NO. 1 OF 2
 CFB-3914



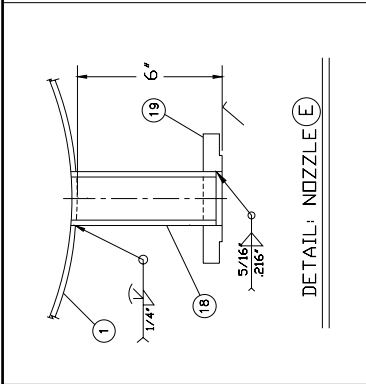
DETAIL: NOZZLES (J1, J3)



DETAIL: NOZZLES (J2, J4)



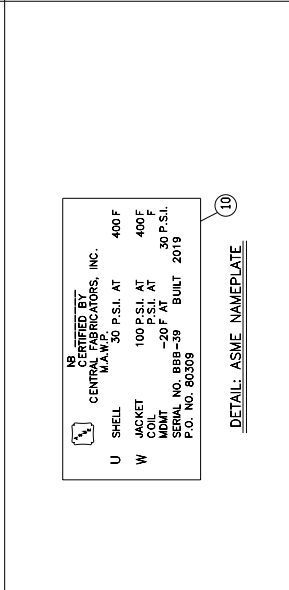
DETAIL: NOZZLES (B, C, D)



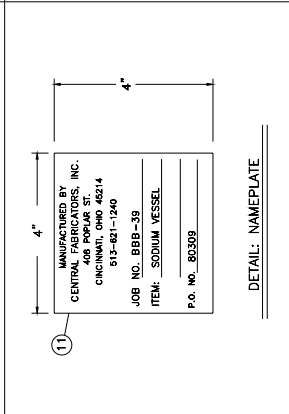
DETAIL: NOZZLE (E)



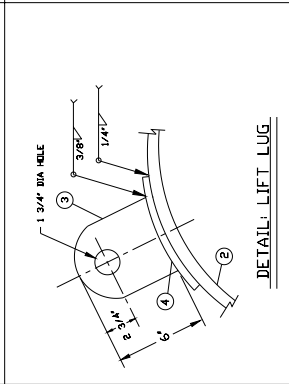
DETAIL: ASME NAMEPLATE (10)



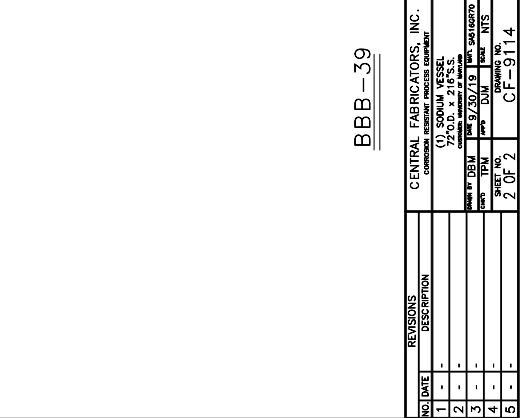
DETAIL: NAMEPLATE (11)



DETAIL: LIFT LUG (E)



DETAIL: MANHOLE/NOZZLE (A)



DETAIL: SADDLE

BBB-39

| NO. | DATE | REVISIONS DESCRIPTION |
|-----|------|-----------------------|
| 1 | - | - |
| 2 | - | - |
| 3 | - | - |
| 4 | - | - |
| 5 | - | - |

CENTRAL FABRICATORS, INC.
 CENTRAL FABRICATORS COMPANY
 408 POPULAR STREET
 CINCINNATI, OHIO 45214
 (U) SODIUM VESSEL
 72" O.D. x 21'6" S.S.
 DRAWN BY DBM DATE 9/30/19
 CHECKED BY JPM DATE 10/1/19
 DESIGNED BY DJM DATE 10/1/19
 APPROVED BY NTS DATE 10/1/19
 PROJECT NO. 2 UT-2
 DRAWING NO. CT-9114

Appendix B: Standard Operation Procedure

We present only the Extraction SOP for reasons of brevity. The Insertion SOP is very similar and edited from this SOP. Contact the author of this dissertation for more information.

11/10/20

3M Sodium Transfer from Sphere to Tank SOP

TRANSFER PREPARATIONS: Describes the preparations to be done in the lab and in the experiment before day one of sodium transfer operation.

Potential Hazards

Fire: NO

Pressure: NO

Temperature: NO

Tripping: YES

→ Wear closed-toe shoes, walk carefully

Fall from height: YES

→ Do not lean over railings, keep both hands on railings when going up or down stairs

- Clear out top of the cube.
 - Remove all electronics from the top of the cube and sphere.
 - Maintain only temperature measurement devices and battery chargers.
 - Change two ports.
 - install the Sphere Transfer Port with the lip seal secured by the lip seal holder.
 - install visualization port.
 - Inert sphere/pressure testing.
 - Remove inner motor.
 - Remove the inner motor frame.
 - Remove the outer motor.
 - Remove the outer motor frame.
 - Install flooring on top of the cube at the former inner motor frame/outer motor location.
 - Visually inspect oil plumbing lines, ensure there are no leaks.
 - Check the drain in the trench.
 - Ensure water flows, no clogs.
 - Check scrubber/blower connections.
 - Turn on the blower from inside Shed.
 - Check both power sources for the blower.
 - Change the power source outside while the blower is ON.
 - Check vent connections
 - Overhead vent configuration
- Prepare the Tank Connections:**
- Make sure the storage tank is still inert at 0.5 psi.
 - Connect transfer line to storage tank.
 - Close Valve E on Storage Tank.
 - Perform a leak check of the transfer line configuration:* Install Valve B2 flange set up (add photo) to end of transfer line (Valve C). Add 10 psi using Primary

3-m Gas System, opening valve H5 and B2. When done, close H5 and B2 and disconnect the blue hose (flex line between valve H5 and B2. See diagram 1-a). Check on day two of operations.

- Set the transfer line in position on top of the cube.
- Locate Dip Tube and situate on top of the cube.

DAY ONE BEFORE RUN CHECKLIST: Describes the steps to be done during the day one, and before the beginning of the operations.

- Clear all steps in "Transfer preparations" section
- Locate PPE and fire resistant clothing (jacket, gloves, safety glasses, helmets w/shield, closed-toe shoes)
- Locate and test walkie-talkies
- Prerequisite weather conditions: no ice/snow conditions outside
- Perform pre-heater check
 - Visually inspect for leaks
- Check water supply for scrubber in Ling room (0204D)
 - Energize solenoid in Shed
 - Ensure water flows
 - Check vents are set for the overhead blower system.
 - If cold: drain outside lines with valve outside trapdoor
- Check liquid nitrogen supply and fire suppression system
 - 2 dewars required: One on the top of the cube and other near the tank in front of the motor drivers.
 - Minimum weight: 231 kg (100kg of liquid nitrogen plus 131 kg of the dewar)
 - Connect power and hose to dewar liquid port and open dewar liquid valve
 - Test fire suppression system by pressing red LN₂ button briefly (until liquid is visibly ejecting)
- Check the LN₂ gun next to tank (until liquid is visibly ejecting)
- Check UPS battery backup for solenoid valves
- Check oil system
 - Ensure system is connected
 - Ensure all valves are operable
- Check nitrogen gas supply
 - 6 bottles required
 - Minimum pressure: 2200 psi for each bottle
 - At the Transfer Gas Manifold:

173

- Set the output pressure to 10 psi at pressure regulators (R1-R4) and open valves according to Diagram 3: Valves N1-N5 Open, Valves N6, N7 Closed.
- Check that the flexible metal hose is attached to the 3-m gas port (valve A2 closed, H2 open)
- Install check valve above G1 valve on the tank gas port

START PUMP/HEATER CHECKLIST

Located in Shed, on Sodium computer

Program Initialization Startup [AWAITING UPDATED CODE]

- Open to edit notes.txt file for daily operations notes
- On sodium desktop, open command line terminal:
 - cd /data/bin/3mcontrol
 - python3 bigsister15.py
 - Click "OK" through warnings about missing vibflag and status.dat
 - <Ctrl-S> or click "menu -> start" to start control program. Time should start updating.
 - Cycle bypass valve to 99/closed
 - Click up arrow to 3
 - Type "99"
 - Confirm blue "Closed" light for bypass valve lit on control box
 - Back to 1/open
 - Click down arrow to 97
 - Type "1"
 - Confirm orange "Open" light for bypass valve lit on control box
 - Ensure valves at pipe penetrations through wall are open
 - Ensure that outside cooling units are valved off
 - Start pump
 - Press white "ON" button on control box
 - Listen to ensure pump is on
 - Visually inspect pumping system for leaks
 - Turn off pump
 - End bigsister15.py
 - Click red "x"

DAY ONE: Heating Operations

At least two people required for day one heating sodium operations

Training Requirements:

- Sodium Safety Training
- UMD Campus Safety Training

Before Beginning Run

- Call campus police 301-405-3333: "beginning hot sodium operations in ERF Bldg #223"
- Check high bay for clear egress around the cube and high-bay. **Do not proceed until all three of the following items are addressed.**
 - Ensure two exit doors are operable with a clear path to each.
 - Inspect for clutter, combustible materials and remove as needed.
 - Check class D materials and portable fire extinguishers are present.

Program Initialization Startup

- Open to edit notes.txt file for daily operations notes
- On sodium desktop, open four command line terminals
 - Terminal 1:
 - cd /data/bin/3mcontrol
 - mkdir /data/3m/<today's date in mmddyy format> (example: mkdir /data/3m/060413)
 - chmod 777 /data/3m/<today's date>
 - python3 plotter2.py &
 - Terminal 2:
 - cd /data/bin/3mcontrol
 - python3 bigsister15.py
 - Click "OK" through warnings about missing vibflag and status.dat
 - <Ctrl-S> or click "menu -> start" to start control program. Time should start updating.
 - Terminal 3:
 - cd /data/bin/3mcontrol
 - python3 smoke4.py
 - Terminal 4:
 - cd /data/bin/3mcontrol
 - ./wtemplog

note: wtemplog program is prone to crashing. If it crashes, 3m.php3 web status page will display "Missing or old wtemp.log, reading directly..." <Ctrl-C> and start again.

- open web browser and go to the status page, oil status page, and LOCAL camera page:

<http://sodium.umd.edu/3m.php3>
<http://sodium.umd.edu/oil.php>
<http://localhost/cam/>

important note: chrome and other browsers cannot open enough simultaneous connections to view the camera feeds and status pages from ***the same host*** so

always use sodium.umd.edu for status pages and localhost or 192.168.1.1 for the cameras

Gather infrared cameras and chargers in Shed

- Test cameras/chargers
- Plug cameras in to charge

- Ensure that oil system is plumbed for appropriate operation - Heating ONLY Sphere:
 - Valve O1 open
 - Valve O2 open
 - Valve O3 closed.
 - Valve O4 closed.
- Start pump (press white "ON" button on control box)
 - Listen to ensure pump is on
 - Visually inspect pumping system (check inside the cube as well) for leaks
 - If leak is found:
 - Turn system off, fix leak, proceed ONLY after system is confirmed with no leaks
- Put on PPE and fire resistant clothing
 - jacket
 - gloves
 - safety glasses
 - helmet w/shield
 - protective work boots
- Check thermometry
 - Check ambient room temperature readouts on control computer
 - Ensure all temperature readouts are within 1-2 degrees of one another

Heating

- At Sodium computer:
 - Set heaters to 100% in bigsisiter.py GUI



- Monitor gas pressure with camera as sphere starts to heat
 - <http://sodium.umd.edu/cam>
 - name '3m' , password *****
 - Ensure gas pressure in sphere: <= 1psig
 - When pressure starts to approach 1 psig (on order of 15 min. to one hour):
 - Close 3-m N₂ line at A3: Close valve H3.

- Vent sphere pressure down to <0.5 psig using lever at manifold connected to A3.
- Close valve A3.
- Remove gas manifold from A3.
- Attach oil bubbler to A3.
- SLOWLY open valve A3.

Caution: oil can spray if opened too quickly

- Make sure "gas handling" camera can see the bubbler

- Monitor bubbler to make sure it's bubbling
 - If bubbler camera has failed:
 - STOP heating
 - Repair/replace camera as necessary
 - Proceed ONLY when issue is cleared by PI
 - If bubbler has stopped:
 - STOP heating
 - Check connections between bubbler and sphere
 - Check hot oil system functioning
 - Proceed ONLY when issue is cleared by PI
 - Monitor <http://sodium.umd.edu/3m.php3>
 - Make sure wtemplog program hasn't crashed
 - {ADD CRASH MESSAGE HERE}
 - If wtemplog has crashed:
 - STOP heating
 - Re-run Terminal 4 commands
 - ./wtemplog
- note: wtemplog program is prone to crashing. If it crashes, 3m.php3 web status page will display "Missing or old wtemp.log, reading directly.." <Ctrl-C> and start again.*

End of Day

- Set heater power to 0.
 - Wait 2 minutes
- Turn heaters **off** at circuit breaker
- Turn pump **off**. Make sure you can hear the pump turning off. If not sure, go and visually inspect the pump outside.
- Close Valve A3.
- Remove bubbler.
- Flow gas through gas line for 30 seconds: Open Valve H3.
 - set gas regulator to 0.5 psig
 - attach to sphere port valve A3.
 - open valve A3.
- Adjust "Gas Handling Cam" to view gas gauge
- Verify outside that pump is **off** and that the heaters are off with IR camera
- Monitor **all** temperatures in system graph to ensure they are decreasing over time
- End plotter2.py
 - Click red "x"

175

- End bigsister15.py
 - Click red "x"
- Keep wtemplog open and running
- Keep smoke5.py open and running
- Call campus police 301-405-3333: "ending hot sodium operations for the day in ERF bldg #223".

DAY TWO: Continuing heating and Sodium Transfer

At least two people required for Continuing Heating Operation

Before Beginning Run

- Call campus police 405-5333: "beginning day of hot sodium operations in ERF Bldg #223"
- Check high bay for clutter and clear egress

Check the Tank Connections

- Make sure the storage tank is still inert at 0.5 psi.
- Check that the transfer line is still at 10 psi with valve E closed.
 - If not, redo all transfer line connections and perform another leak check. Make sure gaskets are in good condition. Turn the bolts in on alternate order until ALL are firmly tight.
 - If still at 10 psi. Slowly open Valve B2 to release pressure. Disconnect Valve B2 flange set up from the transfer line and install it on the dip tube. (Use new gasket)

BEFORE RUN CHECKLIST

- Clear all steps in "Transfer preparations" section
- Locate PPE and fire resistant clothing (jacket, gloves, safety glasses, helmets w/shield)
- Locate and test walkie-talkies
- Prerequisite weather conditions: no ice/snow conditions outside
- Perform pre-heater check
 - Visually inspect for leaks
- Check water supply for scrubber in Ling room (0204D)
 - Energize solenoid in Shed
 - Ensure water flows
 - Check vents are set for the overhead blower system.
 - If cold: drain outside lines with valve outside trapdoor
- Check liquid nitrogen supply and fire suppression system
 - 2 dewars required: One on the top of the cube and other near the tank in front of the motor drivers.

- Minimum weight: 231 kg (100kg of liquid nitrogen plus 131 kg of the dewar)
- Connect power and hose to dewar liquid port and open dewar valve
- Test fire suppression system by pressing red LN₂ button briefly (10 seconds)
- Check that LN₂ gun work
- Check battery backup for solenoid valves
- Check oil system
 - Ensure system is connected
 - Make sure all valves are operable
- Check nitrogen gas supply
 - 5 bottles required
 - Minimum pressure: 2000 psi for each bottle
 - Install bottles and open valves according to Diagram 3: Valves N1-N5 Open. Valve N6 Closed.
- Check ventilation system
 - Turn on blower from inside Shed
 - Check both power sources for blower
 - Change power source outside while blower is ON

In Shed, at Sodium computer:

Program Initialization Startup

- Open to edit notes.txt file for daily operations notes
- On sodium desktop, open four command line terminals
 - Terminal 1:
 - `cd /data/bin/3mcontrol`
 - `mkdir /data/3m/<today's date in mmddyy format>` (example: `mkdir /data/3m/060413`)
 - `chmod 777 /data/3m/<today's date>`
 - `python3 plotter2.py &`
 - Terminal 2:
 - `cd /data/bin/3mcontrol`
 - `python3 bigsister15.py`
 - Click "OK" through warnings about missing vibflag and status.dat
 - `<Ctrl-S>` or click "menu -> start" to start control program. Time should start updating.
 - Terminal 3:
 - `cd /data/bin/3mcontrol`
 - `python3 smoke4.py`
 - Terminal 4:
 - `cd /data/bin/3mcontrol`

- ❑ **./wtemplog**
note: wtemplog program is prone to crashing. If it crashes, 3m.php3 web status page will display "Missing or old wtemp.log, reading directly.." <Ctrl-C> and start again.

- ❑ open web browser and go to the status page, oil status page, and LOCAL camera page:

<http://sodium.umd.edu/3m.php3>
<http://sodium.umd.edu/oil.php>
<http://localhost/cam/>

important note: chrome and other browsers cannot open enough simultaneous connections to view the camera feeds and status pages from ***the same host*** so always use sodium.umd.edu for status pages and localhost or 192.168.1.1 for the cameras

Pump/heater starting

- ❑ Put on PPE and fire resistant clothing
 - ❑ jacket
 - ❑ gloves
 - ❑ safety glasses
 - ❑ helmet w/shield
 - ❑ protective work boots
- ❑ Check thermometry
 - ❑ Check ambient room temperature readouts on control computer from [insert code here]
 - ❑ Ensure all temperature readouts are within 1-2 degrees of one another
 - ❑ Gather infrared cameras and chargers in Shed
- ❑ Test cameras/chargers
- ❑ Plug cameras in to charge
- ❑ Ensure that oil system is plumbed for appropriate operation - Heating ONLY Sphere:
 - ❑ Valve O1 open
 - ❑ Valve O2 open
 - ❑ Valve O3 closed.
 - ❑ Valve O4 closed.
- ❑ Start pump (press white "ON" button on control box)
 - ❑ Listen to ensure pump is on
 - ❑ Visually inspect pumping system (check inside the cube as well) for leaks
 - ❑ If leak is found:
 - ❑ Turn system off, fix leak, proceed ONLY after system is confirmed with no leaks
- ❑ Set heaters to 100% in main control program

Heating

- ❑ Monitor gas pressure with camera as sphere starts to heat
<http://sodium.umd.edu/cam>
 - ❑ name '3m' , password *****
 - ❑ Ensure gas pressure in sphere: <= 1psig
 - ❑ When pressure starts to approach 1 psig (on order of 15 min. to one hour):
 - ❑ Close 3-m N₂ line at A3: Close valve H3.
 - ❑ Vent sphere pressure down to <0.5 psig using lever at manifold connected to A3.
 - ❑ Close valve A3.
 - ❑ Remove gas manifold from A3.
 - ❑ Attach oil bubbler to A3.
 - ❑ SLOWLY open valve A3.

Caution: oil can spray if opened too quickly

 - ❑ Make sure "gas handling" camera can see the bubbler
- ❑ Monitor bubbler to make sure it's bubbling
 - ❑ If bubbler camera has failed:
 - ❑ STOP heating
 - ❑ Repair/replace camera as necessary
 - ❑ Proceed ONLY when issue is cleared by PI
 - ❑ If bubbler has stopped:
 - ❑ STOP heating
 - ❑ Check connections between bubbler and sphere
 - ❑ Check hot oil system functioning
 - ❑ Proceed ONLY when issue is cleared by PI
- ❑ Monitor <http://sodium.umd.edu/3m.php3>
- ❑ Make sure wtemplog program hasn't crashed
 - ❑ If wtemplog has crashed:
 - ❑ STOP heating
 - ❑ cd /data/bin/3mcontrol
 - ❑ ./wtemplog
- ❑ Monitor temperature and look for plateau at approximately 95°C when sodium is melting
When shell bottom temperature measurement >115°C:
 - ❑ Close bubbler valve A3
 - ❑ Remove bubbler
 - ❑ Store in downstairs cabinets
- ❑ Monitor pressure to make sure it remains between 0-5 PSI
 - ❑ reduce pressure using valve A3 if > 5 PSI
- ❑ Heat approximately 10° more to 115°C

Tank Heating Procedure

- ❑ When temperature reaches 115°C start heating the tank by setting Oil Valves in the proper position.
 - ❑ Open Valves O4.(See diagram 5)
 - ❑ Slowly open Valve O3.
- ❑ Check Valves Status

- Valve O1 open
- Valve O2 open
- Valve O3 open
- Valve O4 open.
- Turn down heating to 50% at a few degrees below operating temperature (120°C)
- Continue to monitor the temperature on the sphere.
 - Goal: maintain 120 +/- 5 C
 - If temperature shows a negative slope, make slight adjustments to heating settings in response.

- Place O-ring and O-ring holder in position after ValveB by sliding it upward from the bottom of the dip tube.



- Connect dip tube to N₂ gas line (Valve B2 to Primarily 3-m Gas System - Valve H5)
- Open Valve B2 and close Valve H5.
- Suspend the dip tube with the crane and pulley system above the port A connected to the Primary 3-m Gas System. (See diagram 1-a)

Sodium Transfer SOP

At least six people are required for this hot sodium operation in addition to the PI.

Requirements

- Two individuals on top of the cube with liquid nitrogen extinguisher
 - responsible for reading temperature and pressure sensors on top of the cube
 - responsible for dip tube insertion
- Two individuals next to the storage tank with liquid nitrogen extinguisher
 - responsible for checking the transfer line for leaks
- One individual in the control room
 - responsible for monitoring temperature and cameras.
- One individual between the Storage Tank and control room monitoring the SOP and coordinating the whole procedure.
- Ensure SOP and Failure Mode Decision Tree are in accessible locations for every member of the team.
- Make sure the storage tank is still pressurized at 0.5 psi.
- Locate laser height sensor and FLIR thermal camera and bring to the top of the cube.
- Locate the second thermal camera (phone attachment) to be used downstairs.
- Run

Transfer monitor

- At sodium computer launch terminal and launch `pycharm` command the PyCharm app will appear
- Open `transfer monitor project` at /data/bin/transfer_monitor
- Run python code `hello.py`, Now the application is running and available at sodium.umd.edu:2020
- Set a laptop connected to wifi on the top of the cube and open sodium.umd.edu:2020
- In case of errors read manual available at the application, if necessary reboot the app

Dip tube preparation

- Cap dip tube with Gas Flange (Valve B2) removed from transfer line at the beginning of day two.

Dip tube insertion

- When temperature has reached approximately 120°C
 - Set the pressure on the Primarily 3-m Gas System to 0.5 psi.
 - Valve N₂ out of the Sphere using A3 until it reaches 0.5 psi.
 - Flow N₂ through the dip tube by opening valve H5 for 2 minutes.
 - Ensure valve status: (Diagram 1-A)
 - Valve B open
 - Valve B2 open
 - Valve H3 open
 - Valve H5 open
 - Valve H2 closed
 - Valve H4 closed
 - Valve A closed
 - Valve A3 open.
- Place the dip tube in position, right above Valve A.
- Reduce pressure on the Sphere to 0.5 psi by valving air out using A3
- Place the tip of the dip tube through the lip seal of the extraction flange until it hits the Valve A inner ball.
- Slowly open the Valve A on the extraction flange while holding the dip tube -
 - 1 operator manually stabilizing dip tube
 - 1 operator using pulley system to lower dip tube
- Insert the dip tube into the sodium (It should slide around the inner sphere thanks to its curvature and the inclination of the valve A)
 - Stop when the dip tube touches the bottom of the outer sphere
- Make sure the dip tube is inserted at the correct height and angle:
 - Check for references angles and markups on the dip tube and dip tube flange
 - Adjust position of dip tube as necessary.
- Tighten o-ring on the flange above value A.
- Secure the dip tube in place using Dip Tube Spacers.



179

- Close Valve B
- Close Valve H5.
- Close Valve B2.
- Ensure valve status: (Diagram 1-a)
 - Valve A open.
 - Valve H2 closed.
 - Valve H4 closed.
 - Valve B closed.
 - Valve B2 closed.
 - Valve H3 open.
 - Valve A3 open.
- Lock out valve B closed.
- Remove Gas Flange from dip tube (Valve B2).
- Open Valve C 45 degrees.
- Connect transfer line flange to the dip tube flange (see Diagram 1-b).
- Ensure pressure in the storage tank should be **0.5±0.1 psi**. Adjust using valve G1 on the Storage tank if necessary.
- Fully Open Valve C.
- Start heating the transfer line until temperature reaches 120C. Use the Autotransformer to lower voltage until temperature stabilizes.
- Ensure valve D is open.
- Ensure valve E is open.

- Ensure valve status:
 - Valve A open.
 - Valve C open.
 - Valve D open.
 - Valve E open.
 - Valve B closed.
 - Valve H2 closed.
 - Valve H4 closed.
 - Valve H3 open.

- Ensure temperature on sphere around 120C +/- 5C
- On Transfer Gas Manifold:**
 - Open valve A2 on Transfer Gas Port (TGP) in the Sphere.
 - Open valve H2 on the Transfer Gas Manifold (TGM).

- Close valve A3 on the Sphere.
- Close valve H3 on Primary 3-m Gas System.
- Monitor increase in pressure in sphere to **10 ± 0.1 psi**.

- Ensure Storage Tank pressure is **0.5 ± 0.1 psi**.
- Stop incoming gas to the Storage Tank:
 - Close Valve G2 on Tank Gas Port (TGP) (See Diagram 1-b).
- Open **Valve G1** on Tank Gas Port (TGP) to release the pressure to 0 psi.

- Ensure valve status:
 - Valve A open.
 - Valve C open.
 - Valve D open.
 - Valve E open.
 - Valve H2 open.
 - Valve A2 open.
 - Valve B closed.
 - Valve H4 closed.
 - Valve H3 closed.
 - Valve A3 closed.
 - Valve G1 open.
 - Valve G2 closed.

BEGINNING EXTRACTION

- Open valve B**

NOTE: Sodium should start flowing into the tank. Use infrared thermometry and temperature sensor to see temperature raising on transfer line and Storage Tank.

- Monitor the pressure at P1.
- Increase transfer gas pressure to avoid sphere pressure decreases.
 - In case of partial vacuum:
 - Prepare to partially close Valve B.

NOTE: During a nominal transfer, static pressure in the sphere should be 10 ± 1 psi throughout the transfer. The incoming gas flow rate should be about 2-3 L/s. The sodium level should decrease 0.5-2 inches per minute as measured by the laser rangefinder depending on the level. Temperature should be less than 130 C.

- Keep monitoring pressure sensors during the extraction.
- Check the sodium level of the 3M system using thermal camera and visualization port.
- Check the sodium level on the storage tank using the IR camera.

- Use the laser height sensor to measure and log the level of sodium in the sphere approximately every 10 minutes.

NOTE: Time for emptying is approximately 2 hours

Finishing

- Check that sodium flow stops by different means: hearing, pressure decreasing on 3-m and flow rate increase, temperature decreasing on transfer line.
- When sodium flux stops:
 - Lift the dip tube 10 cm.
 - Secure dip tube with the Dip Tube Spacer.
 - Stop gas flow from the Transfer Gas Manifold:
 - Close A2.
 - Close H2.
 - Set the pressure on the sphere to 1 psi on the Primary 3-m Gas System.
 - Open valve H3 on Primary 3-m Gas System.
 - Open valve A3.
- Close Valve C on the transfer line.
- Close Valve B on the dip tube.
- Turn off transfer line heaters
- Close Valve G1 on Tank Gas Port.
- Open Valve G2 on Tank Gas Port.
- Set pressure regulators to maintain 1 psi pressure in both 3M and storage tank during the cool down.
- Ensure valves status:
 - Valve A open.
 - Valve D open.
 - Valve E open.
 - Valve A3 open.
 - Valve B closed.
 - Valve C closed.
 - Valve H2 closed.
 - Valve H4 closed.
 - Valve H3 open.
 - Valve A2 closed.
 - Valve G1 closed.
 - Valve G2 open.

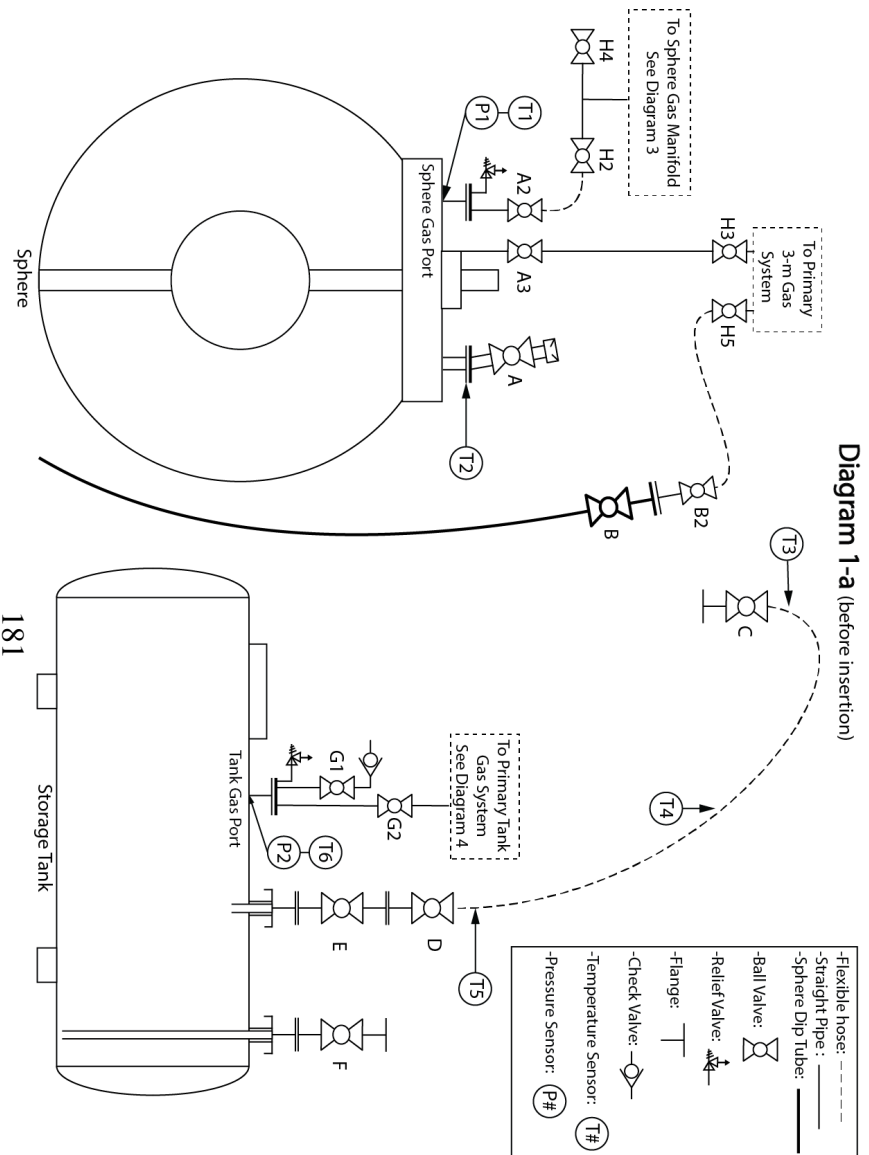
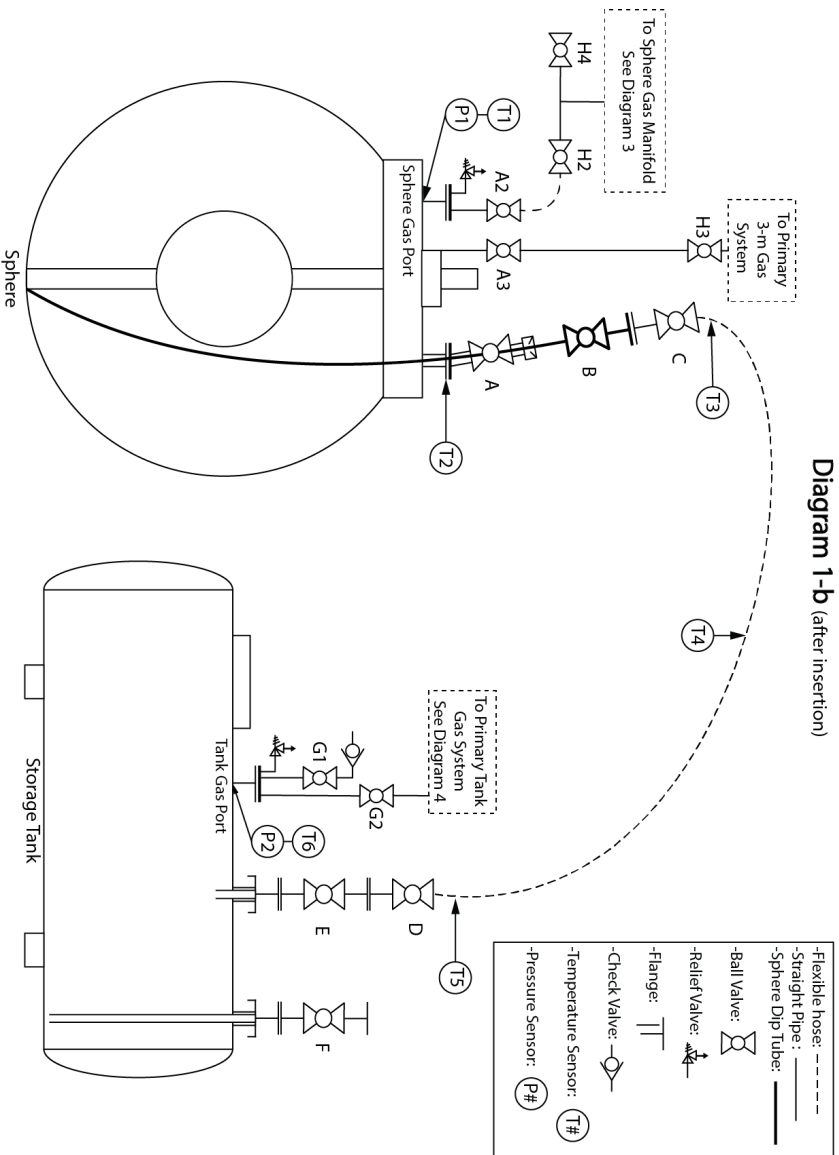
180

End of Run SOP

- In Shed, on Sodium computer:
 - Set 3M heater power to 0 in bigsister.py GUI.
- Turn pump off

- Check pump is off.
- Remove main power from the heater control system.
- DO NOT LEAVE until all temperatures are decreasing everywhere.
- Call campus police 301-405-3333: "end of hot sodium transfer operations."
- Prepare for cleaning the dip tube the next day after cooling down.

END OF SODIUM REMOVAL SOP



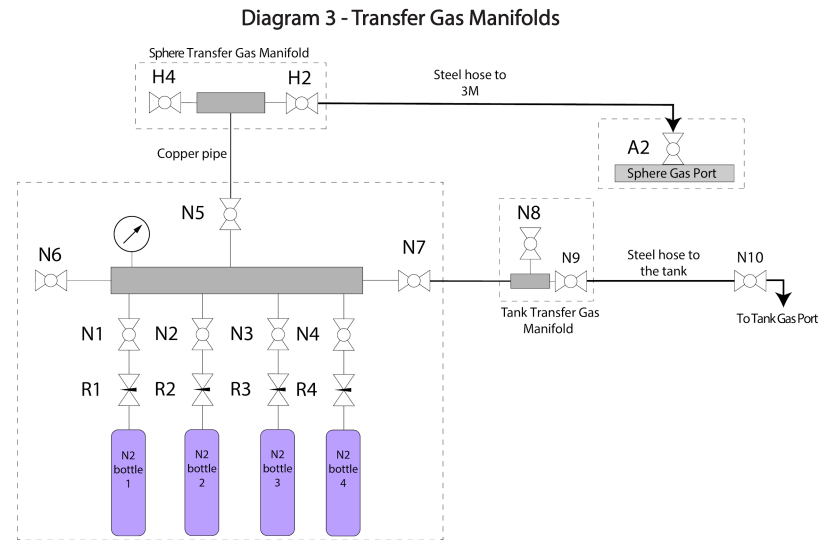
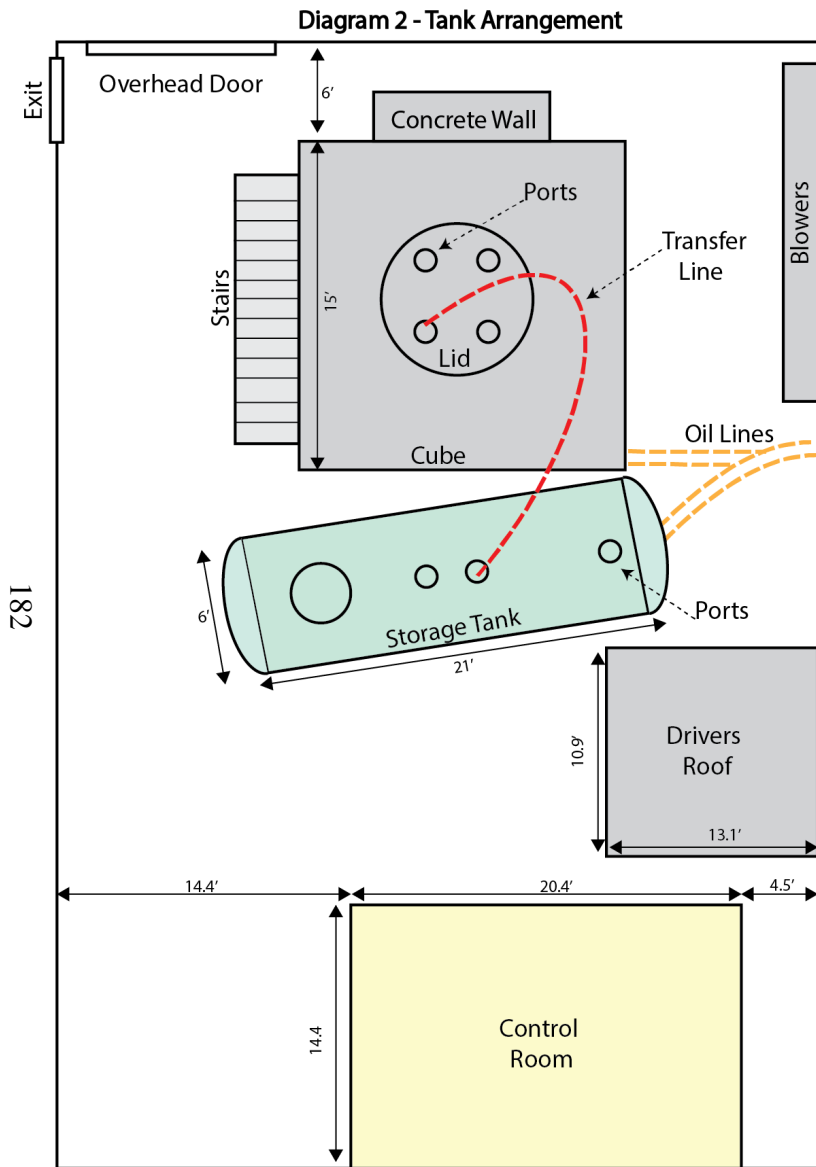
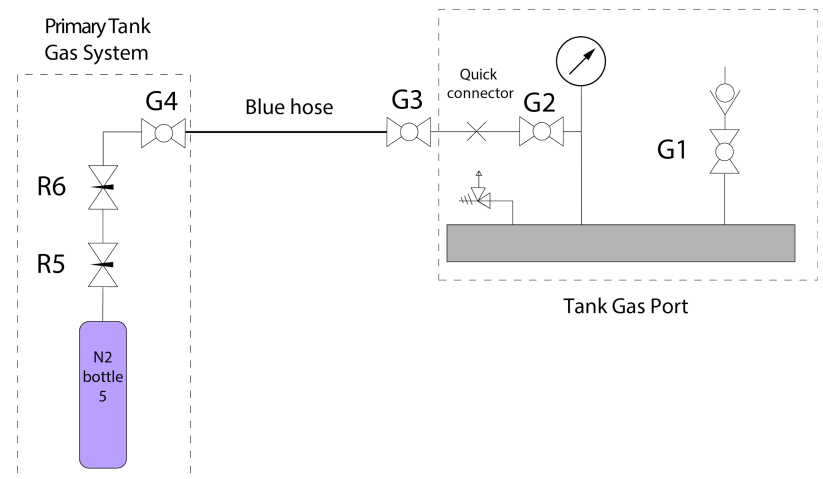


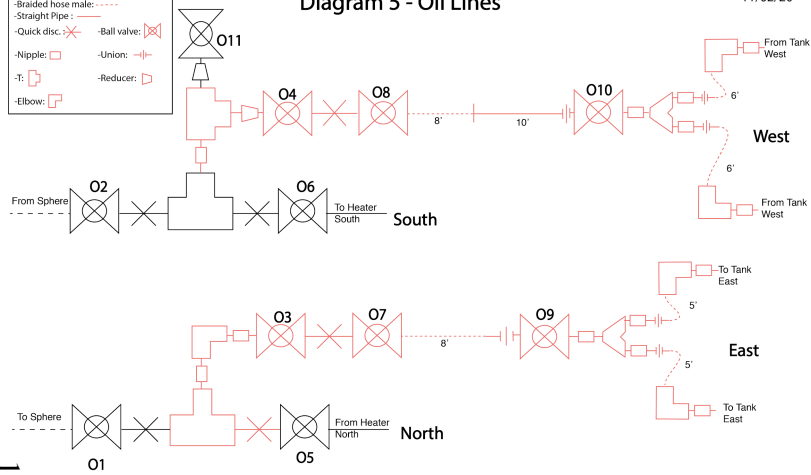
Diagram 4 - Primary Tank Gas System



- Braided hose male: - - - - -
- Straight Pipe: ———
- Quick disc: 
- Nipple: 
- T: 
- Elbow: 
- Ball valve: 
- Union: 
- Reducer: 

Diagram 5 - Oil Lines

11/02/20



183

Bibliography

- [1] M. S. Paoletti and D. P. Lathrop. Angular Momentum Transport in Turbulent Flow between Independently Rotating Cylinders. *Physical Review Letters*, 106(2):024501, January 2011. ISSN 0031-9007, 1079-7114. doi: 10.1103/PhysRevLett.106.024501. URL <https://link.aps.org/doi/10.1103/PhysRevLett.106.024501>.
- [2] Daniel R. Sisan, Nicolás Mujica, W. Andrew Tillotson, Yi-Min Huang, William Dorland, Adil B. Hassam, Thomas M. Antonsen, and Daniel P. Lathrop. Experimental Observation and Characterization of the Magnetorotational Instability. *Physical Review Letters*, 93(11):114502, September 2004. doi: 10.1103/PhysRevLett.93.114502. URL <https://link.aps.org/doi/10.1103/PhysRevLett.93.114502>. Publisher: American Physical Society.
- [3] Douglas H. Kelley, Santiago Andrés Triana, Daniel S. Zimmerman, Barbara Brawn, Daniel P. Lathrop, and Donald H. Martin. Driven inertial waves in spherical Couette flow. *Chaos: An Interdisciplinary Journal of Nonlinear Science*, 16(4):041105, December 2006. ISSN 1054-1500. doi: 10.1063/1.2390555. URL <https://aip.scitation.org/doi/10.1063/1.2390555>. Publisher: American Institute of Physics.
- [4] Daniel S. Zimmerman, Santiago Andrés Triana, Henri-Claude Nataf, and Daniel P. Lathrop. A turbulent, high magnetic Reynolds number experimental model of Earth's core. *Journal of Geophysical Research: Solid Earth*, 119(6):4538–4557, 2014. ISSN 2169-9356. doi: 10.1002/2013JB010733. URL <https://agupubs.onlinelibrary.wiley.com/doi/abs/10.1002/2013JB010733>.
- [5] Sabrina Sanchez, Alexandre Fournier, Katia J. Pinheiro, Julien Aubert, Sabrina Sanchez, Alexandre Fournier, Katia J. Pinheiro, and Julien Aubert. A mean-field Babcock-Leighton solar dynamo model with long-term variability. *Anais da Academia Brasileira de Ciências*, 86(1):11–26, March 2014. ISSN 0001-3765. doi: 10.1590/0001-37652014111212. URL http://www.scielo.br/scielo.php?script=sci_abstract&pid=S0001-37652014000100011&lng=en&nrm=iso&tlng=en. Publisher: Academia Brasileira de Ciências.
- [6] Emile Alglave and J. Boulard. *The Electric Light: Its History, Production, and Applications*. D. Appleton, 1884. Google-Books-ID: zh5pbMMwARQC.

- [7] Andrew D. Gilbert. Chapter 9 - Dynamo Theory. In S. Friedlander and D. Serre, editors, *Handbook of Mathematical Fluid Dynamics*, volume 2, pages 355–441. North-Holland, January 2003. doi: 10.1016/S1874-5792(03)80011-3. URL <https://www.sciencedirect.com/science/article/pii/S1874579203800113>.
- [8] Dudley M. L., James Reginald William, and Roberts Paul Harry. Time-dependent kinematic dynamos with stationary flows. *Proceedings of the Royal Society of London. A. Mathematical and Physical Sciences*, 425(1869):407–429, October 1989. doi: 10.1098/rspa.1989.0112. URL <https://royalsocietypublishing.org/doi/abs/10.1098/rspa.1989.0112>.
- [9] David Gubbins, C. N. Barber, S. Gibbons, and J. J. Love. Kinematic Dynamo Action in a Sphere. I Effects of Differential Rotation and Meridional Circulation on Solutions with Axial Dipole Symmetry. *Proceedings: Mathematical, Physical and Engineering Sciences*, 456(1998):1333–1353, 2000. ISSN 1364-5021. URL <https://www.jstor.org/stable/2665526>. Publisher: The Royal Society.
- [10] K. Finke and A. Tilgner. Simulations of the kinematic dynamo onset of spherical Couette flows with smooth and rough boundaries. *Physical Review E*, 86(1):016310, July 2012. doi: 10.1103/PhysRevE.86.016310. URL <https://link.aps.org/doi/10.1103/PhysRevE.86.016310>.
- [11] Johannes Wicht. Flow instabilities in the wide-gap spherical Couette system. *Journal of Fluid Mechanics*, 738:184–221, January 2014. ISSN 0022-1120, 1469-7645. doi: 10.1017/jfm.2013.545. URL https://www.cambridge.org/core/product/identifier/S0022112013005454/type/journal_article. Publisher: Cambridge University Press.
- [12] Daniel P. Lathrop and Cary B. Forest. Magnetic dynamos in the lab. *Physics Today*, 64(7):40–45, July 2011. ISSN 0031-9228. doi: 10.1063/PT.3.1166. URL <https://physicstoday.scitation.org/doi/10.1063/PT.3.1166>.
- [13] Santiago Andres Triana. *Inertial waves in a laboratory model of the Earth's core*. PhD thesis, 2011. URL <https://drum.lib.umd.edu/handle/1903/11480>. Accepted: 2011-07-06T05:43:37Z.
- [14] Daniel Zimmerman. *Turbulent Shear Flow in a Rapidly Rotating Spherical Annulus*. PhD thesis, 2010. URL <https://drum.lib.umd.edu/handle/1903/11184>. Accepted: 2011-02-19T07:00:21Z.
- [15] Edward R. Benton. Kinematic dynamo action with helical symmetry in an unbounded fluid conductor: Part 2. Further development of an explicit solution for the prototype case of lortz. *Geophysical & Astrophysical Fluid Dynamics*, 12(1):345–358, January 1979. ISSN 0309-1929. doi: 10.1080/03091927908242696. URL <https://doi.org/10.1080/03091927908242696>. Publisher: Taylor & Francis eprint: <https://doi.org/10.1080/03091927908242696>.

- [16] A Gailitis, O Lielausis, E Platacis, S Dement'ev, A Cifersons, G Gerbeth, T Gundrum, F Stefani, M Christen, and G Will. Magnetic field saturation in the Riga dynamo experiment. *PHYSICAL REVIEW LETTERS*, 86(14):3024–3027, April 2001. ISSN 0031-9007. doi: 10.1103/PhysRevLett.86.3024.
- [17] Mickaël Bourgoïn, Louis Marié, François Pétrélis, Cécile Gasquet, Alain Guigon, Jean-Baptiste Luciani, Marc Moulin, Frédéric Namer, Javier Burguete, Arnaud Chiffaudel, François Daviaud, Stephan Fauve, Philippe Odier, and Jean-François Pinton. Magnetohydrodynamics measurements in the von Kármán sodium experiment. *Physics of Fluids*, 14(9):3046–3058, September 2002. ISSN 1070-6631, 1089-7666. doi: 10.1063/1.1497376. URL <http://aip.scitation.org/doi/10.1063/1.1497376>.
- [18] Gary A. Glatzmaiers and Paul H. Roberts. A three-dimensional self-consistent computer simulation of a geomagnetic field reversal. *Nature*, 377(6546):203–209, September 1995. ISSN 1476-4687. doi: 10.1038/377203a0. URL <https://www.nature.com/articles/377203a0>. Number: 6546 Publisher: Nature Publishing Group.
- [19] Akira Kageyama and Tetsuya Sato. Computer simulation of a magnetohydrodynamic dynamo. II. *Physics of Plasmas*, 2(5):1421–1431, May 1995. ISSN 1070-664X. doi: 10.1063/1.871485. URL <https://aip.scitation.org/doi/abs/10.1063/1.871485>. Publisher: American Institute of Physics.
- [20] Ataru Sakuraba and Paul H. Roberts. Generation of a strong magnetic field using uniform heat flux at the surface of the core. *Nature Geoscience*, 2(11):802–805, November 2009. ISSN 1752-0908. doi: 10.1038/ngeo643. URL <https://www.nature.com/articles/ngeo643>. Number: 11 Publisher: Nature Publishing Group.
- [21] N. Schaeffer, D. Jault, H.-C. Nataf, and A. Fournier. Turbulent geodynamo simulations: a leap towards Earth's core. *Geophysical Journal International*, 211(1):1–29, October 2017. ISSN 0956-540X, 1365-246X. doi: 10.1093/gji/ggx265. URL <http://academic.oup.com/gji/article/211/1/1/3906752/Turbulent-geodynamo-simulations-a-leap-towards>.
- [22] Johannes Wicht and Sabrina Sanchez. Advances in geodynamo modelling. *Geophysical & Astrophysical Fluid Dynamics*, 113(1-2):2–50, March 2019. ISSN 0309-1929. doi: 10.1080/03091929.2019.1597074. URL <https://doi.org/10.1080/03091929.2019.1597074>. Publisher: Taylor & Francis eprint: <https://doi.org/10.1080/03091929.2019.1597074>.
- [23] E. J. Spence, K. Reuter, and C. B. Forest. A Spherical Plasma Dynamo Experiment. *The Astrophysical Journal*, 700(1):470–478, July 2009. ISSN 0004-637X. doi: 10.1088/0004-637X/700/1/470. URL <https://doi.org/10.1088%2F0004-637x%2F700%2F1%2F470>. Publisher: IOP Publishing.
- [24] D. Schmitt, T. Alboussière, D. Brito, P. Cardin, N. Gagnière, D. Jault, and H. C. Nataf. Rotating spherical Couette flow in a dipolar magnetic field: Experimental study of magneto-inertial waves. *J. Fluid Mech.*, 604:175–197, 2008. doi: 10.1017/S0022112008001298.

- [25] H. C. Nataf, T. Alboussiere, D. Brito, P. Cardin, N. Gagniere, D. Jault, and D. Schmitt. Rapidly rotating spherical Couette flow in a dipolar magnetic field: An experimental study of the mean axisymmetric flow. *PHYSICS OF THE EARTH AND PLANETARY INTERIORS*, 170(1-2):60–72, September 2008. ISSN 0031-9201. doi: 10.1016/j.pepi.2008.07.034.
- [26] Siegfried Grossmann, Detlef Lohse, and Chao Sun. High-Reynolds Number Taylor-Couette Turbulence. *Annual Review of Fluid Mechanics*, 48(1):53–80, 2016. doi: 10.1146/annurev-fluid-122414-034353. URL <https://doi.org/10.1146/annurev-fluid-122414-034353>.
- [27] Sander G. Huisman, Dennis P. M. van Gils, Siegfried Grossmann, Chao Sun, and Detlef Lohse. Ultimate Turbulent Taylor-Couette Flow. *Physical Review Letters*, 108(2):024501, January 2012. ISSN 0031-9007, 1079-7114. doi: 10.1103/PhysRevLett.108.024501. URL <https://link.aps.org/doi/10.1103/PhysRevLett.108.024501>.
- [28] X. Chavanne, F. Chill\‘{a}, B. Castaing, B. Hébral, B. Chabaud, and J. Chaussy. Observation of the Ultimate Regime in Rayleigh-Bénard Convection. *Physical Review Letters*, 79(19):3648–3651, November 1997. ISSN 0031-9007, 1079-7114. doi: 10.1103/PhysRevLett.79.3648. URL <https://link.aps.org/doi/10.1103/PhysRevLett.79.3648>.
- [29] Gregory S. Lewis and Harry L. Swinney. Velocity structure functions, scaling, and transitions in high-Reynolds-number Couette-Taylor flow. *Physical Review E*, 59(5):5457–5467, May 1999. doi: 10.1103/PhysRevE.59.5457. URL <https://link.aps.org/doi/10.1103/PhysRevE.59.5457>. Publisher: American Physical Society.
- [30] Daniel P. Lathrop, Jay Fineberg, and Harry L. Swinney. Transition to shear-driven turbulence in Couette-Taylor flow. *Physical Review A*, 46(10):6390–6405, November 1992. doi: 10.1103/PhysRevA.46.6390. URL <https://link.aps.org/doi/10.1103/PhysRevA.46.6390>.
- [31] Thomas H. van den Berg, Charles R. Doering, Detlef Lohse, and Daniel P. Lathrop. Smooth and rough boundaries in turbulent Taylor-Couette flow. *Physical Review E*, 68(3):036307, September 2003. ISSN 1063-651X, 1095-3787. doi: 10.1103/PhysRevE.68.036307. URL <https://link.aps.org/doi/10.1103/PhysRevE.68.036307>.
- [32] B. Dubrulle and F. Hersant. Momentum transport and torque scaling in Taylor-Couette flow from an analogy with turbulent convection. *The European Physical Journal B - Condensed Matter and Complex Systems*, 26(3):379–386, April 2002. ISSN 1434-6036. doi: 10.1140/epjb/e20020103. URL <https://doi.org/10.1140/epjb/e20020103>.
- [33] Bruno Eckhardt, Siegfried Grossmann, and Detlef Lohse. Torque scaling in turbulent Taylor-Couette flow between independently rotating cylinders. *Journal of Fluid Mechanics*, 581:221–250, June 2007. ISSN 0022-1120, 1469-7645. doi: 10.1017/S0022112007005629. URL https://www.cambridge.org/core/product/identifier/S0022112007005629/type/journal_article.

- [34] Ronald T. Merrill, M. W. McElhinny, and Phillip L. McFadden. *The magnetic field of the earth: paleomagnetism, the core, and the deep mantle*. Number v. 63 in International geophysics series. Academic Press, San Diego, Calif, 1996. ISBN 978-0-12-491245-8.
- [35] S. Chandrasekhar. *Hydrodynamic and Hydromagnetic Stability*. Dover, New York, 1961.
- [36] E. L. Koschmieder. *Bénard cells and Taylor vortices*. Cambridge monographs on mechanics and applied mathematics. Cambridge University Press, Cambridge [England] ; New York, 1993. ISBN 978-0-521-40204-0.
- [37] F. H. Busse. Bounds for turbulent shear flow. *Journal of Fluid Mechanics*, 41(1):219–240, March 1970. ISSN 1469-7645, 0022-1120. doi: 10.1017/S0022112070000599. URL <http://www.cambridge.org/core/journals/journal-of-fluid-mechanics/article/bounds-for-turbulent-shear-flow/0FBE2D21B8755E4D001E8651F42ECEBC>. Publisher: Cambridge University Press.
- [38] Arnaud Prigent, Bérengère Dubrulle, Olivier Dauchot, and Innocent Mutabazi. The Taylor-Couette Flow: The Hydrodynamic Twin of Rayleigh-Bénard Convection. In Innocent Mutabazi, José Eduardo Wesfreid, and Etienne Guyon, editors, *Dynamics of Spatio-Temporal Cellular Structures: Henri Bénard Centenary Review*, Springer Tracts in Modern Physics, pages 225–242. Springer, New York, NY, 2006. ISBN 978-0-387-25111-0. doi: 10.1007/978-0-387-25111-0_13. URL https://doi.org/10.1007/978-0-387-25111-0_13.
- [39] A. Barik, S. A. Triana, M. Hoff, and J. Wicht. Triadic resonances in the wide-gap spherical Couette system. *Journal of Fluid Mechanics*, 843:211–243, May 2018. ISSN 0022-1120, 1469-7645. doi: 10.1017/jfm.2018.138. URL <http://www.cambridge.org/core/journals/journal-of-fluid-mechanics/article/triadic-resonances-in-the-widegap-spherical-couette-system/36DB3C7127C67765D67F799CF05964A3>. Publisher: Cambridge University Press.
- [40] P. H. Roberts. Kinematic Dynamo Models. *Philosophical Transactions of the Royal Society of London. Series A, Mathematical and Physical Sciences*, 272(1230):663–698, 1972. ISSN 0080-4614. URL <http://www.jstor.org/stable/74140>. Publisher: The Royal Society.
- [41] R Stieglitz and U Muller. Experimental demonstration of a homogeneous two-scale dynamo. *PHYSICS OF FLUIDS*, 13(3):561–564, March 2001. ISSN 1070-6631. doi: 10.1063/1.1331315.
- [42] R. Monchaux, M. Berhanu, M. Bourgoïn, M. Moulin, Ph. Odier, J. F. Pinton, R. Volk, S. Fauve, N. Mordant, F. Petrelis, A. Chiffaudel, F. Daviaud, B. Dubrulle, C. Gasquet, L. Marie, and F. Ravelet. Generation of a magnetic field by dynamo action in a turbulent flow of liquid sodium. *PHYSICAL REVIEW LETTERS*, 98(4), January 2007. ISSN 0031-9007. doi: 10.1103/PhysRevLett.98.044502.

- [43] André Giesecke, Tobias Vogt, Thomas Gundrum, and Frank Stefani. Nonlinear Large Scale Flow in a Precessing Cylinder and Its Ability To Drive Dynamo Action. *Physical Review Letters*, 120(2):024502, January 2018. ISSN 0031-9007, 1079-7114. doi: 10.1103/PhysRevLett.120.024502. URL <https://link.aps.org/doi/10.1103/PhysRevLett.120.024502>.
- [44] Douglas H. Kelley, Santiago Andrés Triana, Daniel S. Zimmerman, Andreas Tilgner, and Daniel P. Lathrop. Inertial waves driven by differential rotation in a planetary geometry. *Geophysical & Astrophysical Fluid Dynamics*, 101(5-6):469–487, October 2007. ISSN 0309-1929. doi: 10.1080/03091920701561907. URL <https://doi.org/10.1080/03091920701561907>. Publisher: Taylor & Francis _eprint: <https://doi.org/10.1080/03091920701561907>.
- [45] Woodrow L. Shew and Daniel P. Lathrop. Liquid sodium model of geophysical core convection. *Physics of the Earth and Planetary Interiors*, 153(1):136–149, November 2005. ISSN 0031-9201. doi: 10.1016/j.pepi.2005.03.013. URL <https://www.sciencedirect.com/science/article/pii/S0031920105001755>.
- [46] Daniel S. Zimmerman, Santiago Andrés Triana, and D. P. Lathrop. Bi-stability in turbulent, rotating spherical Couette flow. *Physics of Fluids*, 23(6):065104, June 2011. ISSN 1070-6631. doi: 10.1063/1.3593465. URL <https://aip.scitation.org/doi/full/10.1063/1.3593465>.
- [47] S. A. Triana, D. S. Zimmerman, and D. P. Lathrop. Precessional states in a laboratory model of the Earth’s core. *Journal of Geophysical Research: Solid Earth*, 117(B4), 2012. ISSN 2156-2202. doi: 10.1029/2011JB009014. URL <https://onlinelibrary.wiley.com/doi/abs/10.1029/2011JB009014>. _eprint: <https://onlinelibrary.wiley.com/doi/pdf/10.1029/2011JB009014>.
- [48] Michel Rieutord, Santiago Andrés Triana, Daniel S. Zimmerman, and Daniel P. Lathrop. Excitation of inertial modes in an experimental spherical Couette flow. *Physical Review E*, 86(2):026304, August 2012. ISSN 1539-3755, 1550-2376. doi: 10.1103/PhysRevE.86.026304. URL <https://link.aps.org/doi/10.1103/PhysRevE.86.026304>.
- [49] E Bullard and H Gellman. Homogeneous dynamos and terrestrial magnetism. *Philosophical Transactions of the Royal Society of London. Series A, Mathematical and Physical Sciences*, 247(928):213–278, 1954.
- [50] P. A. Davidson. *An Introduction to Magnetohydrodynamics*. Cambridge University Press, 2001.
- [51] H. K. Moffatt. *Magnetic field generation in electrically conducting fluids*. Cambridge monographs on mechanics and applied mathematics. Cambridge University Press, Cambridge [Eng.] ; New York, 1978. ISBN 978-0-521-21640-1.

- [52] Stephen Childress and Andrew D. Gilbert. *Stretch, twist, fold: the fast dynamo*. Number m37 in Lecture notes in physics. Springer, Berlin ; [New York], 1995. ISBN 978-3-540-60258-3.
- [53] Takahiro Nakajima and Masaru Kono. Kinematic dynamos associated with large scale fluid motions. *Geophysical & Astrophysical Fluid Dynamics*, 60(1-4):177–209, November 1991. ISSN 0309-1929, 1029-0419. doi: 10.1080/03091929108220003. URL <https://www.tandfonline.com/doi/full/10.1080/03091929108220003>.
- [54] J. X Love and David Gubbins. Optimized kinematic dynamos. *Geophysical Journal International*, 124(3):787–800, March 1996. ISSN 0956540X, 1365246X. doi: 10.1111/j.1365-246X.1996.tb05638.x. URL <https://academic.oup.com/gji/article-lookup/doi/10.1111/j.1365-246X.1996.tb05638.x>.
- [55] I. V. Khalzov, B. P. Brown, C. M. Cooper, D. B. Weisberg, and C. B. Forest. Optimized boundary driven flows for dynamos in a sphere. *Physics of Plasmas*, 19(11):112106, November 2012. ISSN 1070-664X, 1089-7674. doi: 10.1063/1.4764048. URL <http://aip.scitation.org/doi/10.1063/1.4764048>.
- [56] R. Holme. Optimised axially-symmetric kinematic dynamos. *Physics of the Earth and Planetary Interiors*, 140(1):3–11, November 2003. ISSN 0031-9201. doi: 10.1016/j.pepi.2003.07.003. URL <http://www.sciencedirect.com/science/article/pii/S0031920103001614>.
- [57] D. N. Tomin and D. D. Sokoloff. Magnetic field in a fluctuating ABC flow. *Astronomy Letters*, 35(5):321–325, May 2009. ISSN 1562-6873. doi: 10.1134/S1063773709050053. URL <https://doi.org/10.1134/S1063773709050053>.
- [58] Mingtian Xu. Impact of small scale turbulent flows on dynamo actions. *Physics Letters A*, 379(6):577–580, March 2015. ISSN 0375-9601. doi: 10.1016/j.physleta.2014.12.009. URL <http://www.sciencedirect.com/science/article/pii/S0375960114012286>.
- [59] Ashley P. Willis. Optimization of the Magnetic Dynamo. *Physical Review Letters*, 109(25):251101, December 2012. doi: 10.1103/PhysRevLett.109.251101. URL <https://link.aps.org/doi/10.1103/PhysRevLett.109.251101>. Publisher: American Physical Society.
- [60] D. Holdenried-Chernoff, L. Chen, and A. Jackson. A trio of simple optimized axisymmetric kinematic dynamos in a sphere. *Proceedings of the Royal Society A: Mathematical, Physical and Engineering Sciences*, 475(2229):20190308, September 2019. doi: 10.1098/rspa.2019.0308. URL <https://royalsocietypublishing.org/doi/10.1098/rspa.2019.0308>. Publisher: Royal Society.
- [61] F. Stefani, G. Gerbeth, and A. Gailitis. Velocity Profile Optimization for the Riga Dynamo Experiment. In A. Alemany, Ph. Marty, and J. P. Thibault, editors, *Transfer Phenomena in Magnetohydrodynamic and Electroconducting Flows: Selected papers of the PAMIR Conference held in Aussois, France 22–26 September 1997*, Fluid Mechanics and Its

- Applications, pages 31–44. Springer Netherlands, Dordrecht, 1999. ISBN 978-94-011-4764-4. doi: 10.1007/978-94-011-4764-4_3. URL https://doi.org/10.1007/978-94-011-4764-4_3.
- [62] Xiaojue Zhu, Ruben A. Verschoof, Dennis Bakhuis, Sander G. Huisman, Roberto Verzicco, Chao Sun, and Detlef Lohse. Wall roughness induces asymptotic ultimate turbulence. *Nature Physics*, 14(4):417–423, April 2018. ISSN 1745-2481. doi: 10.1038/s41567-017-0026-3. URL <https://www.nature.com/articles/s41567-017-0026-3>.
- [63] Ruben A. Verschoof, Xiaojue Zhu, Dennis Bakhuis, Sander G. Huisman, Roberto Verzicco, Chao Sun, and Detlef Lohse. Rough-wall turbulent Taylor-Couette flow: The effect of the rib height. *The European Physical Journal E*, 41(10):125, October 2018. ISSN 1292-8941, 1292-895X. doi: 10.1140/epje/i2018-11736-2. URL <http://link.springer.com/10.1140/epje/i2018-11736-2>.
- [64] D. J. Tritton. *Physical fluid dynamics*. Oxford science publications. Clarendon Press ; Oxford University Press, Oxford [England] : New York, 2nd ed edition, 1988. ISBN 978-0-19-854489-0 978-0-19-854493-7.
- [65] L. D. Landau and E. M. Lifshitz. *Fluid Mechanics*. Theoretical Physics. Elsevier, Oxford, England, second edition, 2004.
- [66] G. K. Batchelor. *An introduction to fluid dynamics*. Cambridge University Press, 1967.
- [67] B. R. Morton. The generation and decay of vorticity. *Geophysical & Astrophysical Fluid Dynamics*, 28(3-4):277–308, April 1984. ISSN 0309-1929. doi: 10.1080/03091928408230368. URL <https://doi.org/10.1080/03091928408230368>. Publisher: Taylor & Francis _eprint: <https://doi.org/10.1080/03091928408230368>.
- [68] Henk Tennekes and John L. Lumley. *A First Course in Turbulence*. March 1972. doi: 10.7551/mitpress/3014.001.0001. URL <https://direct.mit.edu/books/book/4831/A-First-Course-in-Turbulence>.
- [69] Peter S Bernard and James M Wallace. *Turbulent Flow Analysis, Measurement, and Prediction*. 2002. ISBN 978-0-471-27538-1. URL <https://nbn-resolving.org/urn:nbn:de:101:1-201502081113>. OCLC: 904819316.
- [70] Ph Cardin, L. F. Cugliandolo, and Centre national de la recherche scientifique (France), editors. *Dynamos: École d’été de physique des Houches, session LXXXVIII, 30 July-24 August 2007: École thématique du CNRS*. Elsevier, Amsterdam ; Boston, 1st ed edition, 2008. ISBN 978-0-08-054812-8. Meeting Name: Ecole d’été de physique théorique (Les Houches, Haute-Savoie, France) OCLC: ocn229026040.
- [71] A. Gailitis, O. Lielausis, B. G. Karasev, I. R. Kirillov, and A. P. Ogorodnikov. The Helical MHD Dynamo. In J. Lielpeteris and R. Moreau, editors, *Liquid Metal Magnetohydrodynamics*, Mechanics of Fluids and Transport Processes,

- pages 413–419. Springer Netherlands, Dordrecht, 1989. ISBN 978-94-009-0999-1. doi: 10.1007/978-94-009-0999-1_50. URL https://doi.org/10.1007/978-94-009-0999-1_50.
- [72] Andrew D. Gilbert. Fast dynamo action in the Ponomarenko dynamo. *Geophysical & Astrophysical Fluid Dynamics*, 44(1-4):241–258, December 1988. ISSN 0309-1929. doi: 10.1080/03091928808208888. URL <https://doi.org/10.1080/03091928808208888>. Publisher: Taylor & Francis eprint: <https://doi.org/10.1080/03091928808208888>.
- [73] Keith Moffatt. The amplification of a weak applied magnetic field by turbulence in fluids of moderate conductivity. *Journal of Fluid Mechanics*, 11(4):625–635, December 1961. ISSN 1469-7645, 0022-1120. doi: 10.1017/S0022112061000779. URL <https://www.cambridge.org/core/journals/journal-of-fluid-mechanics/article/amplification-of-a-weak-applied-magnetic-field-by-turbulence-in-fluids/C6D880513AE4ECF5B37352B3B7F439C1>. Publisher: Cambridge University Press.
- [74] M. D. Nornberg, E. J. Spence, R. D. Kendrick, C. M. Jacobson, and C. B. Forest. Measurements of the magnetic field induced by a turbulent flow of liquid metal. *Physics of Plasmas*, 13(5):055901, May 2006. ISSN 1070-664X. doi: 10.1063/1.2173614. URL <https://aip.scitation.org/doi/10.1063/1.2173614>. Publisher: American Institute of Physics.
- [75] Romain Monchaux, Michael Berhanu, Sebastien Aumaitre, Arnaud Chiffaudel, Francois Daviaud, Berengere Dubrulle, Florent Ravelet, Stephan Fauve, Nicolas Mordant, Francois Petrelis, Mickael Bourgoin, Philippe Odier, Jean-Francois Pinton, Nicolas Plihon, and Romain Volk. The von Karman Sodium experiment: Turbulent dynamical dynamos. *PHYSICS OF FLUIDS*, 21(3), March 2009. ISSN 1070-6631. doi: 10.1063/1.3085724.
- [76] Peter Linstrom. NIST Chemistry WebBook, NIST Standard Reference Database 69, 1997. URL <http://webbook.nist.gov/chemistry/>. type: dataset.
- [77] J.K. Fink and L. Leibowitz. Thermodynamic and transport properties of sodium liquid and vapor. Technical Report ANL/RE-95/2, 94649, U.S. Department of Energy Office of Scientific and Technical Information, January 1995. URL <http://www.osti.gov/servlets/purl/94649-gXNdLI/webviewable/>.
- [78] Rubén E. Rojas, Artur Perevalov, Till Zürner, and Daniel P. Lathrop. Experimental study of rough spherical Couette flows: Increasing helicity toward a dynamo state. *Physical Review Fluids*, 6(3):033801, March 2021. doi: 10.1103/PhysRevFluids.6.033801. URL <https://link.aps.org/doi/10.1103/PhysRevFluids.6.033801>. Publisher: American Physical Society.
- [79] William Thielicke and Eize J. Stamhuis. PIVlab – Towards User-friendly, Affordable and Accurate Digital Particle Image Velocimetry in MATLAB. *Journal of Open Research Software*, 2, October 2014. ISSN 2049-9647. doi: 10.5334/jors.bl. URL <http://openresearchsoftware.metajnl.com/articles/10.5334/jors.bl/>.

- [80] D. J. Tritton. *Physical fluid dynamics*. Oxford science publications. Clarendon Press ; Oxford University Press, Oxford [England] : New York, 2nd ed edition, 1988. ISBN 978-0-19-854489-0 978-0-19-854493-7.
- [81] Hermann Schlichting and Klaus Gersten. *Boundary-Layer Theory*. Springer Berlin Heidelberg, Berlin, Heidelberg, 2017. ISBN 978-3-662-52917-1 978-3-662-52919-5. doi: 10.1007/978-3-662-52919-5. URL <http://link.springer.com/10.1007/978-3-662-52919-5>.
- [82] B Dubrulle, O Dauchot, F Daviaud, PY Longaretti, D Richard, and JP Zahn. Stability and turbulent transport in Taylor-Couette flow from analysis of experimental data. *PHYSICS OF FLUIDS*, 17(9), September 2005. ISSN 1070-6631. doi: 10.1063/1.2008999.
- [83] A. Tilgner. Driven inertial oscillations in spherical shells. *Physical Review E*, 59(2):1789–1794, February 1999. doi: 10.1103/PhysRevE.59.1789. URL <https://link.aps.org/doi/10.1103/PhysRevE.59.1789>. Publisher: American Physical Society.
- [84] Finke Konstantin. *Kinematic dynamo onset and magnetic field saturation in rotating spherical Couette and periodic box simulations*. PhD thesis, Georg-August-Universität Göttingen, Göttingen, 2013.
- [85] N. Yokoi. Cross helicity and related dynamo. *Geophysical & Astrophysical Fluid Dynamics*, 107(1-2):114–184, February 2013. ISSN 0309-1929. doi: 10.1080/03091929.2012.754022. URL <https://doi.org/10.1080/03091929.2012.754022>.
- [86] F. Pétrélis, N. Mordant, and S. Fauve. On the magnetic fields generated by experimental dynamos. *Geophysical & Astrophysical Fluid Dynamics*, 101(3-4):289–323, June 2007. ISSN 0309-1929. doi: 10.1080/03091920701523410. URL <https://doi.org/10.1080/03091920701523410>.
- [87] Thomas John, Ralf Stannarius, and Ulrich Behn. On-Off Intermittency in Stochastically Driven Electrohydrodynamic Convection in Nematics. *Physical Review Letters*, 83(4):749–752, July 1999. doi: 10.1103/PhysRevLett.83.749. URL <https://link.aps.org/doi/10.1103/PhysRevLett.83.749>. Publisher: American Physical Society.
- [88] Agris Gailitis, Olgerts Lielausis, Sergej Dement’ev, Ernests Platacis, Arnis Cifersons, Gunter Gerbeth, Thomas Gundrum, Frank Stefani, Michael Christen, Heiko Hänel, and Gotthard Will. Detection of a Flow Induced Magnetic Field Eigenmode in the Riga Dynamo Facility. *Physical Review Letters*, 84(19):4365–4368, May 2000. doi: 10.1103/PhysRevLett.84.4365. URL <https://link.aps.org/doi/10.1103/PhysRevLett.84.4365>. Publisher: American Physical Society.
- [89] Henri-Claude Nataf and Nadege Gagniere. On the peculiar nature of turbulence in planetary dynamos. *COMPTES RENDUS PHYSIQUE*, 9(7):702–710, September 2008. ISSN 1631-0705. doi: 10.1016/j.crhy.2008.07.009.
- [90] J.-F. Pinton and R. Labbé. Correction to the Taylor hypothesis in swirling flows. *Journal de Physique II*, 4(9):1461–1468, September 1994. ISSN 1155-4312, 1286-4870. doi:

10.1051/jp2:1994211. URL <http://jp2.journaldephysique.org/10.1051/jp2:1994211>.

- [91] Douglas H. Kelley. *Rotating, hydromagnetic laboratory experiment modelling planetary cores*. PhD thesis, 2009. URL <https://drum.lib.umd.edu/handle/1903/9100>. Accepted: 2009-07-02T05:30:49Z.
- [92] Rodolfo Ostilla-Mónico, Erwin P. van der Poel, Roberto Verzicco, Siegfried Grossmann, and Detlef Lohse. Exploring the phase diagram of fully turbulent Taylor–Couette flow. *Journal of Fluid Mechanics*, 761:1–26, December 2014. ISSN 0022-1120, 1469-7645. doi: 10.1017/jfm.2014.618. URL https://www.cambridge.org/core/product/identifier/S0022112014006181/type/journal_article.
- [93] Dennis P. M. van Gils, Sander G. Huisman, Siegfried Grossmann, Chao Sun, and Detlef Lohse. Optimal Taylor–Couette turbulence. *Journal of Fluid Mechanics*, 706: 118–149, September 2012. ISSN 0022-1120, 1469-7645. doi: 10.1017/jfm.2012.236. URL https://www.cambridge.org/core/product/identifier/S0022112012002364/type/journal_article.